Universidade de Aveiro Departamento de Física
2009

João Cunha de Sequeira Amaral

Estudos em acoplamentos magnéticos e efeito magnetocalórico

Studies on magnetocaloric and magnetic coupling effects

Dissertação apresentada à Universidade de Aveiro para cumprimento dos requisitos necessários à obtenção do grau de Doutor em Física, realizada sob a orientação científica do Doutor Vítor Brás de Sequeira Amaral, Professor Catedrático do Departamento de Física da Universidade de Aveiro e co-orientação do Doutor João Pedro Esteves de Araújo, Professor Auxiliar do Departamento de Física da Faculdade de Ciências da Universidade do Porto.

Apoio financeiro da FCT e do FSE no âmbito do III Quadro Comunitário de Apoio.

Aos meus pais e família.

o júri

presidente

Prof. Doutor Henrique Manuel Morais Diz
Professor Catedrático da Universidade de Aveiro

Prof. Doutor Bernard Barbara
Director de Investigação, Instituto Néel, CNRS, Grenoble – França

Prof. Doutor José Fernando Ferreira Mendes
Professor Catedrático da Universidade de Aveiro

Prof. Doutor Vítor Brás de Sequeira Amaral
Professor Catedrático da Universidade de Aveiro

Prof. Doutor Karl G. Sandeman
Investigador da Faculdade de Ciências Naturais do Imperial College, Londres – Reino Unido

Prof. Doutor João Pedro Esteves de Araújo
Professor Auxiliar da Faculdade de Ciências da Universidade do Porto

agradecimentos

Passados quatro anos de investigação associados ao meu doutoramento, sinto-me privilegiado pelas numerosas colaborações e amizades que fiz. Há uma lista extensa de pessoas às quais somente palavras escritas não são suficientes para mostrar o meu apreço pela ajuda, companhia, amizade, colaboração, troca de ideias e todos os momentos bem passados. Fazer uma lista de todas as pessoas a quem agradeço seria fastidioso, enquanto que mencionar só algumas seria deselegante. Sendo assim, irei ser breve: a todos que me acompanharam, quer nos bons ou maus momentos, deixo aqui o mais sincero agradecimento.

palavras-chave

Materiais magnéticos, transições de fase, acoplamento magnético, efeito magnetocalórico

resumo

O presente trabalho apresenta novas metodologias desenvolvidas para a análise das propriedades magnéticas e magnetocalóricas de materiais, sustentadas em considerações teóricas a partir de modelos, nomeadamente a teoria de transições de fase de Landau, o modelo de campo médio molecular e a teoria de fenómeno crítico. São propostos novos métodos de escala, permitindo a interpretação de dados de magnetização de materiais numa perspectiva de campo médio molecular ou teoria de fenómeno crítico. É apresentado um método de estimar a magnetização espontânea de um material ferromagnético a partir de relações entropia/magnetização estabelecidas pelo modelo de campo médio molecular. A termodinâmica das transições de fase magnéticas de primeira ordem é estudada usando a teoria de Landau e de campo médio molecular (modelo de Bean-Rodbell), avaliando os efeitos de fenómenos fora de equilíbrio e de condições de mistura de fase em estimativas do efeito magnetocalórico a partir de medidas magnéticas. Efeitos de desordem, interpretados como uma distribuição na interacção magnética entre iões, estabelecem os efeitos de distribuições químicas/estruturais nas propriedades magnéticas e magnetocalóricas de materiais com transições de fase de segunda e de primeira ordem.

O uso das metodologias apresentadas na interpretação das propriedades magnéticas de variados materiais ferromagnéticos permitiu obter: 1) uma análise quantitativa da variação de spin por ião Gadolínio devido à transição estrutural do composto $Gd_5Si_2Ge_2$, 2) a descrição da configuração de *cluster* magnético de iões Mn na fase ferromagnética em manganites da família La-Sr e La-Ca, 3) a determinação dos expoentes críticos β e δ do Níquel por métodos de escala, 4) a descrição do efeito da pressão nas propriedades magnéticas e magnetocalóricas do composto $LaFe_{11.5}Si_{1.5}$ através do modelo de Bean-Rodbell, 5) uma estimativa da desordem em manganites ferromagnéticas com transições de segunda e primeira ordem, 6) uma descrição de campo médio das propriedades magnéticas da liga $Fe_{23}Cu_{77}$, 7) o estudo de efeitos de separação de fase na família de compostos $La_{0.70-x}Er_xSr_{0.30}MnO_3$ e 8) a determinação realista da variação de entropia magnética na família de compostos de efeito magnetocalórico colossal $Mn_{1-x-y}Fe_xCr_yAs$.

Contents

Chapter 1

The magnetocaloric effect

The magnetocaloric effect (MCE) was discovered by the german physicist Emil Warburg in 1881 [1]. The effect consists in a change of the temperature of a magnetic material that results from thermal coupling between the lattice and the magnetic degrees of freedom, from a change in applied magnetic field. The discovery of Warburg was made while studying a sample of iron. This points us to the fact that the MCE can have enough intensity as to create an easily observable change in the temperature of the magnetic material. All magnetic materials present a MCE, but its dependence on external factors will be correlated to the individual properties of the magnetic system.

The fist major advance in magnetocaloric applications occurred in the late 1920s when cooling via adiabatic demagnetization was independently proposed by Debye [2] and Giauque [3]. The application of the adiabatic demagnetization process made it possible to reach the very low temperature value of 0.25 K in the early 1930s [4], by using an applied field of 0.8 T and 61 g of the paramagnetic salt $Gd_2(SO_4)_3{\cdot}8H_2O$ as the magnetic refrigerant.

A technique to study magnetic materials based on the MCE had a great impact on the 1950s and 1960s [5], where the MCE of a material was measured as to determine the spontaneous magnetization of materials when the magnetic domain effect prevented its measurement by bulk magnetometry.

The range for further applications of the MCE was increased in 1967, when Resler and Rosensweig [6] proposed a thermomagnetic power source based on the MCE of iron. This device would operate between 770°C (ferromagnetic to paramagnetic transition temperature of iron) and 500°C, with an efficiency of 15%.

The first room-temperature magnetic refrigeration device was idealized by G. V. Brown in 1976 [7]. Based on the MCE of metallic Gd, this device was built and achieved a temperature range of 47°C, from 46°C to -1°C (encompassing the magnetic transition temperature of Gd), using an applied magnetic field of 7 Tesla.

A major advance in the magnetocaloric studies of materials and applications was reported by the group of Pecharsky and Gschneidner in 1997 [8], as the first experimental observation of

the so-called giant MCE. The discovery of materials that show a MCE up to three times higher than the most promising magnetic refrigeration materials at the time gave a tremendous boost to magnetocaloric research either in materials or devices. From then on, other reports of giant MCE materials have been presented. The common denominator of a giant MCE material is the first-order character of the magnetic transition, usually as the result of a magnetostructural coupling.

More recently, the colossal MCE was reported by the group of Sérgio Gama [9]. The large values of MCE (up to two orders of magnitude higher than previous MCE values) was a very surprising result. The theoretical limit of magnetic entropy change is broken by these colossal MCE materials, and set forth the expectation of an enormous boost to magnetic cooling device efficiency.

At the time of writing, magnetic refrigeration device design is a very active field of research. Over thirty magnetic refrigeration devices are known to exist in research institutes around the world [10]. Theoretical and experimental studies of the magnetocaloric effect in materials is also a thriving field in science, and an almost exponential increase of published articles in the theme has occurred since the discovery of the giant MCE in 1997, as seen in Figure 1.1, from Ref. [10].

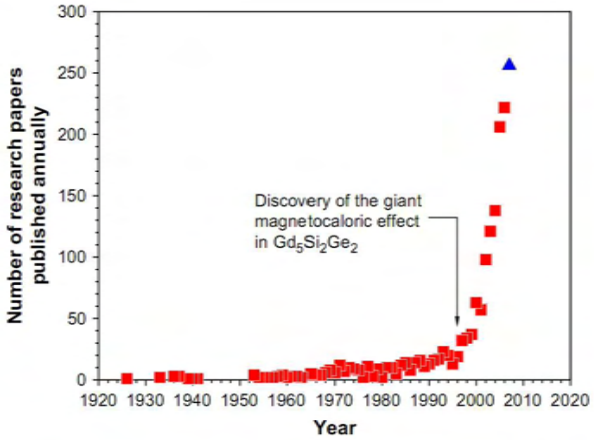

Figure 1.1: The number of research papers published annually over the past 80 years containing the word "magnetocaloric" in the title, abstract, or among the keywords, from Ref. [10]. The blue triangle represents papers published from January to July of 2007.

1.1 Background

In this section, a preliminary description of the MCE phenomenon will be made. A simplified microscopical description will establish the fundamental driving force behind the MCE, and an overview of the basic thermodynamics behind the MCE will also be presented. As described in the previous section, the MCE results from the thermal coupling between

the lattice and the magnetic degrees of freedom. In general terms, the magnetic degrees of freedom correspond to the magnetic entropy. Let us consider a paramagnetic material under adiabatic conditions, with and without an external magnetic field, as shown in Figure 1.2.

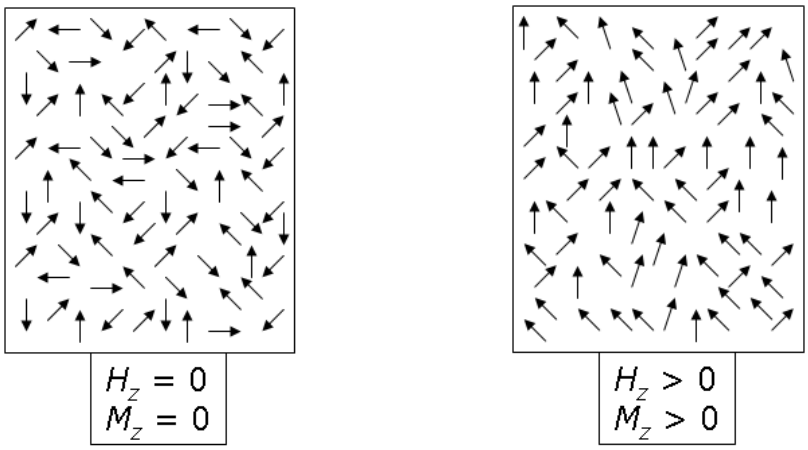

Figure 1.2: Paramagnetic material under a) null applied external field and b) external applied magnetic field.

The application of this external magnetic field changes the magnetic entropy of the system, since there is a change in the magnetic degrees of freedom for each of the spins. For this simplified example, there is a decrease of magnetic entropy when we apply the external field. So if we consider the temperature of the system as T, when applying the external magnetic field H, there occurs a change in magnetic entropy of ΔS. This change of entropy will then correspond to a heat flux Q [11]:

$$Q = T\Delta S \tag{1.1}$$

The thermal coupling between the purely magnetic part of the material to its lattice will then produce a change in temperature, that will depend on the specific heat C_p of the material.

$$\Delta T = \frac{Q}{C_p} \tag{1.2}$$

In the example of Figure 1.2, there is a reduction of magnetic entropy when magnetic field is applied. Consequently, as the total entropy is conserved (under adiabatic conditions), there occurs a positive heat flux to the lattice, corresponding to a positive vale of ΔT. In other words, when applying a magnetic field, the material heats up due to the MCE, and will cool down when the field is removed.

In a more macroscopic description, we can construct a more complete set of thermody-

namic relations, considering the bulk magnetization M as the thermodynamic variable of the system.

We define the internal energy of the system, U, as a function of the extensive variables entropy, volume and magnetization:

$$U = U(S, V, M) \tag{1.3}$$

which, in differential form leads to:

$$dU = TdS - pdV + HdM, \tag{1.4}$$

which defines the intensive parameters T, p and H.

By using the following Maxwell relation,

$$\left(\frac{\partial S}{\partial H}\right)_{T,V} = \left(\frac{\partial M}{\partial T}\right)_{H,V} , \tag{1.5}$$

we obtain, in isothermal and isochoric conditions:

$$dS = \left(\frac{\partial M}{\partial T}\right)_{H,V} dH, \tag{1.6}$$

a direct relation between entropy change, the variation of M with T at a constant H, and a change in H.

If we consider the specific heat at constant H, the adiabatic temperature change is given as

$$C_H dT = -\left(\frac{\partial M}{\partial T}\right)_{H,V} dH. \tag{1.7}$$

1.2 Applications

The application of the MCE in the adiabatic demagnetization process proposed by Giauque and Debye [4] follows the isothermal/adiabatic thermal cycle shown in Figure 1.3:

An alternate process to the isothermal/adiabatic cycle was presented by Brown [7], for a near room-temperature magnetic refrigeration device. Figure 1.4 shows the entropy versus temperature plot, and Figure 1.5 shows a schematic representation of the device motion step along the cooling cycle.

It is worth noting that after Brown's device in 1976, there were no breakthrough advances in room-temperature magnetic cooling technology, until the discovery of the giant MCE in 1997. As important as that discovery was, another strong driving force behind new developments in magnetic cooling devices were the advances in permanent magnet technology. Brown's device used a 7 T superconducting magnet as a field source. Such a device was unfeasible as a general purpose cooling device, and so magnetic cooling was pretty much a

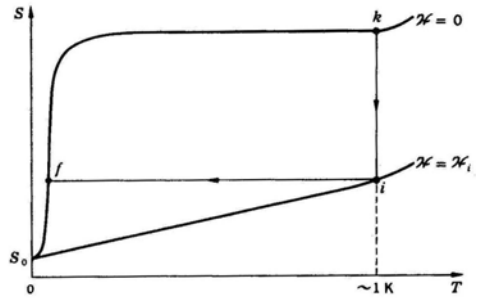

Figure 1.3: Thermal cycle of the adiabatic demagnetization cycle. The isothermal (k→ i) and adiabatic (i→ f) processes were proposed by Giauque and Debye to obtain sub-Kelvin temperatures, from Ref. [12].

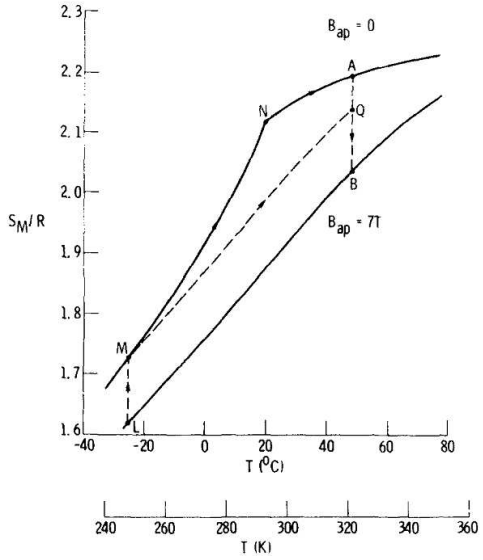

Figure 1.4: Magnetic Stirling cycle as proposed by Brown for a near-room temperature magnetic refrigeration device, using Gd metal [7].

commercially unviable technology. The high value of applied magnetic field (over 2T) that can now be obtained by arrays of permanent magnets such the NdFeB alloy makes a magnetic cooler much more attractive in terms of being a practical device. This is visible in the field sources of the most recent magnetic cooling prototypes, as shown in Figure 1.6.

The driving force behind the strong recent development of magnetic refrigeration technology is the fact that the cooling efficiency of a magnetic cooling device (60 % of Carnot efficiency) can be much larger than a gas compression cycle (usually no larger than 15 % due to the low efficiency of compressors), together with the fact that magnetic refrigeration uses no gases, lowering its environmental impact in terms of global warming, compared to vapor refrigeration cycles.

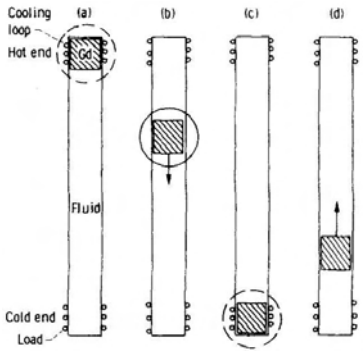

Figure 1.5: Schematic representation of the device motion in the steps of the magnetic cooling cycle (Figure 1.4) of Brown [7].

Name	Location	Announcement date	Type	Max. cooling power (W)	Max. ΔT (K)	Max. magnetic field[a] (kOe)	Regenerator material	Reference
Univ. Quebec, Trois Rivieres	Trois Rivieres, Quebec, Canada	Feb. 2004	Reciprocating	2	14	20 (S)	Gd–R alloys[b]	Richard et al. (2004)
George Washington Univ.	Ashburn, Virginia, USA	June 2005	Reciprocating	?	5	20 (P)	Gd pwdr.	Shir et al. (2005)
Nanjing Univ.	Nanjing, China	Sept. 27, 2005	Reciprocating	40	25	14 (H)	Gd pwdr. $Gd_5(Si,Ge)_4$ pwdr.	Lu et al. (2005)
Tokyo Inst. Tech.	Yokohama, Japan	Sept. 27, 2005	Rotary	60	4	7.7 (P)	Gd–R alloys[b]	Okamura et al. (2006)
Univ. Victoria	Victoria, Canada	Sept. 27, 2005	Reciprocating	?	50	20 (S)	Gd–R alloys[b]	Rowe et al. (2005)
Astronautics	Madison, Wisconsin, USA	Sept. 27, 2005	Rotary	50	25	15 (P)	Gd, Gd alloys[b] $La(Fe,Si)_{13}H_x$	Zimm et al. (2006)
Sichuan Univ.	Chengdu, China	April 11, 2007	Rotary	40	11.5	15 (P)	Gd particles	Chen et al. (2007)
Astronautics	Madison, Wisconsin, USA	April 12, 2007	Rotating magnet	220	11	14 (H)	Gd plates	Zimm et al. (2007)
Sichuan Univ.	Chengdu, China	April 12, 2007	Rotary	?	6.2	7.8 (P)	Gd sheets in water	Tang et al. (2007)
Univ. Victoria	Victoria, British Columbia, Canada	April 13, 2007	Rotary	?	13	14 (H)	Gd particles	Tura and Rowe (2007)
Chelyabinsk State Univ.	Chelyabinsk, Russia	April 13, 2007	Rotary	?	?	9 (P)	Gd and Heusler alloy	Buchelnikov et al. (2007)
Tokyo Inst. Tech.	Yokohama, Japan	April 13, 2007	Rotary	540	7.5	11 (P)	Gd spheres	Okamura et al. (2007)
Univ. Ljubljana	Ljubljana, Slovenia	April 13, 2007	Rotary	?	?	9.7 (P)	Various	Poredos and Sarlah (2007)

a Magnetic field source: S = superconducting magnet; P = permanent magnet; H = Halbach magnet.
b Layered bed.

Figure 1.6: Magnetic cooling prototypes announced between 2004 and 2007 [10].

1.3 Measuring the magnetocaloric effect

The two thermodynamic parameters that describe the MCE, the adiabatic temperature change ΔT_{ad} and isothermal entropy change ΔS_M can be estimated by several methods, using results from thermal/calorimetric and magnetization measurements [13].

1.3.1 Adiabatic temperature change

The adiabatic temperature change ΔT_{ad} can be directly measured as the temperature difference of the material before and after the field change, which is simply:

$$\Delta T_{\mathrm{ad}} = T_{H_{\mathrm{final}}} - T_{H_{\mathrm{initial}}} \ . \tag{1.8}$$

By performing the direct measurement on various initial temperature values and field values, the dependence of ΔT_{ad} on T and ΔH is determined. There are several experimental considerations that need to be taken into account when performing these adiabatic temperature change measurements. First of all, the method to measure temperature needs to be adequate. If temperature is measured by a thermocouple, the mass of the thermocouple itself needs to be sufficiently lower than that of the sample, so that heat flow from sample to thermocouple is negligible compared to the energy change due to the magnetocaloric process. Also, the induction of current from the applied magnetic field change in the thermocouple needs also to be minimized by geometry, and/or removed from the directly acquired results. A non-contact thermal method can also be used. This methodology would present a solution to some of the limitations of measuring temperature change with a thermocouple. Additional concerns would arise, namely the response time of the sensor, any possible internal inductions effects due to the field change and also calibration issues dependent on the sensor type.

ΔT_{ad} can be indirectly determined by measuring the specific heat at constant pressure, C_p, under an applied magnetic field change, together with magnetization measurements:

$$\Delta T_{\mathrm{ad}}(T, H) = -\int_0^{H'} \frac{T}{C(T,H)} \left(\frac{\partial M}{\partial T}\right)_H dH \tag{1.9}$$

1.3.2 Isothermal magnetic entropy change

The most usual way to estimate the magnetic entropy change is by performing isothermal magnetization measurements. We will go into further detail on this topic later in this work. A simplified approach to estimate ΔS_M from magnetization measurements is by integrating the Maxwell relation shown in Eq. 1.5:

$$\Delta S_M = \int_0^{H'} \left(\frac{\partial M}{\partial T}\right) dH, \tag{1.10}$$

which, by numerically approximation can be calculated by

$$\Delta S_M = \sum_0^{H'} \left(\frac{M_{i+1} - M_i}{T_{i+1} - T_i}\right) \Delta H_i, \tag{1.11}$$

where i identifies each measured isotherm.

Specific heat (C_p) measurements can also be used to indirectly determine ΔS_M, by measuring at different applied magnetic fields:

$$\Delta S_M = \int_0^{T'} \frac{C_p(T,H) - C_p(T,0)}{T} dT \tag{1.12}$$

It is worth noting that numerical approximations are present in the various methodologies presented here. The limitations of the usual numerical procedures have been extensively analyzed in a seminal work of Pecharsky and Gschneidner [14].

1.4 Materials research

The intensity of the MCE (either ΔT_{ad} or ΔS_M), is clearly of critical importance when considering a material as a potential magnetic cooling device component. The temperature range that can be obtained, as well as the thermal power of the device is related to the amount of isothermal magnetic entropy change per field cycle (or corresponding adiabatic temperature change). Eq. 1.7 shows us that at a constant H, the entropy change is proportional to $\partial M/\partial T$. This explains why Giauque and MacDougall used a paramagnetic salt to obtain sub-Kelvin temperatures, and also why Gd was chosen by Brown as the active magnetic refrigeration material. Gd is a ferromagnetic material with ferromagnetic/paramagnetic transition temperature (Curie temperature - T_C) $\sim$ 293 K. At a constant H, $M(T)$ of a ferromagnetic material can easily be schematically described, as shown in Figure 1.7.

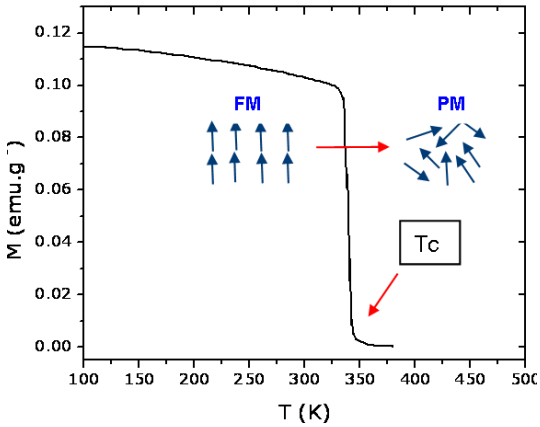

Figure 1.7: Schematic representation of magnetization versus temperature of a ferromagnetic material near its Curie temperature.

Since the maximum value of $\partial M/\partial T$ of a ferromagnetic material occurs in the vicinity of its Curie temperature, the operating temperature range of a ferromagnetic refrigerant material is defined. With a T_C near room temperature, Gd is the most widely used magnetic refrigerant material for room-temperature applications. Values of magnetic entropy change ΔS_M and

adiabatic temperature change ΔT_{ad} of Gd are commonly used as the basis to compare the magnetocaloric properties of other materials. Figure 1.8 shows ΔT_{ad} and ΔS_M of Gd due to an applied field change of 7 T [7].

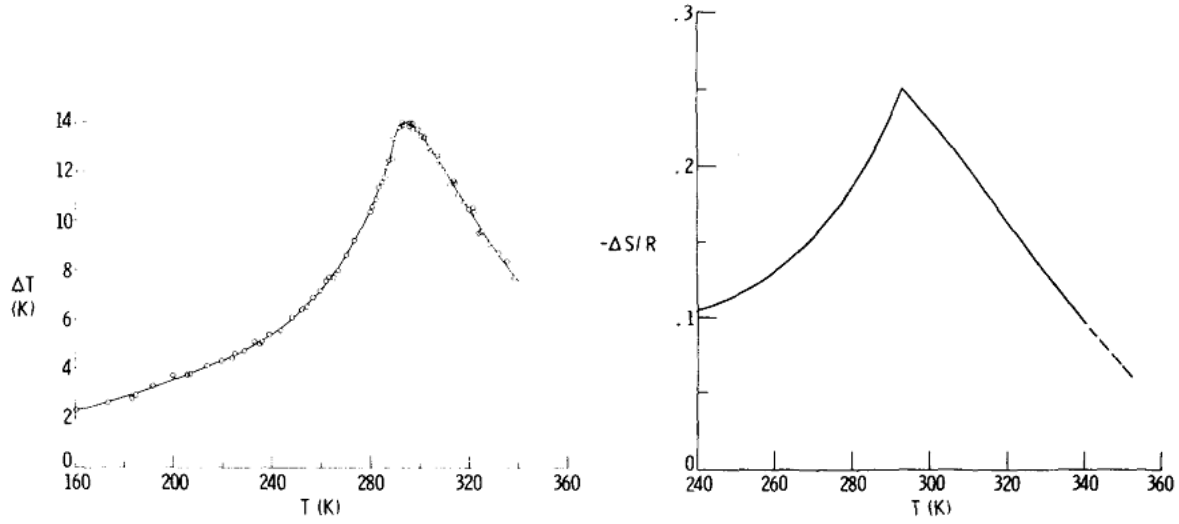

(a) (b)

Figure 1.8: a) Adiabatic temperature change and b) isothermal magnetic entropy change of Gd, under an applied magnetic field change of 7 T [7].

Another important definition to take into account when considering the magnetocaloric properties of a material in terms of applications is the relative cooling power (RCP), defined as:

$$\mathrm{RCP} = \Delta S_M(\mathrm{max}) \times \delta T_{\mathrm{FWHM}}. \tag{1.13}$$

The RCP gives us an idea of the cooling efficiency of the material in the vicinity of a transition, since the full width at half maximum of the entropy change curve is taken into account. Figure 1.9 shows Nickel as an example of calculating RCP.

There are alternative ways to quantify the applicability of a material for magnetic cooling applications. A magnetic cooling capacity (q), can be calculated using the definition of Gschneidner *et al.* [15]:

$$q = \int_{FWHM} \Delta S_M dT, \tag{1.14}$$

which takes into account in a more rigorous way the shape of the magnetic entropy curve, and not just the maximum and FWHM. Apart from some exceptions, particularly from the group of Provenzano and Shull [16], the simpler RCP calculation is the most widely used.

The units chosen to indicate the value of ΔS_M are also in need of consideration. The most usual units chosen are $\mathrm{JK^{-1}kg^{-1}}$. Other possibilities are $\mathrm{mJK^{-1}mol^{-1}}$ and $\mathrm{mJK^{-1}cm^{-3}}$. The

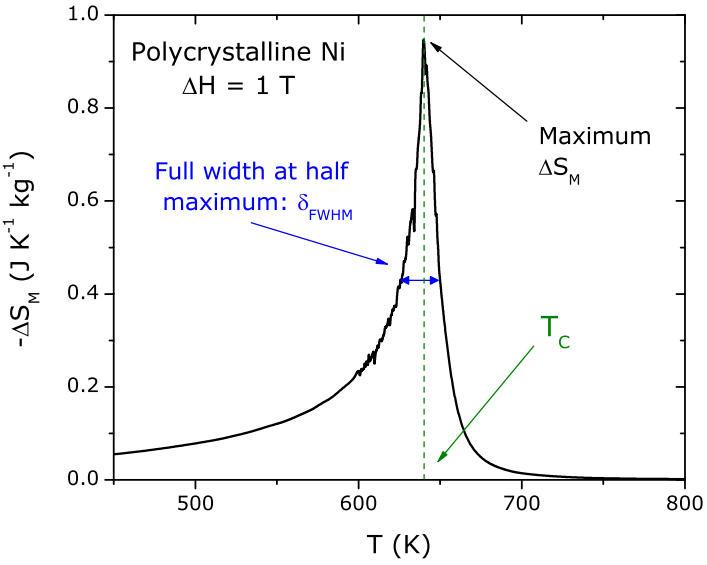

Figure 1.9: Determination of the relative cooling power of Ni, corresponding to an applied magnetic field change from 0 to 1 T.

reason behind the generalized use of the $\mathrm{JK^{-1}kg^{-1}}$ units is one of convenience, since ΔS_M is usually determined from magnetization measurements, which are typically normalized to mass, not volume. In terms of applications, the choice of $\mathrm{mJK^{-1}cm^{-3}}$ units is more practical, since the amount of material to be used in a device is normally limited by volume, not weight. Choosing the $\mathrm{mJK^{-1}mol^{-1}}$ units allows the comparison of the magnetocaloric properties of materials in a more fundamental way, since weight and volume do not affect the final value. In this work, we will present our results in the more usual $\mathrm{JK^{-1}kg^{-1}}$ units.

1.5 The giant magnetocaloric effect

Understandably, metallic Gd has been the prototypical magnetic material for room-temperature magnetocaloric. The high value of entropy change, together with the T_C value of around room-temperature made this so. In 1997, Pecharsky and Gschneidner [8] first reported on the existence of the giant magnetocaloric effect, in $Gd_5Si_2Ge_2$. Figure 1.10 shows the magnetic entropy change and adiabatic temperature change of this material, compared to Gd.

Both the magnetic entropy change and adiabatic temperature change are considerably higher than those of Gd, exceeding "the reversible (with respect to an alternating magnetic field) magnetocaloric effect in any known magnetic material by at least a factor of 2" [8].

Quoting the authors, this is due to a "first order ferromagnetic (I) $\leftrightarrow$ ferromagnetic (II) phase transition at 276 K and its unique magnetic field dependence".

This milestone work re-ignited the widespread interest in the magnetocaloric properties

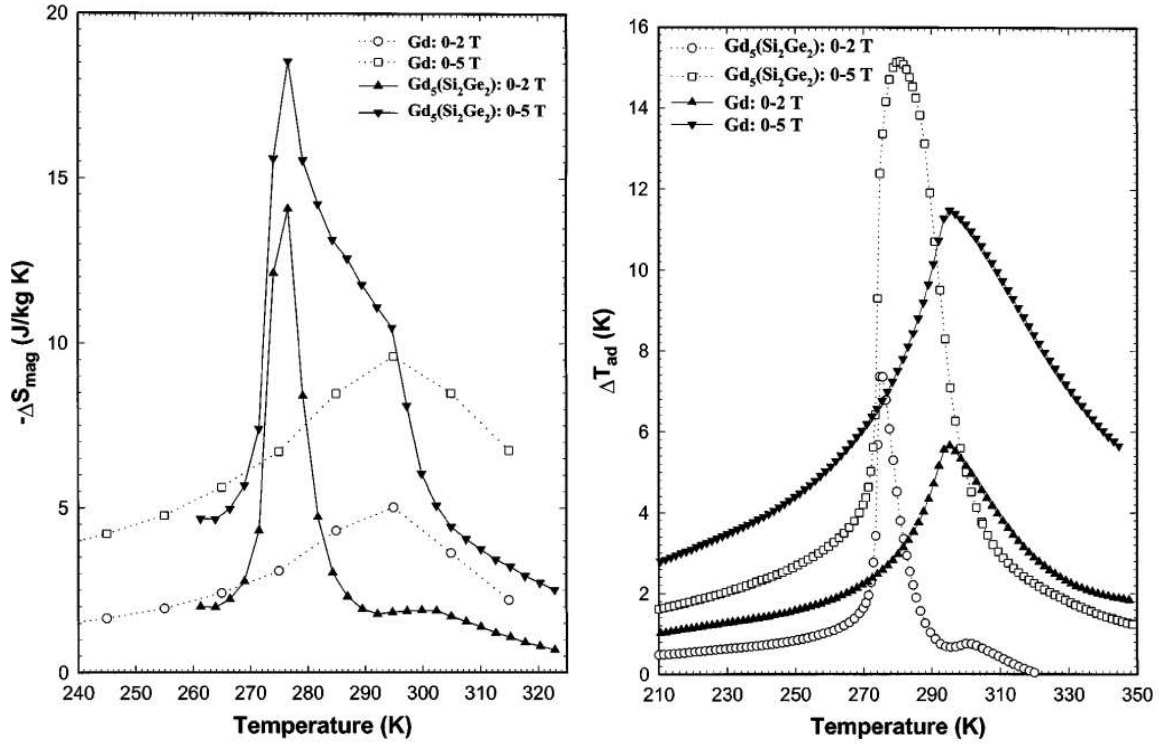

Figure 1.10: a) Magnetic entropy change and b) adiabatic temperature change of $Gd_5Si_2Ge_2$, under an applied magnetic field change from 0 to 2, and from 0 to 5 T, compared to Gd [8].

of materials, with a large focus on first-order phase transitions, to study this giant MCE. This effect was later observed in many types of materials, including the itinerant-electron La-Fe-Si system [17, 18, 19], $MnAs_{1-x}Sb_x$ [20], $MnFeP_{0.45}As_{0.55}$ [21], manganite systems [22], shape-memory alloys [23], RCo_2 alloys [24], and others [25, 26, 10], all sharing the first-order nature of the transition.

The general consensus for the reason behind the large values of magnetic entropy change is the sum of the entropy changes associated with the transition. Compared to a second-order magnetic phase transition system, the lattice entropy change due to the structural/volume change and electron entropy change can be comparable to the magnetic entropy change in a first-order transition system. This has been explored by many authors, in an attempt to separate the contributions to the total entropy change, in many materials, such as the RSiGe alloys [27, 28], and the LaFeSi alloys [29]. This topic will be analyzed in further detail later.

1.6 The colossal magnetocaloric effect

With an intense search for giant magnetocaloric materials for room-temperature magnetic refrigeration applications underway, Gama and co-workers reported on the existence of a pressure-induced Colossal magnetocaloric effect, in MnAs, as shown in Figure 1.11 from Ref. [9].

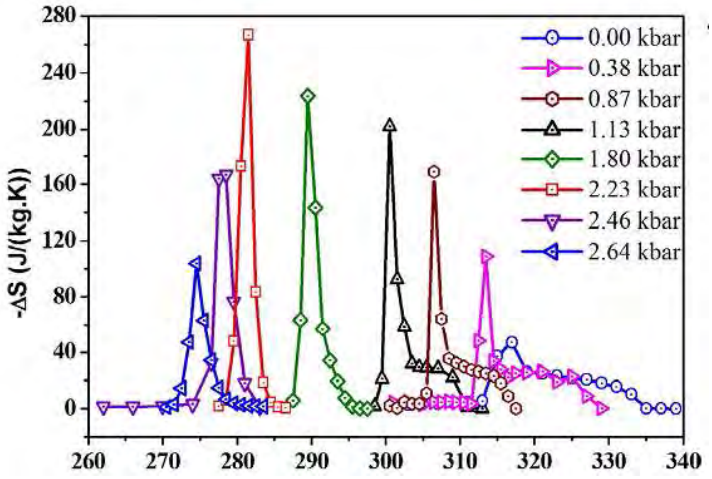

Figure 1.11: Magnetic entropy change from a field change of 5 T of MnAs, under various applied pressure values [9].

The reported values of magnetic entropy change, over two orders of magnitude higher than normal values, even exceeding the theoretical limit of magnetic entropy change ($R\ln[2S+1]$ for spin S), justified the 'colossal' term.

This colossal magnetocaloric effect was afterwards reproduced under ambient pressure, by chemical substitution by Fe, Cu or Cr [30, 31, 32]. The justification behind the colossal MCE was put forth [30, 31, 33], but its existence has been questioned by other groups [34, 35]. We will give further insight to this discussion later.

Chapter 2

Theoretical background and models

In this chapter, a brief overview of magnetism theory will be presented, to give the necessary background to the models that will be later described and used. The first section of this chapter will describe some basic results of the statistical mechanics of magnetic spins, with particular focus on describing magnetic entropy.

The first theory to be presented is the Landau theory of phase transitions. As we will see later, Landau theory is able to describe second- and first- order phase transitions, phenomenologically defining the effects of magnetoelastic coupling, electron condensation [36] and correlation effects [37] on magnetic phase transitions.

The molecular mean-field theory, including the Bean-Rodbell model for magnetoelastic coupling will also be presented. Mean-field theory, as opposed to Landau theory, gives a somewhat more defined physical interpretation of the parameters in play, and can describe magnetization behavior near saturation.

A short introduction to the theory of critical point phenomena will also be presented. Critical phenomena is an invaluable model to study the critical behavior of second-order phase transitions. A particular interest will be given to the scaling relations resulting from the theory.

2.1 Quantum mechanics of simple paramagnets

2.1.1 Magnetization and entropy

Let us assume a system of N identical magnetic atoms with total angular momentum J and magnetic moment $\vec{\mu}_J$. Considering the system as a group of non-interacting particles, the only contribution to the Hamiltonian comes from the interaction with the applied magnetic field, $\vec{H}_0$. Since all particles are identical, we need only to consider the Hamiltonian for a single atom.

$$\mathcal{H} = -\vec{\mu}_J \cdot \vec{H}_0 \tag{2.1}$$

We consider $\vec{H}_0$ to be along the z-axis, and so

$$\mathcal{H} = -\mu_{J_z} H_0 \tag{2.2}$$

The eigenvalues of $\mathcal{J}_z$ are $m = J, J-1, \ldots, -J$. And so the eigenvalues E_m of $\mathcal{H}$ are

$$E_m = -g\mu_B m H_0, m = J, J-1, \ldots, -J \tag{2.3}$$

where g is the Landé factor. The partition function is then

$$Z_J = \sum_{m=-J}^{J} e^{g\mu_B m H_0 / k_B T} \tag{2.4}$$

which can be expressed in the form

$$Z_J(x) = \sum_{m=-J}^{J} e^{mx/J} = \frac{\sinh\left(\frac{2J+1}{2J}x\right)}{\sinh\left(\frac{1}{2J}x\right)} \tag{2.5}$$

where $x = g\mu_B J H_0 / k_B T$, a ratio between magnetic and thermal energies.

The total magnetization (M) of the N atoms is then

$$M = N < \mu_{J_z} >= Ng\mu_B < J_z > \tag{2.6}$$

The thermal equilibrium value of $< J_z >$ can then be calculated:

$$M = Ng\mu_B \frac{Tr\left[J_z e^{-\mathcal{H}/k_B T}\right]}{Z_J(x)} = Ng\mu_B \frac{\sum_{m=-j}^{j} m e^{mx/J}}{Z_J(x)} \tag{2.7}$$

the previous expression can be reduced to the form

$$M = Ng\mu_B J \mathcal{B}_J(x) \tag{2.8}$$

where $\mathcal{B}_J$ is the Brillouin function, defined as

$$\mathcal{B}_J(x) = \frac{2J+1}{2J} \coth\left(\frac{2J+1}{2J}x\right) - \frac{1}{2J} \coth\frac{x}{2J} \tag{2.9}$$

which is a smooth monotonous increasing function, where $0 \leq \mathcal{B}(x) \leq 1$. For high values of x, where $\mathcal{B}(x) = 1$, the saturation magnetization value is obtained:

$$M_{sat} = Ng\mu_B J. \tag{2.10}$$

The Brillouin function allows us to establish the following relation for the magnetic entropy:

$$S_J = Nk_B \left[\ln Z_J(x) - x\mathcal{B}_J(x)\right] \tag{2.11}$$

which, for a null applied field is equal to $Nk_B \left[\ln (2J+1)\right]$.

The previous equation allows us to calculate the maximum magnetic entropy change between a totally ordered magnetic state, where $M = Ng\mu_B J$, and a totally disordered state, where $M = 0$. Since the magnetic entropy value is null in a totally magnetically ordered state, the maximum magnetic entropy change is simply

$$\Delta S_J^{max} = S_J|_{M=M_S} - S_J|_{H=0} = -NK_B \ln(2J+1) \tag{2.12}$$

This well established limit of magnetic entropy change will be important for further discussions.

2.2 The Landau Theory of phase transitions

2.2.1 Concept

Landau [38] underlined the importance of symmetry when considering a phase transition. When a magnetic system is in the paramagnetic state, it is isotropic, and so there is no defined preferential direction. If the system changes into a ferromagnetic state, the onset of spontaneous magnetization then breaks the rotation symmetry of the system, as is it now anisotropic since $\vec{M}$ has a defined direction. The transition between two states of different symmetry cannot be smooth, since a given symmetry either exists or doesn't. A phase transition (of second order) should separate the two states of different symmetries. This reasoning brings us into defining an order parameter, that adequately describes the state of the system and its phase transitions. According to Landau, any system parameter that is null in the symmetric state and non-null in the non-symmetric state can be an order parameter.

The continuity of the change of state in a phase transition of the second kind is expressed by the fact that the order parameter takes arbitrarily small values near the transition point. Considering the neighbourhood of this point, we expand the free energy of the system in powers of the order parameter η [38]:

$$\Phi(P,T,\eta) = \Phi_0 + \Phi_1\eta + \Phi_2\eta^2 + \Phi_3\eta^3 + \ldots \tag{2.13}$$

Symmetry conditions [11] determine that in the case of magnetic phase transitions only the even powers remain. If there exists an external field whose action depends on the order parameters, even without knowing the nature of this field, we may formulate some general

considerations. If the thermodynamic potential is defined as a function of p, T and η, the mean (equilibrium) value of η is given by

$$\eta_{eq} = \frac{\partial \Phi(p,T,h)}{\partial h}. \tag{2.14}$$

In order to ensure that this relation is satisfied within Landau theory, an extra term of $-\eta h$ is added to the free energy expansion.

For an homogeneous ferromagnetic system, the immediate order parameter is magnetization (the projection of $\vec{M}$ on a given axis). Magnetization is then a thermodynamic parameter that is needed to specify the macroscopic state of a system. The corresponding external field is the applied magnetic field, and so the "magnetic Gibbs free energy" [11] expansion is (up to 6^{th} order)

$$G - G_0 = a(T)M^2 + \frac{b(T)}{2}M^4 + \frac{c(T)}{3}M^6 - MH. \tag{2.15}$$

In order for the expansion to describe the general properties of a magnetic system, the a parameter is considered proportional to $(T - T_C)$, reproducing the discontinuities of specific Heat at T_C.

To determine the value of M when $H \neq 0$, we then calculate the derivative in M of the free energy and equal it to zero:

$$\frac{\partial G}{\partial M} = a(T)M + b(T)M^3 + c(T)M^5 - MH = 0 \tag{2.16}$$

which can then be rewritten in the following way:

$$\frac{H}{M} = \frac{1}{2}a(T)M^2 + \frac{1}{4}b(T)M^4 + \frac{1}{6}c(T)M^6 - MH \tag{2.17}$$

Estimating the entropy from the temperature derivative of the Gibbs free energy expansion (Eq. 2.15) results in

$$-S_M(T,H) = \left(\frac{\partial G}{\partial T}\right)_H = \frac{1}{2}a'M^2 + \frac{1}{4}b'M^4 + \frac{1}{6}c'M^6 \ , \tag{2.18}$$

where a', b' and c' are the temperature derivatives of the Landau expansion coefficients, and M the magnetization value obtained from the minimization of the free energy expansion (Eq. 2.16).

We have maintained the generality of the temperature dependence of the b and c Landau parameters up to this point. If we consider them to be temperature independent, in this simplified description the first term of the expansion in Eq. 2.18 is temperature independent and is equal to 1/2 of the inverse Curie constant:

$$-S(\sigma) = \frac{3}{2}\frac{J}{J+1}Nk_B\sigma^2, \tag{2.19}$$

for a number N of J spins, and where σ is the relative magnetization, defined as $\sigma = M/M_{\text{sat}}$.

In the ferromagnetic state the system has a spontaneous magnetization and the $\sigma = 0$ state is never attained. Explicitly, from Eq. 2.19, this corresponds to:

$$-\Delta S(\sigma) = \frac{3}{2}\frac{J}{J+1}Nk_B(\sigma^2 - \sigma^2_{\text{spont}}), \tag{2.20}$$

when describing the entropy change due to a field change. In graphical terms, this results in a shift of the isothermal ΔS_M vs M^2 plots in the ferromagnetic region, with an horizontal drift from the origin corresponding to the value of $M^2_{\text{spont}}(T)$, while for $T > T_C$ the ΔS_M vs M^2 plots start at a null M value.

2.2.2 The Arrott plots and relation with Landau theory

The Arrott plots [39] are a convenient way to plot isothermal magnetization data, that allows an immediate visual estimation of the type of magnetic order of a material, as well as, in a case of a ferromagnet, a quick estimation of its Curie temperature value. This is achieved by plotting M/H as a function of M^2.

There is a direct and immediate relation between the Arrott plots and Landau theory, since M/H and M^2 are present in the state function (Eq. 2.17). So, by plotting magnetization data in an Arrott plot, polynomial fits of isothermal M/H versus M^2 will give us an estimation of the Landau parameters a, b and c, as well as their dependence on temperature. As an example of this approach, let us consider experimental magnetization data of a second-order phase transition manganite, $La_{0.665}Er_{0.035}Sr_{0.3}MnO_3$.

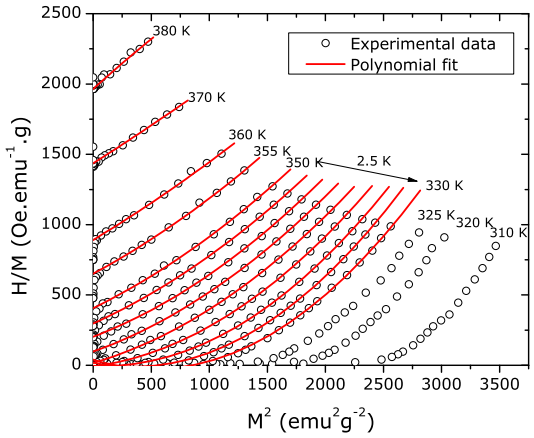

Figure 2.1: Arrott plots for $La_{0.665}Er_{0.035}Sr_{0.3}MnO_3$, and corresponding 2nd-order polynomial fit for each isothermal curve.

The temperature dependence of the Landau parameters is then obtained. It is then possible to describe the Landau parameters by fitting their temperature dependence with continuous functions, namely polynomials. This methodology can be an effective interpolation scheme, that has a physical basis, compared to purely numerical approximations. An example of temperature dependence of the Landau parameters is shown in Figure 2.2.

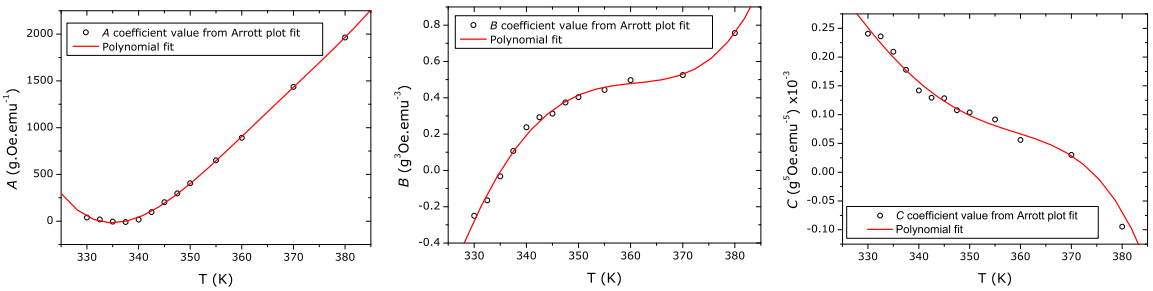

(a) (b) (c)

Figure 2.2: Temperature dependence of the Landau parameters of $La_{0.665}Er_{0.035}Sr_{0.3}MnO_3$, from Arrott plot fits.

The thermodynamics of Landau theory then allows us to perform further analysis. Since the free energy of the system is described, one can easily estimate the magnetic entropy of the system, as a function of temperature and applied magnetic field, by directly applying Eq. 2.18.

Figure 2.3(a) shows the comparison between experimental magnetization data of the $La_{0.665}Er_{0.035}Sr_{0.3}MnO_3$ manganite, compared to the simulation magnetization values obtained from the polynomial fits of the Landau $a(T)$, $b(T)$ and $c(T)$ coefficients from Figure 2.2. Figure 2.3(b) shows the corresponding magnetic entropy behavior, comparing the results from using the Maxwell relation integration of experimental data to the free energy derivative within the Landau theory (Eq. 2.18), which conveniently interpolate in the data range.

2.2.3 First-order phase transitions

Landau theory is also useful to describe the general properties of a first-order phase transition system. These can be summarized as [40]:

- a region of coexistence of two phases,
- a discontinuous jump of the order-parameter at the transition,
- a latent heat which results from the discontinuity of the order parameter. A discontinuous variation should be found at T_C for all the physical quantities proportional to the first-derivatives of the thermodynamic potential,

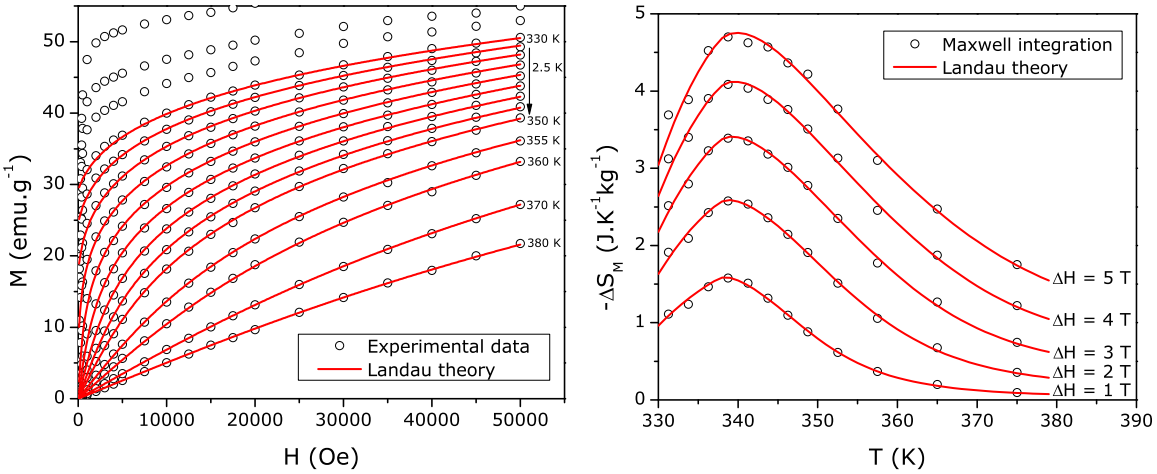

(a) (b)

Figure 2.3: a) Experimental $M(H,T)$ of $La_{0.665}Er_{0.035}Sr_{0.3}MnO_3$ (open dots) and simulations from Landau theory (red lines); b) $\Delta S_M(T)$ behavior from the use of a Maxwell relation and experimental data (open dots) and from the free-energy derivative within Landau theory (red lines).

- specific discontinuities at T_C for the physical quantities related to second-order derivatives of the thermodynamic potential.

The region of coexistence is a consequence of the fact that in a first-order transition, for a given set of parameters (H and T, for a magnetic system), there exist multiple free energy minima. Only the absolute minimum is the equilibrium solution. The remaining minima are referred to as metastable states.

These multiple minima of free energy can be created in a Landau theory of a magnetic system by considering magnetoelastic coupling, or electron condensation/correlation [36, 37] effects. Let us consider magnetoelastic coupling, by introducing an extra term in the free energy expansion, corresponding to an elastic energy from considering an extra order parameter, x, deformation:

$$F_{\text{distortion}} = k_1 x M^2 + \frac{k_2}{2} x^2. \tag{2.21}$$

The first term in 2.21 corresponds to the coupling between lattice and magnetization, while the second term considers purely elastic contributions to the free energy.

By minimizing the free energy by calculating the x value where $\partial(F_{\text{distortion}})/\partial(x) = 0$, the equilibrium position then corresponds to $x = -k_2\ ^2M^4/2k_1$. This leads to a minimum free energy of lattice distortion,

$$F_{\text{distortion}} = -\frac{k_2^2 M^4}{2k_1}. \tag{2.22}$$

The magnetoelastic coupling then affects the Landau expansion of free energy in the fourth-order term (b parameter). A crucial point is that this coupling effect may lead us to negative values of the b parameter, and so, with a positive c, we have multiple minima of the free energy, and so, a first-order phase transition.

As described in Chapter 1, the study of the magnetocaloric effect of first-order magnetic phase transition materials uncovered the giant MCE. From Landau theory, the effect of the structural transition on the magnetic entropy change can be directly interpreted. A summarized version of this work has been published [AA04].

To assess the effect of magnetoelastic coupling on the magnetocaloric effect, we considered a linear dependence of b on T, with slope equal to 67 g Oe emu^{-1}, and a constant c value of 5 $\times$ 10^{-6} g^5 Oe emu^{-5}. These values where obtained from fitting the Arrott plots of magnetization data from a ferromagnetic manganite system. By considering several constant values of the b parameter, the magnetic entropy change is then calculated, as shown in Figure 2.4.

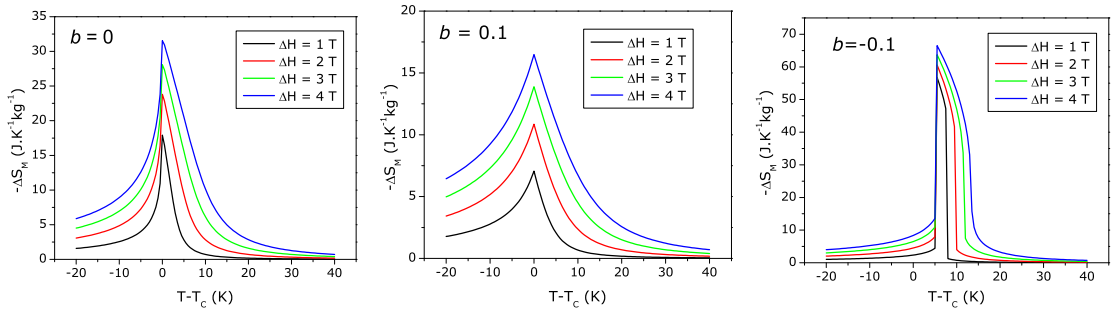

Figure 2.4: Magnetic entropy change from resulting from a a) null, b) positive and c) negative temperature independent Landau b parameter.

Much higher values of magnetic entropy change are observed in the case where the b parameter is negative, and the transition becomes first-order. Still, it is worth mentioning that while there is still a first-order magnetostructural transition, the magnetic entropy change will be linearly dependent on the square of magnetization, since the Landau parameters are independent of temperature, in accordance with Eq. 2.19. In a way, this result tells us that there is no extra entropy change gained from the structural transformation, but there is an increase in entropy change since the magnetization abruptly changes near the transition. In other words, the sharper the transition, the more magnetic entropy change occurs, but even in the presence of a structural transition, no purely structural entropy change is added, in this simplified scenario.

2.3 Molecular mean-field theory and the Bean-Rodbell model

2.3.1 Ferromagnetic order and the Weiss molecular field

A simplified approach to describing ferromagnetic order in a given magnetic material was put forth by Weiss, in 1907 [41]. This concept of a molecular field assumes the magnetic interaction between magnetic moments as equivalent to the existence of an additional internal interaction/exchange field that is a function of the bulk magnetization M:

$$H_{total} = H_{external} + H_{exchange} \text{ and } H_{exchange} = \lambda M, \tag{2.23}$$

where λ is the mean-field exchange parameter.

The general representation of the molecular mean-field model is then

$$\sigma = f\left[\frac{H + \lambda M}{T}\right]. \tag{2.24}$$

where f is the general function that applies in the paramagnetic system (e. g. the Brillouin function).

From a linear approximation of the susceptibility (Curie law):

$$\chi = \frac{M}{H} = \frac{NJ(J+1)g^2\mu_B^2}{3k_BT_C} = \frac{N\mu_{eff}^2}{3k_BT_C}; \tag{2.25}$$

where μ_{eff} is the effective magnetic moment: $\mu_{eff} = g[J(J+1)]^{1/2}\mu_B$.

We define the Curie temperature T_C as the temperature where the ferromagnetic to paramagnetic transition occurs, and there is a divergence in the susceptibility:

$$\chi = \frac{C}{T - T_C}, \text{ where } C = \frac{NJ(J+1)g^2\mu_B^2}{3k_B} \text{ and } T_C = C\lambda. \tag{2.26}$$

The exchange parameter can be estimated from the following relation, as long as N and J are known.

$$\lambda = \frac{3k_BT_C}{Ng^2J(J+1)\mu_B^2} \tag{2.27}$$

Typical values of λ correspond to molecular fields in the order of hundreds of Tesla.

A general result from mean-field theory is that, as long as the λ parameter is independent of temperature, magnetic entropy $S(\sigma)$ of a system with angular moment J can be described as a function of σ alone [13, 42, 43]:

$$S(\sigma) = -Nk_B\left[ln(2J+1) - ln\left(\frac{sinh\left(\frac{2J+1}{2J}\mathcal{B}_J^{-1}(\sigma)\right)}{sinh\left(\frac{1}{2J}\mathcal{B}_J^{-1}(\sigma)\right)}\right) + \mathcal{B}_J^{-1}(\sigma).\sigma\right] \tag{2.28}$$

where N is the number of spins, J the spin value, k_B the Boltzmann constant, σ the reduced

magnetization (M/M_{sat}), and $\mathcal{B}_J$ the Brillouin function for a given J value, whose inverse, $\mathcal{B}_J^{-1}$, can be approximated numerically or using methods and expressions from the literature [44, 45, 46].

From a power expansion of Eq. 2.28, ΔS_M is proportional to M^2, from the mean-field model, for small M values:

$$-S(\sigma) = \frac{3}{2}\frac{J}{J+1}Nk_B\sigma^2 + O(\sigma^4) \ . \tag{2.29}$$

The first term of the expansion is in accordance with Landau theory, for the simplified case where the b and c parameters are temperature independent (Eq. 2.19).

In the next section, we will use both the Landau theory result of Eq. 2.20 and also the non-approximated mean-field entropy relation of Eq. 2.28 to estimate the spontaneous magnetization of ferromagnetic materials, and also to give us some insight on eventual magnetic clustering phenomena.

2.3.2 Estimating spontaneous magnetization

A typical ferromagnetic material will present a magnetic domain structure below T_C, establishing a null net magnetic moment of the bulk sample, even if each single domain is in the ferromagnetic state [47]. By applying a sufficiently strong external magnetic field, this domain structure can be destroyed, making the material behave as a single magnetic domain. The various steps of the dependence of the bulk magnetization as a function of applied magnetic field are presented in Figure 2.5.

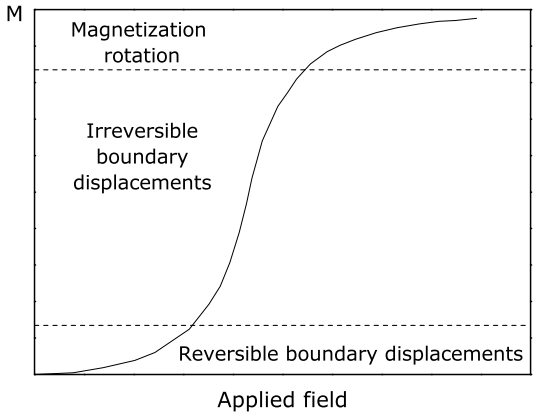

Figure 2.5: Representative magnetization curve, showing the dominant magnetization processes in the different regions of the curve, adapted from Ref. [47].

One of the obvious consequences from the formation of magnetic domains is that the spontaneous magnetization (magnetization at a null external magnetic field) cannot be directly measured by bulk magnetometry techniques. The measured magnetization value will be zero

at a null external applied field, and underestimated until the external field is strong enough to destroy the domain structure.

Interestingly, a classic method to overcome this difficulty in experimental studies of ferromagnetic systems was to study the magnetocaloric effect (adiabatic temperature change) of materials to estimate the spontaneous magnetization [5, 48, 49]. This consisted on directly measuring the adiabatic temperature change ΔT_{ad} of the material, since within a molecular field approach the relation between ΔT_{ad} and the spontaneous magnetization is established. We begin by describing the free energy of a magnetic system.

$$dU = TdS + HdM. \tag{2.30}$$

If we take S and H as independent variables, double differentiation gives

$$\frac{\partial^2 U}{\partial H \partial S} = \left(\frac{\partial T}{\partial H}\right)_S = -\left(\frac{\partial M}{\partial S}\right)_H = -\left(\frac{\partial T}{\partial S}\right)_H \left(\frac{\partial M}{\partial T}\right)_H. \tag{2.31}$$

By definition, the heat capacity at constant field strength is

$$C_H = \left(\frac{\delta Q}{\delta T}\right)_H = T\left(\frac{\partial S}{\partial T}\right)_H. \tag{2.32}$$

Combining this with the previous equation, we have

$$C_H = -T\left(\frac{\partial H}{\partial T}\right)_S \left(\frac{\partial M}{\partial T}\right)_H \tag{2.33}$$

or

$$(\Delta T)_S = \frac{T}{C_H}\left(\frac{\partial M}{\partial T}\right)_H \Delta H. \tag{2.34}$$

If the initial expression of dU is differentiated with respect to S and M, the adiabatic change in temperature may be expressed in terms of ΔM instead of ΔH:

$$(\Delta T)_S = \frac{T}{C_M}\left(\frac{\partial H}{\partial T}\right)_M \Delta M, \tag{2.35}$$

where c_M is the heat capacity (per unit volume) at constant magnetization.

Taking the general representation of the molecular mean-field model (eq. 2.24), we may evaluate $(\partial H/\partial T)_M$ by differentiating with respect to H and T, holding M constant:

$$0 = \frac{T\partial H - (H + \lambda M)\partial T}{T^2}.f'. \tag{2.36}$$

Therefore

$$\left(\frac{\partial H}{\partial T}\right)_M = \frac{H + \lambda M}{T} \tag{2.37}$$

Leading to the dependence of ΔT on ΔM:

$$\Delta T = \frac{H + \lambda M}{C_M} \Delta M = \frac{\lambda + H/M}{2C_M} \Delta M^2. \tag{2.38}$$

This relation was found to be experimentally confirmed, as long as the applied magnetic field was high enough to effect saturation by orienting the domains parallel to the field. This allowed the estimation of the spontaneous magnetization of various ferromagnetic materials. We show the results for Nickel and Iron, from Ref. [48].

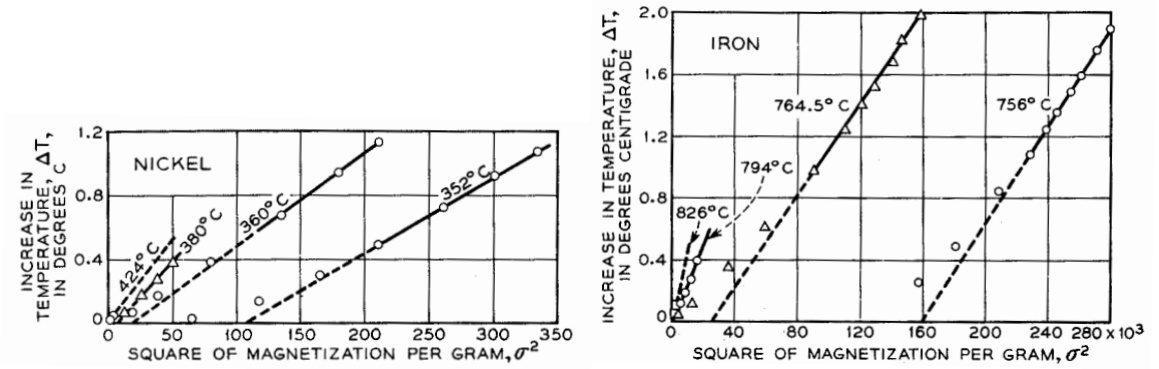

(a) (b)

Figure 2.6: Magnetocaloric rise in temperature as a function of the square of specific magnetization, in a) Nickel, and b) Iron, from Ref. [48].

Still, the main drawback of this approach is the difficulty in measuring ΔT_{ad}. The linear dependence of ΔT is only observed for high fields, when the domains are aligned with the applied magnetic field.

The use of Landau theory and the Arrott plot construction [39] is a useful way to estimate the spontaneous magnetization from bulk magnetization measurements. While this approach is indeed useful, the procedure of fitting polynomial functions to the Arrott plots below T_C is not simple, since if the system is not a trivial ferromagnet ($b =$ constant, $c = 0$), the curvature in the Arrott plot due to the magnetic domain effect is easily interpreted as the curvature due to the c parameter, or vice-versa. The fitting procedure becomes progressively more difficult for lower temperatures, and even more so if there is a temperature dependence of the b and c Landau parameters.

Another method to estimate the spontaneous magnetization is to use the magnetic entropy change ΔS_M, which can be estimated from bulk magnetization measurements [ASA09]. The ΔS_M values are used much in the same way as ΔT_{ad} values, to estimate spontaneous magnetization, since there is a relation between the spontaneous magnetization and magnetic entropy change (eq. 2.20). Since eq. 2.20 comes from an expansion of a mean-field relations in powers of magnetization, it is equivalent to the result from a simple Landau model. It

actually becomes easier to show the benefits of estimating spontaneous magnetization from entropy change compared to fitting the Arrott plots, under a Landau theory perspective. Eq. 2.18 establishes that the magnetic entropy change is a function of magnetization and the temperature derivatives of the Landau coefficients. Consequently, in a $-\Delta S_M$ versus M^2 representation of data, the plots will be linear, even if the value of the Landau parameter c is non-zero. This simplifies considerably the process of estimating the spontaneous magnetization, since a linear relation between entropy change and the square of the magnetization is expected.

Indeed, if a linear relation between $-\Delta S_M$ and M^2 is observed on experimental data of a given magnetic material, a simplified Landau theory (b and c temperature independent) description should yield acceptable results. Figure 2.7 shows $-\Delta S_M$ versus M^2 plot for two manganite systems, a second-order phase transition La-Sr manganite (2.7 a)) and a first-order La-Ca manganite (2.7 b)).

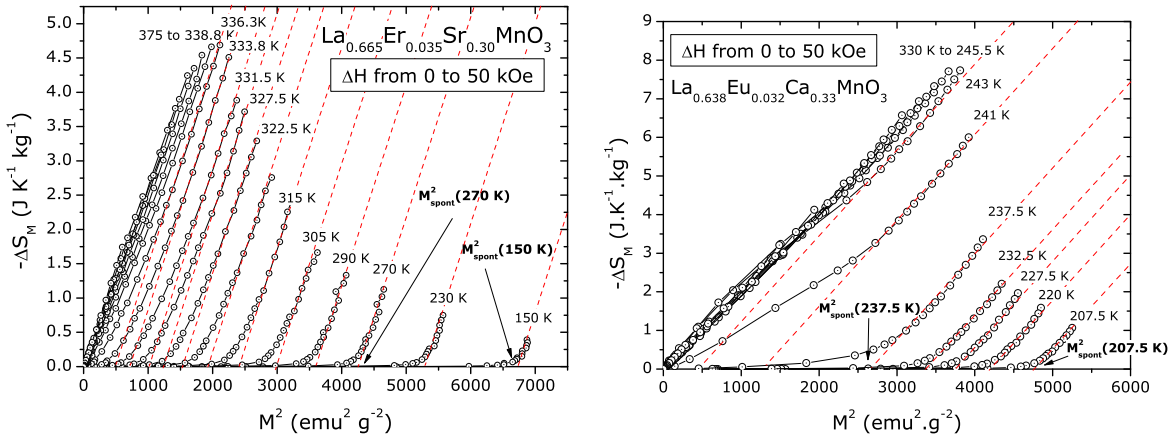

Figure 2.7: Experimental $-\Delta S_M$ versus M^2 for a a) second-order and a b) first-order phase transition ferromagnetic manganite systems.

The approximate linear nature of the $-\Delta S_M$ versus M^2 plots makes the estimation of spontaneous magnetization a simpler affair.

The order-disorder transition is clearly sharper in the first-order system, as expected. For the second-order system, the transition is smoother, spreading out in a wider temperature interval. Eq. 2.20 gives us a physical interpretation to the observed slope in these ΔS_M versus M^2 plots. For the second-order La-Sr manganite, the obtained slope is approximately 29.4 (cgs), corresponding to a Curie constant of 0.0170 (emu K $\mathrm{Oe}^{-1}\mathrm{g}^{-1}$). In the case of the first-order La-Ca manganite, the obtained Curie constant value is approximately 22.4 (cgs), which corresponds to a Curie constant value of 0.0223 (emu K $\mathrm{Oe}^{-1}\mathrm{g}^{-1}$). Both these Curie constant values are, however, not compatible to the expected values for isolated Mn^{+3} or

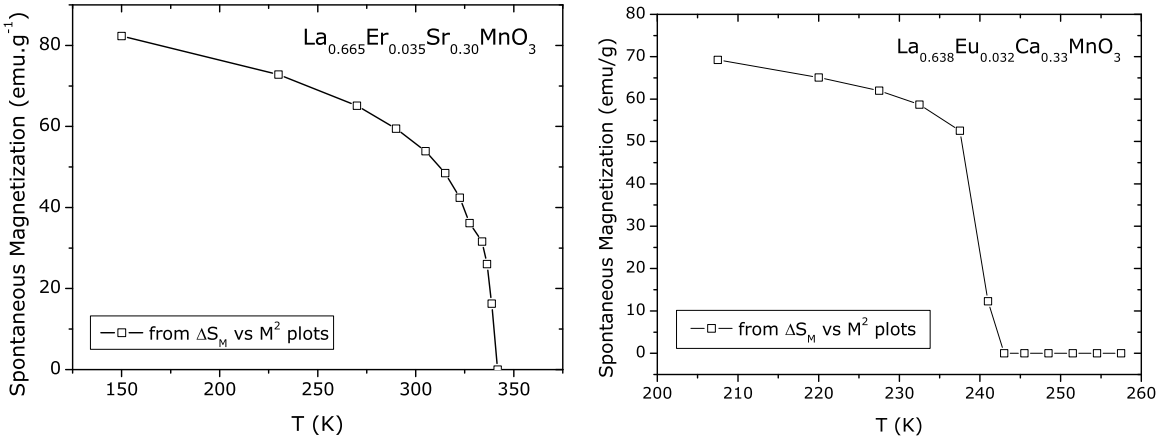

Figure 2.8: Temperature dependence of the spontaneous magnetization estimated from linear fits of $-\Delta S_M$ versus M^2 plots for a a) second-order and a b) first-order phase transition ferromagnetic manganite systems.

Mn^{+4} ions. This will be investigated later in this work.

2.3.3 The Bean-Rodbell model

The Bean-Rodbell model [50] adds a phenomenological description of magneto-volume effects to the classical molecular mean-field model of Weiss. The dependence of exchange interaction on interatomic spacing is then considered, taking into account three new parameters, β, which corresponds to the dependence of ordering temperature on volume, and also the volume compressibility, K and thermal expansion α_1. The formulation behind the model is as follows:

$$T_C = T_0 \left[1 + \beta \left(\frac{v - v_0}{v_0} \right) \right] \ , \tag{2.39}$$

where T_C is the Curie temperature corresponding to a lattice volume of v, while v_0 is the equilibrium lattice volume in the absence of magnetic interactions, corresponding to a Curie temperature of T_0 if magnetic interactions are assumed, but with no magneto-volume effects.

The free energy of the system can therefore be described, taking into account magnetic and volume interactions. For simplicity, we consider a purely ferromagnetic interaction. For a description including anti-ferromagnetic interactions, see Ref. [50].

$$G = G_{\text{field}} + G_{\text{exchange}} + G_{\text{volume}} + G_{\text{pressure}} + G_{\text{entropy}} \tag{2.40}$$

Considering first a spin 1/2 system, and the molecular field exchange interaction, we have that the Gibbs free energy per unit volume is:

$$\begin{aligned} G_v &= -HM_{sat}\sigma - \frac{1}{2}Nk_BT_c\sigma^2 + \frac{1}{2K}\left[\frac{v-v_0}{v_0}\right]^2 + p\left(\frac{v-v_0}{v_0}\right) \\ &- TNk_B\left[\ln 2 - \frac{1}{2}\ln\left(1-\sigma^2\right) - \sigma\ \tanh^{-1}\sigma\right] - TS_{\text{lattice}}. \end{aligned} \tag{2.41}$$

where σ is the reduced magnetization, M_{sat} the saturation magnetization and N the number of particles for volume v_0. While the original description of Bean and Rodbell does not initially consider the lattice entropy, we will keep the generality of the calculations along our description of the model. The lattice entropy term is as follows:

$$S_{\text{lattice}} = 3Nk_B\left[\frac{x}{e^x-1} - ln(1-e^{-x})\right], \tag{2.42}$$

where $x \equiv h\nu/k_BT$ with ν being the phonon frequency. Eq. 2.42 can be expanded via the Debye approximation:

$$S_{\text{lattice}} = Nk_B\left[4 - 3\ \ln\Theta/T + (3/40)(\Theta/T^2) + ...\right] \tag{2.43}$$

where $\Theta \equiv h\nu_{\max}/T$. From the previous expression we obtain:

$$\partial S/\partial v \cong -3Nk_Bd\ \ln(\nu_{\max})/dv = \alpha_1/K \tag{2.44}$$

where α_1 is the thermal expansion coefficient ($\alpha_1 \equiv (1/v)(\partial v/\partial T)_p$) and K is the compressibility ($K \equiv -(1/v)(\partial v/\partial p)_T$).

By substituting Eq. 2.39 into Eq. 2.41, deriving in volume by using also Eq. 2.44, the relation between magnetization and volume that corresponds to the energy minimum is

$$\frac{v-v_0}{v_0} = \frac{1}{2}NKk_BT_0\beta\sigma^2 + Tv_o\alpha_1 - pK \tag{2.45}$$

By substituting the previous relation into the Gibbs free energy (Eq. 2.41), and minimizing in respect to volume, we obtain

$$\begin{aligned} (G_v)_{\min} &= -HM_{sat}\sigma - \frac{1}{2}Nk_BT_0\sigma^2\left[1-\beta(pK-\alpha_1T)\right] \\ &- p^2K/2 - \alpha_1^2T^2/2K + \alpha_1Tp - \frac{1}{2K}(\frac{1}{2}Nk_BT_0\sigma^2\beta)^2 \\ &- TNk_B\left[4 + \ln 2 - \frac{1}{2}\ln(1-\sigma^2) - \sigma\ \tanh^{-1}\sigma\right]. \end{aligned} \tag{2.46}$$

By minimizing as a function of σ, we obtain the implicit dependence of σ on temperature, for spin 1/2.

$$\frac{T}{T_0} = \frac{\sigma}{\tanh^{-1}\sigma}\left(1 - \beta(pK - \alpha_1 T) + \frac{\eta\sigma^2}{3} + M_{sat}H\right) \tag{2.47}$$

where the η parameter defines the order of the phase transition, in the following way:

$$\begin{aligned} \eta &\leq 1 : \text{second-order phase transition} \\ \eta &> 1 : \text{first-order phase transition} \end{aligned}$$

and corresponds to:

$$\eta = \frac{3}{2} N k_B K T_0 \beta^2 \ ; (\text{spin} = 1/2) \tag{2.48}$$

$$\eta_J = \frac{5}{2}\frac{[4J(J+1)]^2}{[(2J+1)^4 - 1]} N k_B K T_0 \beta^2 \ ; (\text{arbitrary J spin}). \tag{2.49}$$

We can rewrite Eq. 2.47, in the more familiar molecular-mean field expression type, $M = f[(H + \lambda \mathrm{M})/\mathrm{T}]$, since $\tanh^{-1}\sigma = (H + \lambda(M,T)M)/T$, (for spin = 1/2):

$$\tanh^{-1}\sigma = \frac{g\mu_B H/2k_B + (1 - \beta pK + \beta\alpha_1 T)T_0\sigma + (\eta/3)T_0\sigma^3}{T}. \tag{2.50}$$

We can therefore consider, in the absence of external pressure, and considering the lattice entropy change small, that the molecular field dependence in magnetization follows the simple form of

$$H_{\text{exchange}} = \lambda_1 M + \lambda_3 M^3. \tag{2.51}$$

Considering a generalized spin system, with no applied pressure, nor the lattice entropy contribution, the implicit dependence of σ on temperature is

$$T(\sigma, H) = \frac{g\mu_B JH/k_B + aT_0\sigma + bT_0\sigma^3}{\mathcal{B}_J^{-1}(\sigma)}, \tag{2.52}$$

where

$$a = \frac{3J}{J+1}, \tag{2.53}$$

$$b = \frac{9}{5}\frac{(2J+1)^4 - 1}{(2(J+1))^4}\eta J = b'\eta J \tag{2.54}$$

and

$$\mathcal{B_J}^{-1}(\sigma) = \frac{\partial S_J}{\partial \sigma}. \tag{2.55}$$

If the lattice entropy change is taken into consideration, the effect corresponds introducing

the $\beta\alpha_1 T$ term into the first-order term of the exchange field, in the same way as the spin 1/2 system.

If we choose to describe the exchange field as $\lambda_1 M + \lambda_3 M^3$, it becomes practical to rewrite the conditions of the model explicitly in terms of the λ_1 and λ_3 parameters, bulk magnetization M, spin and the saturation magnetization, M_{sat}. This corresponds to the following expression, where the η parameter can be defined as:

$$\eta = \lambda_3 / \left[b' T_0 k_B / (g \mu_B J^2 M_{\mathrm{sat}}^3) \right], \tag{2.56}$$

where the b' parameter is previously defined in Eq. 2.54. The λ_3 parameter includes the β (dependence of ordering temperature on volume) and K (compressibility) system variables. The direct consequence of the previous expression is that, by substituting the T_0 value, the ratio of λ_1 and λ_3, together with the system parameters define the nature of the transition, following the next simplified expression:

$$\eta = \frac{3 J^2 M_{sat}^2}{b'} \frac{\lambda_3}{\lambda_1}. \tag{2.57}$$

2.3.4 Numerical approach for simulations

As shown in the previous section, the Bean-Rodbell model can describe a magnetovolume induced first-order phase transition. While the numerical approach to simulate first-order phase transitions in the Landau theory is straightforward (finding the roots of a polynomial and then which of the two local minima corresponds to the absolute free energy minimum), in the case of the Bean-Rodbell model the case is more complicated in computational terms. Even in the more simple second-order phase transition, solving the transcendental equation $M = f[(H + \lambda M)/T]$ cannot be done algebraically, and so numerical methods are employed. The classic visual representation of the numerical approach is presented in Figure 2.9.

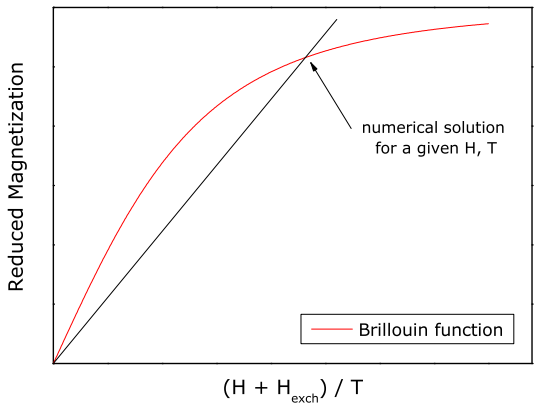

Figure 2.9: Graphical solution of the mean-field state equation, adapted from Ref. [47].

This graphical approach is easily converted into numerically finding the roots of the following function:

$$M_{\text{sat}}\mathcal{B}_J(J, \lambda_1, \lambda_3, M, H, T) - M(H, T); \tag{2.58}$$

Finding the roots of the above equation can be numerically achieved by using the imbedded Matlab function "fzero", which determines the roots of continuous, single variable functions and is an optimized version of the classic bisection method for root finding.

For the first-order phase transition, there are multiple solutions that need to be calculated, corresponding to the stable (equilibrium), metastable and unstable branches. Figure 2.10 shows a representation of these solutions.

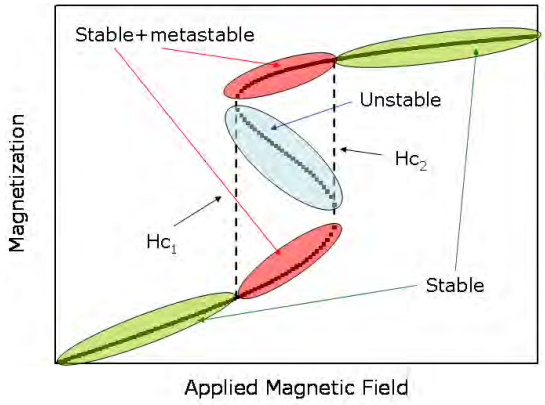

Figure 2.10: The multiple solution branches from the roots of Eq. 2.58, for a first-order transition from the Bean-Rodbell model.

The methodology for obtaining the various M solutions in this situation is more numerically intensive than in a second-order system, but falls along the same lines, apart from subdividing the interval of magnetization values into multiple sub-intervals to search for the multiple roots.

In order to calculate the critical field value H_c and consequently the full equilibrium solution (stable branch), the Maxwell construction [11] is applied, which consists of matching the energy of the two phases, in the so-called equal-area construction, as shown in Figure 2.11.

In numerical terms, applying this graphical methodology becomes a matter of integrating the areas between the metastable and unstable solutions, between the Hc_1 and Hc_2 field values, until the value of area 1 is equal to area 2. This operation is numerically intensive, but manageable for realistic field interval values. The most important numerical concern is adequately reproducing all branches (solutions), in a way that the algorithm correctly integrates each area. In programming terms, this becomes a complicated problem, but becomes controllable by a careful definition of the various number of roots of the functions, and developing an

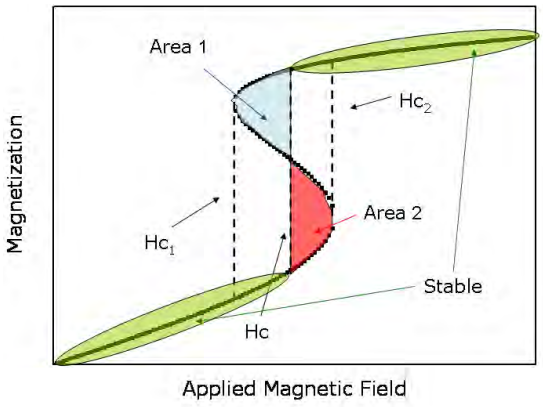

Figure 2.11: The Maxwell construction for determining the critical field H_c and the full equilibrium solution, for a first-order magnetic phase transition system.

optimized integration algorithm for each independent situation that can appear within this approach. While these concerns are of importance in the confidence of the simulations and algorithm efficiency, the programming/algorithm details will not be discussed in detail here.

2.3.5 Estimating magnetic entropy change

Within the molecular field model, the relation between the magnetic entropy and the magnetic equation of state is simply defined (Eq. 2.55). Let us consider that the magnetic equation of state is a generalized f function, and so $M = f[(H + \lambda(M,T)M)/T]$. We can then integrate the magnetic entropy relation:

$$S_M = \int f^{-1}(M)dM. \tag{2.59}$$

So to calculate the entropy change between two distinct field values H_1 and H_2:

$$-\Delta S_M(T)_{\Delta H} = \int_{M|_{H_1}}^{M|_{H_2}} f^{-1}(M)dM. \tag{2.60}$$

where $f^{-1}(M)$ is simply the argument of the state function for a given magnetization value:

$$f^{-1}(M) = \frac{H + \lambda(M,T)M}{T}. \tag{2.61}$$

We can generalize the previous result by considering an explicit dependence of the exchange field in temperature. We rewrite the previous equation as

$$f^{-1}(M) = \frac{H}{T} + \frac{\lambda(M,T)M}{T} \rightarrow H = Tf^{-1}(M) - \lambda(M,T)M \tag{2.62}$$

and using the following Maxwell relation [11]:

$$\left(\frac{\partial S}{\partial M}\right)_T = -\left(\frac{\partial H}{\partial T}\right)_M, \tag{2.63}$$

entropy can be estimated by

$$\Delta S(T)_{H_1 \to H_2} = -\int_{M_{H1}}^{M_{H2}} \left(\frac{\partial H}{\partial T}\right)_M dM, \tag{2.64}$$

leading to

$$-\Delta S_M(T)_{H_1 \to H_2} = \int_{M|_{H_1}}^{M|_{H_2}} \left(f^{-1}(M) - \left(\frac{\partial \lambda}{\partial T}\right)_M M\right) dM. \tag{2.65}$$

Compared to Eq. 2.60, the derivative $\partial\lambda/\partial T$ directly affects the result. We shall explore the use of Eq. 2.60 to calculate the magnetic entropy change and compare it to the use of the Maxwell relation.

2.4 Critical phenomena in magnetism

2.4.1 Background

It is well known that fluctuations near the critical point, which are not taken into account in 'classic' thermodynamic theories such as the Landau theory of phase transitions and the mean-field model, play a crucial role on the properties of materials near the phase transition.

Classical thermodynamics does correctly predict the existence of divergences in the relevant physical properties near a phase transition, establishing an analytic 'shape' or form of these divergences [11]. Detailed experimental measurements in many systems have shown that the analytic form of the divergences is not as predicted, showing evidence of an underlying process inexplicable in classical thermodynamics.

One of the first observations of the effect of fluctuations near a phase transition was made in 1869, by Thomas Andrews [51, 52], reporting on the critical opalescence of fluids, namely near the critical point of the liquid-vapor transition in water, where it becomes milky and opaque in a narrow range of temperature and applied pressure.

Since the entropy change in a ferromagnetic-paramagnetic transition has its maximum near the transition, it may be important to go beyond the descriptions from classic theories of phase transitions.

The theory of critical phenomena aims to better describe the discontinuities that occur in second-order phase transitions, by defining a set of critical exponents.

Let us define two reduced variables, t and h,

$$t = \frac{T - T_C}{T_C}, \qquad h = \frac{\mu H}{k_B T_C}, \tag{2.66}$$

which parameterize the "distance" to the critical point, $T = T_C$ and $H = 0$ (μ is the magnetic moment). Experimental measurements of magnetic systems show that the magnetization, susceptibility, specific heat and entropy at the critical point obey a power law:

$$\begin{aligned} M(T) &\propto t^{\beta}, & M(h) &\propto h^{1/\delta}, \\ \chi(T) &\propto t^{-\gamma}, & C(T) &\propto t^{-\alpha}, \\ & S(h) \propto h^{\psi}. \end{aligned}$$

α, β, γ, δ and ψ are then examples of the so-called critical exponents, and within Landau and mean-field theory they present the values $\beta = 1/2$, $\alpha = 0$, $\gamma = 1$, $\delta = 3$ and $\psi = 2/3$ [53].

2.4.2 Universality classes

The interest behind the critical exponents is that they are, unlike T_C, largely independent of interatomic distance and such, are to a degree *universal*, and depend only in a few fundamental parameters. In a practical point of view, this means that whatever the model parameters, like the a, b, and c parameters within Landau theory, and the exchange parameters λ_1 and λ_3 within mean-field theory, the critical behavior of the system will be largely unaffected, and the critical exponents remain unchanged. This has made the study of critical phenomena (not only in magnetism) a very rich field in physics. The various critical exponents for relevant models are presented in the following table, adapted from Ref. [54]:

Universality class	Symmetry of order parameter	α	β	γ	δ
3D Ising	2-component scalar	0.10	0.33	1.24	4.8
3D X-Y	2-dimensional vector	0.01	0.34	1.30	4.8
3D Heisenberg	3-dimensional vector	-0.12	0.36	1.39	4.8
mean-field/Landau	-	0 (disc.)	1/2	1	3

2.4.3 Relations between critical exponents

The study of the theory of critical phenomena and a massive amount of experimental research has resulted in relations between critical exponents. For the background behind the formulation of these relations, Refs. [54, 53, 55, 56] present an excellent read. These relations are mainly the consequence of thermodynamical arguments based in the curvature of the free energy near transitions, and as such are formally inequalities. Following Stanley's eloquent writing: "(...) experimental results, as well as theoretical work on the Ising model for $d = 2$ and 3, suggest that the Rushbrooke inequality may well be obeyed as an equality. This is, in fact, one of the predictions of the (non-rigorous) scaling law theory of exponents (...)" we shall present the main exponent relations as equalities.

$$\begin{aligned} \gamma &= \beta(\delta - 1) && \text{Widom,} \\ \alpha + 2\beta + \gamma &= 2, && \text{Griffiths,} \\ \alpha + \beta(\delta + 1) &= 2, && \text{Rushbrooke.} \end{aligned}$$

2.4.4 Scaling relations

An approach to the study of the thermodynamics of critical behavior is the so-called static scaling law or homogeneous function approach. The presumption behind this method is that the free energy is a first-order homogeneous function. A function $f(r)$ is by definition homogeneous if for all the values of the parameter λ ,

$$f(\lambda r) = g(\lambda) f(r). \tag{2.67}$$

where the $g(\lambda)$ is of the form

$$g(\lambda) = \lambda^p, \tag{2.68}$$

and the p parameter is generally called the degree of homogeneity.

The last relations can be generalized into an arbitrary number of x_n variables. Considering a magnetic system and the relevant scaling parameters, the following scaling relations are obtained [57, 53].

$$\frac{h}{|t|^{\beta\delta}} = f_{\pm}(\frac{m}{|t|^{\beta}}) \tag{2.69}$$

where $m = (M - M_{spont}(T))/M_{sat}$, and

$$\frac{S}{h^{\psi}} = f_{\pm}(\frac{t}{h^{\psi/1-\alpha}}) \tag{2.70}$$

where $\psi = \frac{1-\alpha}{\beta\delta}$ and $f_{\pm}$ are the scaling functions appropriate for both sides of the scale (above or below T_C).

Figure 2.12 shows the scaling plot of magnetization data of the insulating ferromagnet CrB_3.

Later in this thesis, we will explore how these universal scaling relations can be used to determine the values of the scaling parameters.

2.4.5 The modified Arrott plot

In the seminal work of Arrott and Noakes, [60], a modified Arrott plot construction was presented, as a consequence of the following equation of state:

$$\left(\frac{H}{M}\right)^{(1/\gamma)} = \frac{T - T_C}{T_1} + \left(\frac{M}{M_1}\right)^{1/\beta} \tag{2.71}$$

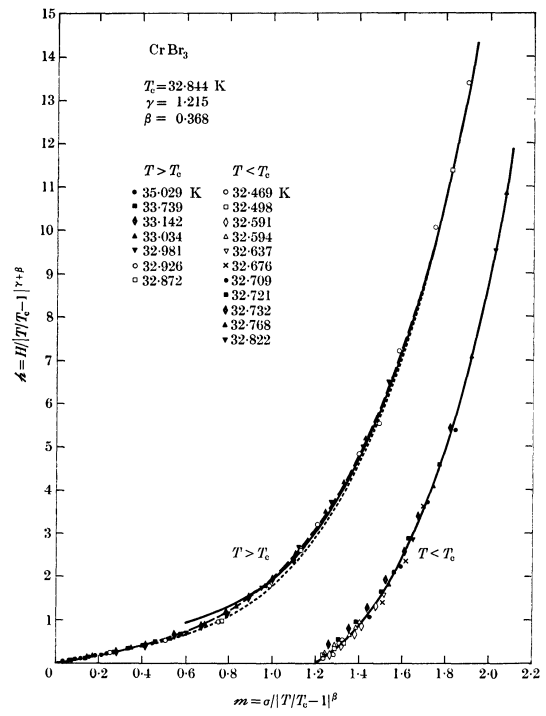

Figure 2.12: Scaled magnetic field h is plotted against scaled magnetization m for the insulating ferromagnet $CrBr_3$, using data from seven supercritical ($T > T_C$) and from eleven subcritical ($T < T_C$) isotherms. Here $\sigma = M/M_{spont}$, from Refs. [58, 59].

where T_1 is a free fitting term, and M_1 the saturation magnetization.

The formulation of such an equation of state is equivalent to linear $(H/M)^{1/\gamma}$ versus $M^{1/\beta}$ plots, with lines parallel and evenly spaced in temperature. Under the mean-field model or Landau theory, since $1/\gamma = 1$ and $1/\beta = 2$, the modified Arrott plot becomes its original formulation. The modified Arrott plot presents a visual way to assess the universality class of a given magnetic system near its transition temperature: searching for the adequate values of β and γ that remove the curvature from the modified Arrott plot, as shown for Nickel [60] in Figure 2.13:.

While this is a valid approach, Arrott and Noakes themselves argue in the original paper about the difficulties and practical shortcoming of this approach to accurately determine the value of critical exponents in this way. We shall discuss this point further on.

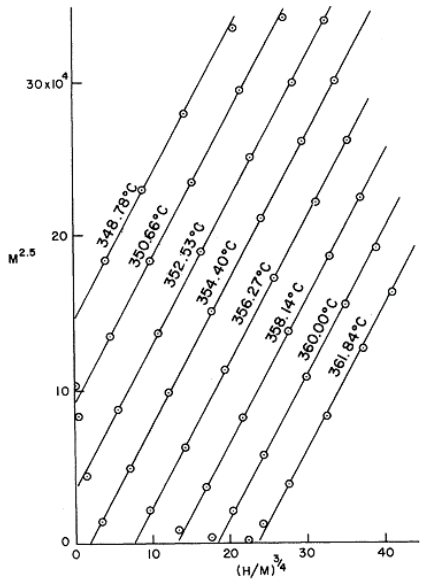

Figure 2.13: The modified Arrott plot for bulk magnetization of a polycrystalline Nickel sample, and $\beta = 0.4$ and $\gamma = 4/3$, from Ref. [60].

Chapter 3

A molecular mean-field scaling method

3.1 Methodology

As presented in chapter 2.3, the molecular mean-field theory gives us a simple and often effective tool to describe a ferromagnetic system. If one is studying magnetization data from a given material, obtaining the mean-field parameters from experimental data is not immediate. To do so, one usually needs to set the spin value and/or the number of ions N, and the mean-field state is function is the Brillouin function or Langevin function (for a high spin value). From then on, the λ_1 parameter can be obtained from low-field M versus T measurements and a linear Curie-Weiss law fit of the inverse susceptibility. Subsequent fits to each $M(H)$ isotherm can then be performed. Such an approach can be quite complex, particularly if one considers a system where the magnetic ions can have different spin states, such as mixed-valence manganites, where the ratio between ions needs to be previously assumed [61]. Obtaining higher orders of the mean-field exchange parameter (λ_3, λ_5, etc.) can be done by performing simulations to describe experimental data, as done by Bean and Rodbell to describe MnAs [50].

A different approach to obtain the mean-field parameters from experimental magnetization data is presented here, based on data scaling. A summarized version of this work has been published in 2007 [ASA07]. We consider the general mean field law, $M(H,T) = f((H + H_{exch})/T)$, where the state function f is not pre-determined, and that λ (as in $H_{exch} = \lambda M$) may depend on M and/or T. Then for corresponding values with the same M, $(H+H_{exch})/T)$ is also the same, the value of the inverse $f^{-1}(M)$ function:

$$\frac{H}{T} = f^{-1}(M) - \frac{H_{exch}}{T} \tag{3.1}$$

By taking H and T groups of values for a constant M and Eq. 3.1, the plot of H/T versus

$1/T$ is linear if λ does not depend on T. The slope is then equal to H_{exch}, for each M value. Then, each isomagnetic line is shifted from the others, since its abscissa at $H/T = 0$ is simply the inverse temperature of the isotherm which has a the spontaneous magnetization equal to the M value. This is shown in Figure 3.1.

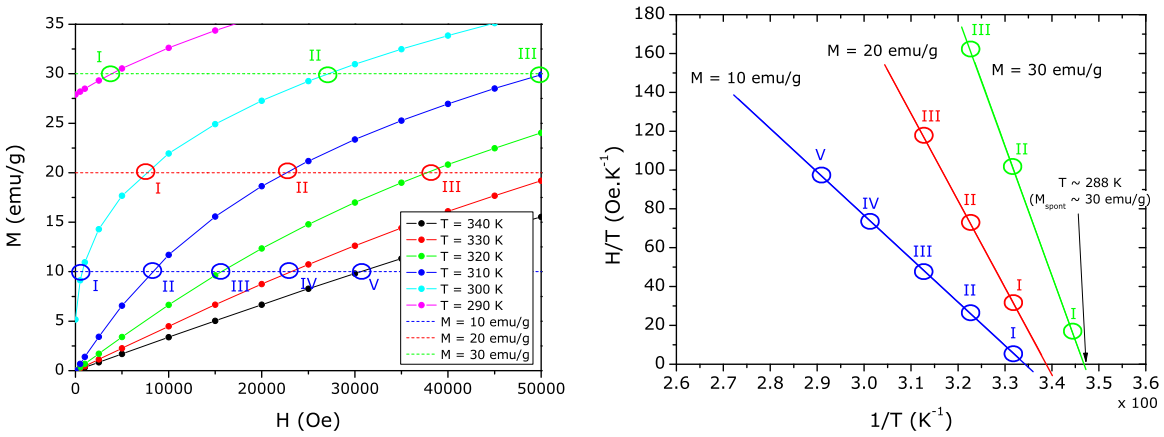

(a) (b)

Figure 3.1: a) Isomagnetic (M = 10, 20 and 30 emu/g) points from mean-field generated data in an M versus H plot (lines are eye-guides), and b) corresponding H/T versus $1/T$ plot (lines are linear fits to isomagnetic points).

In a similar fashion, a simple case of a constant λ (i. e. independent of M and T), a plot of H/MT versus $1/T$ will show parallel lines for all M values, with slope equal to H_{exch}/M, which in turn is equal to λ.

In a first-order phase transition, the discontinuity of $M(H,T)$ means that when interpolating data for constructing the isomagnetic curves, care should be taken not to interpolate the discontinuity in $M(H,T)$. This is shown in Figure 3.2 and is a direct consequence of there being a region in the H/T versus $1/T$ plot that has no data, much like the preceding $M(H,T)$ plot.

Extrapolating this linear relation within this region will not present any real physical result, namely any relation to the spontaneous magnetization, which has a discontinuous jump. This point will be clearer in further simulation results.

From Eq. 3.1, the dependence of the exchange field on M is obtained directly. In principle, one can expect that the exchange field is given by a series of odd powers of M, $H_{exch} = \lambda M = \lambda_1 M + \lambda_3 M^3 + \ \ldots$. This follows from the frequently found expansion of the free energy in powers of M, e.g. when considering magnetovolume effects within the mean-field model by the Bean-Rodbell model as described in section 2.3. Note that the demagnetizing factor is intrinsically taken into account as a constant contribution to λ_1:

$$H_{total} = H_{applied} + H_{exch} - DM = H_{applied} + (\lambda_1 - D)M + \lambda_3 M^3 + \ldots \qquad (3.2)$$

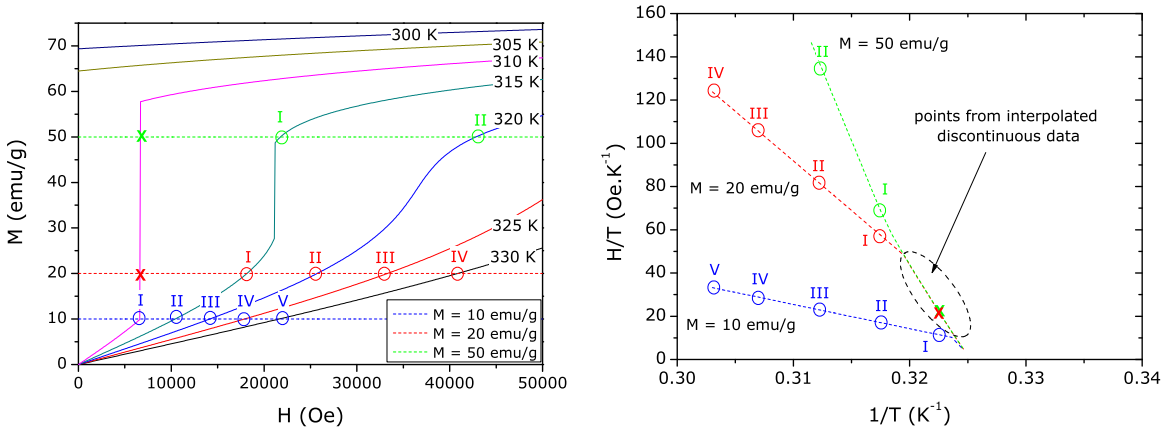

(a) (b)

Figure 3.2: a) Isomagnetic (M = 10, 20 and 30 emu/g) points from mean-field generated data in an M versus H plot (lines are eye-guides), and b) corresponding H/T versus $1/T$ plot (lines are linear fits to isomagnetic points).

where D is the demagnetizing factor, in the simple assumption of an uniform magnetization.

After obtaining H_{exch}, the second step of this method consists on building the scaling plot of M versus $(H + H_{exch})/T$, where data should collapse to the one curve that describes the system, the f function. Analyzing the f function is a further important step to study magnetic systems and to compare the results of theoretical microscopic models.

The above mentioned collapse on the scaling plot can be used to evaluate the validity of the mean-field analysis. In this sense the method is self-consistent: only if H_{exch} has been properly evaluated, will the points collapse into a single curve.

3.2 Second-order phase transition

As a first immediate example of this methodology, let us consider mean-field generated data, for a spin 2 system, with saturation magnetization of 100 emu g^{-1} and $T_C \sim 300$ K. No dependence of λ on T was considered. M versus H data, from 290 to 330 K, at a 1 K temperature step and 100 Oe feld step, are shown in Figure 3.3(a).

We then plot H/T versus $1/T$ at constant values of magnetization, following Eq. 3.1, as shown in Figure 3.3(b):

Since λ does not depend on T, there is a linear behavior of the isomagnetic curves, which are progressively shifted into higher $1/T$ values. From Eq. 3.1, the slope of each isomagnetic line of Figure 3.3(b) will then give us the dependence of the exchange field in M, as shown in Figure 3.4(a).

Having determined the $\lambda(M)$ dependence, we can now proceed to scale all the magnetization data, to determine the mean-field state function, as shown in Figure 3.4(b).

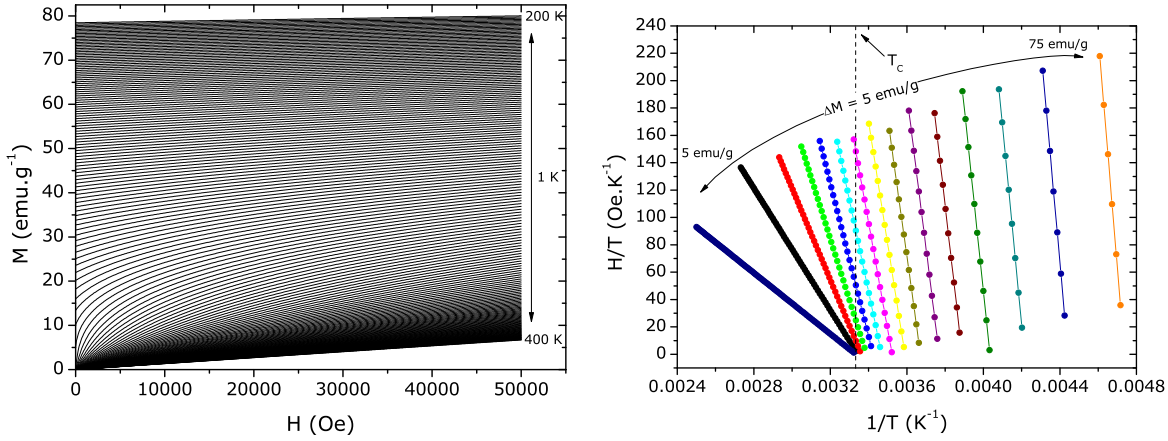

(a) (b)

Figure 3.3: a) Isothermal magnetization versus applied magnetic field, from 200 to 400 K, at a 1 K temperature step and 100 Oe field step and b) Isomagnetic H/T versus $1/T$ plot, of data from the molecular mean-field model, from $M = 5$ emu/g (dark blue line) to $M = 75$ emu/g (orange line), with a 5 emu/g step.

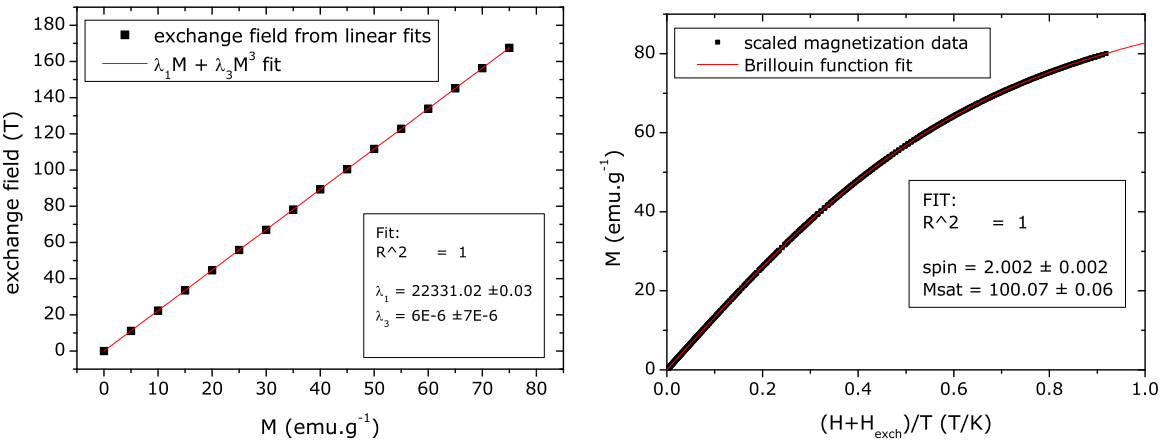

(a) (b)

Figure 3.4: a) Fit of the exchange field dependence on M. Solid squares represent the slope of each isomagnetic curve, from Figure 3.3(b) and b) Brillouin function fit of scaled data from the mean-field model, from Figure 3.3(a).

As expected, the scaled data closely follows a Brillouin function, with spin 2, and a saturation magnetization of 100 emu g^{-1}. We can then describe, interpolate and extrapolate $M(H,T)$ at will, since the full mean-field description is complete (exchange parameters and state function).

3.3 First-order phase transition

As shown previously, this approach is also valid if a first-order magnetic phase transition in considered. There is no fundamental difference on the methodology, apart from the expected higher order terms of $\lambda(M)$. Care must be taken when interpolating $M(H)$ data within the irreversibility zone, so that no values of M correspond to the discontinuities. We simulate a first-order magnetic phase transition by adding a λ_3 dependence of the molecular exchange field, equal to 1.5 (Oe emu^{-1} g)^3, to the previous second-order transition parameters. Isothermal magnetization data is shown in Fig 3.5(a). The discontinuity in magnetization values is visible, and we can estimate that the critical field is around 2.5 T, for this simulation parameters.

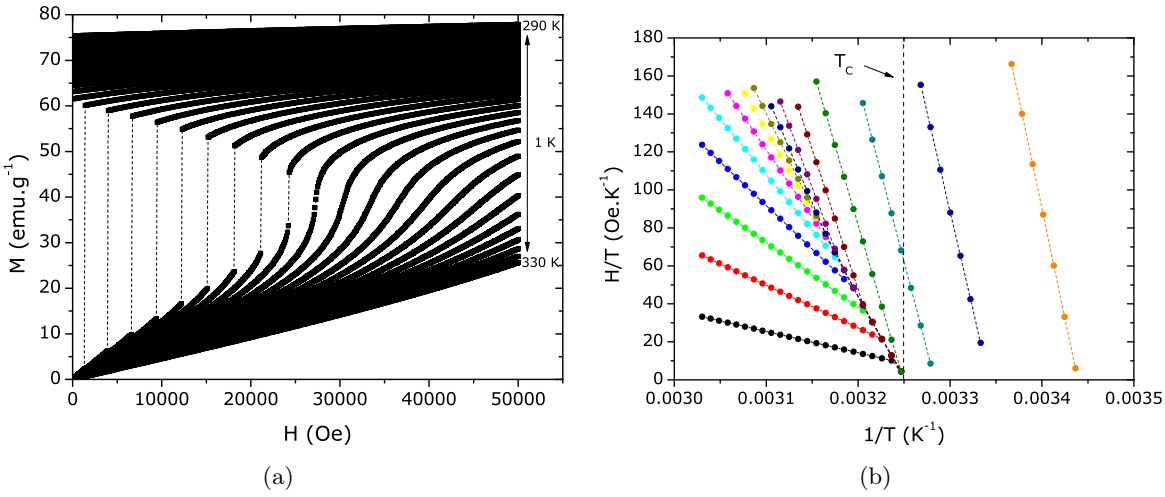

(a) (b)

Figure 3.5: a) Isothermal M versus H data of a first-order magnetic phase transition, from the Bean-Rodbell model and b) corresponding isomagnetic H/T versus $1/T$ plot, for a first-order mean-field system, and a 5 emu g^{-1} step.

From the $M(H,T)$ data, we plot the corresponding isomagnetic H/T versus $1/T$ plot, as shown in Figure 3.5(b).

As shown previously in Figure 3.2 b), if interpolations in $M(H,T)$ are done within the discontinuities, points that do not follow the expected linear behavior appear. These points should not be included for the linear fits to determine $\lambda(M)$. In the rest of the plot, the linear relation between H/T and $1/T$ is kept, as expected. Linear fits are then easily made to each isomagnetic line, and we obtain the exchange field dependence on magnetization, as shown in Figure 3.6(a).

The $\lambda_1 M + \lambda_3 M^3$ dependence of the mean-field exchange parameter is well defined. We obtain λ_1 and λ_3 values that are, within the fitting error, equivalent to the initial parameters. This shows us that the first-order nature of the transition and the associated discontinuities should not affect this mean-field scaling methodology.

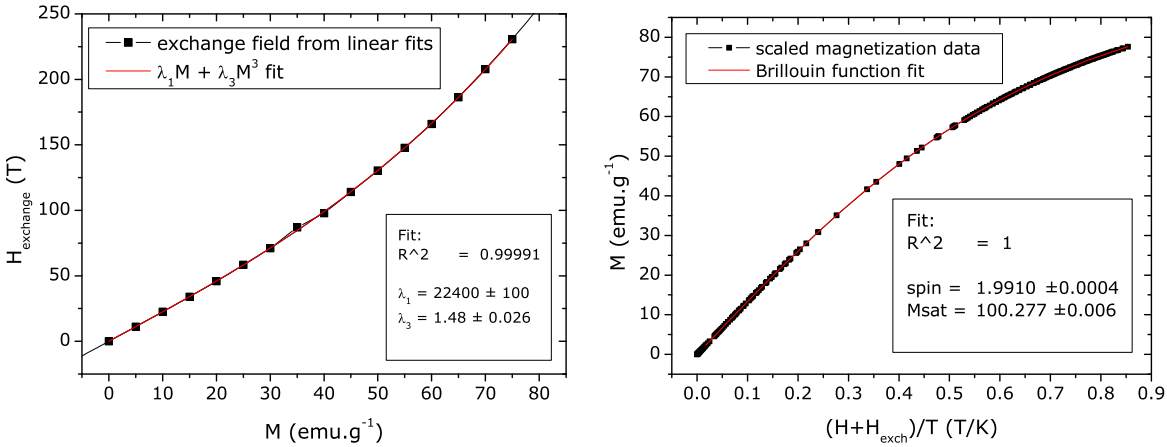

(a) (b)

Figure 3.6: a) Exchange field fit for a first-order mean-field system, with the $\lambda_1 M + \lambda_3 M^3$ law, and b) corresponding mean-field scaling plot and Brillouin function fit.

We can then construct the scaling plot, using the obtained λ_1 and λ_3 parameters, as shown in Figure 3.6(b).

From the scaling plot and the subsequent fit with the Brillouin function, we obtain values of spin and saturation magnetization close to the the initial parameters of the simulation.

3.4 Applications

In the previous section, we have shown how it is possible to obtain directly from bulk magnetization data, and only considering the mathematical properties of the general mean-field expression $M = f[(H + \lambda M)/T]$, a direct determination of the molecular field exchange parameter λ and its dependence on M, and the mean-field state function f, which will contain information on the magnetic entities in play, and their interactions.

One immediate application for this method is to use this description of the magnetic properties of the system as a way to interpolate/extrapolate experimental data, and/or as a smoothing criteria to noisy $M(H, T)$ and corresponding $\Delta S_M(T)$ curves. It is worth mentioning that while this can be also performed within Landau theory, since the mean-field theory is not limited to small M values, the mean-field description of the system can have a broader application range: lower T and higher H values, up to saturation. Still, the methodology presented here is time-consuming, even with optimized numerical data analysis programs. When considering experimental magnetization data for $T < T_C$, care must be taken to adequately disregard data from the magnetic domain region (low fields). Of course, this also affects the Arrott plot fittings of the Landau theory methodology presented previously.

Still, the ability to determine the mean-field parameters directly from experimental data

becomes attractive taking in mind that one can estimate magnetic entropy (and consequently magnetic entropy change) within the mean-field model, by using Eq. 2.65, reproduced here for convenience.

$$-\Delta S_M(T)_{H_1 \to H_2} = \int_{M|_{H_1}}^{M|_{H_2}} \left(f^{-1}(M) - \left(\frac{\partial \lambda}{\partial T} \right)_M M \right) dM.$$

And so not only can the $M(H,T)$ values be interpolated/extrapolated, the entropy curves and their dependence in field and temperature can also be easily interpolated and extrapolated. This becomes particularly appealing if one wishes to make thermal simulations of a magnetic refrigeration device, and, within a physical model (and not by purely numerical approximations), the magnetocaloric response of the material, at a certain temperature and a certain field change is directly calculated. As an example of this approach, bulk isothermal magnetization data of two ferromagnetic manganite systems will be analyzed in this section.

Figure 3.7(a) shows the magnetization data of the ferromagnetic, second-order phase transition $La_{0.665}Er_{0.035}Sr_{0.30}MnO_3$ manganite, obtained by SQUID measurements at IFIMUP-IN. Figure 3.7(b) shows the isomagnetic H/T versus $1/T$ plot, up to 50 emu/g in a 5 emu/g step, which could be reduced in order to have more points.

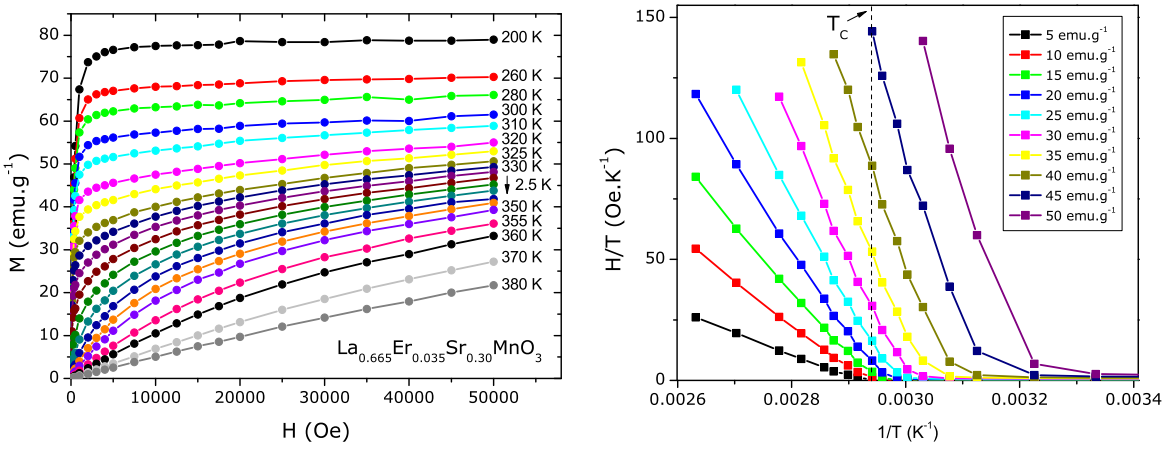

Figure 3.7: a) Magnetization data of $La_{0.665}Er_{0.035}Sr_{0.30}MnO_3$ and b) corresponding isomagnetic H/T versus $1/T$ plot. Lines are eye-guides.

Each point at constant M is obtained from data interpolation os the isothermal $M(H)$ data. From linear fits to the H/T versus $1/T$ plot, the dependence of the exchange field in magnetization is directly obtained (Figure 3.8(a)). The exchange field is fitted to a $\lambda_1 M + \lambda_3 M$ function. The scaling plot is then constructed, as shown in Figure 3.8(b).

For calculation purposes, the scaling function of Figure 3.8(b) was described as an odd-terms polynomial function. The Figure shows some data point that are clearly deviated from

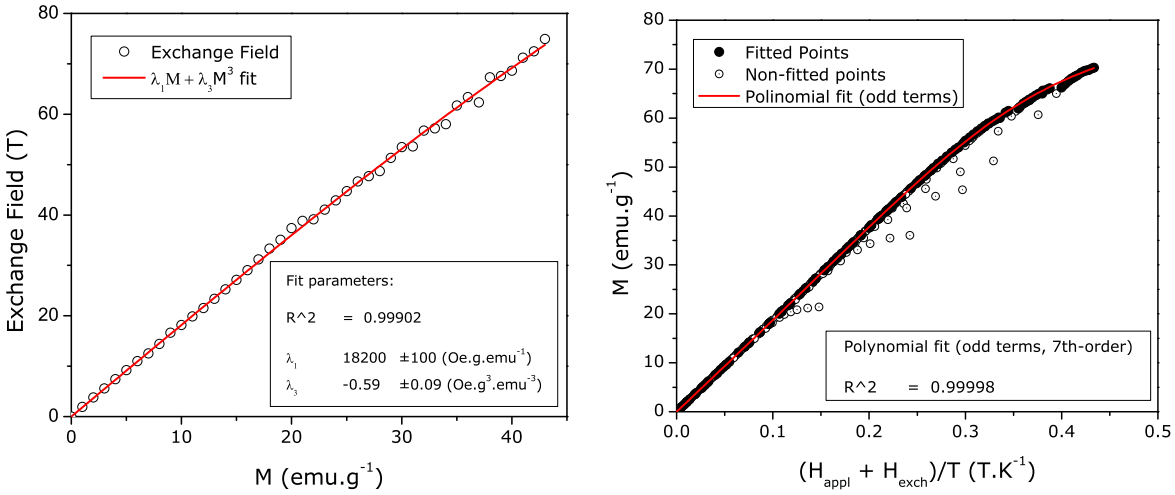

(a) (b)

Figure 3.8: Interpolating a) experimental $M(H,T)$ data and b) magnetic entropy change results by mean-field simulations for the second-order phase transition manganite $La_{0.665}Er_{0.035}Sr_{0.30}MnO_3$.

the scaling function. These points correspond to the magnetic domain region (low fields, $T < T_C$). With the exchange field and mean-field state function described, the magnetic behavior of this material can then be simulated. Also, magnetic entropy change can be calculated from the mean-field relation of Eq. 2.65. Result from these calculations, together with the experimental $M(H,T)$ data and $\Delta S_M(H,T)$ results from Maxwell relation integration are shown in Figure 3.9.

A good agreement between the experimental $M(H,T)$ curves and the mean-field generated curves with the obtained parameters is obtained. The entropy results show some deviations, particularly near T_C. While the mean-field theory does not consider fluctuations near T_C, these deviations can be attributed to that fact. Still, as we will see later, by considering disorder effects (chemical/structural inhomogeneity), a better description of magnetocaloric properties will be obtained.

We now consider bulk magnetization data of a the first-order ferromagnetic phase transition $La_{0.638}Eu_{0.032}Ca_{0.33}MnO_3$ manganite. Figure 3.10(a) shows isothermal magnetization data obtained from SQUID measurements, and Figure 3.10(b) shows the corresponding isomagnetic H/T versus $1/T$ plot.

The exchange field H_{exch} dependence on magnetization (Figure 3.11(a)) and the mean-field state function (Figure 3.11(b)) are then obtained.

Like the previous example of the second-order manganite, the mean-field state function f is fitted to a polynomial function, for calculation purposes. With the λ_1 and λ_3 exchange parameters and the f function described, $M(H,T)$ simulations can be performed, and com-

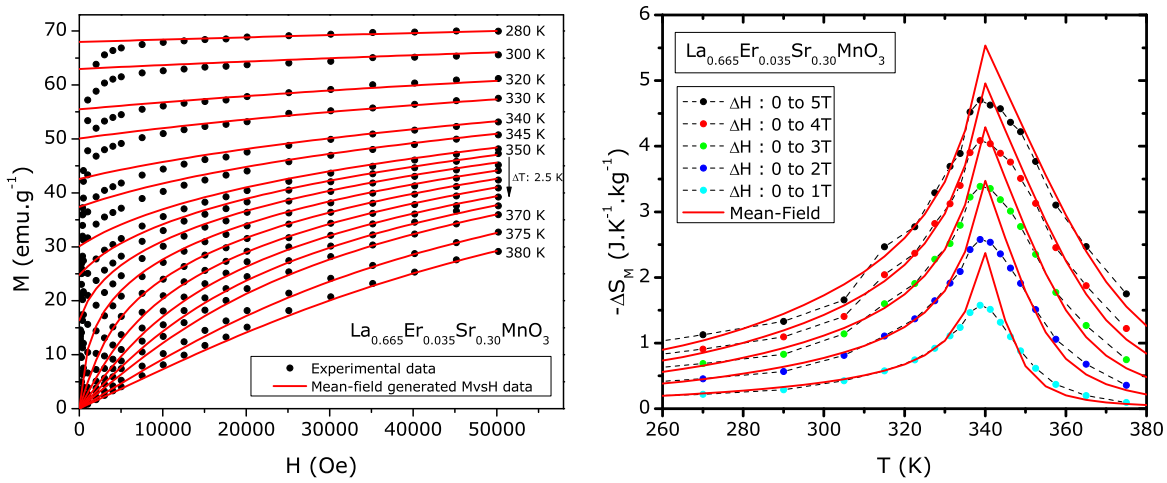

(a) (b)

Figure 3.9: Interpolating a) experimental $M(H,T)$ data and b) magnetic entropy change results by mean-field simulations for the second-order phase transition manganite $La_{0.665}Er_{0.035}Sr_{0.30}MnO_3$.

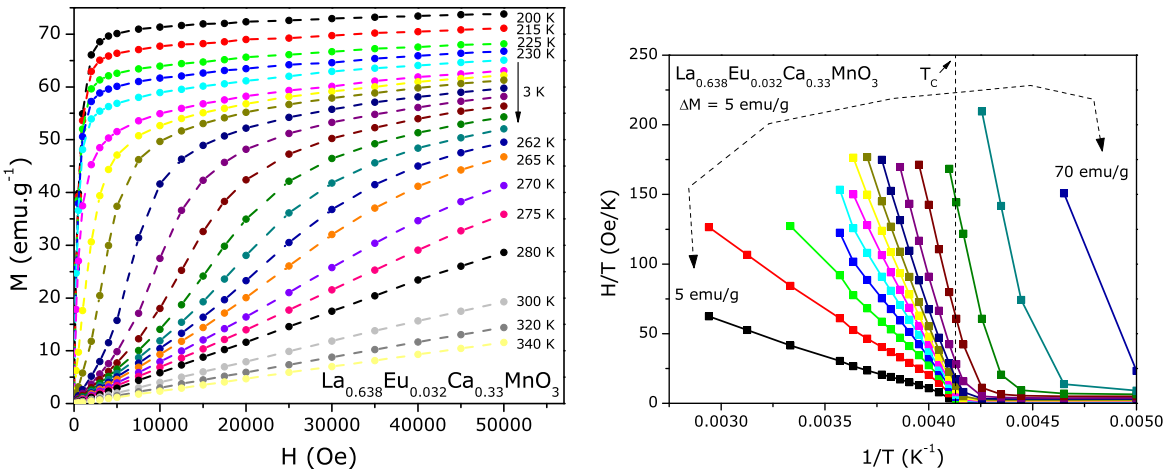

(a) (b)

Figure 3.10: a) Magnetization data of $La_{0.638}Eu_{0.032}Ca_{0.33}MnO_3$ and b) corresponding isomagnetic H/T versus $1/T$ plot. Lines are eye-guides.

pared to the experimental values. Also, magnetic entropy change can be estimated from the mean-field relation of Eq. 2.65 and compared to results form the use of the Maxwell relation. Results are shown in Figure 3.12.

The results of this mean-field scaling method are also very promising for this first-order phase transition system. There are some deviations in the irreversibility region of the $M(H,T)$ plot, and also the simulated entropy curves are slightly sharper, and present a higher maxi-

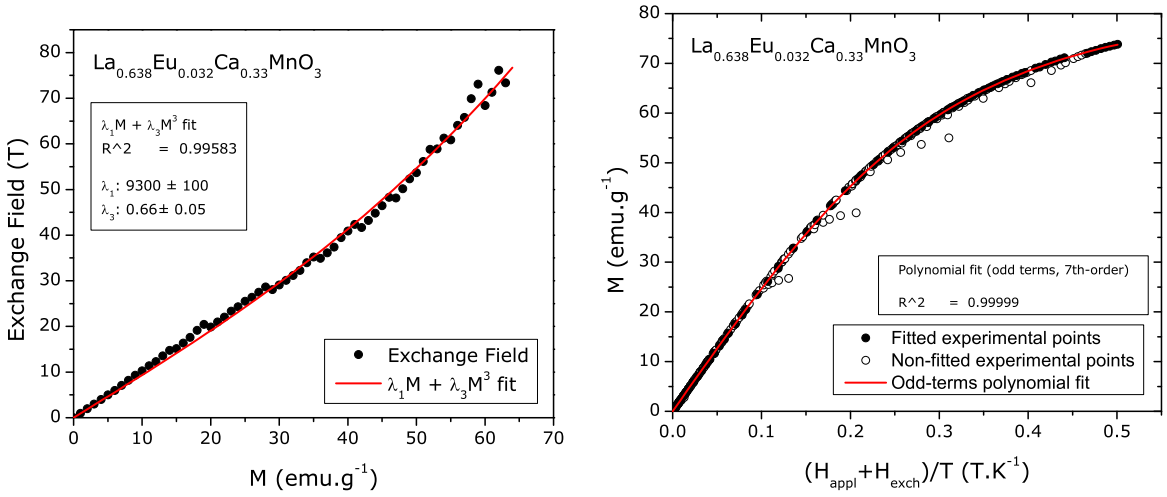

Figure 3.11: Interpolating a) experimental $M(H,T)$ data and b) magnetic entropy change results by mean-field simulations for the second-order phase transition manganite $La_{0.665}Er_{0.035}Sr_{0.30}MnO_3$.

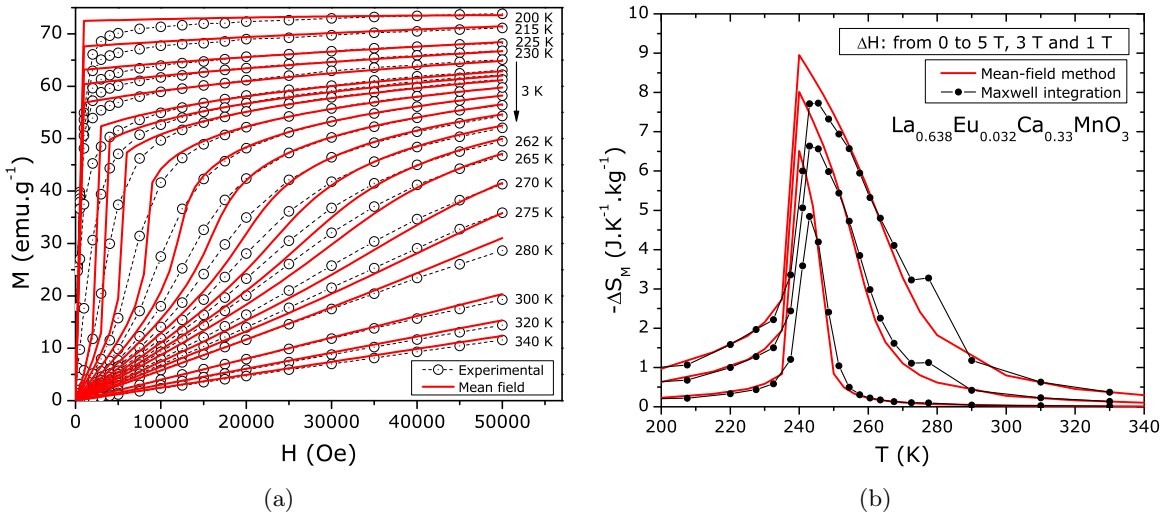

Figure 3.12: Interpolating a) experimental $M(H,T)$ data and b) magnetic entropy change results by mean-field simulations, of the first-order phase transition manganite $La_{0.638}Eu_{0.032}Ca_{0.33}MnO_3$.

mum value. As we will see later, these deviations can be attenuated by considering disorder effects.

The insight that can be gained from the use of this methodology for a given magnetic system can be of great interest. In a simplistic approach, we can say that if this scaling method does not work, then the system does not follow a molecular mean-field behavior,

and other methods need to be pursued in order to interpret the magnetic behavior of the system. It is important to emphasize that this scaling analysis is global, in the sense that it encompasses the consistency of the whole set of magnetization data.

The methodology described here has allowed a study of superferromagnetic behavior in FeCu alloys [SAA+09]. The study of a non-trivial dependence of the exchange field on the magnetization has allowed the description of the magnetic properties of the system as a superferromagnetic clusters of Fe ions, in two different cluster sizes and configurations. This study will be presented in chapter 7.

3.5 Limitations

Of course, there are limitations to the use of this method, even if one is successful in determining the exchange field parameters and, from what appears to be a good scaling plot, determine the mean-field exchange function. For extensive and smooth $M(H,T)$ data, interpolating isomagnetic data should not pose a real problem, but choosing which points in the H/T versus $1/T$ to fit or to disregard (due to magnetic domains or from the discontinuities of first-order transitions) can remove the confidence on the final scaling plot, and consequently on the mean-field state function.

It is indeed a time consuming task to consider some variations on the linear fittings of the H/T versus $1/T$ plots, and then create a different scaling plot, qualitatively evaluate the quality of the new scaling plot compared to the previous one, and then proceed to determine the f function. This motivated a search for an alternative method to produce the scaling plot, in a hope to have a quantitative method to evaluate the quality of data scaling, and consequently automatize the process of searching for the 'best' scaling parameters and consequently the 'best' data scaling. Ultimately, this would correspond to an increase in the confidence of the physical interpretation of the scaled function.

In a way, the objective is to be able to handle data-scaling in a similar way to fitting functions, where a 'goodness of fit' parameter exists, and the fitting procedure merely looks for the best fit by comparing the value of this parameter to previous fits.

In the next chapter, we propose a definition of a 'goodness of scaling' parameter, that can quantitatively define the quality of data scaling, and so be used in data scaling problems as a method to quantitatively and objectively search for the best data scaling parameters for a given scaling approach, not limited to the mean-field case.

Chapter 4

A goodness of scaling parameter

The mean-field scaling method presented in chapter 3 has given us a new approach to analysing magnetization data and directly determine if the system under study can be adequately described in a molecular mean-field perspective. Obtaining the mean-field parameters required some degree of data interpolation and replotting in isomagnetic curves, as well as performing linear fits for each magnetization value considered. In this chapter, we present another methodology that can be used in scaling studies, including the application of the molecular mean-field model and magnetovolume effects by the Bean-Rodbell model. Instead of analysing data to obtain the mean-field parameters and then scaling the magnetization data, a method to analyze the 'scaling goodness' of a scaling plot would allow the direct search of the sought mean-field parameters. This way, a totally unbiased numerical method could be used, with the confidence that the final scaling plot would be the best possible. The only choice would be the assumption on how many parameters are required. As will be seen later, this methodology is not limited to mean-field scaling, but can be used in many studies, including the search for critical exponents.

To our knowledge, the only reference in the bibliography that proposes a method to quantify the quality of scaling (or data collapse) is the work of Bhattacharjee and Seno in 2001 [62]. As eloquently put by the authors, "given the importance of scaling in wide varieties of problems, it is imperative to have an appropriate measure to determine the 'goodness of collapse' – not to be left to the eyes of the beholder". Their methodology overcomes the main difficulty (not knowing *a priori* the scaling function) by calculating a region of overlap between points in the scaling plot, and then by 4-points polynomial interpolation, describe a function that crosses these regions of overlap. The best scaling plot is then the one where the sum of residuals is minimum. The method presented by Bhattacharjee and Seno has three major drawbacks, namely that the region of overlap is defined in only one axis, numerical intensiveness, since for each N data points, the distance between each point is calculated, and also in the polynomial interpolation step.

The method presented in this thesis has two main goals: the 'goodness of scaling' pa-

rameter should analyze the scaling quality simultaneously in the x and y axis, and using the method should be simple and not numerically intensive in a way as to make it unpractical.

4.1 Methodology

The methodology is straightforward. Let us consider a system that follows a known universal law, and that a scaling plot can be constructed. In general terms, this scaling construction depends on scaling variables. By considering a range of these scaling variables, multiple scaling plots can be constructed. For each of the scaling plots, a 'goodness of scaling' parameter is calculated. This parameter is obtained by analysing the scaling plots, and looking for the ones where the area of the plotted data set is minimum.

The idea behind this approach is that if an universal behavior is present on the experimental data, then the scaling plot where the plotted data occupies the minimum area corresponds to the maximum amount of data overlap, and so, the best scaling that can be achieved. Figure 4.1 gives a schematic representation of this reasoning.

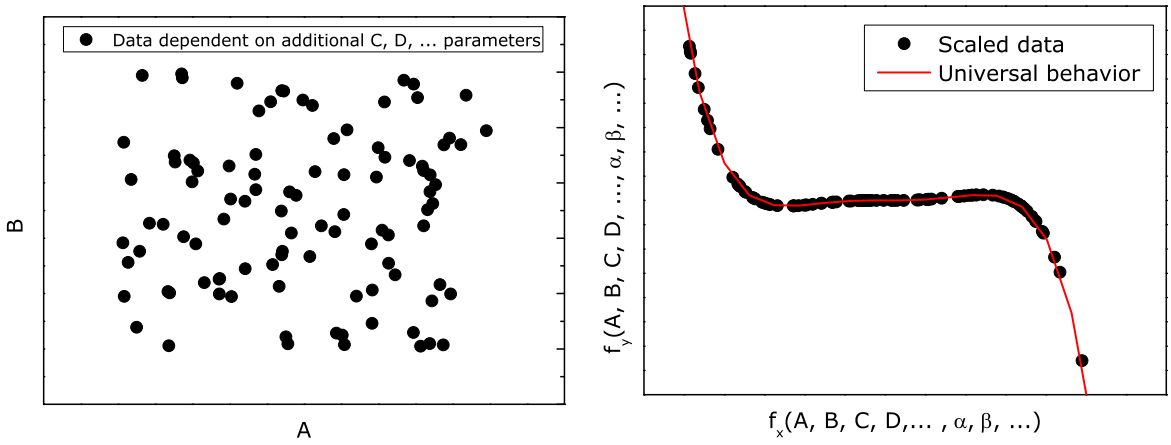

(a) (b)

Figure 4.1: Schematic representation of data scaling. a) is the original data set, and by a change in the axes, depending on the considered universal law, as shown in b), graphical data overlap will occur, revealing the universal behavior.

Consider a system, where several quantities (A, B, C, D, ...) are related to each other. Consider we measure the values of A and B, for a multitude of C, D, ... values, as shown in Figure 4.1(a). If it is possible to describe an universal function that relates all quantities between themselves, this universal behavior will be evident in a adequate scaling plot, as shown in Figure 4.1(b). It is possible that the universal behavior depends on scaling parameters, represented by α, β, etc. In such a case, there can only be a good scaling plot if we know the values of these scaling parameters. Still, if we have a reasonable amount of data, the best scaling plot will present the most data overlap. As a consequence of this, the best scaling plot

will be the one where the area occupied by the plotted data is minimum. By this reasoning, it is possible to search for the adequate scaling parameters by plotting several scaling plots, each resulting from the chosen set of scaling parameters, and searching for the one where the area occupied by the graphical representation of data is minimum.

This kind of method has two immediate advantages: firstly, it makes data scaling quality quantitative, objectifying these studies; secondly, this simplifies scaling studies by being able to easily become an automated numerical process.

In order to analyze data using this methodology, a Matlab routine was developed. Our first example is for mean-field scaling, where the considered universal law was $M = f[H + \lambda_1 M + \lambda_3 M^3]/T$, and so assuming the dependence of H_{exch} as a two parameter function of M. Experimental data is then magnetization, applied magnetic field and temperature, and the scaling parameters are the mean-field exchange parameters λ_1 and λ_3. f is an unknown function which can only be correctly determined if the correct scaling parameters are used. The crucial part of the code that establishes the values of the 'goodness of scaling' parameter, and was developed for this purpose, is as follows:

For a set of $M(H,T)$, for each pair of (λ_1, λ_3) values, a normalized scaling plot is drawn and exported as an image file.

```
scaled_x(j,i) = (H(j)+lambda1(lambda1_count)*M(j,i)
                +lambda3(lambda3_count)*M(j,i).^3)/T(i);
scaled_y(j,i) = M(j,i);
max_x=max(max(scaled_x));
max_y=max(max(scaled_y));
plot(scaled_x./max_x,scaled_y./max_y,'linewidth', 0.1,'Color','k'),
                axis([-0.01 1.01 -0.01 1.01]),axis off;
print -dtiff grafico -r300
```

This image file is then analyzed, simply counting the number of pixels used in the graphical representation of the scaling plot:

```
I=imread('grafico.tif');
Ib=rgb2gray(I);
Ib_dither=dither(Ib);
white(lambda1_count,lambda3_count)=size(find(Ib_dither == 1),1);
black(lambda1_count,lambda3_count)=size(find(Ib_dither == 0),1);
simple_ratio(lambda1_count,lambda3_count)=
        =(black(lambda1_count,lambda3_count)./
        ./(black(lambda1_count,lambda3_count)+
        +white(lambda1_count,lambda3_count)));
```

And so for each (λ_1, λ_3) pair, a value is assigned that corresponds to a 'goodness of scaling' parameter. The best scaling parameters can then be found by plotting the 'goodness

of scaling' parameters of each scaling plot versus the values of λ_1 and λ_3. These plots can be either 2D contour plots, or 3D mesh plots. One of the advantages of this method is that it is totally automatic, and so the detail in step and interval of the scaling parameters is only limited by computing time. Another important advantage is that this method is of course much more rigorous than the usual qualitative (visual) observation of the quality of scaling plots on paper or screen. Also, the resolution of the exported plots is much greater than normal screen resolutions, and it would be unfeasible for a person to distinguish one scaling plot from another and look for the best scaling parameters visually. We will clarify this point by exemplifying the use of this method.

4.2 Application example: mean-field magnetization data

4.2.1 Second-order phase transition

Let us start with the second-order phase transition mean-field generated data from Figure 3.3(a), obtained with spin 2, $\lambda_1 = 22331$ Oe emu^{-1}g ($T_C \sim 300$ K), $\lambda_3 = 0$, and saturation magnetization set as 100 emu g^{-1}. We set the range of λ_1 values to be tested from 20000 to 24000 (step 100) Oe g emu^{-1}, and λ_3 values from 0 to 2 (step 0.05) Oe (emu/g)$^{-3}$.

To exemplify the detail that can be obtained by pixel counting of high-resolution images, we plot 4 scaling plots, at the rather distinct extreme values of (λ_1, λ_3) and the initial values (Figure 4.2).

Even at this figure size, it is difficult, if not impossible, to visually distinguish the relative quality of scaling between the five plots. Only by a careful examination of each plot (by zooming-in the high resolution image) can we make any observations. This is shown in the inset of Figure 4.2. The quality of the scaling is indeed dependent on the parameter values, as varying 'thicknesses' becomes apparent. Of course, if one is to search for the correct mean-field exchange parameters by this visual method, it not only would be a tedious procedure, it would be qualitative and not at all rigorous.

We use the simulated M versus H data, and use the 'goodness of scaling' method to search for the best exchange parameters. Figure 4.3 shows the result of this analysis, in the form of a normalized 'goodness of scaling' parameter versus the values of λ_1 and λ_3, in a contour plot format (Figure 4.3(a)) and 3D mesh plot (Figure 4.3(b)).

A well-defined minimum appears near $\lambda_1 = 22300$ Oe (emu/g)$^{-1}$ and $\lambda_3 = 0$ Oe (emu/g)$^{-3}$, which is the region of the exchange parameters used for the simulation. The sensitivity of this method is limited to the step size in the scaling variables. To a lesser extent, other factors come into play, related to the graphical method of analysing the scaling plots and data overlap. Sensitivity is affected by the size and shape of the chosen data symbols. A circular data point representation is the obvious choice, but setting the size of each plotted data point is not arbitrary. Indeed, if each data point is too small, there may be no data

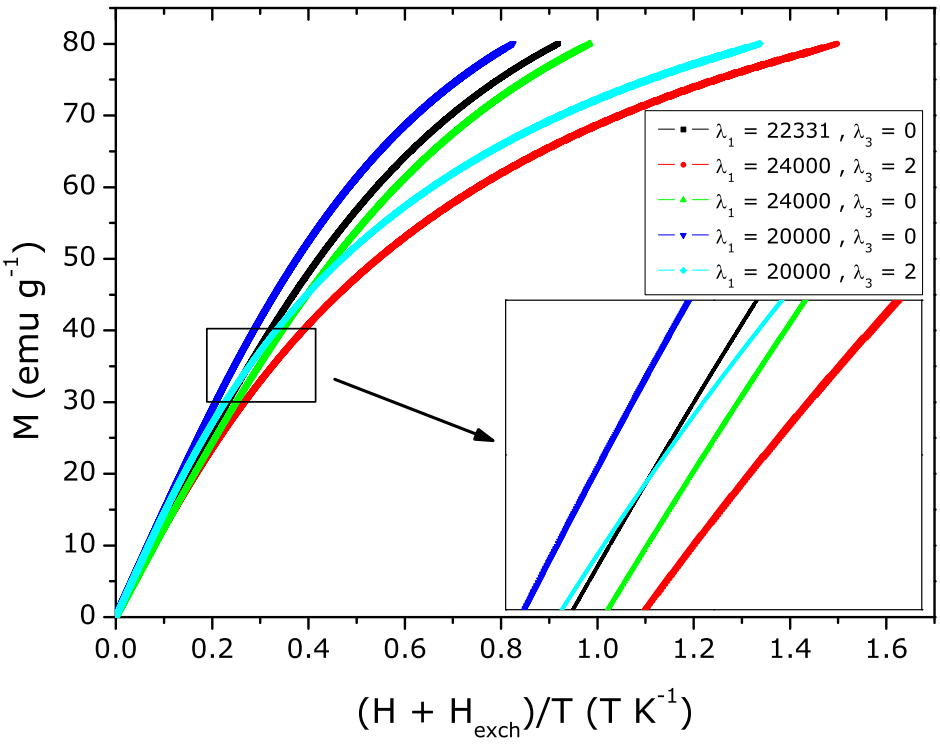

Figure 4.2: Mean-field scaling plots for various exchange parameter values. Inset shows zoomed area.

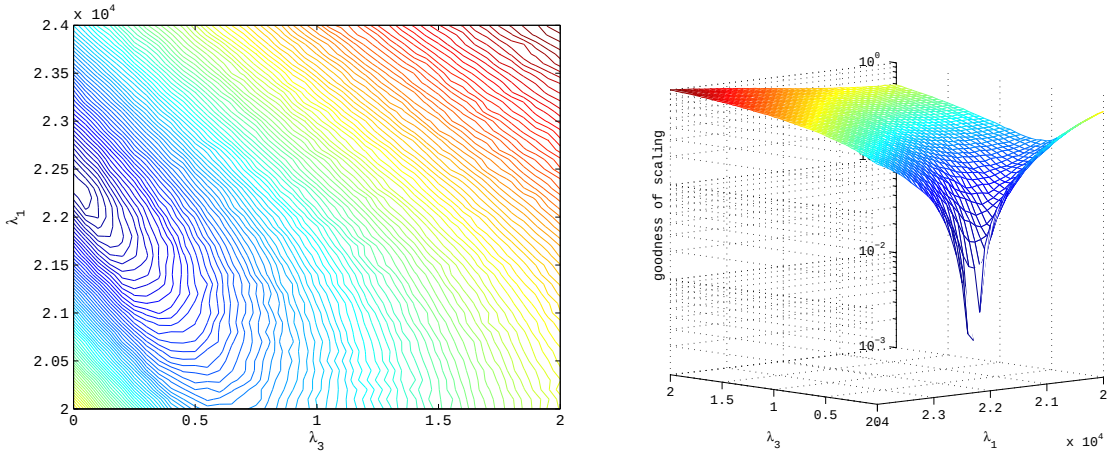

(a) (b)

Figure 4.3: a) mesh and b) contour plots of the 'goodness of scaling' parameter as a function of the mean-field exchange parameters λ_1 and λ_3, for the magnetization data of Figure 3.3(a).

overlap. If each circle is too big, there is some loss in sensitivity. This is not a major issue if there is a large number of data points. There is also the possibility to interpolate the data,

simply by plotting the scaling plot with lines connecting each data point. Of course, this should only be done when the data can be interpolated (no discontinuities). The sensitivity of the method is also affected by the resolution of the image file corresponding to the scaling plot. For higher resolution plots, there is a consequent increase in sensitivity, at the cost of extended computing time. In practical terms, this does not significantly affect the results of this methodology. The plot resolution can easily be high enough so that it is not really an issue, and the data point size is easily set to a reasonable value. These parameters only affect the sensitivity, and not the final result.

When considering a first-order phase transition system, the scaling plot should consist of a representation of scaled data in discrete circular points due to the discontinuities present in the $M(H,T)$ data. In the following section, we apply the same 'goodness of scaling' method to search for the mean-field exchange parameters of a first-order magnetic phase transition system, from the Bean-Rodbell model.

4.2.2 First-order phase transition

We apply the same method to first-order phase transition results (Figure 3.5(a)), resulting from a mean-field system with spin 2, $\lambda_1 = 22331$ Oe emu^{-1}g ($T_C \sim 300$ K), and a magnetoelastic coupling parameter of $\lambda_3 = 1.5$ Oe (emu/g)$^{-3}$, corresponding to an η parameter ~ 1.45. Results are presented in Figure 4.4.

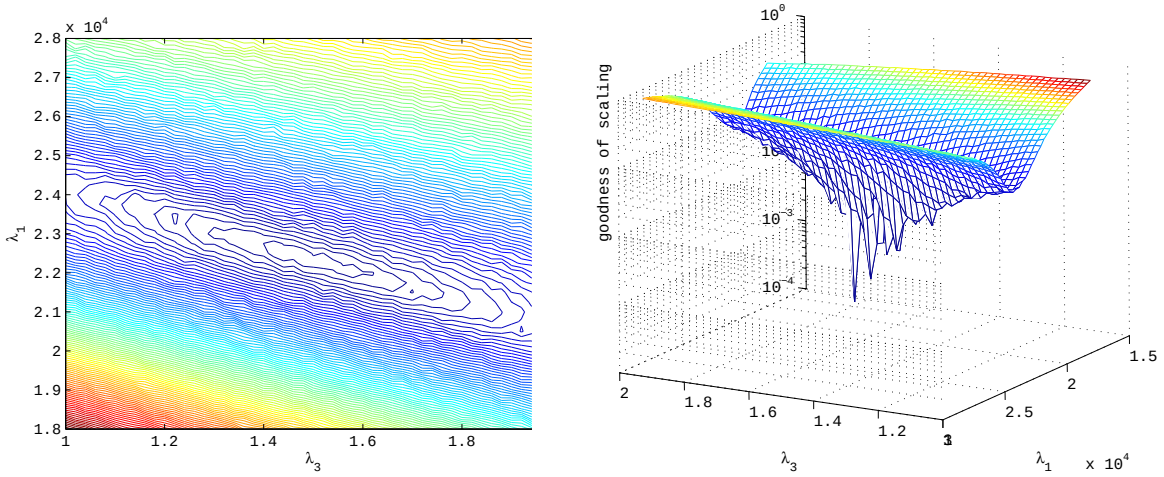

Figure 4.4: a) mesh and b) contour plots of the 'goodness of scaling' parameter as a function of the mean-field exchange parameters λ_1 and λ_3, of a first-order transition system, for the magnetization data of Figure 3.5(a).

A well defined minimum is visible in the $\lambda_1 \sim 22300$ Oe (emu/g)$^{-1}$, $\lambda_3 \sim 1.5$ Oe (emu/g)$^{-3}$ region. As explained previously, due to the discontinuities present, the data representation

of the scaling plots was done with no lines connecting the scaled data points, in order not to interpolate a discontinuous data set.

It is also important to assess the robustness of this scaling methodology, when the data under analysis has an added noise component.

4.2.3 Noisy data

Random noise was added to the previously used magnetization data of both the second-order and first-order systems. A random 1% noise was introduced using the Matlab random number generator function. A 1% error in experimental data would make it of very limited use in regular analysis, and only by statistical methods would it be possible to confidently analyze the data. Still, we take the data 'as-is', and use the 'goodness of scaling' method to verify the resulting scaling parameters obtained.

Second-order phase transition

Figure 4.5(a) shows *very* noisy magnetization data, resulting from adding 1% of random noise to the second-order phase transition data of Figure 3.3(a) ($\lambda_1 = 22331$, $\lambda_3 = 0$) , and Figure 4.5(b) the resulting contour plot, from the goodness of scaling method.

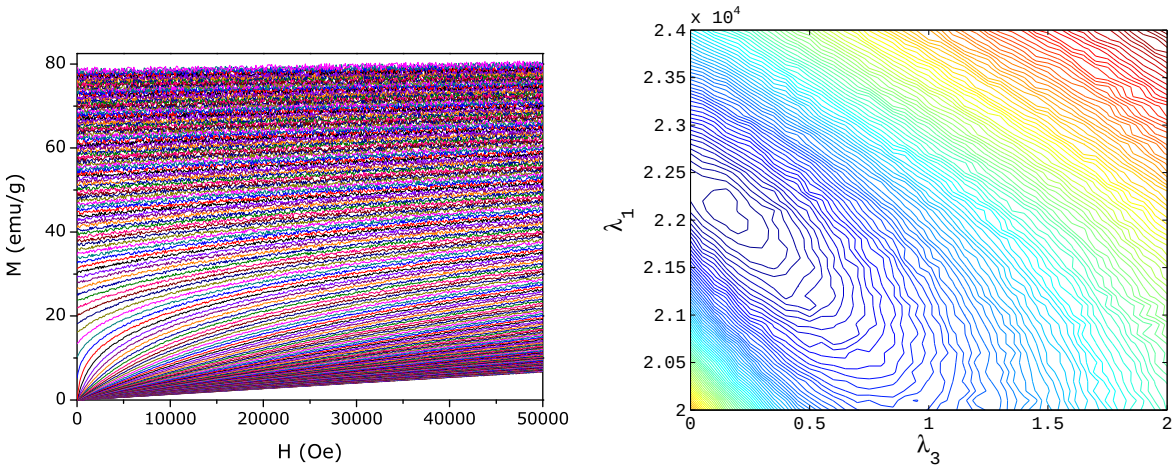

(a) (b)

Figure 4.5: a) mesh and b) contour plots of the 'goodness of scaling' parameter as a function of the mean-field exchange parameters λ_1 and λ_3, of a second-order transition system (data of Figure 3.3(a)), with added random 1 % noise.

There is a shift of ~ 0.15 of the λ_3 parameter, while the λ_1 has only a negligible shift. Note that the size of area that delimits the (λ_1, λ_3) pairs with a comparable scaling quality is much larger than the resulting one of the data with no noise added (Figure 4.3(a)). In terms of data with errors, this is very much a worst-case scenario, and so the result is quite

satisfactory. The shift in the obtained λ_3, although considerable, does not invalidate the use of this methodology in noisy data.

First-order phase transition

Let us now consider noisy data of a first-order system, and see how the introduction of random noisy affects the determination of the scaling parameters.

Figure 4.6(a) again shows *very* noisy magnetization data, this time obtained from adding 1% random noise to the mean-field generated data of Figure 3.5(a). Figure 4.6(b) shows the corresponding contour plot, obtained by the 'goodness of scaling' method.

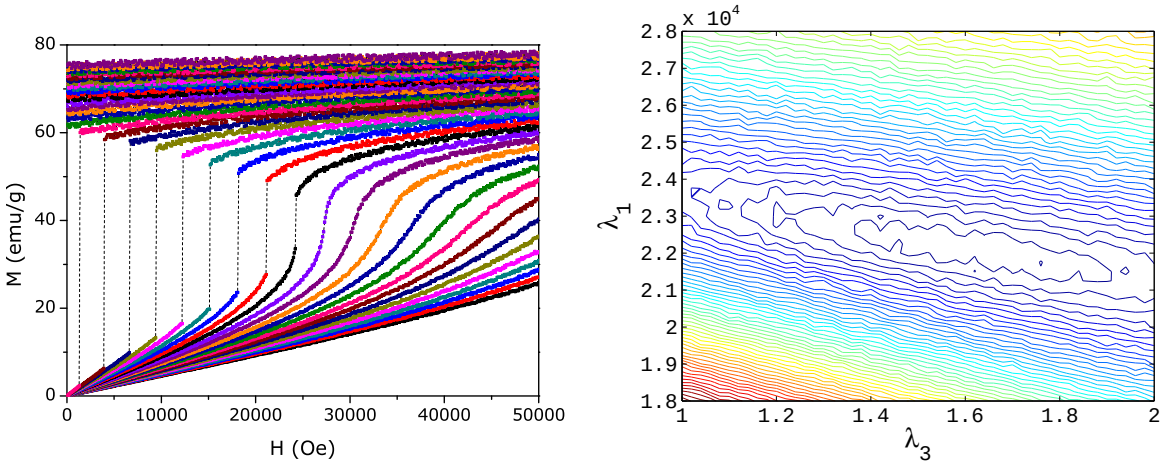

(a) (b)

Figure 4.6: a) mesh and b) contour plots of the 'goodness of scaling' parameter as a function of the mean-field exchange parameters λ_1 and λ_3, of a first-order transition system (data of Figure 3.5(a)), with added random 1 % noise.

In this case we see a minimal increase of the λ_3 value (from 1.5 to 1.56) and a minimal decrease of the λ_1 value (from 22331 to 22000). Again, the region that delimits the (λ_1, λ_3) with comparable scaling quality is much broader, compared to the contour plot for the data with no added noise (Figure 4.4(a)).

These results show us that a graphical method to determine the best scaling parameters is possible, and with good results, even using very noisy data. Since the methodology is generic, it can be used in the search for scaling parameters in other theories, like critical point phenomena.

4.3 Critical phenomena scaling studies

Let us recap the scaling relations for magnetization and magnetic entropy that were presented earlier, in section 2.4 of this thesis (Eqs. 2.69 and 2.70):

$$\frac{h}{|t|^{\beta\delta}} = f_{\pm}(\frac{m}{|t|^{\beta}})$$

and

$$\frac{S}{h^{\epsilon}} = f_{\pm}(\frac{t}{h^{\psi/1-\alpha}})$$

where $\psi = \frac{1-\alpha}{\beta\delta}$ and recalling that $t = \frac{T-T_C}{T_C}$.

The scaling plot of magnetization depends on the M, H and T variables, and the scaling parameters β, δ and T_C. Note that in the ferromagnetic region, the spontaneous magnetization comes into play, which makes scaling below T_C dependent on other parameters which may not be immediately obtainable. Still, above T_C the 'goodness of scaling' method can be easily applied, albeit with three scaling parameters, making the numerical method more time-consuming than mean-field scaling. Of course, one can estimate T_C from any other method (usually the maximum derivative of $M(T)$), and so work with only two scaling parameters. Still, as we will see further when analysing experimental data, correctly determining the T_C value will have a big impact on the scaling quality and consequently the value of the critical exponents.

While scaling the magnetic entropy data is also possible, we should raise some questions on its usefulness. The first point is that when estimating magnetic entropy change values from magnetization, the numerical calculation introduces numerical errors, which may play an important role on data scaling. Also, the obtained scaling exponent values (α, β or ψ), can be easily calculated from the β, δ exponents obtained from scaling magnetization, by using the well-known relations between critical exponents.

Critical phenomena scaling explored in this work will then be focussed on scaling the magnetization data, directly obtained experimentally. Of course, the scaling of entropy should be appropriate to analyzing thermal measurements.

4.4 On the search for universal behaviour

The usefulness to defining a 'goodness of scaling' parameter is not limited to magnetization studies. A plethora of work is continuously being published in the search of universal behavior (generally power laws) in a wide range of topics, ranging from economics [63], biology [64], sociology [65], geology [66], astronomy [67], etc. The scaling methodology in these works is usually re-plotting data in log-log plots, revealing an universal behavior. Again, there are usually scaling parameters present, whose values are determined in a qualitative way.

The methodology presented here can be applied in these studies, hopefully simplifying and presenting a more rigorous approach to generalized power-law scaling studies, particularly in cases where the scaling parameters have some physical meaning.

In this thesis, the 'goodness of scaling' method will be applied in experimental mean-field

and critical point phenomena studies of magnetization data of ferromagnetic materials. As we have seen previously, there is a universal scaling law present in both theories, and the scaling parameters give us insight on the physics of the system under study. In first-order phase transitions, critical phenomena theory cannot be formally applied, and so mean-field theory scaling will be used. For second-order phase transitions, critical point theory scaling can be applied for data near the transition. Only if the critical exponents resemble the mean-field values can mean-field scaling be explored, particularly in data near T_C.

Chapter 5

The magnetocaloric effect in first-order magnetic phase transitions

5.1 Estimating magnetic entropy change from magnetization measurements

As discussed in chapter 1, the most common way to estimate the magnetic entropy change of a given magnetic material is from isothermal bulk magnetization measurements. While a very direct approach is possible, by integrating the Maxwell relation (Eq. 1.5), the validity of such an approach has been questioned for the case of a first-order magnetic phase transition. The first argument comes from purely numeric considerations, since the discontinuities of the thermodynamic parameters, common to first-order transitions, will make the usual numerical approximations less rigorous in their vicinity. Since the first reports of materials presenting the giant MCE, anomalous 'spikes' in the $\Delta S_M(T)$ plots are commonly seen in literature, for first-order systems. Figure 5.1, from Ref. [68], shows an example of the so-called magnetocaloric peak effect, present in results form magnetization measurements, but does not appear in calculations using specific heat data.

Indeed, the most immediate culprit for these peaks to occur would be the numerical approximations, which become less rigorous near the transition [20]. The peak effect has also been discussed in other perspectives, most notably by Pecharsky and Gschneidner [68] and Giguère *et al.* [69], for the case of $Gd_5Si_2Ge_2$. Their arguments behind the presence of the entropy peak (and its absence in results for calorimetric measurements) differed considerably. Pecharsky and Gschneidner argue that [68]:

> "The obvious sharp peak observed in $\Delta S_M(T)$ calculated from magnetization data significantly exceeds that calculated from heat capacity and is most likely

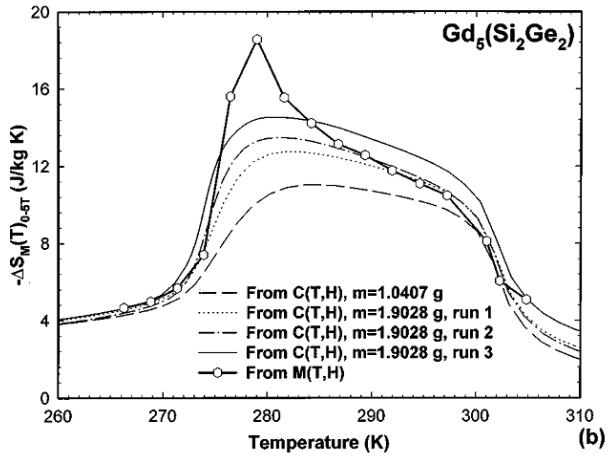

Figure 5.1: Differences in estimating magnetic entropy change from magnetization measurements (solid line, open points) and calorimetric measurements (solid and dashed lines), in $Gd_5Si_2Ge_2$, from Ref. [68].

associated with the fact that the magnetic transition occurs simultaneously with the crystal structure change in this alloy system. The magnetization data reflect only the changes in the magnetic entropy and are insensitive to the overlapping changes in the lattice entropy, while heat capacity data reflect the change in the combined entropies (lattice, electronic and magnetic), thus providing more reliable magnetocaloric effect values."

Giguère *et al.* in contrast argue that [69]:

"The sudden, discontinuous entropy change is related to the phase transition itself, and is approximately independent of the applied field. The field shifts the transition only to higher temperatures. This entropy change cannot be calculated from the Maxwell relations, for two reasons: (i) It is not a magnetic entropy change, and (ii) M(T) or M(H) is not a continuous, derivable function. For first order transitions, the Clausius-Clapeyron equation offers a way to calculate the entropy change."

The arguments are in almost total disagreement with each other. The only point in common is that the direct use of the Maxwell relation on magnetization data would only report on the change of magnetic entropy, and not the change in 'non-magnetic' (lattice/electronic) entropy. Our analysis of this subject starts exactly in this point. What is 'magnetic entropy' and 'non-magnetic' entropy change, and why would non-magnetic entropy changes be invisible in magnetization measurements.

5.1.1 Thermodynamics

Let us go back to some basics. As stated in chapter 1, to estimate entropy change from specific heat measurements, one needs to measure C_p in both zero and non-zero applied field. The difference between curves, integrated in T, will then correspond to the entropy difference between the $H = 0$ and $H \neq 0$ conditions (Eq. 1.12). This is rigorously the magnetocaloric effect, as seen by isothermal entropy change. On the other hand, magnetic measurements give us the bulk magnetization value, which is then used as a thermodynamic variable. If the dependence of M on H and T is known, then the magnetic entropy change is easily calculated (Eq. 1.10). The only possible entropy change that is invisible in magnetization measurements would then be the non-magnetically coupled entropy change in lattice/electronic degrees of freedom. Now, magnetization is defined thermodynamically as

$$M(H,T,p) = \left(\frac{\partial G}{\partial H}\right)_{T,p}, \tag{5.1}$$

so any change of the Gibbs free energy of system due to a change in applied field will then result on a change of the M value. In other words, any change within the thermodynamic system that occurs due to a change in applied field has repercussions in M. And so the full magnetic entropy change is obtainable from $M(H,T)$. This point of view will become clearer upon investigating a magnetovolume coupling induced first-order phase transition. As we will show, the use of the Clausius-Clapeyron relation does not allow us to calculate 'non-magnetic entropy' variations, as the entropy change due to the lattice volume change is directly calculated from the use of the Maxwell relation. It is helpful to have a visual sense of the application of the Maxwell relation on magnetization data to obtain entropy change, as we will discuss in the following section. A summarized version of the following section is given in [AA09b].

5.1.2 Visual representation

Let us consider a second-order phase transition system. M is a valid thermodynamic parameter, i.e., the system is in thermodynamic equilibrium and is homogeneous. Numerically integrating the Maxwell relation (Eq. 1.11) corresponds to integrating the magnetic isotherms in field, and dividing by the temperature difference:

$$\Delta S_M = \sum_0^{H'} \left(\frac{M_{i+1} - M_i}{T_{i+1} - T_i}\right) \Delta H_i = \frac{\int_0^{H'} \left[M(T_{i+1},H) - M(T_i,H)\right] dH}{T_{i+1} - T_i} \tag{5.2}$$

which has a direct visual interpretation:

If the transition is first-order, there is an 'ideal' discontinuity in the M vs. H plot. Still, apart from expected numerical difficulties, the area between isotherms can be estimated, as shown if Figure 5.3.

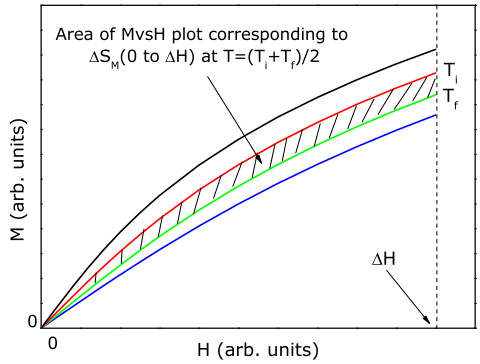

Figure 5.2: Schematic diagram of a second-order M vs. H plot, showing the area between magnetic isotherms. From Eq. 5.2 this area directly relates to the entropy change.

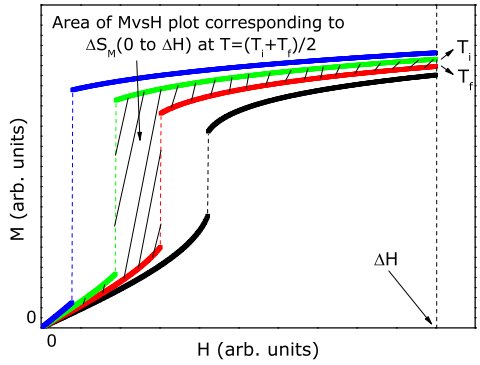

Figure 5.3: Schematic diagram of a first-order M vs. H plot, showing the area between magnetic isotherms. From Eq. 5.2 this area directly relates to the entropy change.

The Clausius-Clapeyron relation is presented in Eq. 5.3

$$\left|\frac{\Delta T}{\Delta H_C}\right| = \left|\frac{\Delta M}{\Delta S}\right|, \tag{5.3}$$

where ΔM is the difference between magnetization values before and after the discontinuity for a given T, ΔH_C is the shift of critical field from ΔT and ΔS is the difference between the entropies of the two phases.

The use of the Clausius-Clapeyron relation to estimate the entropy change due to the first-order nature of the transition also has a very direct visual interpretation, as shown in Figure 5.4:

From comparing Figures 5.3 and 5.4, we can see how all the magnetic entropy variation that can be accounted for with magnetization as the order parameter is included in calculations using the Maxwell relation. This is explicitly shown in Figure 5.5.

All the magnetic entropy change is accounted for in calculations using the Maxwell relation. So there is no real gain nor deeper understanding of the systems to be had from the use

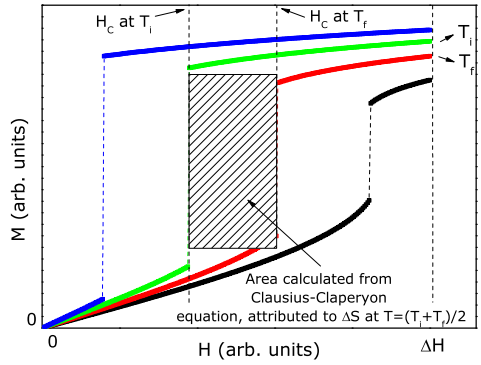

Figure 5.4: Schematic diagram of the area for entropy change estimation from the Clausius-Clapeyron equation, from a M vs. H plot of a magnetic first-order phase transition system.

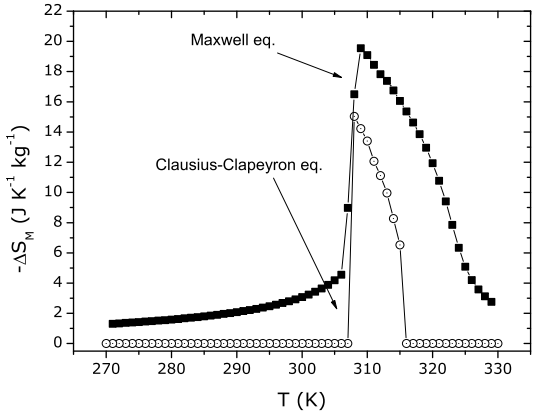

Figure 5.5: Magnetic entropy change versus temperature, estimated from the Maxwell relation (full symbols) and corresponding entropy change estimated from the Clausius-Clapeyron relation (open symbols).

of the Clausius-Clapeyron relation to estimate magnetic entropy change. The 'non-magnetic entropy' is indeed accounted for by the Maxwell relation. The argument that the entropy peak exists, but specific heat measurements measure the lattice and electronic entropy in a way that conveniently smooths out this peak, is in contrast with the previously shown results. The entropy peak effect does not appear in calculations on purely simulated magnetovolume first-order transition systems, which seems to conflict with the arguments from Pecharsky and Gschneidner.

Of course, all of this reasoning and arguments have a common presumption: M is a valid thermodynamic parameter. In truth, for a first-order transition, the system can present metastable states, and so the measured value of M may not be a good thermodynamic parameter, and also the Maxwell relation is not valid. In the following section, the consequences of using non-equilibrium magnetization data on estimating the magnetocaloric effect is discussed.

5.2 Irreversibility effects

As shown in sections 2.2 and 2.3, both the Landau theory of phase transitions and the molecular mean-field model describe the general properties of a first-order magnetic phase transition. We will begin the discussion of irreversibility effects on the MCE by using Landau theory. A summarized version of this work has been published [AA09a].

In the previous discussion in section 2.2, the absolute minimum of free energy was considered as providing the M value. By considering the two free energy minima of G, the limits of the metastability region are defined, which, in a simplified approach, can be considered as the kinetic limit in terms of observing these metastable states. The equilibrium solution arises from the absolute minimum of free energy. By considering the existence of the metastable states, we are then able to define three sets of magnetization curves. Figure 5.6 shows M versus H data resulting from the use of Landau coefficients that describe a magneto-volume induced first-order phase transition material with $T_C \sim 195$ K: $a = 25(T-180)$ (g.Oe.emu^{-1}), $b = -0.18$ (g.Oe.emu^{-1})^3 and $c = 2.33 \times 10^{-5}$ (g.Oe.emu^{-1})^5. The metastable limits are presented, in analogy to increasing and decreasing field measurements.

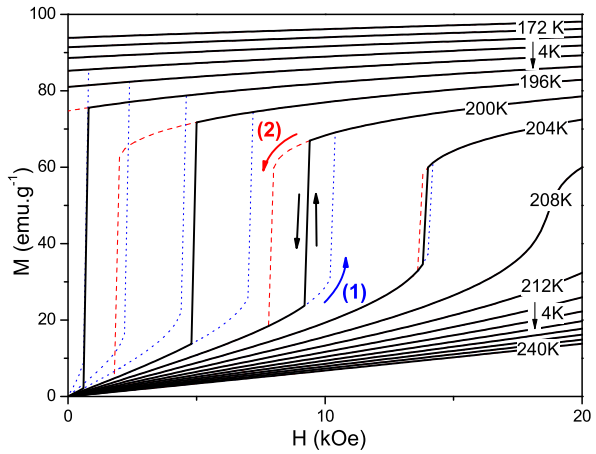

Figure 5.6: M versus H isotherms from Landau theory, for a first-order transition, with equilibrium (solid lines) and nonequilibrium (dashed and dotted lines).

We use the three sets of curves and with the usual procedure of using Eq. 1.10, we estimate ΔS_M for equilibrium and the two metastable limits, where $\Delta S_M = S_M(T,H) - S_M(T,0)$. We compare these results with the use of the free energy derivative (Eq. 2.18) as shown in Figure 5.7.

The use of the Maxwell relation on these non-equilibrium data produces visible deviations, and in the case of metastable solution (2), the obtained peak shape is quite similar to that reported by Pecharsky and Gschneidner for $Gd_5Si_2Ge_2$ [68]. In this case $\Delta S_M(T)$ values from caloric measurements follow the half-bell shape of the equilibrium solution, but from magnetization measurements, an obvious sharp peak in $\Delta S_M(T)$ appears. Similar deviations

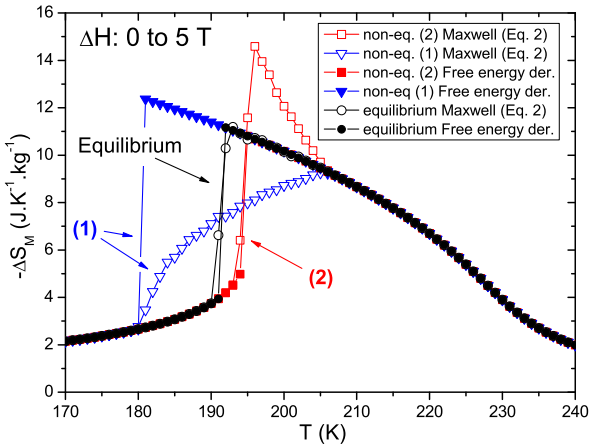

Figure 5.7: (color online) ΔS_M versus T for equilibrium and nonequilibrium solutions, from Maxwell relation (open symbols) or from Eq. 2.18 (full symbols), for Landau theory M vs. H data from 0 to 5 T.

have been interpreted as a result of numerical artifacts [20], but are not present in a first-order system with no visible hysteresis [17].

As we have discussed earlier in section 2.2, if the Landau b and c parameters are independent of temperature, the magnetic entropy is linear in M^2, above T_C. If we consider values of entropy obtained by the use of the Maxwell relation on non-equilibrium data, we expect that this linear relation is broken. Figure 5.8 shows this effect.

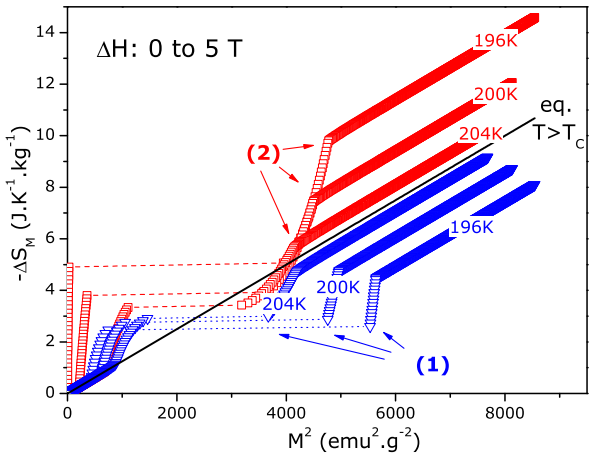

Figure 5.8: ΔS_M vs M^2 isotherms in nonequilibrium conditions, from Maxwell relation integration of Landau theory M vs. H data (open symbols), and in equilibrium for $T > T_C$, from the free energy derivative (solid line).

The abnormal behavior of the ΔS_M vs M^2 curves under nonequilibrium makes analysis like those in Refs. [43, 70] more difficult. Shifts and deviations on the ΔS_M vs M curves, that were interpreted as lattice entropy change or magnetic clustering can come solely from

the misuse of the Maxwell relation. Note how the over/underestimation of ΔS_M produces parallel shifts on the ΔS_M vs M^2 plots, when H is greater than the critical value.

We have shown how the approximation of using the Maxwell relation on non-equilibrium data can reproduce and so explain the observation of the magnetic entropy 'peak' effect. It is of interest to verify if this overestimation of ΔS_M holds up in higher fields and eventually exceeds the theoretical limit of magnetic entropy change, as well as to consider a stronger first-order transition, with a consequently larger T and H region with magnetic irreversibility.

Since values of M near saturation need to be considered, we use the molecular mean-field model. As we have shown in section 2.3, magnetic entropy change can be calculated directly from the mean-field parameters, and state function (Eq. 2.60). For our analysis, the molecular exchange field is taken as $H_{exch} = \lambda_1 M + \lambda_3 M^3$, where λ_3 describes magneto-volume effects, following the Bean and Rodbell formulation [50]. The value of λ_1 value was chosen to give a $\Theta_p \sim 300K$. We have not introduced any dependence of λ on T. The Brillouin function was used, with a spin of $J = 2$, $g = 2$, and the saturation magnetization value was set to 100 emu.g^{-1}. These values aim to generally represent a first-order phase transition, not a particular magnetic system.

M vs. H curves for a first-order magnetic transition, with a region of irreversibility between 300 and 316 K, and critical field of 2.5 T, resulting from a λ_3 parameter equal to 1.5 Oe (emu/g)$^{-3}$, were calculated. The Maxwell construction [11] was used to determine the equilibrium solution (matching of the energy of the two phases).

Like the results from Landau theory, we can compare ΔS_M from a model-specific relation (Eq. 2.60) to results from the Maxwell relation for equilibrium and non-equilibrium solutions. For the parameter values shown above, the overestimation of ΔS_M from using the Maxwell relation in nonequilibrium can be as high as 1/3 of the value obtained under equilibrium, for an applied field change of 5 T.

For large values of H, where M is near saturation in the paramagnetic region, the upper limit to magnetic entropy change, $\Delta S_M(\max) = N k_B \ln(2J + 1)$, is reached, which for the chosen model parameters is $\sim$ 60 J.K^{-1}.kg^{-1}. However, this is in excess by around 10% by the use of the Maxwell relation to non-equilibrium values. If a stronger magneto-volume coupling is considered ($\lambda_3 = 8$ Oe (emu/g)$^{-3}$), the limit can be in excess by $\sim$ 30 J.K^{-1}kg^{-1}, clearly breaking the thermodynamic limit of the model and falsely producing a colossal magnetocaloric effect, as shown in Figure 5.9.

The mean-field model also allows the study of mixed-state transitions, by considering a proportion of phases (high and low magnetization) within the metastability region. Magnetization curves are shown in the inset of Figure 5.10, for $\lambda_3 = 2$ Oe (emu/g)$^{-3}$, corresponding to a critical field $\sim$ 10T. The mixed-phase temperature region is from 328 to 329 K, where the proportion of FM phase is set to 25% at 329 K, 50% at 328.5 K and 75% at 328 K.

The deviation resulting from using the mixed-state M vs. H curves and Eq. 1.10 to

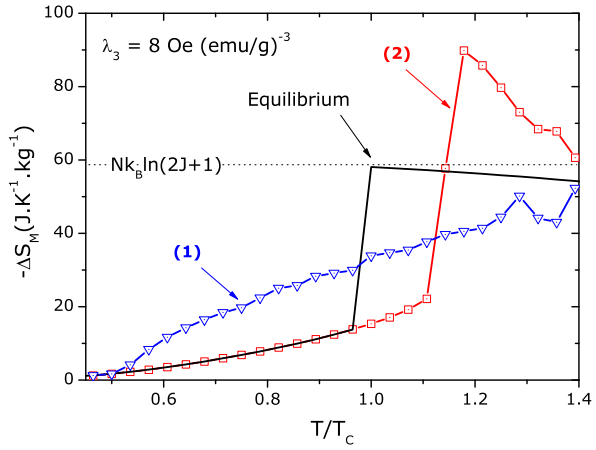

Figure 5.9: $-\Delta S_M(T)$, obtained from the use of the Maxwell relation on equilibrium (black line) and metastable (colored lines) magnetization data from the Bean-Rodbell model with a magnetic field change of 1000 T.

estimate ΔS_M is now larger compared to the previous results, as shown in Figure 5.10, since now the system is also inhomogeneous, further invalidating the use of the Maxwell relation. The thermodynamic limit to entropy change is again falsely broken. Note how the temperatures that exceed the limit of entropy change are the ones that include mixed-phase data to calculate ΔS_M from Eq. 1.10.

This result shows how the estimated value of ΔS_M can be greatly increased solely as a consequence of using the Maxwell relation on magnetization data from a mixed-state transition, which is the case of materials that show a colossal magnetocaloric effect [34]. It is worth noting that, at this time, there are no calorimetric measurements that confirm the existence of the colossal magnetocaloric effect, and its discovery came from magnetization data and the use of the Maxwell relation.

For a system that shows mixed-phase behaviour and the colossal MCE, measurements of magnetic field dependent specific heat do not show the high values of magnetic entropy change, that is obtained from using the Maxwell relation on magnetization data. Let us take as an example results of the $La_{0.7}Pr_{0.3}Fe_{11.5}Si_{1.5}$ system, from Ref. [34]. Figure 5.11(a) shows the magnetic entropy change estimated for a field change of 5 T.

As we see in Figure 5.11(a), the entropy change estimated from magnetization and specific heat follow the same behaviour, except near the transition, which corresponds to the experimentally observed range of mixed-phase behaviour. By plotting both the magnetic entropy change curves as a function of the square of magnetization, with data of Ref. [34], (Figure 5.11(b)), we see that the expected linear relation is pretty much followed, except on the point with the abnormally high $-\Delta S_M$ value.

The previous analysis has revealed the origin of the colossal magnetocaloric effect: if a first-order magnetic phase transition shows evidence of mixed-phase behavior, then it is

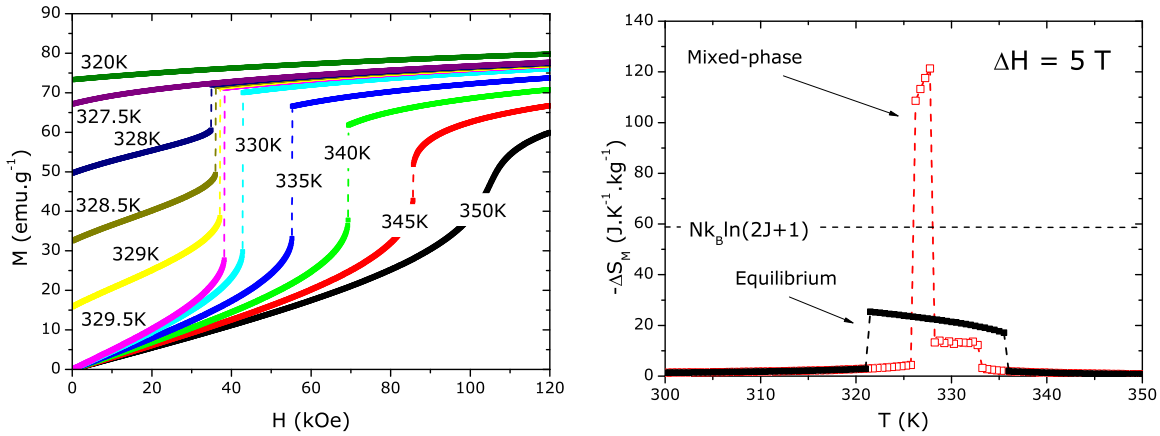

(a) (b)

Figure 5.10: a) M vs. H isotherms of a mixed-phase system from the mean-field model and b) corresponding $\Delta S_M(T)$ for ΔH=5T from Maxwell relation (open symbols), and of the equilibrium solution (solid symbols).

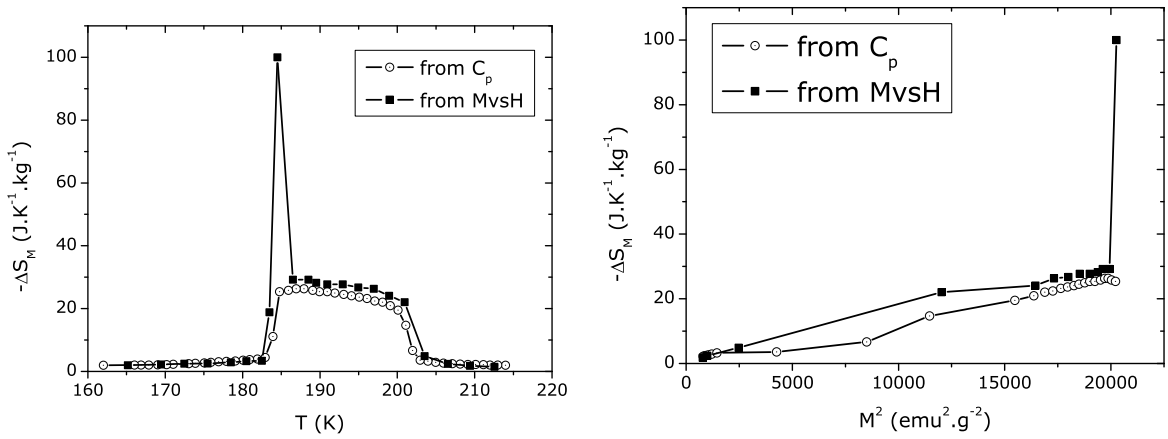

(a) (b)

Figure 5.11: a) magnetic entropy change versus temperature, estimated from specific heat and isothermal magnetization measurements of $La_{0.7}Pr_{0.3}Fe_{11.5}Si_{1.5}$, from Ref. [34] and b) corresponding relation of entropy change and the square of magnetization.

macroscopically inhomogeneous, and so the use of the Maxwell relation (which presumes an homogeneous system) to estimate magnetic entropy change from magnetization measurements will produce erroneous results, including the 'colossal' entropy peak. In the next section, a method to correct these erroneous magnetocaloric estimations is presented.

5.3 Estimating the magnetocaloric effect from mixed-phase data

It is possible to describe a mixed-phase system, by defining a percentage of phases x, where one phase has an $M_1(H,T)$ magnetization value and the other will have an $M_2(H,T)$ magnetization value. In a coupled magnetostructural transition, one of the phases will be in the ferromagnetic state (M_1) and the other (M_2) will be paramagnetic. By changing the temperature, the phase mixture will change from being in a high magnetization state (ferromagnetic) to a low magnetization state (paramagnetic), and so the fraction of phases (x) will depend on temperature. Explicitly, this corresponds to considering the total magnetization M_{total} of the system as

$$M_{\text{total}} = x(T)M_1 + (1 - x(T))M_2 \ , \tag{5.4}$$

for $H < H_c(T)$ and $M = M_1$ for $H > H_c(T)$, where x is the ferromagnetic fraction in the system (taken as a function of temperature only), M_1 and M_2 are the magnetization of ferromagnetic and paramagnetic phases, respectively and H_c is the critical field at which the phase transition completes.

So if we substitute the above formulation in the integration of the Maxwell relation (Eq. 1.10), used to estimate magnetic entropy change, we can establish entropy change up to a field H as

$$\Delta S_{\text{cal}} = \frac{d}{dT}\int_0^H \left[xM_1 + (1-x)M_2\right] dH' = \frac{\partial x}{\partial T}\int_0^H (M_1 - M_2)dH' + \Delta S_{\text{avg}} \tag{5.5}$$

for $H < H_c$, where

$$\Delta S_{\text{avg}} = x\int_0^H \frac{\partial M_1}{\partial T}dH' + (1-x)\int_0^H \frac{\partial M_2}{\partial T}dH'. \tag{5.6}$$

Out of these terms, ΔS_{avg} is due to the weighted contribution of the ferro- and paramagnetic phase in the system while the first term results from the phase transformation that occurred in the system during temperature and field variation. In order to obtain the entropy change up to a field above the critical magnetic field H_c, its temperature dependence plays an important role (latent heat contribution) and total entropy change can be formulated as

$$\begin{aligned}\Delta S_{\text{cal}} &= \frac{\partial}{\partial T}\int_0^{H_c(T)} [xM_1 + (1-x)M_2]\, dH' + \frac{\partial}{\partial T}\int_{H_c(T)}^{H} M_1 dH' \\ &= \frac{\partial x}{\partial T}\int_0^{H_c(T)} (M_1 - M_2) dH' + (1-x)\frac{\partial}{\partial T} H_c \left[M_1 - M_2\right]_{CT} + \Delta S_{\text{avg}} \\ &+ \int_{H_c}^{H} \frac{\partial M_1}{\partial T} dH'. \end{aligned} \tag{5.7}$$

The first term in the previous expression represents the contribution of phase transformation, while the second term represents the fraction (1-x) of the latent heat contribution which is measured in the calorimetric experiment in the region of mixed state (since part of the sample is already in the ferromagnetic state, at zero field) and the last two terms are solely from the magnetic contribution.

For both $H < H_c$ and $H > H_c$ cases, the contribution due to the temperature dependence of mixed phase fraction ($\partial x/\partial T$) represents the main effect from nonequilibrium in the thermodynamics of the system and therefore creates major source of error in the entropy calculation.

These calculations tell us that by estimating magnetic entropy change using the Maxwell relation and data from a mixed-phase magnetic system adds a non-physical term, which, as we will see later, can be estimated from analysing the magnetization curves and the $x(T)$ distribution. Let us use mean-field generated data and a smooth sigmoidal $x(T)$ distribution, as shown in Figure 5.12.

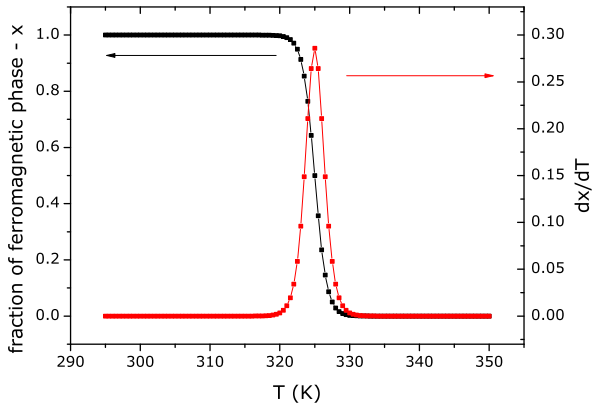

Figure 5.12: Distribution of ferromagnetic phase of system, and its temperature derivative.

Such a wide distribution will then produce M versus H plots that strongly show the mixed-phase characteristics of the system, since the step-like behaviour is well present, as shown in Figure 5.13(a). Using the Maxwell relation to estimate magnetic entropy change, we obtain the peak effect, exceeding the magnetic entropy change limit (Figure 5.13(b)).

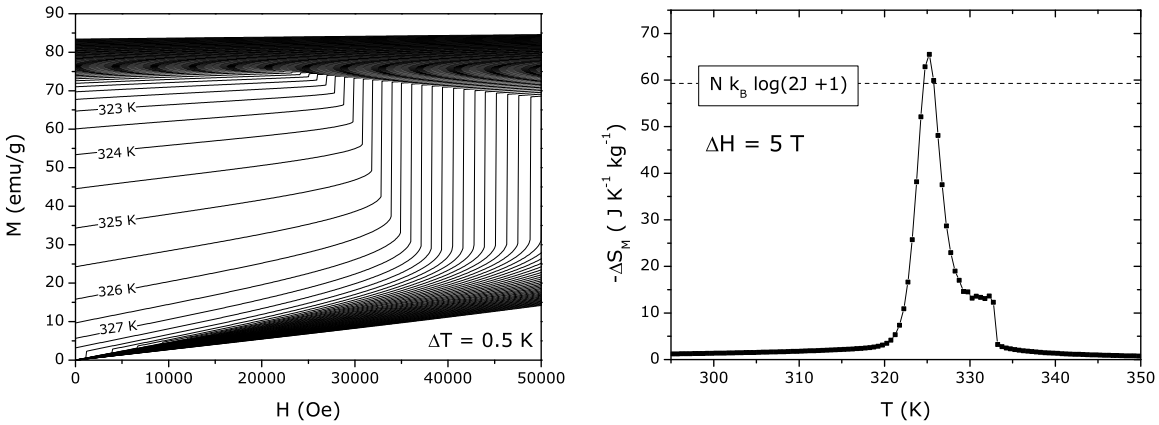

(a) (b)

Figure 5.13: a) Isothermal M versus H plots of a simulated mixed-phase system, from 295 to 350 K (0.5 K step) and b) magnetic entropy change values resulting from the direct use of the Maxwell relation.

As the entropy plot shows us, the shape of the entropy curve and the $\partial x/\partial T$ function (Figure 5.12) share a similar shape. This points us to Eqs. 5.5 or 5.7. It seems that the left side of the entropy plot may just be the result of the presence of the mixed-phase states, while for the right side of the entropy plot, there is some 'true' entropy change hidden along with the $\partial x/\partial T$ contribution. By using Eqs. 5.5 or 5.7, we present a way to separate the two contributions, and so estimate more trustworthy entropy change values. We plot the entropy change values obtained directly from the Maxwell relation, as a function of $\partial x/\partial T$. This is shown in Figure 5.14, for the data shown in Figures 5.13(a) and 5.12.

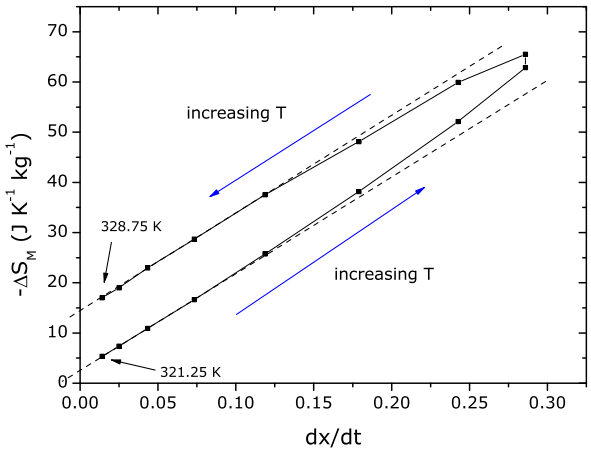

Figure 5.14: Entropy change, as obtained from the use of the Maxwell relation of mixed-phase magnetization data, versus $\partial x/\partial T$.

Plotting entropy change as a function of the temperature derivative of the phase distri-

bution gives us a tool to remove the false $\partial x/\partial T$ contribution to the entropy change. As we can see in Figure 5.14, there is a smooth dependence of entropy in $\partial x/\partial T$, which allows us to extrapolate the entropy results to a null $\partial x/\partial T$ value, following the approximately linear slope near the plot origin (dashed lines of Figure 5.14). This slope is constant as long and the magnetization difference between phases ($M_1 - M_2$) is approximately constant, which is observed in strongly first-order materials. The results of eliminating the $\partial x/\partial T$ contribution to the Maxwell relation result are presented in Figure 5.15.

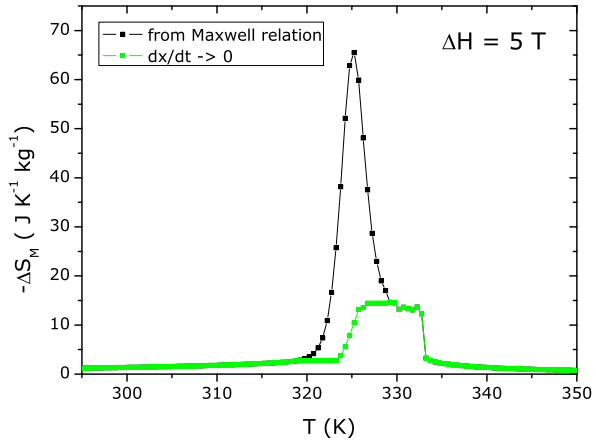

Figure 5.15: Entropy change, as obtained from the use of the Maxwell relation of mixed-phase magnetization data, versus T, and values extrapolated to $\partial x/\partial T \rightarrow 0$.

By eliminating the contribution of the temperature derivative of the mixed-phase fraction, the entropy 'peak' effect is eliminated, in a justified way. The resulting entropy curve resembles the results obtained from specific heat measurements when compared to results from magnetic measurements, as seen in Refs. [34] (Figure 5.11(a) of this work) and [35], among others.

However, this corrected entropy is always less than the value in equilibrium condition. This is because we deal with a fraction (1-x) of the phase M_2 remaining to transform which will give a fraction of latent heat entropy (Eq. 5.7) since part (x) of phase is already transformed at zero field. This average entropy change weighted by the fraction of each phase present, can be measured in calorimetric experiments. We regard x and its temperature dependence $\partial x/\partial T$ as parameters that can be externally manipulated by changing the measurement condition or the sample history and should therefore be carefully handled to obtain the true entropy calculation.

We can conclude that, for a first-order magnetic phase transition system, estimating magnetic entropy change from the Maxwell relation can give us misleading results. If the system presents a mixed-phase state, the entropy 'peak' effect can be even more pronounced, clearly exceeding the theoretical limit of magnetic entropy change. Our subsequent analyses of exper-

imental data will then consider this fact. However, as we shall see further, if a system presents disorder effects, such as chemical or structural distributions, these irreversibility effects can become less evident.

Chapter 6

Disorder effects in ferromagnets

6.1 Second-order phase transitions

6.1.1 General Remarks

Real ferromagnetic materials are inevitably strained, chemically impure, contain lattice defects, are delimited by surfaces, etc. Theoretically simulating such a system is a numerically intensive task, and so the complexity and computational effort of using a microscopic model to describe a disordered system makes this approach generally unpractical.

In this work, disordered magnetic materials will be modeled adapting the phenomenological theories discussed previously. While the use of Landau theory to study distributions and their effect in magnetic and magnetocaloric properties has been presented by Romanov *et al.* [71] in second-order magnetic phase transitions, our approach will be to use the molecular mean-field model and the Bean-Rodbell formulation to describe these inhomogeneity effects in second- and first-order phase transition systems. The main results of this approach to second-order systems have been published [ATR$^+$08].

For second-order systems, our approach will be to consider a distribution of the mean-field λ_1 parameter. The reasoning behind this analysis is similar to that presented in the seminal work of Aharoni (Ref. [72]), but together with studying the effect of inhomogeneity in the methodologies associated with the use of Arrott plots, we will focus on its effect on the MCE.

6.1.2 Initial simulations

We consider a second-order phase transition material, simulated from the molecular mean-field model. The chosen model parameters were spin=2, a saturation magnetization of 100 emu g^{-1}, and a mean-field exchange parameter λ_1 corresponding to a $T_C \sim 300$ K. Through this section, simulations from the 'pure' system and also the system with a Gaussian distribution of T_C with a full width at half maximum of 20 K will be presented. The magnetization of the disordered material is a sum of the magnetization of each 'part' of the material:

$$M(H,T,\text{distribution}) = \sum_n M_n(H,T) f(T_C) \tag{6.1}$$

where f is the normalized T_C distribution (in this case a Gaussian distribution), and $M_n(H,T)$ is the magnetization corresponding to the n-th T_C value.

Figure 6.1(a) shows the M versus H plots, from 200 to 400 K, calculated up to H=5 T, and a temperature step of 1 K, with the considered distribution with a 20K FWHM in T_C. The corresponding 'pure' system (Figure 6.1(b)) shows, in general terms, a similar behaviour.

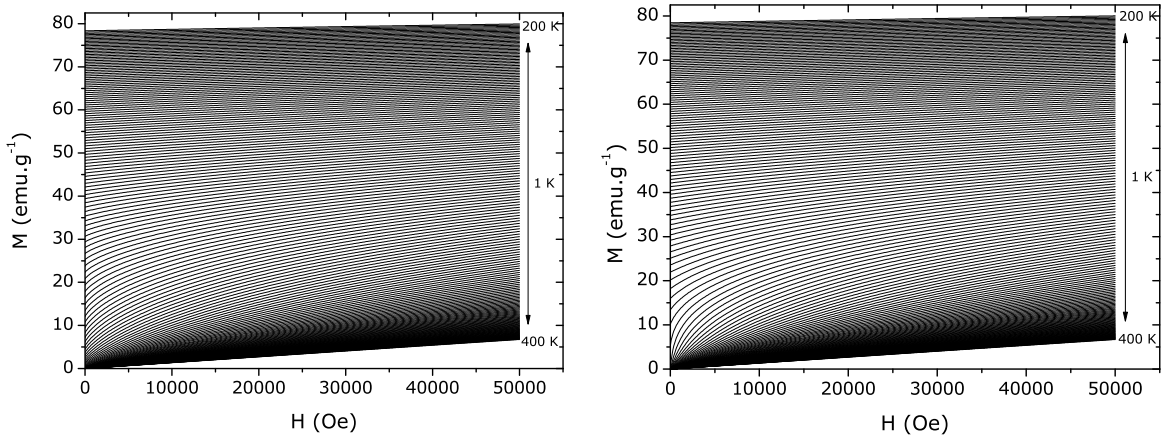

Figure 6.1: a) Isothermal magnetization versus applied magnetic field, from 200 to 330 K, at a 1 K temperature step and 100 Oe field step, from the molecular mean-field model, with a Gaussian T_C distribution with 20 K FWHM and b) corresponding 'pure' system.

Indeed, the effect of a T_C distribution should be clearer on low-field values. Figure 6.2(a) shows the M versus T dependence on applied magnetic field, and at zero field, the zero applied magnetic field curve is not as sharp as the one of the 'pure' system (Figure 6.2(b)). This effect is also clearly seen in the temperature derivative of the magnetization (figure insets).

Another way to verify the effect of the distribution on low-field measurement is to plot the temperature dependence of the inverse susceptibility. For typical values used in experimental M versus T measurements, around 100 Oe, the system with the distribution shows an inflexion above the T_C value of the majority phase (Figure 6.3(a)). This inflexion will naturally limit the applicability of the linear Curie law near T_C. In the 'pure' system (Figure 6.3(b)), we see the expected linear dependency of the inverse susceptibility, up to T_C.

As pointed out by Aharoni in Ref. [72], a distribution in the magnetic interaction will produce curvatures in the isothermal Arrott plots, as reproduced in Figure 6.4(a). The effects of the distribution mainly affect the low field data, but can nonetheless affect the search of critical exponents, if one chooses to search for a linear behavior in the modified Arrott plots.

Since we have introduced a broadening of the T_C values of the system, it is expected also

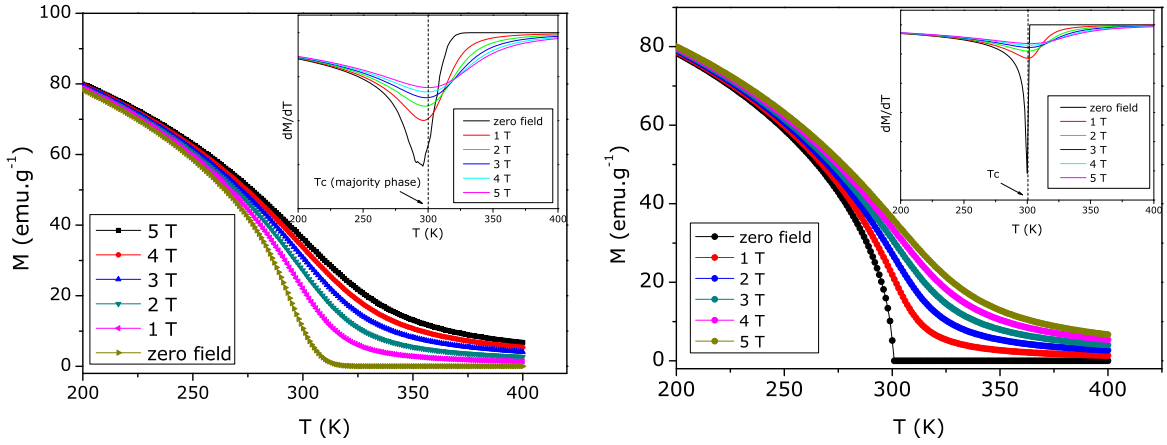

Figure 6.2: Isothermal magnetization vs. applied magnetic field, from 290 to 330 K, at a 1 K temperature step and 100 Oe field step, from the molecular mean-field model, with a Gaussian T_C distribution with 20 K FWHM and b) corresponding 'pure' system. Insets show the temperature derivative of magnetization.

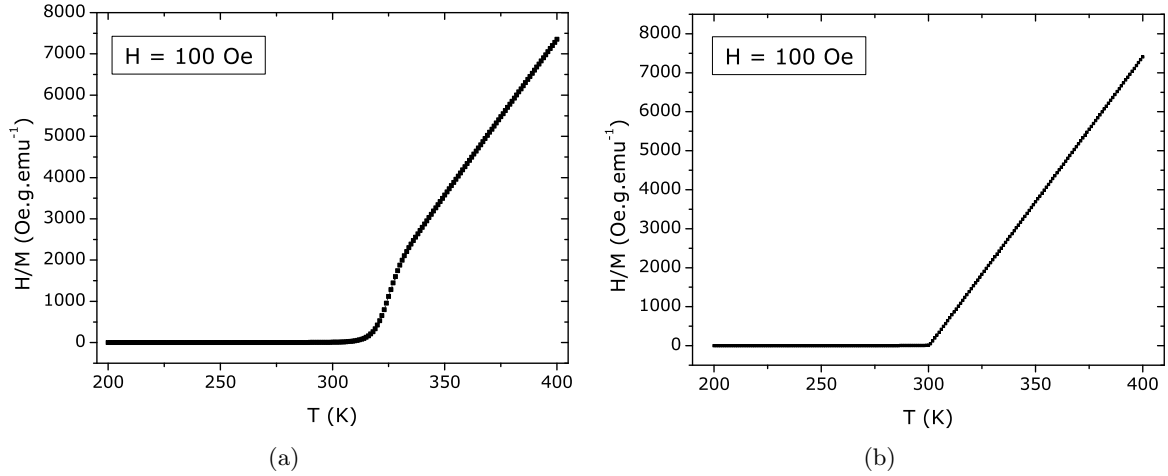

Figure 6.3: Inverse susceptibility versus temperature, from 200 to 400 K, at a 1 K temperature step and 100 Oe applied magnetic field, from the molecular mean-field model, with a Gaussian T_C distribution with 20 K FWHM and b) corresponding 'pure' system.

that the magnetic entropy change peak will broaden, and loose its well-defined maximum. Figure 6.5(a) shows this effect. Comparing with the 'pure' system (Figure 6.5(b)), we see how not only does the peak become less defined, but also the maximum value of $-\Delta S_M$ becomes substantially lower (around 10%), and the peak shifts to lower temperatures (a direct consequence of the maximum $\partial M/\partial T$ also shifting to lower temperatures). It also appears that the entropy curve becomes wider, and we shall explore this in detail later on.

Landau theory has presented us with a simple linear relation between magnetic entropy

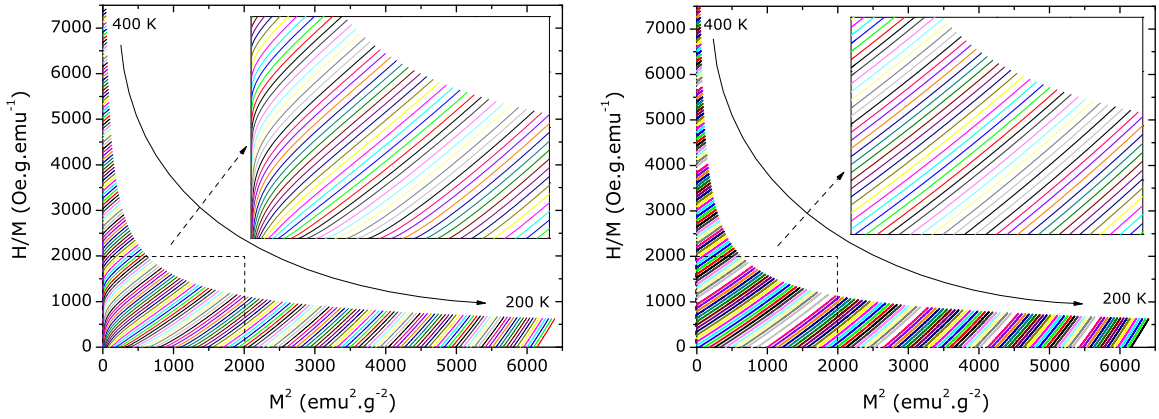

Figure 6.4: a) Arrott plot of mean-field generated data, with a Gaussian 20 K FWHM T_C distribution. b) Corresponding 'pure' data. Insets show zoomed data, near T_C.

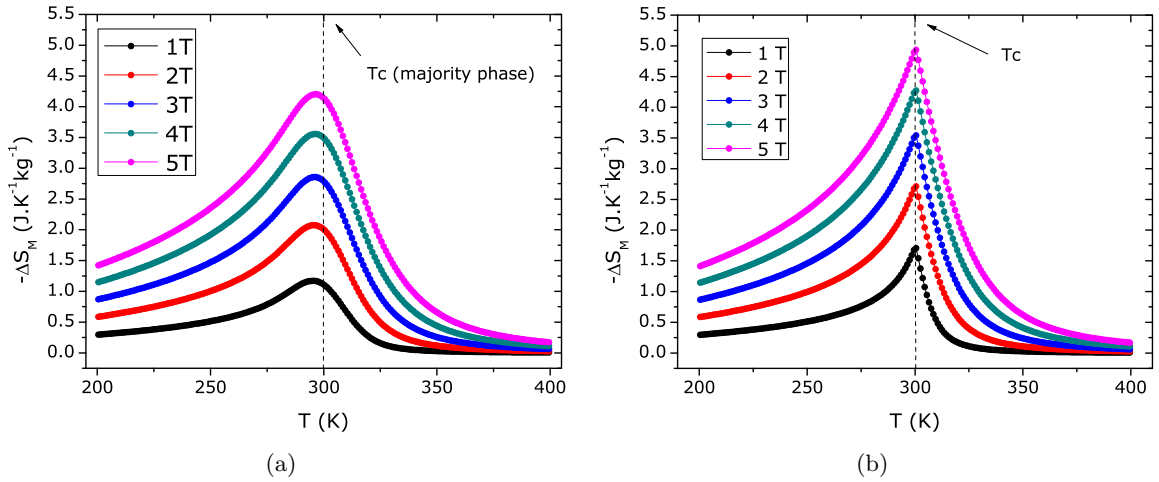

Figure 6.5: Magnetic entropy change versus temperature, for an applied field change from 0 to 1, 2, 3, 4 and 5 T, for an a) 20 K FWHM Gaussian T_C distribution, and b) corresponding 'pure' system.

change and the square of magnetization (Eq. 2.19). In a system that presents a T_C distribution, we have some points that need to be taken into consideration before studying the relation between entropy and magnetization. First of all, if we are considering an inhomogeneous system, estimating the magnetic entropy change from the Maxwell relation would be formally incorrect. Luckily, estimating the magnetic entropy change from the integration of the Maxwell relation will give us a 'partially correct' result. As we have shown previously in Eq. 6.1, when considering an inhomogeneous system, its bulk magnetic properties are the sum of each of its parts, and we consider each one to have different magnetic behavior. So

the total magnetization value can be considered as a discrete (normalized) sum:

$$M_{\text{total}} = \sum_n M_n(H,T), \tag{6.2}$$

where M_i is the magnetization of each of the materials distribution of magnetic interactions.

So we use the total value of magnetization M_{total}, and its dependence on H and T together with the Maxwell relation to estimate magnetic entropy change:

$$-\Delta S_M = \int_0^{H'} \left(\frac{\partial M_{\text{total}}}{\partial T}\right)_H dH' = \int_0^{H'} \left(\frac{\partial \sum_n M_n(H,T)}{\partial T}\right)_H dH' \tag{6.3}$$

from the additive properties of summations and integrals, we then have that

$$-\Delta S_M = \sum_n \int_0^{H'} \left(\frac{\partial M_n(H,T)}{\partial T}\right)_H dH' \tag{6.4}$$

We then can conclude that the use of the Maxwell relation to magnetization data of an inhomogeneous second-order magnetic material will present us with a correct estimation of magnetic entropy change, as long as the distribution itself is independent of H and T. Still, the linear relation between magnetic entropy and the square of magnetization, valid for each of the M_n parts of the sample, will not be valid for the total magnetization value. Let us consider a simplified Landau model, where only the A parameter is non-zero.

$$-\Delta S_M = \sum_n -\frac{1}{2} A'_n M_n^2 \neq -\frac{1}{2}\left(\sum_n A'_n M_n\right)^2 \tag{6.5}$$

The non-linearity of the relation means that $-\Delta S_M$ is not proportional to the square of the total magnetization of the material. Deviations from this linear relation will appear, which will be more visible with a wider distribution.

Figure 6.6(a) shows $-\Delta S_M$ versus M^2_{total}, for the system with the 20K FWHM magnetic interaction distribution. Compared with the 'pure' system (Figure 6.6(b)), we can see how the linear relation and the superposition of curves for $T > T_C$ is deformed.

Still, for T values a bit outside the distributed T_C range, the curvature effect is less visible, and, for instance, an estimative of the spontaneous magnetization will not be seriously affected by the distribution.

6.1.3 The effect on relative cooling power

As shown in the previous section (see Figures 6.5(a) and 6.5(b)), the effect of the distribution on the magnetic entropy change dependence corresponds to a decrease in the maximum value, together with an increase in the width of the $-\Delta S_M(T)$ curve. When considering the relative cooling power of the material, we then have two opposite effects. We study the

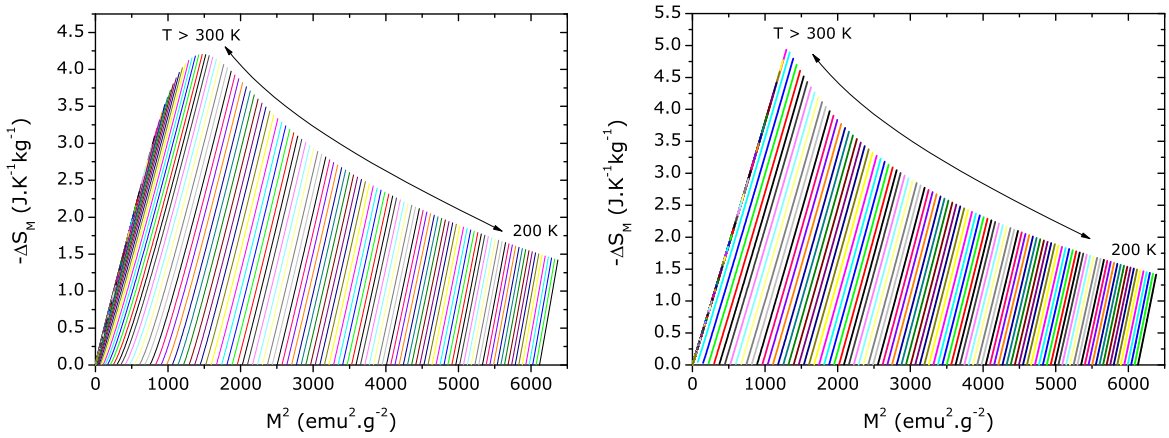

Figure 6.6: Magnetic entropy change versus the square of magnetization, for mean-field data, of an a) inhomogeneous and a b) homogeneous system.

dependence of the relative cooling power with the width of the distribution. Figure 6.7(a) shows the considered T_C distributions and Figure 6.7(b) shows the corresponding RCP value, for an applied magnetic field change of 1 T.

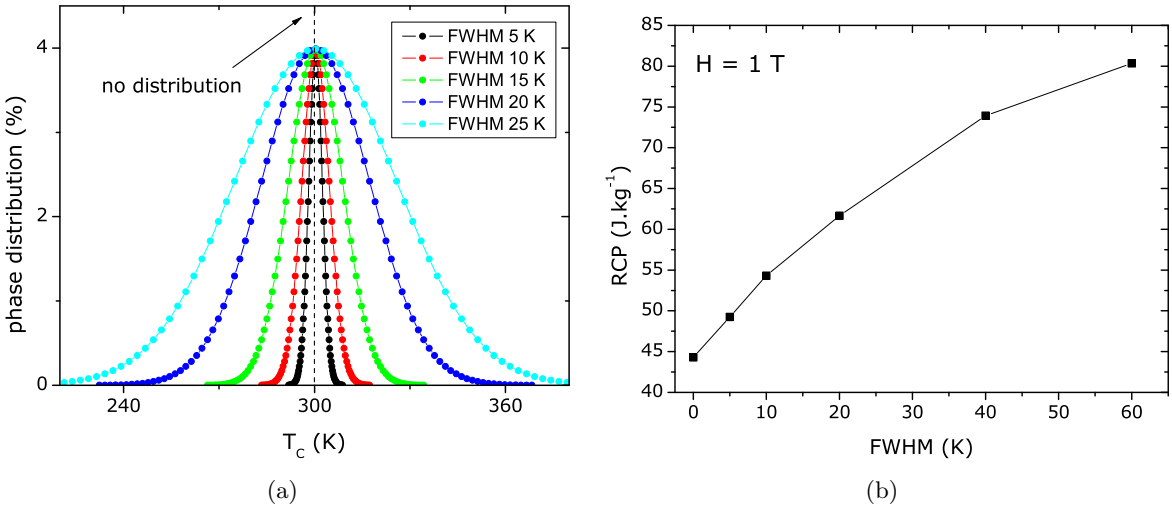

Figure 6.7: Several Gaussian distributions of T_C with increasing FWHM, and corresponding dependence of relative cooling power.

We see that the effect of the distribution turns out to increase the RCP value by a fair amount ($\sim 50\%$ for a 20 K FWHM T_C distribution), almost doubling in value if a much wider distribution is considered. The increase of the FWHM of the $\Delta S_M(T)$ curve overcomes the negative effect of the lowering of the maximum entropy change value.

This study has a clear conclusion in terms of magnetic cooling applications and the search

for magnetic refrigerant materials. In a way, we can say that controlling the homogeneity of the sample may be important to control the operating temperature range of a magnetic refrigerator, and may even have a strong enough effect as to suppress the need to have a thermal cascade system, in a given application.

6.2 First-order phase transitions

6.2.1 General remarks

As seen in sections 3 and 4, determining the mean-field parameters from experimental data and then generating the M versus H plots does not present a very good overall description of the magnetization dependence on field of the first-order $La_{0.638}Eu_{0.032}Ca_{0.33}MnO_3$ system, as shown in Figure 3.12, particularly in the magnetic irreversibility region. While this may be due to several simplifications of the model used, one improvement to the model can be to consider the effect of a chemical/structural distribution in the magnetic/thermal irreversibility properties.

As discussed in section 2.3, the magnetic interaction is described by the λ_1 parameter, while the η (or λ_3) parameter phenomenologically describes the systems compressibility and dependence of the magnetic interaction on volume. As one would assume that the compressibility does not depend explicitly on volume, the volume dependence of magnetic interaction should also not depend explicitly on volume itself. Following this reasoning, the effect of heterogeneity, be it structural, chemical, or even pressure induced, can be described, in a simplified way, by some sort of distribution of the λ_1 parameter, much like the description done before.

For a second-order magnetic phase transition, as described in section 6.1, the Bean-Rodbell η parameter has a < 1 value . By considering first-order transitions, the η parameter now needs to be > 1. Since the η parameter depends on λ_1, for a sufficiently wide distribution of the λ_1 parameter, the total magnetic system can have a composite-like combined second- and first-order behavior.

We can expect that:

- A distribution should soften the characteristic first-order discontinuities of the $M(H)$, $M(T)$ and $\Delta S_M(T)$ plots.

- In the irreversibility region, the critical field for each isotherm should present a non-infinite slope, which should be directly dependent on the width of the distribution.

- Irreversibility effects should also be less visible, and the use of equilibrium thermodynamic relations on non-equilibrium solutions should have a less obvious effect than in a 'pure' system.

6.2.2 Initial simulations

We shall consider a simple system, where the mean-field function is the Brillouin function with a spin value of 2, saturation magnetization set to 100 emu.g^{-1}. The λ_1 parameter distribution was centered to 22331 Oe (emu/g)$^{-1}$, so that the T_0 of the majority phase is again $\sim$ 300 K, with a 5 K FWHM. The λ_3 parameter was fixed at 1.5 Oe (emu/g)$^{-3}$, which obeys the $\eta \geq 1$ condition along all the distribution.

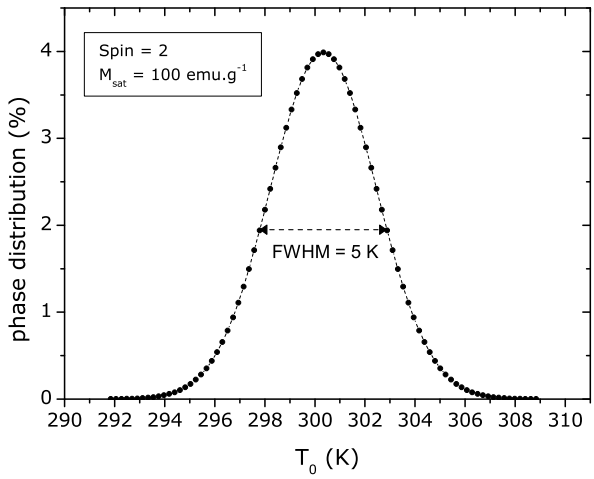

Figure 6.8: Gaussian phase distribution, for T_0 centered at $\sim$ 300 K, with a FWHM of 5 K. Full points indicate λ_1 values used for simulations.

While the number of λ_1 values used in calculations (81 in Figure 6.8), should be as high as possible to describe a smooth distribution, the computation time needs to be taken into consideration, and so the number of λ_1 values is such that the change in critical field for each λ_1 value step is below the field step considered in the simulations (100 Oe in this case).

To adequately compare the results of considering this distribution, the results of the 'pure' system, i.e. only the majority phase, will also be presented.

Figure 6.9(a) shows the magnetization dependence on temperature of the system with a 5 K FWHM distribution. Compared to the M versus H behavior of the 'pure' system (Figure 6.9(b)) we see how the discontinuities are indeed broadened, and are now inflections. Compared to the second-order simulations of chapter 6.1, the effects of even a small (5K FWHM) T_C distribution are much more visible in M versus H data of a first-order system than a 20 K FWHM distribution in a second-order transition (for $T_C \sim 300$ K).

Analyzing the magnetization versus temperature behaviour (Figure 6.10(a)), we note the broadening of the transition, which, in this M versus T representation can be mistaken by a loss of the first-order nature of the material, but is in truth, just a sum of many first-order transition at different T_C values.

The inverse susceptibility behavior of the material is also affected by the chemical/structu-

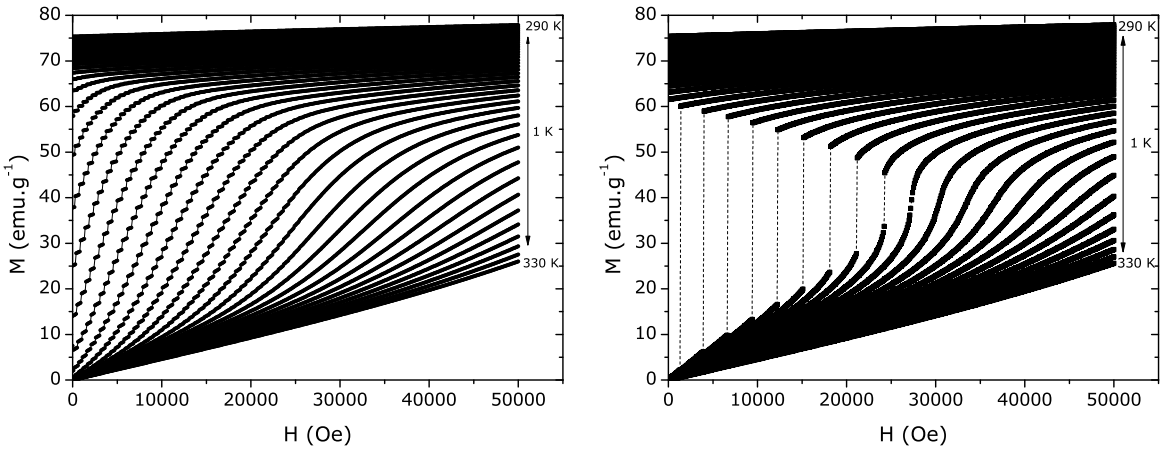

Figure 6.9: Isothermal magnetization vs. applied magnetic field, from 290 to 330 K, at a 1 K temperature step and 100 Oe field step, for a a) 5K wide Gaussian T_0 distribution, and a b) 'pure' system.

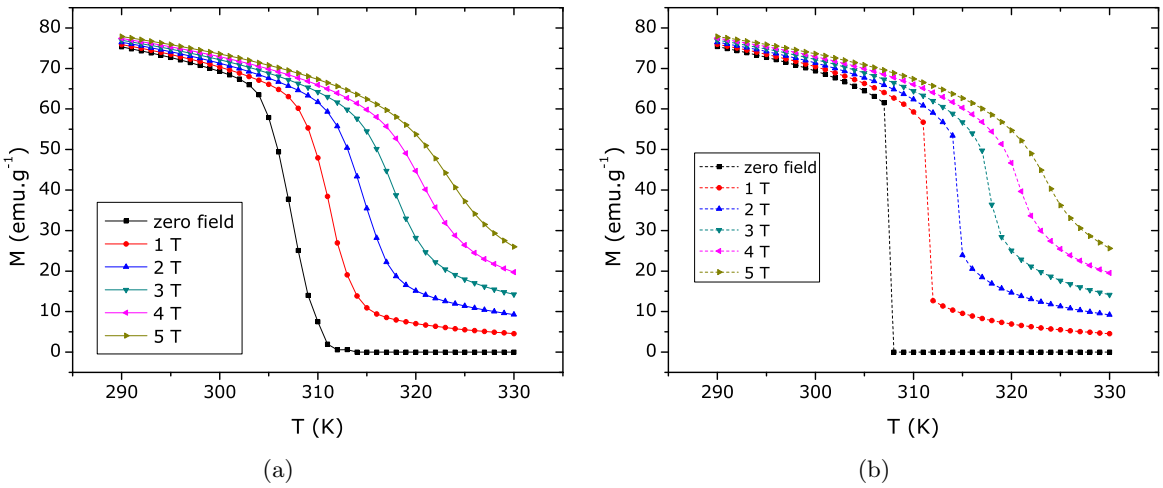

Figure 6.10: Magnetization vs. temperature at constant applied field, from 0 to 5 T, at a 1 T step, for a a) 5K wide Gaussian T_0 distribution, and a b) 'pure' system.

ral distribution, as shown in Figure 6.11(a), compared to the 'pure' system of Figure 6.11(b), for an applied magnetic field of 100 Oe.

We see how the inverse susceptibility plots loose the discontinuity by effect of the distribution. Depending on the characteristics of the distributions present in a real magnetic system, the inverse susceptibility plot may appear to reveal complex magnetic behavior near T_C, but that may be the sole effect of distributions.

Let us see the effect of a distribution in the Arrott plots of a first-order material. While in the second-order phase transition system, the effects were mainly some induced curvature

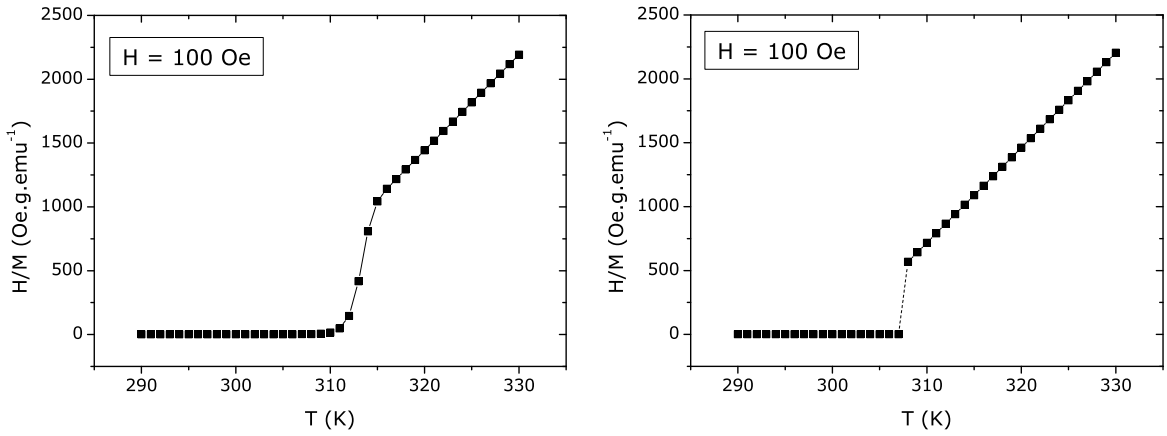

(a) (b)

Figure 6.11: Inverse susceptibility at an applied field of 100 Oe, as a function of temperature, in a 1 K step, for a a) 5K wide Gaussian T_0 distribution, and a b) 'pure' system.

on the plots, in this case the effect is quite different. Figure 6.12(a) shows the Arrott plot of the inhomogeneous system, where the discontinuities present in the 'pure' system (Figure 6.12(b)), are now smooth.

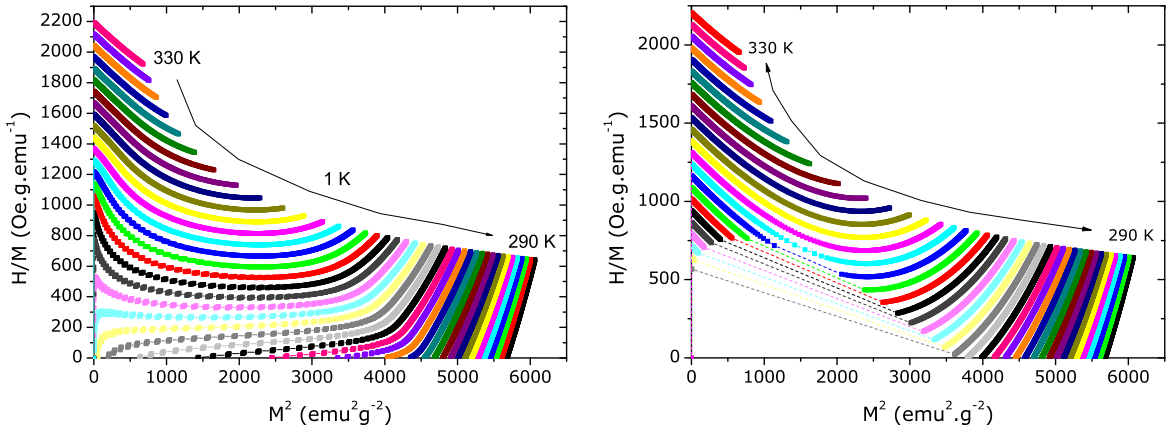

(a) (b)

Figure 6.12: Arrott plot of a first-order magnetic phase transition system with a a) 5K wide Gaussian T_0 distribution, and a b) 'pure' system.

The drastic effect of distributions on the Arrott plot presents also a complex scenario when analysing experimental magnetization data. Much like the second-order analysis, there are induced curvatures in the Arrott plot. Still, the most serious consequence of the distribution is that the smoothing of the discontinuities presents us with continuous isothermal plots, which may be erroneously fitted in an Arrott plot/Landau theory analysis.

Let us now analyze the effect of a distribution on the magnetic entropy change. Figure

6.13(a) shows $-\Delta S_M(T)$ of the system with a T_0 distribution of 5 K, and Figure 6.13(b) the corresponding 'pure' system.

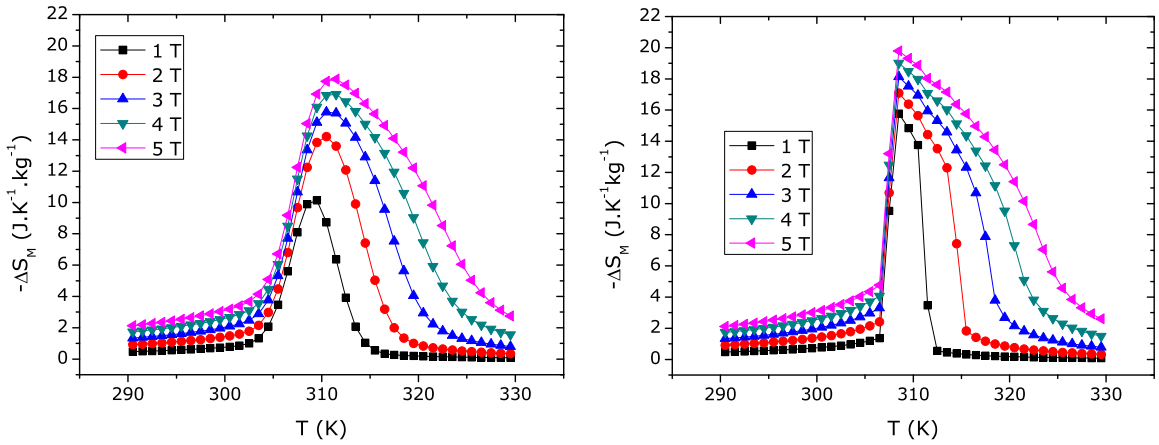

Figure 6.13: Isothermal magnetic entropy change versus temperature for applied field changes from 1 to 5 T, for a a) 5K wide Gaussian T_0 distribution, and a b) 'pure' system.

There is a very remarkable effect in the entropy curves, due to the distribution in T_C values. Not only is the discontinuity in entropy smoothed as expected, the dependence of entropy change with field is also quite different. While for the 'pure' system a ΔH value of 1 T would be sufficient to achieve an high value of ΔS_M ($\sim$ 18 J^{-1} K kg^{-1}), for the inhomogeneous system this value is reduced to 8 J^{-1} K kg^{-1} and so the values of ΔH need to be higher in order to reach similar entropy change values of the 'pure' system, much like in the second-order simulated results. This effect can be interpreted as follows: since for the inhomogeneous system there is also a consequent distribution of critical field values ($H_c(T)$), the applied field value needs to be higher in order to induce the magneto/structural transformation in all the system. In terms of applications, this makes a disordered first-order system a worse candidate than the same system in a purer form.

Let us analyze the effect of distribution on the $\Delta S_M(M^2)$ plots. As discussed in the previous chapter, the Maxwell relation can be confidently used in an inhomogeneous system to estimate magnetic entropy change, but the non-linear relation of entropy with magnetization will not be valid if one considers the total magnetization value. Figure 6.14(a) shows the $-\Delta S_M(M^2)$ plots of the inhomogeneous system, and Figure 6.14(b) the corresponding plot of the 'pure' system.

As we can see, there are deviations from the linear behaviour in both the inhomogeneous system and the 'pure' one. Interestingly, the numeric artifacts from the use of the Maxwell relation on discontinuous data of the pure system become less visible in the inhomogeneous system, since the $M(H,T)$ discontinuities are in that case smoothed out due to the distribu-

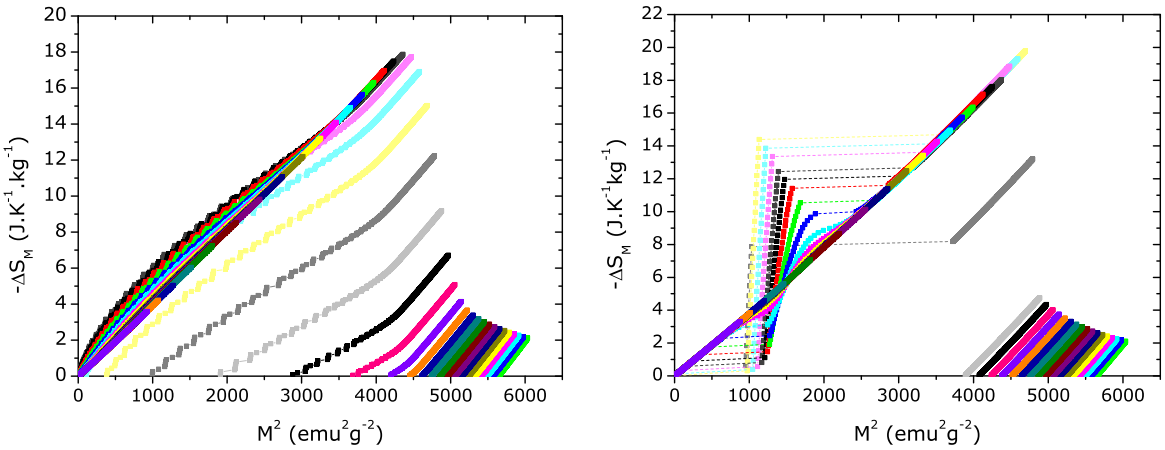

Figure 6.14: Isothermal magnetic entropy change vs. M^2 from 290 to 330 K, at a 1 K temperature step, for a a) 5K wide Gaussian T_0 distribution, and a b) 'pure' system, using the Maxwell relation.

tion. Figure 6.14(a) now presents a considerable range of slope values in the paramagnetic region, which makes it difficult to estimate the Curie constant from these plots. Also, estimating spontaneous magnetization in the ferromagnetic phase may be erroneously affected if one considers the smooth areas of the curves in low applied field, which is solely a result of the distribution.

6.2.3 Dependence on distribution width

As we have seen, the existence of a distribution softens the first-order characteristics of the measured magnetization properties. Let us consider now several Gaussian distributions of varying width, ranging from the 'pure' system, up to a FWHM of 8 K, as shown in Figure 6.15.

We can assess the effects of these disorder conditions in the entropy change calculations, by estimating entropy change up to a given field value (1 T in this example), for the considered distribution width values. This is shown in Figure 6.16.

A wider T_C distribution compared to the temperature step (1K) creates a very noticeable effect in the entropy curve shape. The wider the distribution, the entropy curve becomes similar in shape to the distribution itself. In a rough way, this can give us an indication of the amount of disorder present in the magnetic system.

Of course, while this effect has direct importance when we consider the magnetocaloric properties, other effects are largely dependent on the distribution width, since the properties that showed discontinuities in a 'pure' system are now continuous. The discontinuity is replaced by a smooth transition, with a dependence on the width of the distribution. As

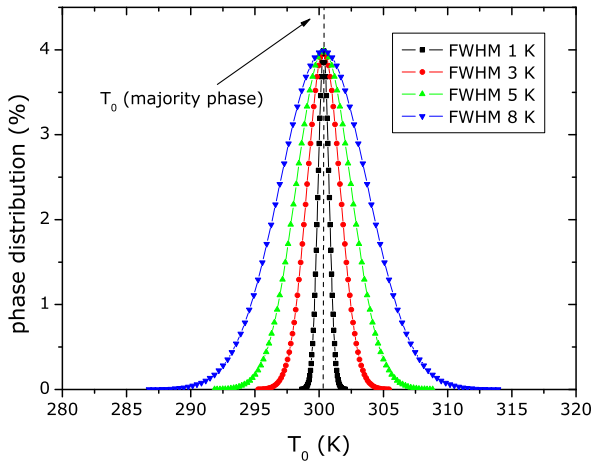

Figure 6.15: Several Gaussian distributions of T_0 with FWHM from 1 to 8 K.

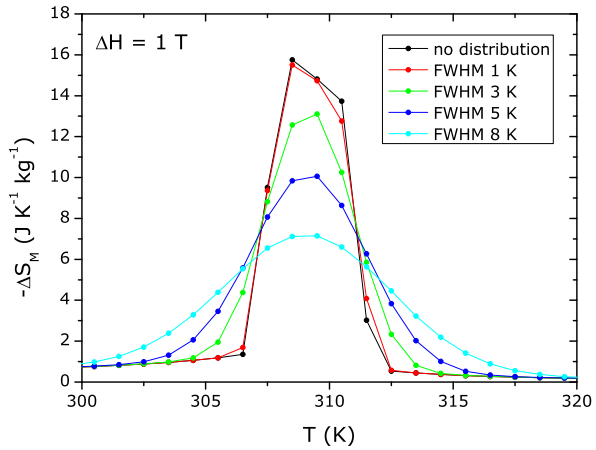

Figure 6.16: Isothermal magnetic entropy change versus temperature for applied change from 0 to 1 T, for several T_0 distributions.

shown previously, the M versus H plots can also give us a good indication of the width of the distribution. Figure 6.17(a) shows the M versus H plots up to 5 T for different distribution width, for a temperature value inside the irreversibility region ($T = 313$ K). It is worth noting that mean-field simulations of a disordered first-order system take a considerable amount of computational time, even with several optimizations to the algorithm. The small 'steps' that are visible in the M versus H plots are due to the numerical approximation (finite division) of the distribution.

The discontinuity present in the 'pure' system regularly becomes smoother as the distribution becomes wider. Plotting the temperature dependence of the inverse susceptibility at a low applied field of 100 Oe (Figure 6.17(b)), we see how the change in the behavior of the susceptibility due to the distribution width is harder to interpret.

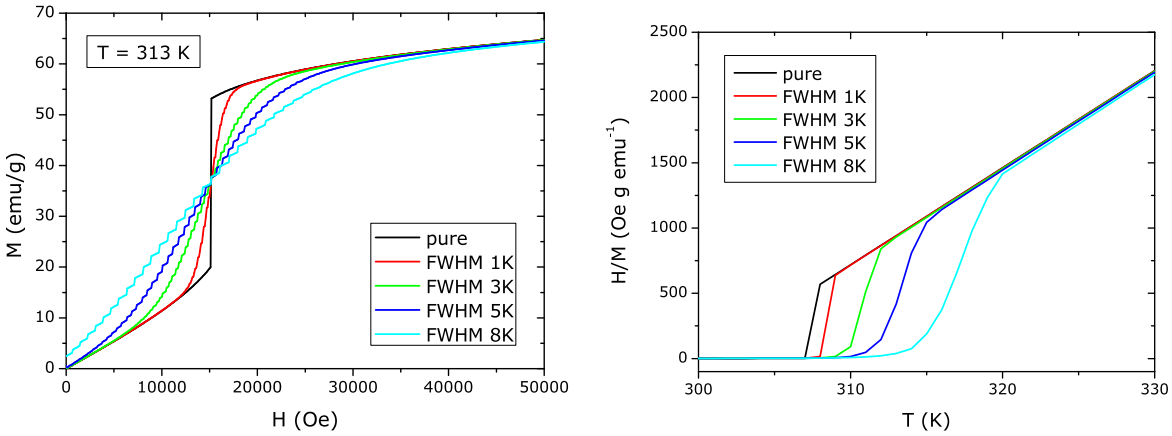

(a) (b)

Figure 6.17: a) M versus H plots of a first-order transition system, at T=313 K, for different widths of distributions of magnetic interaction, in mean-field calculations, and b) corresponding inverse susceptibility versus T plots for an applied field of 100 Oe.

The calculations we have shown in this section will allow us to interpret experimental data from first-order phase transitions, taking into consideration the expected consequences from eventual disorder effects.

6.2.4 Irreversibility effects in an inhomogeneous first-order system

The smoothing of the M versus H plots due to disorder effects will also affect the non-equilibrium solutions. Figure 6.18(a) shows the isothermal magnetization dependence on applied magnetic field, including the non-equilibrium solutions, of the 5 K FWHM T_0 distribution inhomogeneous system. Figure 6.18(b) shows the corresponding 'pure' system results.

As expected, the M versus H behaviour of the metastable solution is also greatly affected by the inhomogeneity of the system. The shape and width of the considered distribution plays a major role in this scenario. From this result we see how varied the non-equilibrium behaviour of a real, inhomogeneous first-order system can be, since it is so sensitive to the homogeneity of the sample.

Let us now consider the use of the Maxwell relation to estimate magnetic entropy change for the previous $M(H,T)$. As discussed in chapter 5, the use of the Maxwell relation in non-equilibrium conditions will present us with erroneous results. If we now consider the effects of distributions in these non-equilibrium results, another scenario comes into play. Figure 6.19(a) shows the $\Delta S_M(T)$ plots resulting from estimating magnetic entropy change from the use of the Maxwell relation on equilibrium and non-equilibrium magnetization data of Figure 6.18(a). Compared to the 'pure' system (Figure 6.18(b)), we see a considerable decrease on the effects of using non-equilibrium data to estimate magnetic entropy change. The disorder

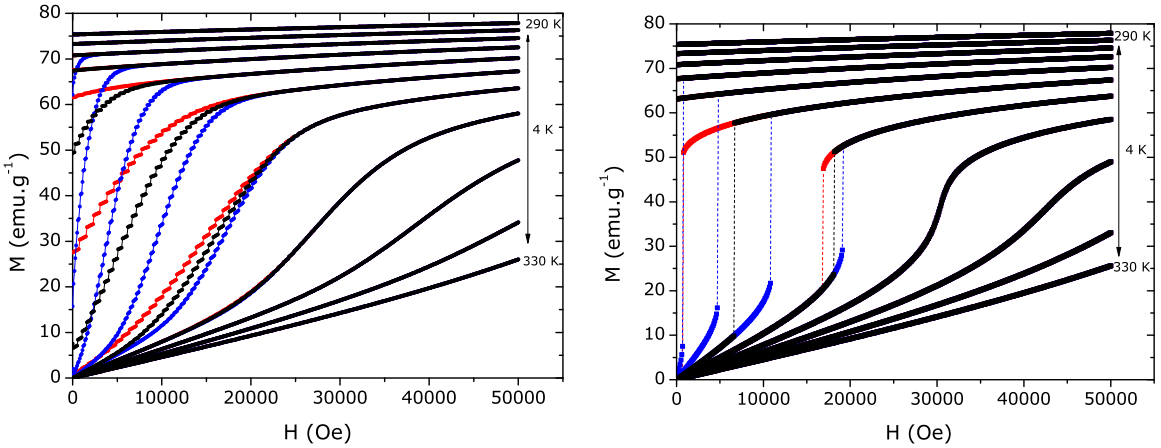

Figure 6.18: Isothermal magnetization versus applied magnetic field, from 290 to 330 K, at a 4 K temperature step and 100 Oe field step, including the metastability limits, for a a) 5K wide Gaussian T_C distribution, and a b) 'pure' system.

somewhat masks the effects of the erroneous application of the Maxwell relation to estimate the magnetocaloric effect using non-equilibrium magnetization data.

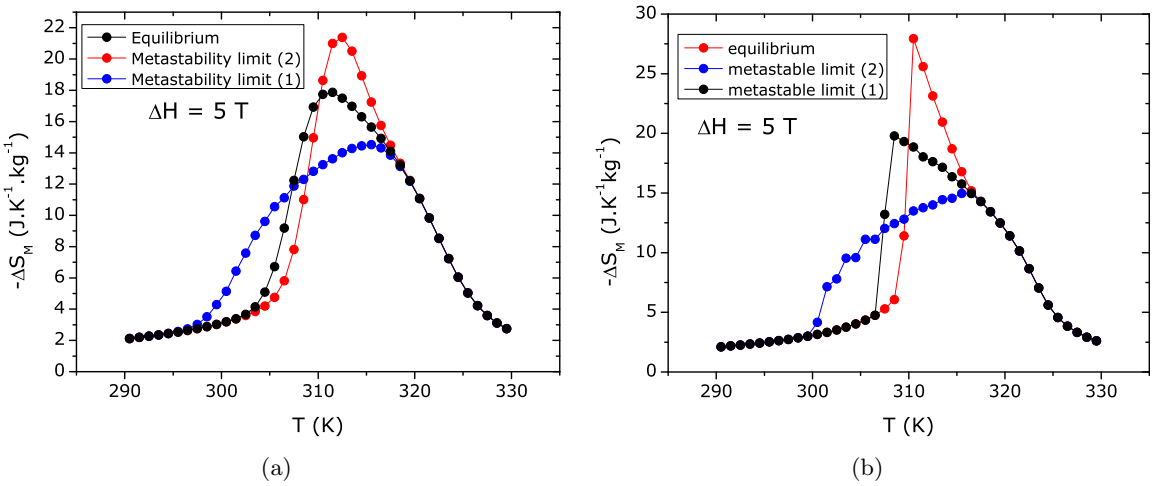

Figure 6.19: Isothermal magnetic entropy change vs. temperature, for an applied field change of 5 T, including the result from the use of the Maxwell relation on the two metastability limits, for a a) 5K wide Gaussian T_C distribution, and a b) 'pure' system.

We then conclude that a magnetic interaction distribution has a strong effect on MCE estimation from magnetic measurements, especially in first-order systems. As we will observe later in this work, the existence of a chemical/structural distribution will be an ever-present factor when analysing experimental magnetization data for MCE studies.

6.3 Effect on data analysis procedures

One expects that the existence of a distribution, which is not taken into account by the methodologies described in chapters 3 and 4, will affect their use. Using the previous simulation results as an example, we shall present the effect of chemical/structural distribution on the scaling methods, on all relevant steps of the mean-field scaling method, and also on the goodness of scaling method. The results of analyzing a disordered first-order system will be presented, since it presents us with the most complex scenario.

6.3.1 Mean-field scaling

We start with an inhomogeneous system, with a gaussian distribution with a 5 K FWHM in T_0 (see Figure 6.15). Plotting the H/T versus $1/T$ should now present some deviation from the linear behaviour of a homogeneous system. This deviations should be dependent on the broadness of the distribution. Figure 6.20(a) shows the isomagnetic H/T versus $1/T$ plots and Figure 6.20(b) shows the same plot construction of the corresponding 'pure' system, from data of Figure 6.9.

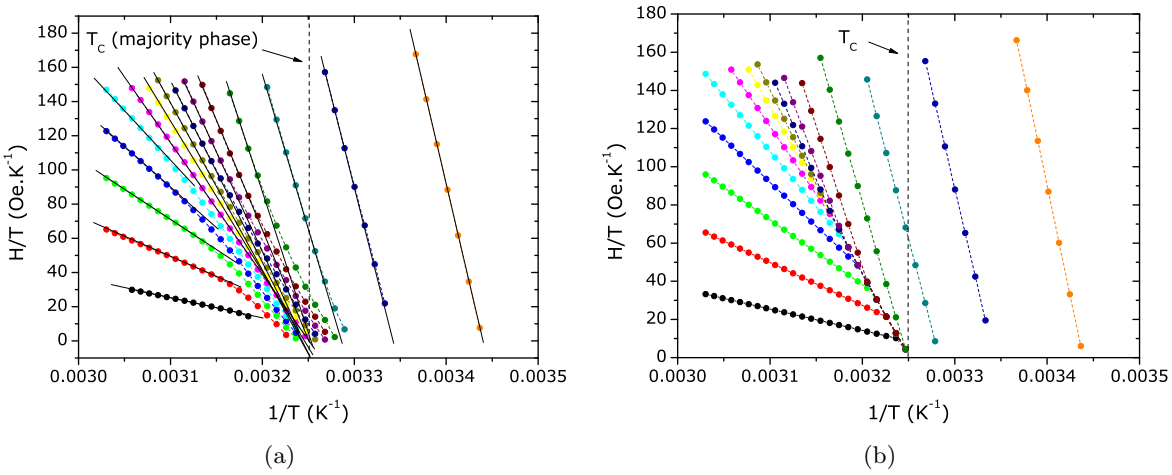

(a) (b)

Figure 6.20: Isomagnetic H/T vs. $1/T$ plot, from 5 (left) to 75 emu/g (right), and a 5 emu/g step, for a a) 5K wide Gaussian T_C distribution, and a b) 'pure' system, from data of Figure 6.9. Solid lines show linear fits.

As can be seen in detail, the plot area that deviates more significantly from the linear behavior is near T_C. This is expected, since the distribution in centered on the T_C of the majority phase. Naturally, this deviation from linearity of the isomagnetic H/T versus $1/T$ plots will make this mean-field scaling methodology slightly harder to apply.

Still, we obtain a dependence of the exchange field on magnetization, that still is close to the assumed $H_{\text{exch}} = \lambda_1 M + \lambda_3 M^3$ condition. Figure 6.21(a) shows the exchange field versus magnetization plot, for the inhomogeneous system, and Figure 6.21(b) the corresponding plot

of the 'pure' system.

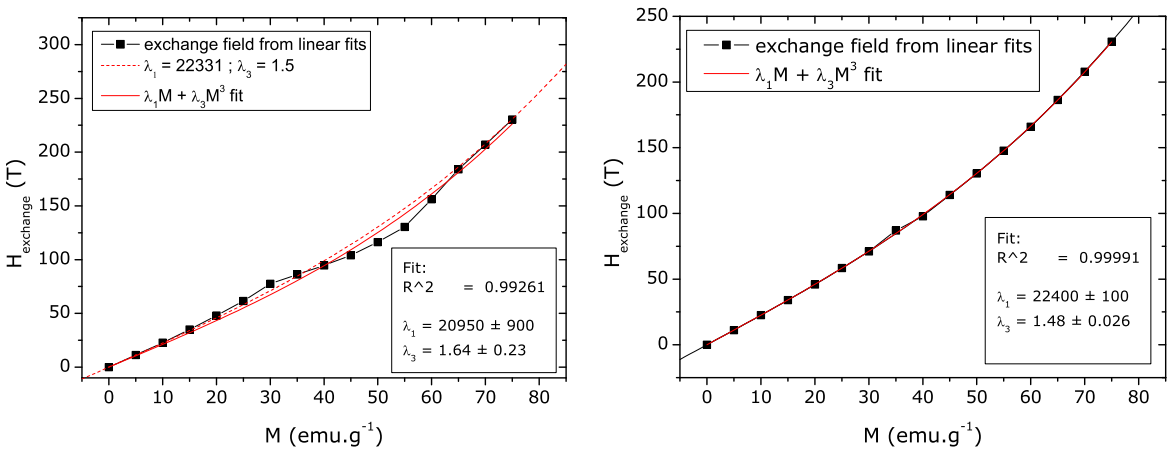

(a) (b)

Figure 6.21: Exchange field in function of magnetization, and corresponding $\lambda_1 M + \lambda_3 M^3$ fit, for a a) 5K wide Gaussian T_C distribution, and a b) 'pure' system.

As can be observed, a visible deviation from the cubic dependence of exchange field results from the methodology. In truth, this deviation comes from the interpolation of $M(H)$ for isomagnetic curves. Since now the discontinuities of the 'pure' $M(H)$ plots have been smoothed out, some values of M are considered for the interpolation and affect the results. We fit the exchange field versus M dependence with the usual $H_{\text{exch}} = \lambda_1 M + \lambda_3 M^3$ equation, to assess the deviations that are produced in the obtained exchange parameter values. As we can see from Figure 6.21(a), a deviation of $< 10\%$ from the majority phase λ_1, λ_3 values is obtained.

We can then use the λ_1, λ_3 parameters from the exchange field fit, and assess the quality of data scaling, as well as the deviations obtained on the Brillouin function fit, and the resulting spin and N (or saturation magnetization) values. Figure 6.22(a) shows the result for the inhomogeneous system, and Figure 6.22(b) the corresponding result for the 'pure' system.

As can be seen, the Brillouin function fits are (at this scale) seemingly of good quality, as also seen from the goodness of fit parameter (R^2) which is very close to 1. The spin values obtained from the Brillouin function fit to the inhomogeneous system scaling plot also presents an $\sim 10\%$ deviation from the 'pure' system spin. The saturation magnetization is much closer, however.

It is worth pointing out that the data used for this scaling approach reaches magnetization only up to 80% of the saturation value. The fact that the Brillouin fit points to a saturation magnetization value with only a 2% deviation from the exact value is a sign that as long as the scaled data presents some curvature that is accurately fitted by the Brillouin function, the M_{sat} (or N) value obtained by the fit will be a solid estimative, even with this distribution.

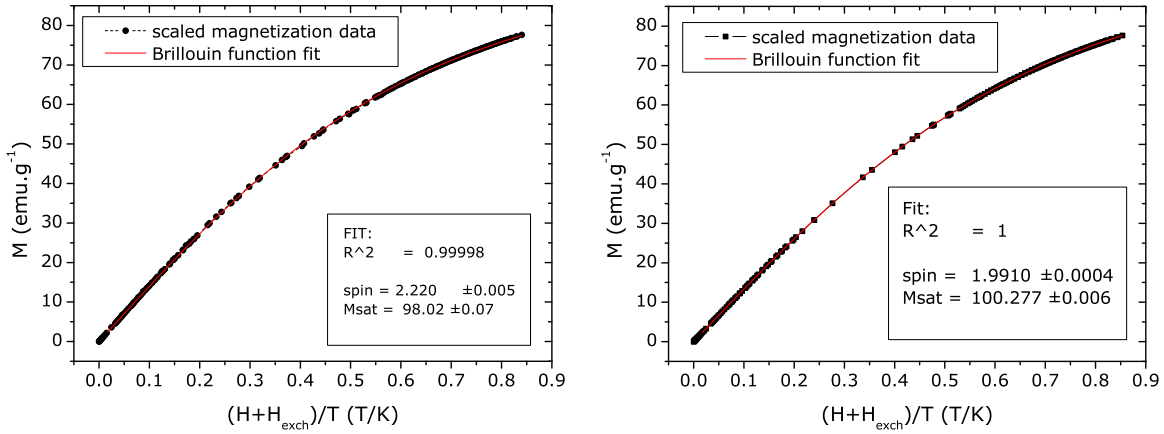

(a) (b)

Figure 6.22: Scaled magnetization data, and corresponding Brillouin function fit, for a a) 5K wide Gaussian T_0 distribution, and a b) 'pure' system.

6.3.2 Goodness of scaling method

The results of the mean-field 'goodness of scaling' methodology of chapter 4 will also be affected by the inhomogeneity of the system, since the method searches for the most adequate pair of exchange parameters (λ_1, λ_3) to produce the highest quality scaling plot. This presumes that there there is a single pair of (λ_1, λ_3), i. e. that the system is pure.

The well-defined parameters that correspond to the 'pure' system's best scaling plot should be less well defined in the disordered system, and the 3D mesh representation should give us a broader shape, related to the broadness of the structural/chemical distribution that is considered. Since we have shown that a symmetrical distribution of T_C values may result in asymmetrical effects in the magnetic properties, we may expect a shift of the 'best' scaling parameter values for the disordered system, and not only a simple broader range of (λ_1,λ_3) values that present the best scaling plots.

Figure 6.23(a) shows the contour plot resulting from the 'goodness of scaling' method presented in chapter 4, applied to the magnetization data of the mean-field simulated first-order phase transition with T_C distribution shown in Figure 6.9(a), and Figure 6.23(b) shows the corresponding plot for the pure system (Figure 6.9(b)).

In the contour plot representation, the range of (λ_1,λ_3) values that result in the best scaling plot are visually delimited. Comparing the contour plots, it is possible to see that the disordered system presents a broader range of 'best' (λ_1,λ_3) values, compared to the pure system. Still, the area is not centered around the pure $\lambda_1 = 22331$ Oe $(\text{emu/g})^{-1}$, $\lambda_3 = 1.5$ Oe $(\text{emu/g})^{-3}$) values. It is shifted to higher values of λ_1 (23800 Oe $(\text{emu/g})^{-1}$)) and lower values of λ_3 (1.2 Oe $(\text{emu/g})^{-3}$)). This arises from the disorder 'smoothing' the large discontinuous jumps in the $M(H,T)$ plots.

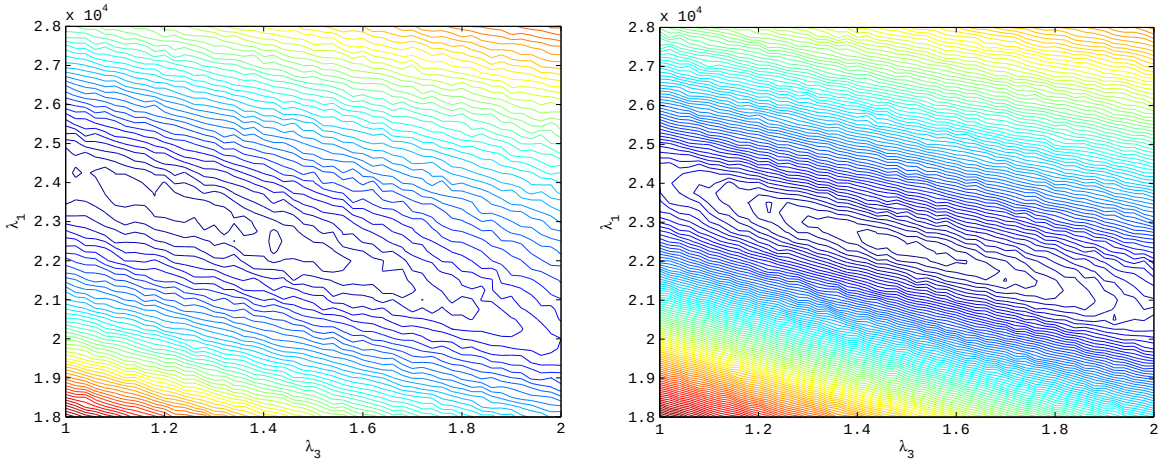

Figure 6.23: Contour plot of the goodness of scaling factor versus (λ_1, λ_3), for a a) 5K wide Gaussian T_C distribution, and a b) 'pure' system.

The mesh representation of the 'goodness of scaling' method can give us some more information on how the best scaling (λ_1, λ_3) pair is less defined in the disordered material. Figure 6.24(a) shows the mesh plot for the disordered system, and Figure 6.24(b) the corresponding mesh plot for the pure system.

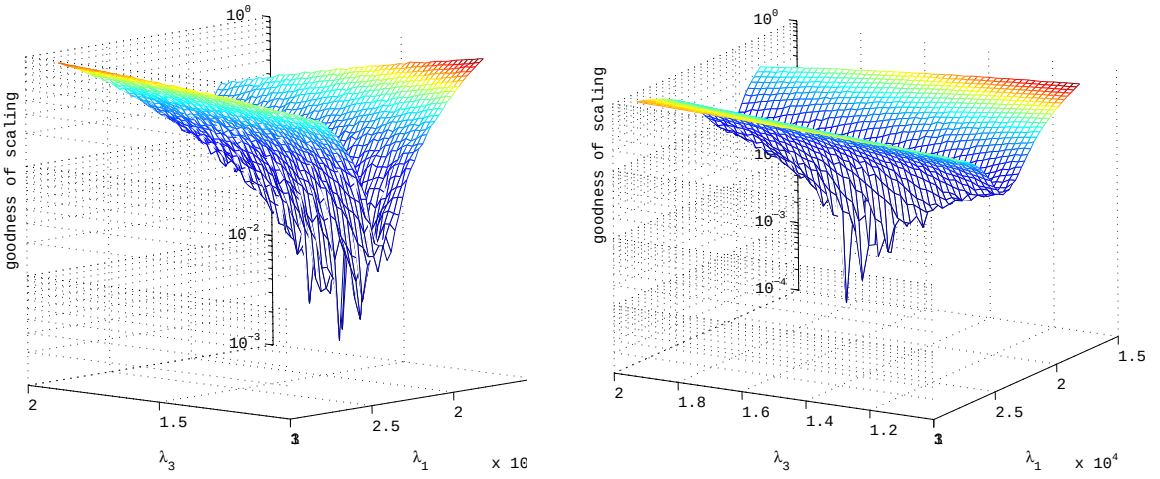

Figure 6.24: Contour plot of the goodness of scaling factor versus (λ_1, λ_3), for a a) 5K wide Gaussian T_C distribution, and a b) 'pure' system.

By plotting the goodness of scaling parameter in a logarithmic scale, we see how the mesh representation shows that the sharp minimum in the pure system is significantly broadened, and shifted to higher λ_1 and lower λ_3 values.

Analyzing a disordered first-order system has allowed us to stress the limits of the goodness of scaling method. It is important to be aware that a T_0 distribution with a width $< 2\%$ of the majority T_C value results in a shift of 6.5% in λ_1 and a 20% shift in the λ_3 parameters. More importantly, the confidence band, as seen in the contour plot, does not include the majority (λ_1, λ_3) values.

When attempting to analyze experimental data from a first-order magnetic system, the 'goodness of scaling' method becomes less reliable than the mean-field scaling method, as a way to obtain the majority (λ_1, λ_3) values. Still, it can give us some initial scaling parameter values to consider. And by considering various distribution widths, good preliminary results can be obtained. Also, when combining these results with an analysis of the magnetocaloric properties of the material, it is possible to verify the agreement between methods.

Chapter 7

Experimental

In previous chapters, new data analysis tools have been described, which help us to better analyze the properties of a magnetic system, from bulk magnetization measurements, as well as the effects of non-homogeneity, mixed-phase or disorder in relevant experimental quantities. The theories behind these approaches have been diversified, from the Landau theory of phase transitions, molecular mean-field theory and scaling concepts. An important point of the methodologies presented is that characteristics of the magnetic system under study, such as homogeneity and magnetic short-range interaction (clustering phenomena) can be addressed, and their effect interpreted and quantified.

In this chapter, the study of several magnetic systems will be presented, using a combination of these developed methods, to gain additional insight to that obtained with usual fitting procedures and partial methods. To this effect, the chosen magnetic systems were:

- Polycrystalline Nickel. This system will allow us to study the applicability of the goodness of scaling method to study critical phenomena. Nickel has been extensively studied in the past under this theory, giving us ample background to compare the results from the method.

- Mechanically alloyed fcc Fe-Cu. The magnetic behavior of the Fe-Cu alloys, near the Curie temperature and the anomalies accompanying the magneto-volume transformations are not yet completely understood. We show that the use of the mean-field scaling method bring further insight to the magnetic properties of this system, taking into account their structural inhomogeneity at a nanoscale level.

- The second-order magnetic phase transition manganites, $La_{0.70}Sr_{0.30}MnO_3$. Manganites are a fascinating magnetic system, which present a multitude of properties, from colossal magnetoresistance to a strong magnetocaloric effect. Manganites are known to present magnetic clustering behavior, as well as usually presenting considerable disorder.

- A first-order phase transition manganite, $La_{0.665}Eu_{0.035}Ca_{0.33}MnO_3$. This manganite

system will present us the opportunity to use the mean-field scaling method to a first-order phase transition system. As will be discussed later, the chemical/structural disorder present in this compound will be taken into consideration, as well as clustering phenomena.

- MnAs and related system with strongly first-order magnetic phase transition, and strong magnetovolume effects, associated to a structural transition, fully coupled with the magnetic transition. The colossal magnetocaloric effect was first reported in this system and consequently, mixed-phase conditions can be observed. A family of $Mn_{1-x-y}Cu_xCr_yAs$ samples allows to study varying mixed-phase conditions.

- A family of second-order phase transition manganites, with chemical substitution in order to study various degrees of chemical/structural disorder effects. From the mean-field simulations of disordered ferromagnetic systems, we see if we can observe similar effects in this series of samples.

- A first-order manganite system with large A-cation disorder, $La_{0.60}Y_{0.06}Ca_{0.33}MnO_3$. This sample will allow us to compare a first-order system with a chemical/structural disorder, greater than in $La_{0.665}Eu_{0.035}Ca_{0.33}MnO_3$ and a $La_{0.7}$-$Ca_{0.3}MnO_3 \pm \delta$ single crystal.

7.1 Metallic polycrystalline Nickel

The magnetic properties of Nickel have been extensively studied, and is one of the most interesting materials to study critical phenomena, with an intense study during the 1960's and 70's [60, 73, 74, 75, 76].

Isothermal magnetization curves, between 300 and 1000 K and applied fields up to 10 kOe were measured in a commercial vibrating sample magnetometer, with a 0.5 K temperature step near the expected value of $T_C \sim 627$ K [47], on a polycrystalline Nickel sample from Alfa Aesar, with 99.995 % purity. Figure 7.1 shows the measured M versus H curves, and the corresponding Arrott plot, near T_C. Two important correction were made to the raw experimental values: the remanent field of the electromagnet and the demagnetizing field. The remanent field of the electromagnet is a simple correction to the recorded field value, obtained using data from the paramagnetic phase (correcting the field value to obtain a null magnetization at a null applied field). The demagnetizing factor was determined from analyzing the Arrott plots, since the demagnetizing factor induces a vertical shift in the Arrott plots, which is particularly visible in the ferromagnetic phase (constant M versus H slope at low fields).

The non-linear nature of the Arrott plot near T_C indicates us that, as expected, Nickel does not follow the critical behavior of a mean-field system near T_C. In a traditional approach,

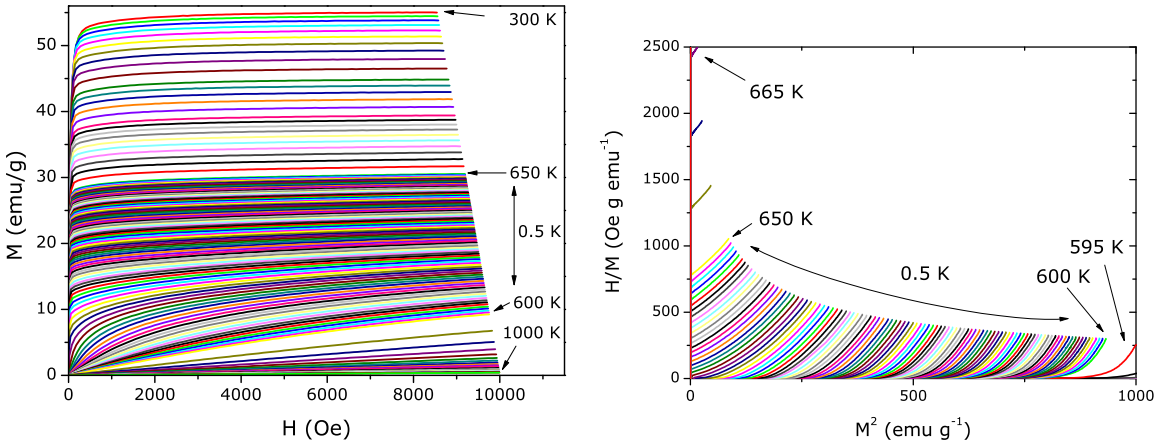

(a) (b)

Figure 7.1: a) Isothermal magnetization curves, between 300 and 1000 K and applied fields up to 1 T and b) corresponding Arrott plot near T_C.

the value of the critical exponents would be either determined by power-law fits in low-field or $T = T_C$ approximations, or looking manually for the set of parameters that would make the modified Arrott plots as linear as possible.

Our approach in this work is to use the global scaling methodology discussed in chapter 4 to search for the best scaling parameters. The first step is to choose data in a temperature range confidently above T_C, but at the same time sufficiently close to T_C so that the critical regime is valid. We choose values at $T > T_C$ so that the magnetic domain effect does not affect data, and also since there is no spontaneous magnetization value to consider in the scaling law.

The scaling plots are then $h/t^{\beta\delta}$ versus m/t^{β}, where m is the reduced magnetization and t is $(T - T_C)/T_C$. In truth, there are three scaling variables, β, δ and T_C. While T_C can be estimated from low-field M vs T measurements, it can also be one of the scaling variables, and determined in the same process as β and δ. We choose this approach, which corresponds to several contour plots, one for each T_C value. The goodness of scaling parameter dependence on the scaling parameters then becomes a 4D function, which can be plotted in 'slices'. A Matlab routine was developed to represent these 4D plots, allowing in a simple interface to change the value of the scaling parameters, but presenting those results is of limited usefulness in a static figure view and will not be shown here.

From an initial estimation of $T_C \sim 626$ K, we choose experimental data for $628K < T <$ 790 K, and a wide range of scaling parameters, ranging from mean-field exponents to values around those of the Ising or Heisenberg models, as well a wide range of T_C values. Note that the temperature range of the data used reaches values up to 25% above T_C. Due to the scaling plot construction, in this case the 'goodness of scaling' method automatically gives

more weight to values near T_C, which is convenient in this analysis. The magnetization data that is relevant is then up to 14 K above T_C ($\sim$ 2% of T_C), as shown in Figure 7.2. When iteratively searching for the best scaling plot, the curves will overlap each other, and so the curves that occupy more plot area (near T_C) have more weight in the 'goodness of scaling parameter' value.

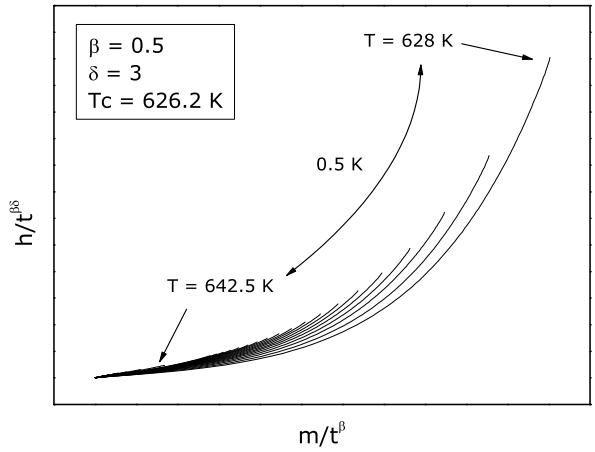

Figure 7.2: Critical phenomena scaling plot of magnetization data of polycrystalline Nickel, using mean-field exponents. Each solid line represents an isotherm for $T > T_C$, in fields up to 10 kOe.

After initial runs, a detailed search for the best values was done within a shorter range of parameters. The range and step size of the parameters used is shown in the following table:

Parameter	minimum	maximum	step
T_C	626 K	627.4 K	0.1 K
β	0.28	0.44	0.001
δ	3.80	4.80	0.01

Figure 7.3 shows the mesh and contour goodness of scale plots, as a function of β and γ, at the resulting 'best' value of T_C, 626.2 K.

A clear, well-defined best scaling occurs for $\beta = 0.372$ and $\delta = 4.56$. We note the excellent agreement of these values to the ones reported by Kouvel and Fisher in 1970 ($\beta = 0.378$ and $\delta = 4.58$ [74]), in an update to their previous values presented in 1964 [73]. Still, to check the internal validity of these parameters, we can plot the modified Arrott plot, including now temperatures below T_C, and verify the linearity near T_C. This is shown in Figure 7.4.

The modified Arrott plot confirms the good values of the critical exponents, since the linearity is observed in a wide range of experimental values, especially above T_C, where there is no domain effect. The value of T_C also appears as a good estimation, since from the plot, we can observe that 626.0 K $< T_C <$ 626.5 K.

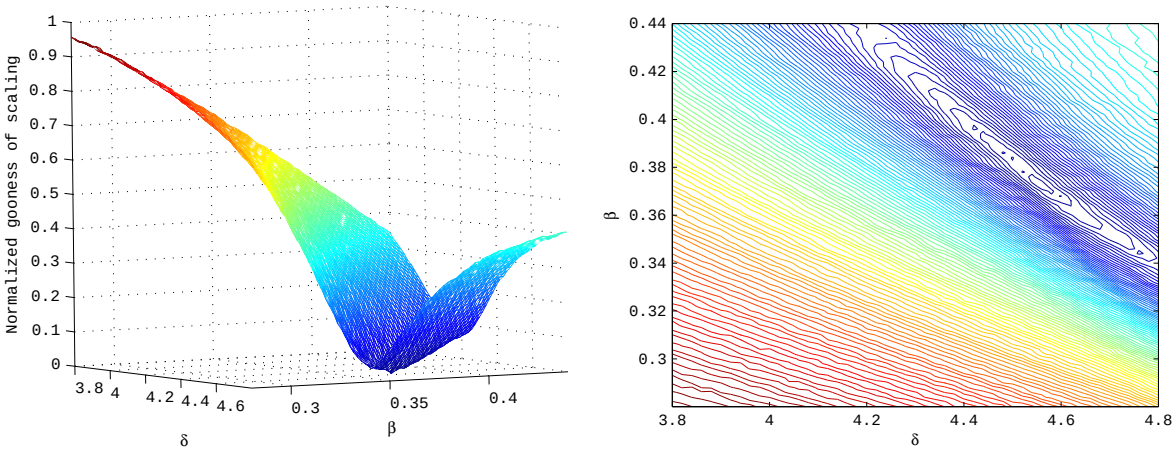

(a) (b)

Figure 7.3: a) mesh and b) contour goodness of scale plots of polycrystalline Nickel, for a search of the critical exponents β and δ, with $T_C = 626.2$ K.

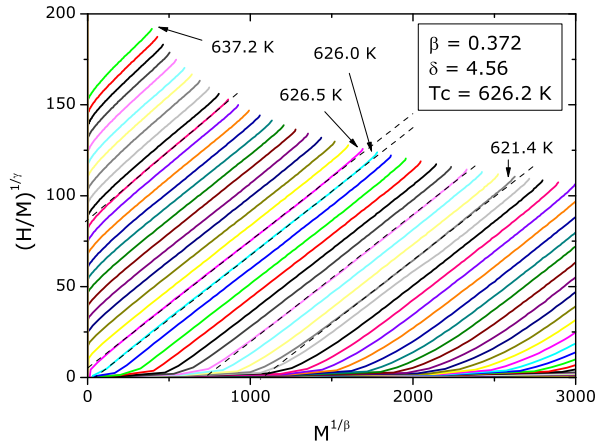

Figure 7.4: Modified Arrott plots of polycrystalline Nickel, with critical exponents and T_C values obtained from the best goodness of scale analysis. Dashed lines show linear fit to selected isotherms.

With the β, δ and T_C parameters defined, the best scaling plot above T_C can be plotted, to visually verify the quality of the 'best' scaling plot. (Figure 7.5).

We now assess if this methodology is in agreement with more classic methods to determine the critical exponent values from magnetization measurements. Figure 7.6 a) shows the power law fit to the critical magnetization versus field isotherm ($T = T_C$). This fit determines the value of the δ exponent. To explicitly show the fit quality and parameter values obtained, we also perform the same fit to the isotherms at experimentally measured T values around T_C. The best power law fit is then obtained for the T_C value that was determined by the 'goodness of scaling' method. Note that only 'true' critical isotherm is able to be adequately

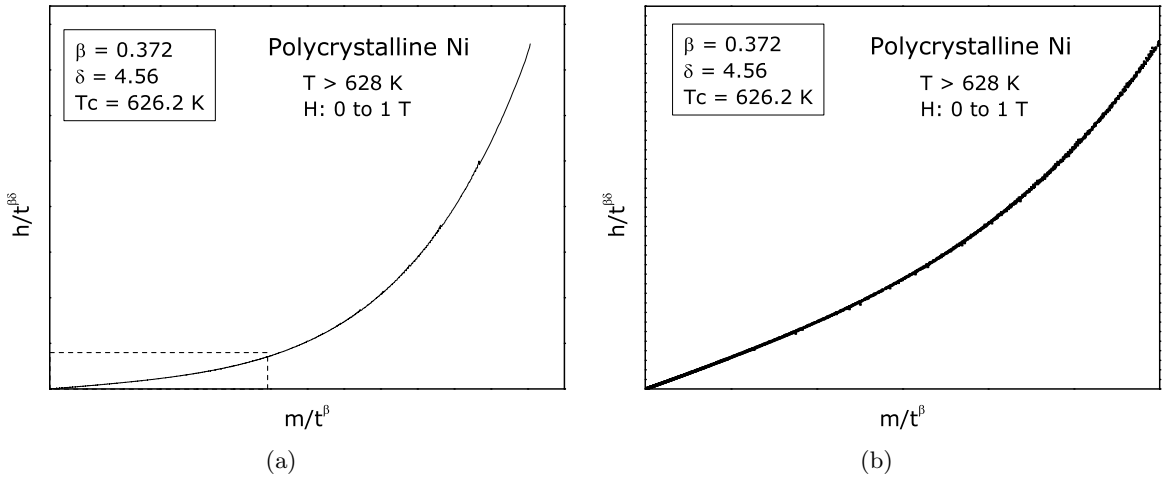

Figure 7.5: a) Best scaling plot obtained for polycrystalline Nickel, above T_C. Dashed box represents the zoomed plot area shown in b).

fitted by the power law up to high field values ($\sim$ 1 T), clearly below the known applied field limit where Nickel shows critical behavior, which is 6 T [76].

If one would consider a shift of less than 0.1% of the T_C value, the corresponding shift in the δ parameter obtained by the exponential fit is above 5%, which tells us how sensitive this 'classic' fitting approach is to the previous determination of the T_C value. If the T_C value was set as 626 K for the scaling method, the best scaling parameters obtained would be $\beta = 0.388$ and $\delta = 4.60$, if T_C is set as 626.5 K, the best scaling would be obtained for $\beta = 0.364$ and $\delta = 4.40$. In this example, the values of the critical exponents obtained from the goodness of scaling method are more robust, and so less sensitive to the correct T_C value, compared to the more classical method of power law fittings. This is due to the fact that by scaling the entire data set, there is an overall analysis of the t, m and h variables.

Since there is no need to fit the critical isotherm, potential problems due to inhomogeneity of the sample (resulting in a distribution of T_C), we avoid fitting "excessively close to T_C", which can produce erroneous values, according to Tishin and Kuz'min [77]. Although this topic has been the target of considerable discussion [78, 79], the method presented here does not need data at *exactly* T_C to be applicable, and so avoids this problem.

The critical exponent γ is usually obtained by fitting the inverse susceptibility data at a zero applied field. We have measured the magnetization versus temperature dependence of Ni for an applied field of 100 Oe, and performed the exponential fit as shown in Figure 7.7.

Since the applied field is considerable, and no remanent field corrections were performed, this fit is merely representative. Nevertheless, the obtained γ value is quite agreeable: 1.32. If we use the β and δ values that result from the 'goodness of scaling' method, by the relation $\delta = 1 + \gamma/\beta$, we obtain the same value, $\gamma = 1.32$, close to $\gamma = 1.34$, from Kouvel [74]. The

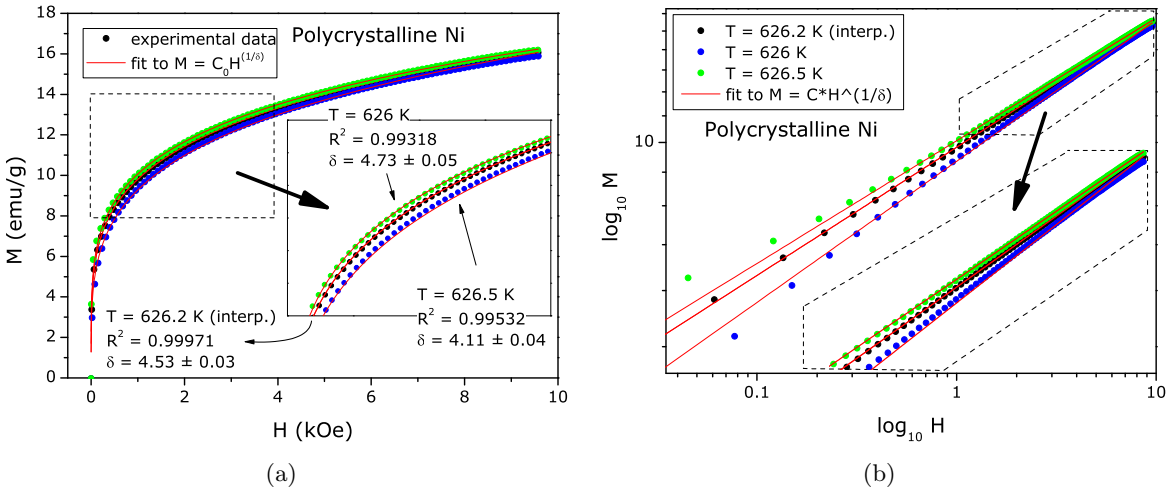

Figure 7.6: Fits of critical isotherm of polycrystalline Ni, for T values of 262, 262.2 and 262.5 K, to determine the δ parameter in a) linear and b) logarithmic scale. Insets show details of selected area.

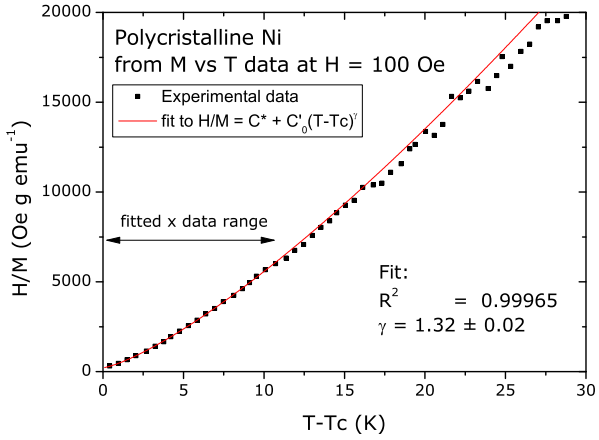

Figure 7.7: Fit of inverse susceptibility versus $T - T_C$, to determine the γ parameter.

temperature range for which the exponential fit holds extends up to ~ 15 K, for $T > T_C$. This value is higher than what would be expected from applying the Ginzburg criterion [53], since for a three dimensional system, fluctuations will dominate the behavior of the material only for low $|T - T_C|^{1/2}$ values. Still, our result is comparable to the ~ 20 K critical temperature range above T_C reported by Connelly *et al.* [80], although somewhat lower than other reported values for Nickel, which have been shown to exceed 50 K [75].

The linearity of the previously shown modified Arrott plot allows us to make an easy estimation of the spontaneous magnetization of this Ni sample, as shown in Figure 7.8(a). The β exponent can be obtained from the power-law fit to the M_{spont} versus $T - T_C$ plot, as shown in Figure 7.8(b). The obtained results compares favourably to the previous estimation,

showing the internal consistency of the results.

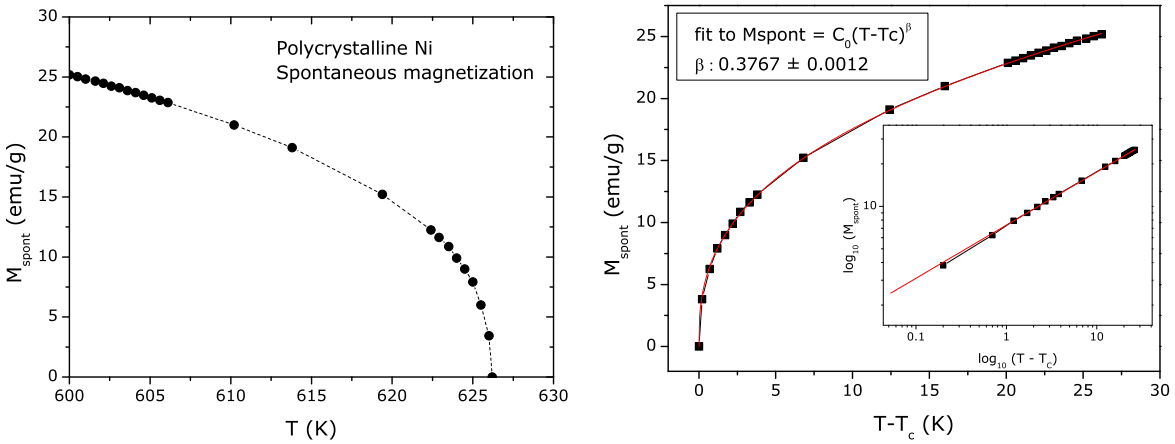

(a) (b)

Figure 7.8: a) Spontaneous magnetization of Ni, with data obtained from linear fits to the modified Arrott plots of Figure 7.4 and b) corresponding power-law fit in linear (main figure) and logarithmic scale (inset).

In summary, we have used this novel scaling methodology to study the critical phenomena behaviour of Nickel, with good results. The obtained values of the critical parameters present the expected results when representing the modified Arrott plot (Figure 7.4) or the global scaling function for magnetization data above T_C (Figure 7.5). Due to the fact that this scaling approach determines the scaling parameters β, δ and T_C simultaneously, the internal consistency of the parameter values is automatically weighed, and so is a robust method. The obtained values are also in good agreement with the bibliography, particularly the seminal works of Kouvel, Comly and Fisher [73, 74].

7.2 Mechanically alloyed fcc Fe-Cu

Non-equilibrium synthesis processes are now in common use to produce a variety of metastable materials, e.g. amorphous alloys, extended solid solutions, out-of-equilibrium crystalline phases and nanostructured materials. The binary Fe-Cu system is one of the most extensively studied among the many systems with positive heats of mixing. Iron and copper are essentially immiscible at room temperature and the equilibrium solubility of Cu in Fe remains as low as 0.14 at. % and 0.61 at. % at 723 K and 923 K, respectively [81].

High-energy ball-milling of Fe and Cu powder mixtures with a starting composition Fe_xCu_{100-x} (at. %) induces the formation of nanostructured solid solutions, either bcc for Fe-rich Fe(Cu) alloys ($x \geq 80$) or fcc for Cu-rich ($x \leq$40-50) Cu(Fe) alloys while two phases (bcc+fcc) coexist in the intermediate range, where, noticeably, both phases have the same composition as the overall alloy [82].

Large magneto-volume effects (with anti-Invar characteristics) were shown to be associated to the ferromagnetism of fcc-FeCu metastable alloys: while pure fcc-Fe (γ-Fe phase) is antiferromagnetic, it becomes ferromagnetic when its lattice is expanded.

The magnetic behavior of the Fe-Cu alloys, near the Curie temperature and the anomalies accompanying the magneto-volume transformations are not yet completely understood. Moreover, an analysis of the ferromagnetic ordering, of the paramagnetic state and the relation(s) with the nanoscale segregation in fcc-FeCu alloys is still lacking, among others, because atomic-level mixing and the possible development of short to medium range clustering in alloys made of elements which show little or no mutual solubility are often difficult to characterize experimentally [83].

In this study, we show how the structural characteristics of the investigated $Fe_{23}Cu_{77}$ alloy at the nanoscale can be inferred from its magnetic properties, by using the mean-field scaling approach described in chapter 3. From X-ray diffraction analysis, the alloy has a mean grain size of $\sim$ 16 nm and is heterogeneous.

Figure 7.9 shows the M versus T behavior for an applied field of 50 Oe and isothermal M versus H from 350 to 230 K. Measurements were performed by Vitor Amaral, using the SQUID magnetometer at IFIMUP-IN.

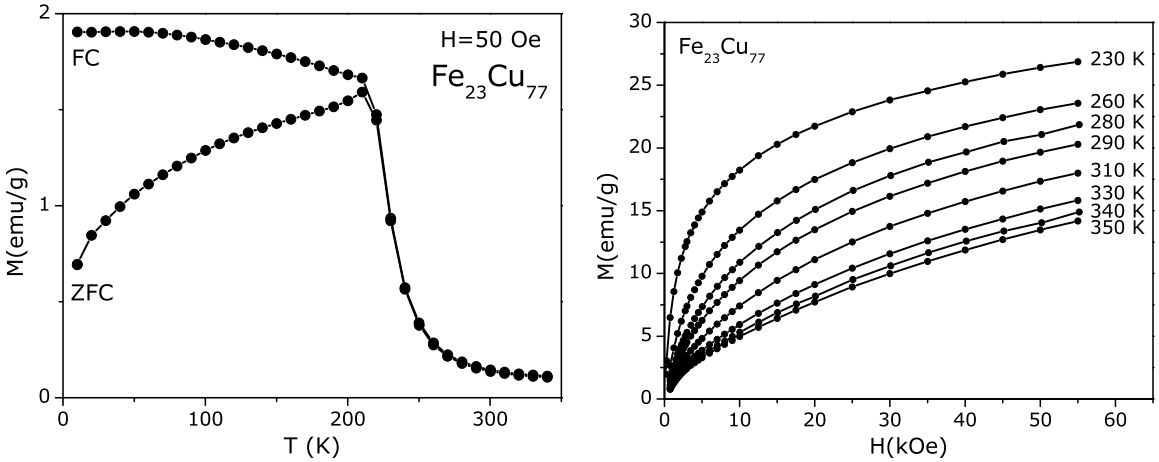

Figure 7.9: a) Temperature dependence of low-field (50 Oe) magnetization M, and b) Field dependence of the Fe-Cu magnetization of the sample milled for 20h in the range H > 500 Oe, after removing the contribution $M_{sat} = 0.55 \pm 0.03$ emu/g, due to the α-Fe phase.

The temperature dependence of M reveals the ferromagnetism of the as-milled Fe-Cu alloy, which orders at $T_C \sim 220$ K. This Curie temperature agrees well with that found for $x = 23$, from the composition dependence of T_C of mechanically alloyed Fe_xCu_{100-x} measured by Socolovsky et al. [84], and with that reported by Martínez-Blanco et al [85] for $x = 25$. The behavior at the highest temperatures of measurements of the present work indicates the

presence of a limiting residual magnetization, associated with the presence of bcc α-Fe. The thermal irreversibility observed in both samples reveals the existence of interactions among the Fe atoms that are not in the form of α-Fe. As will become evident in the following discussion, this irreversibility is associated to ferromagnetic interactions between Fe-rich clusters.

In the raw M versus H data one finds, besides the Fe-Cu contribution, a temperature independent remnant magnetization, $M_r = 0.28$ emu/g for $H = 50$ Oe. To confirm that it is associated with a residual bcc α-Fe content in the sample, we performed an additional $M(T)$ measurement, at an applied field $H = 1000$ Oe, large enough to saturate α-Fe. We find that at high temperatures this $M(T)$ curve can be modelled by a Curie-Weiss term (associated with the Fe-Cu alloy) plus a constant $M_{sat} = 0.55 \pm 0.03$ emu/g, that corresponds to $\sim 0.03\ \mu_B$/Fe i. e. $\sim$1.3% of α-Fe. This α-Fe contribution can be subtracted as a constant contribution for $H >\sim 500$ Oe (after α-Fe saturation) and the Fe-Cu part can be further studied. In the following we will present the analysis of the Fe-Cu magnetization $M = M_{raw} - M_{sat}$, valid for magnetic fields larger than ~ 500 Oe (Figure 7.9(b)).

The first step of the mean-field scaling method is to analyze interpolated M versus H data for constant magnetization values, by plotting H/T vs $1/T$. This is done in Figure 7.10(a) at 1 emu/g step. The slope of the linear portion of each isomagnetic curve (from highest temperatures to a lower limit, ~ 280 K) is used to determine the molecular exchange field H_{exch} as a function of M. One notices that the data at $T = 230$ K, close to the Curie temperature, are clearly out of the temperature region where the mean field approximation can be strictly used, within statistical fluctuations of the data. For higher magnetizations, above 18 emu/g, the linear relations are not reliable, as there are not enough points. This limits our analysis to the range shown in Figure 7.10(b).

A striking outcome of the analysis is that instead of the more common linear dependence of H_{exch} as a function of the magnetization M, one finds a much steeper dependence, which cannot be simply described even by a 3rd order polynomial. At higher magnetization, one finds a limiting linear regime (dashed line) but that does not go through the origin. The full curve in Figure 7.10(b) corresponds to a 5^{th} degree polynomial interpolation, which is taken as a convenient intermediate fitting function.

The plot of the magnetization data for $T \geq 260$ K as a function of the scaling variable $(H + H_{exch})/T$ is presented in Figure 7.11(a). The scaling is observed to be very efficient from $T = 350$ K down to 260 K, whose data deviate slightly only at higher magnetization.

Although the scaling was expected to be reliable for magnetization below about 17 emu/g, the collapse of the data to a single scaling line seems valid for values up to about 23 emu/g. This shows that the molecular exchange field dependence was well described in all that range and even well extrapolated beyond the expected range of validity of the fitting function. The scaling function f, now determined as a function of its natural variable, can be examined consistently by fitting it to some particular model. The shape of $f(x)$ suggests immediately

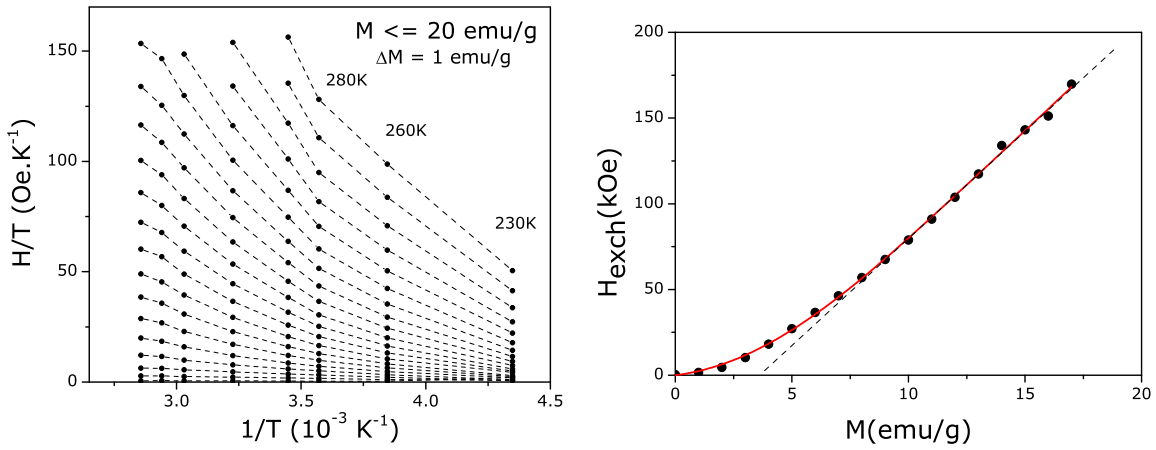

(a) (b)

Figure 7.10: a) isomagnetic H/T versus $1/T$ plot (1 emu/g step). Data at $T = 230$ K are clearly out of the region where the mean field approach can be used; b) molecular exchange field H_{exch} as a function of the magnetization M. The full curve is an interpolating 5th degree polynomial. The dashed line points to a limiting linear regime at higher magnetization.

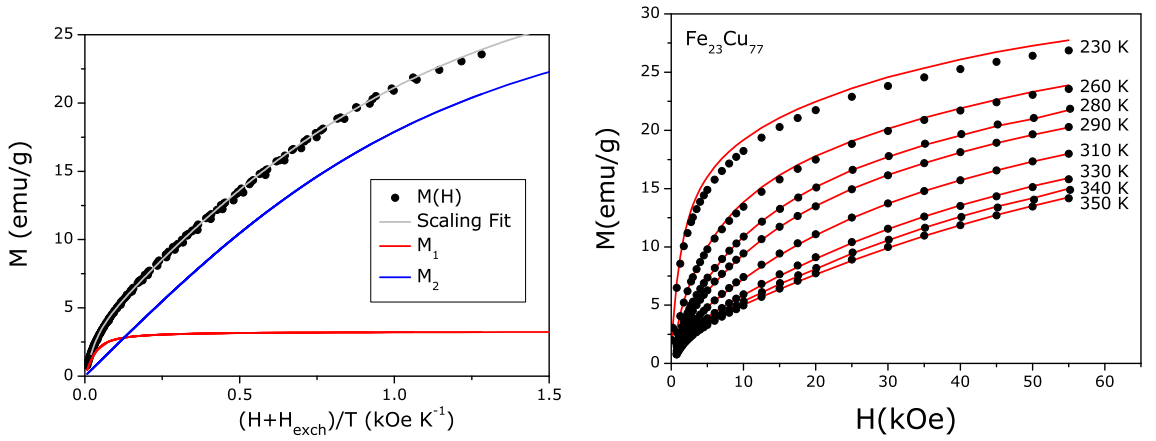

(a) (b)

Figure 7.11: a) Scaling plot of the magnetization data for $T \geq 260$K, including the fitted f function which is a sum of two Langevin contributions (shown separately) as a function of the scaling variable and b) experimental versus simulated isothermal M versus H, calculated using the molecular field model, as discussed further in the text. Calculations for $T = 230$ K are also included although data lies outside the scaling range.

that it cannot be reasonably accounted for by a single Langevin function, as used in the study of many nanocrystalline magnetic alloys. However, $f(x)$ can be fitted by a simple model of a sum of two Langevin contributions:

$$M(H,T) = M_{S1}L_{\mu_1}\left[\frac{(H+H_{exch})}{T}\right] + M_{S2}L_{\mu_2}\left[\frac{(H+H_{exch})}{T}\right], \tag{7.1}$$

for two quite distinct populations of magnetic clusters with different sizes where M_{S1} , μ_1 and M_{S2} , μ_2 are the associated saturation magnetizations and magnetic moments. For each, the ratio M_{Si}/μ_i allows to obtain the respective cluster density (number of clusters per unit mass). The Langevin function for each population is then:

$$L_\mu(x) = coth\left(\frac{\mu x}{k_B}\right) - \frac{k_B}{\mu x}. \tag{7.2}$$

The fitting parameters of the both Langevin functions of Figure 7.11(a) are presented in the following table (including in the error the difference from fits with and without the $T = 260$ K data), along with the average volume density and estimated distance between clusters belonging to the same family:

	M_S (emu/g)	μ (μ_B)	N (cm^{-3})	D (nm)
M_1 (large cluster)	3.25 ± 0.05	860 ± 20	3.5×10^{18}	6.6
M_2 (small cluster)	32.6 ± 0.03	30.5 ± 0.5	9.9×10^{20}	1.0

The larger clusters exhibit a very rapid increase of the magnetization, saturating at values of the order of 10% of the total magnetization. By contrast, the smaller clusters account for 90% of the magnetization and for the slow increase of the magnetization observed in fields up to several kOe. Moreover, the total saturation magnetization obtained from the fit performed in the paramagnetic phase ($M_{S1} + M_{S2} = 35.9$ emu/g), using experimental data values below 25 emu/g, compares well with the experimental saturation magnetization value of 39.8 emu/g, measured at $T = 4.2$ K, subtracting M_{sat} from α-Fe. The magnetization curves can be reconstructed from the fit and are shown in Figure 7.11(b), where the solid lines are calculated using the molecular field model for each temperature. Values for $T = 230$ K, which are situated outside the scaling range, are also included.

Although the scaling analysis seems to yield an overall consistent description of the data, it is essential to understand the very unusual magnetization dependence of the exchange field. The presence of a bimodal distribution of magnetic nanoclusters with quite distinct densities and saturation values gives the clue to the physical meaning. In fact, for a total magnetization higher than ~ 7 emu/g, the contribution from M_1 is saturated (constant). This is the region above which $H_{exch}(M)$ becomes linear (Figure 7.10(b)). Figure 7.12 shows the molecular exchange field H_{exch} plotted as a function of M_2 , the low moment Langevin component of the magnetization (smaller clusters), obtained from the fitting.

A linear relation is indeed found, except for a very small curvature for the highest values, so that one can confidently define a molecular field parameter λ_2 such that $H_{exch} = \lambda_2 M_2$. The slope of the line is the same as the one obtained at higher magnetizations in Figure

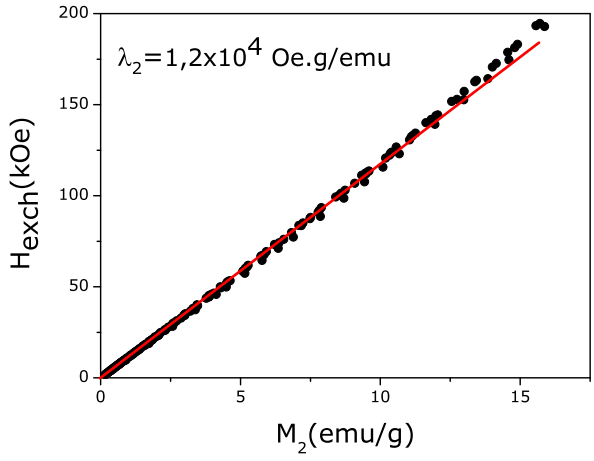

Figure 7.12: Molecular exchange field H_{exch} as a function of M_2, the low moment Langevin component of the magnetization obtained from the fitting. The line has the same slope as the one observed at higher magnetization in Figure 7.10(b).

7.10(b): $\lambda_2 \sim 1.2 \times 10^4$ Oe.g/emu. One may infer from this result that only M_2 contributes significantly to the magnetic interactions in the investigated fcc-FeCu alloy (for both the M_1 and M_2 components), probably because of the much lower density of the large clusters. The mechanism supporting the superferromagnetic state in which there is magnetic percolation of the smallest clusters without physical percolation (as the average intercluster distance is estimated to be ∼1 nm) is most probably the mediation by the conduction electrons of the matrix. These two cluster populations point to a heterogeneous alloy 'microstructure'. We note indeed that a perfectly mixed and disordered fcc $Fe_{23}Cu_{77}$ alloy would be a classical transition metal ferromagnet. Further, techniques of structural characterization like high-resolution transmission electron microscopy (HRTEM) [86] or 3D atom probe [87], applied to ball-milled fcc Fe-Cu alloys, led to conclude that such alloys are heterogeneous.

The bimodal cluster size distribution evidenced by our magnetic measurements is estimated to consist of small clusters with a radius of ~ 0.5 nm ($\sim 11-16$ Fe atoms), and of larger clusters with a radius of ~ 1.5 nm ($\sim 400-450$ Fe atoms). This value is obtained from the magnetic moment per Fe atom and the sample density (8.6 g.cm^{-3}). The uncertainty mainly results from the assumed value of the atomic magnetic moment for each cluster type, which are taken to be in the range 1.94-2.9 μ_B/Fe atom for the smaller clusters and 1.94-2.2 μ_B/Fe atom for the larger clusters. The lower value is obtained from the total saturation magnetization measured at 4.2 K (40.4 emu/g, including the α-Fe phase contribution), giving an average moment of 1.94 μ_B/Fe atom for the whole sample. The higher limits are estimated as follows: Studies of Fe clusters present a decrease of atomic magnetic moment with cluster size, with values reaching 2.9 μ_B/Fe atom in the case of clusters below about 25 atoms [88]. On the other hand, our larger clusters should approach the average value, but clusters with a

few hundred Fe atoms are reported [88] to still have higher than bulk magnetic moment (2.2 μ_B/Fe atom). Values in this range are reported in analogous studies of MA Fe-Cu alloys: a moment of 2.3-2.4 μ_B/Fe atom is reported by Eilon et al. [89] for $Fe_{25}Cu_{75}$. Mashimo et al. [90] give 2.07 μ_B for mechanically alloyed and shock consolidated $Fe_{30}Cu_{70}$, Mazzone et al. [91] give 2.26 μ_B for as-milled $Fe_{30}Cu_{70}$, Yousif et al. [92] give an experimental value of 3.05 μ_B and a theoretical value of 2.65 μ_B for $Fe_{20}Cu_{80}$. A value of 2.23 μ_B/Fe atom is obtained for Fe_xCu_{100-x} from $\mu = 2.85(x-5)/x$ μ_B/Fe atom by Bove et al. [93].

To appear and to interact magnetically as distinct and separated objects, the clusters must be Fe-rich with a Fe-depleted matrix surrounding them. This condition should be verified more promptly in the case of the smaller clusters, which are expected to have higher than average Fe content. Therefore, although the magnetic clusters we consider are embodied in a bulk matrix, the small clusters might be similar to the icosahedral or fcc cuboctahedra cluster (13 atoms), which are particularly stable [88] while the large ones may correspond to Cu-stabilized fcc clusters. The existence of very small grains (1 nm) cannot however be excluded from the HRTEM and 3D atom probe observations reported in the literature [87, 86]. In FeCu alloys, the presence of Cu atoms in the fcc Fe clusters should help stabilizing the fcc nanophase beyond these sizes, at least at temperatures below the magneto-volume transformations, which occur much above room-temperature, at $T \sim 500$ K [94, 95, 96]. The inhomogeneous structure of the clusters, with a progressive deformation, (probably relaxed with respect to the matrix) by the incorporation of Cu atoms, is probably fundamental to the high magnetic moment and magneto-volume effects in these alloys.

In conclusion, from magnetic measurements, we conclude that the nanometer sized grains contain magnetic Fe-rich nanoclusters with a bimodal size distribution. The smaller clusters comprises about 14 atoms, close to a 13 atom icosahedral/cuboctahedral arrangement which is found in multiply twinned and isolated nanoparticles of fcc transition metals and of bcc Fe. The inter-cluster ferromagnetic interactions that lead to a Curie temperature $T_C \sim 220$ K can be described by a mean field determined by the smaller clusters only, which account for 90% of the magnetization.

7.3 Second-order phase transition manganites

7.3.1 $La_{0.70}Sr_{0.30}MnO_3$

Extensive magnetization measurements of a polycrystalline sample of the second-order phase transition $La_{0.70}Sr_{0.30}MnO_3$ manganite were performed. The temperature range was from 348 K to 438.5 K, at a temperature step of 0.5 K and applied fields up to 1 T, at the IFIMUP-IN high-temperature VSM system. Figure 7.13(a) shows the M versus H plots, after corrections due to the demagnetizing effect and remanent field of the coils. The curves do not appear to show any first-order behavior.

The corresponding Arrott plot (Figure 7.13(b)) confirms the second-order nature of this ferromagnetic to paramagnetic transition, since the slope is always positive, which corresponds to a positive Landau B parameter, and so a single free energy minimum in this range. The slight non-linearity of the plot around T_C indicates that the critical exponents should be just slightly different from the mean-field ones.

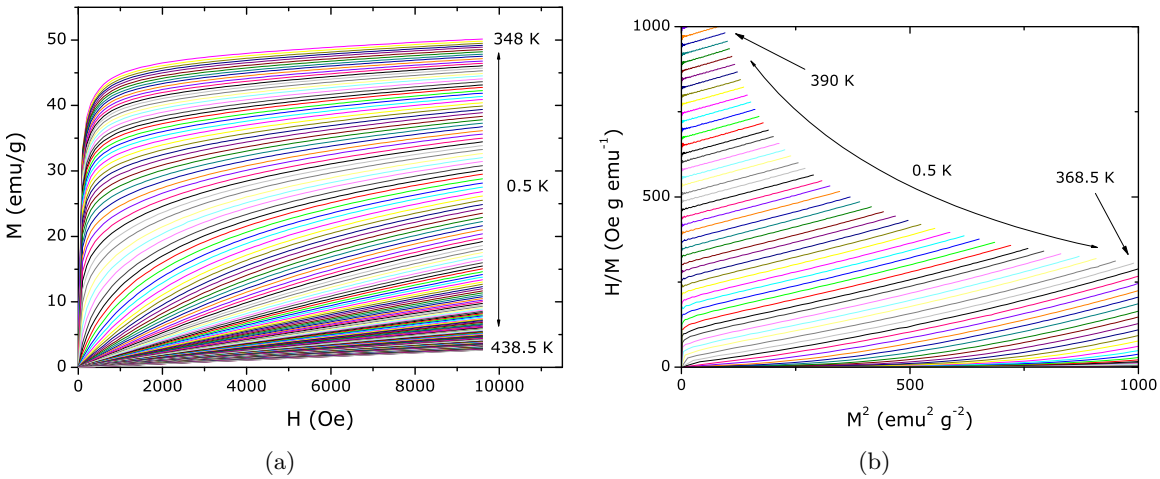

Figure 7.13: a) Isothermal bulk magnetization of polycrystalline $La_{0.70}Sr_{0.30}MnO_3$ versus magnetic field and b) corresponding Arrott plot, near T_C.

We re-plot the isothermal magnetization data at H=100 Oe of Figure 7.13(a), as an isofield M versus T plot, shown in Figure 7.14(a).

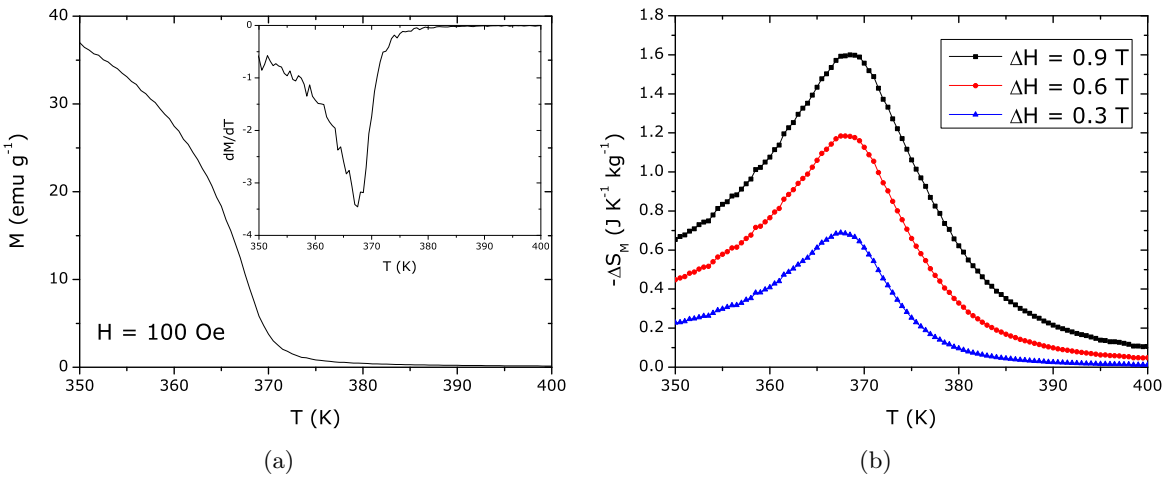

Figure 7.14: a) Magnetization versus temperature of of polycrystalline $La_{0.70}Sr_{0.30}MnO_3$, for H=100 Oe, from isothermal magnetization of Figure 7.13(a). Inset shows the derivative. b) Magnetic entropy change versus temperature, from the Maxwell relation.

The derivative of the M versus T plot, for H=100 Oe (inset of Figure 7.14(a)) shows that

T_C should be $\sim$ 368 K.

For this second-order phase transition system, the Maxwell relation can be confidently used, and so we plot the entropy change versus field change (Figure 7.14(b)). As expected, there is a peak of entropy change, also around 368 K. Since the entropy peak is not that well-defined, we can infer that there is some chemical/structural distribution in this sample. Still, the eventual width of this distribution can be estimated from the simulation shown in chapter 6.1.

This eventual chemical/structural distribution will have its effect in the $-\Delta S_M$ versus M^2 plots, and a deviation from the linear behaviour for $T > T_C$ is expected. Figures 7.15(a) and 7.15(b) show this broadening of slope.

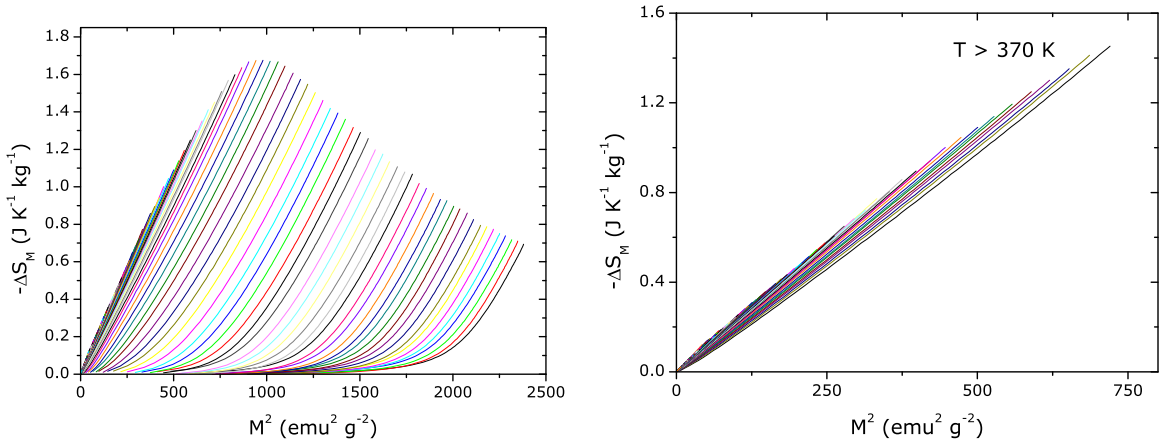

Figure 7.15: a) Magnetic entropy change versus the square of magnetization of of polycrystalline $La_{0.70}Sr_{0.30}MnO_3$, from data shown in Fig 7.13(a) and b) detail for $T > 370$ K.

However, even with this visible amount of chemical/structural distribution, an attempt to estimate the critical exponents was done, by using the goodness of scaling method. With a T_C value set at 367 K, the obtained exponent values were then $\beta = 0.50 \pm 0.01$ and $\delta = 3.8 \pm 0.05$. Still, this analysis resulted in a less defined 'best' scaling parameter region, compared to the previous analysis of the critical behavior of Nickel. Since the obtained parameters were close to the mean-field values, the Arrott plots are approximately linear, and so data is further analyzed under a mean-field perspective.

Let us now focus on the ferromagnetic region of the ΔS_M versus M^2 plots of Figure 7.15(a). Note how the slope of the linear region of each isothermal plot seems constant, as long as we ignore the low field data, corresponding to the magnetic domain region. We find that the apparent slope of this ΔS_M versus M^2 dependence is far from the slope corresponding to the Curie constant of a single Mn^{+4} or Mn^{+3} ion (or any average of these values), so we should assess if by considering short-range clustering order between Mn ions, a more similar

ΔS_M versus M^2 dependence is obtained, in the ferromagnetic region. Figure 7.16(a) shows the experimental ΔS_M versus M^2 plots, for $T < T_C$, together with mean-field simulations of isolated and clustered Mn ions.

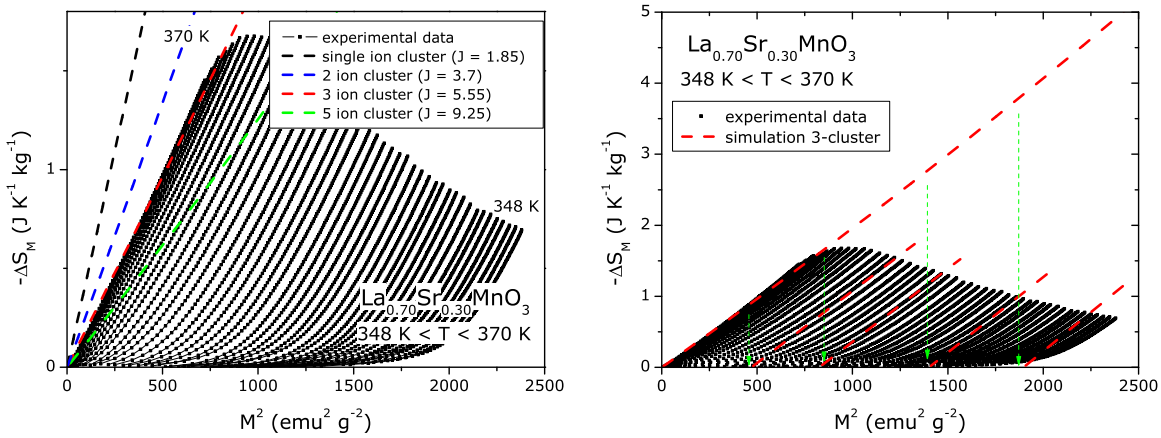

Figure 7.16: a) Magnetic entropy change versus the square of magnetization of of polycrystalline $La_{0.70}Sr_{0.30}MnO_3$, and mean-field simulations of several clustering configurations. b) Three-ion cluster simulation and corresponding shift due to spontaneous magnetization in the ferromagnetic region.

Figure 7.16(a) shows us how the simulation corresponding to a three Mn ion cluster with a total spin of ~ 5.5 reproduces the experimental results much more closely than the isolated ion, or other cluster configurations. To better assess how the 3-ion configuration reproduces the experimental results, we consider the simulated entropy curve up to higher values of M, where a curvature appears. By considering the spontaneous magnetization values for this data range, we can better evaluate the plot curvature. This is shown in Figure 7.16(b). So by just a comparative mean-field analysis of these ΔS_M versus M^2 plots, we can tell that this system should be characterized by short-range ordering phenomena, and therefore the bulk magnetic properties of this material should be better explained as consequence of a three-ion Mn cluster configuration. To continue further, let us consider the scaling approaches developed in this work and see if the mean-field parameters that are obtained will correspond to this hypothesis. Since this is a second-order phase transition system, the value of the λ_1 parameter obtained from mean-field scaling, together with the J and N value obtained from the Brillouin function fit must correspond to a $T_C \sim 370$ K.

Figure 7.17 shows the mean-field goodness of scaling contour plot of magnetization data of the $La_{0.70}Sr_{0.30}MnO_3$ system, for data from $T = T_C$ (~ 370 K) up to $T = 438.5$ K.

The best scaling parameters obtained are between λ_1 values of 12500 and 14500 Oe g emu^{-1}, and λ_3 values of 0 and 0.6 Oe g^3 emu^{-3}. This interval of λ_1 values tells us that the J and N values cannot be the isolated ion values ($1.5 <$ J < 2 ; N $\sim 2.66\times10^{21}$ ions/g),

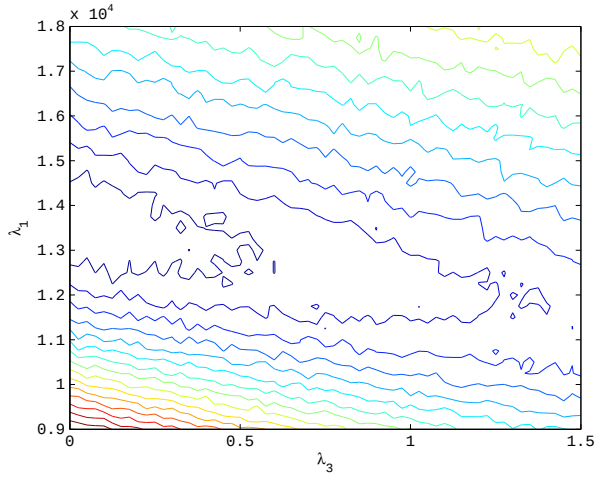

Figure 7.17: Contour plot from the mean-field goodness of scaling method, for data of polycrystalline $La_{0.70}Sr_{0.30}MnO_3$, for $T > T_C$.

since then the estimated T_C values would be between 103 K and 192 K, much different from the experimental T_C value of $\sim$ 370 K. So both the scaling analysis and the ΔS_M versus M^2 point to clustering phenomena. We now have an interval of mean-field exchange parameters to consider for building the scaling plot. Still, the interval is quite broad, and there is not a really well-defined single (λ_1, λ_3) pair that gives us the best scaling plot. To surpass this difficulty, the approach was to make several scaling plots with various (λ_1, λ_3) pairs, and consider the one which gave us the best (lowest χ^2) Brillouin function fit. Figure 7.18(a) shows the scaling plot corresponding to $\lambda_1 = 12800$ Oe g emu^{-1} and $\lambda_3 = 0.46$ Oe g^3 emu^{-3}, and the corresponding Brillouin function fit.

The Brillouin fit of Figure 7.18(a) gives us a spin value of $\sim$ 5.5, with an N value of $\sim$ 9.7×10^{20} ions/g. Considering the λ_1 value and the previous parameters, the T_C value is $\sim$ 368 K, close to the experimentally observed T_C value. Since we have a spin value close to the expected 5.55 average value of a three Mn cluster, and an N value which is very close to 1/3 of the total number of Mn ions, the Curie constant is approximately the same as the previous 3-cluster calculations of the entropy analysis.

Figure 7.18(b) shows the simulated M versus H behavior of the mean-field system with parameters obtained from scaling and the Brillouin function fit, compared to the experimental results. We see that there is a good agreement between the simulations and experimental data, up to values of magnetization around 50% of saturation.

Still, we know that there is a considerable amount of chemical distribution on this sample, which is not taken into consideration in these simulations. Yet, the magnetization simulations of a molecular mean-field system produce good results, as long as a magnetic clustered state is considered. Note that the existence of a clustered state already comes from the direct analysis of the entropy versus magnetization behavior of the system, which determines that

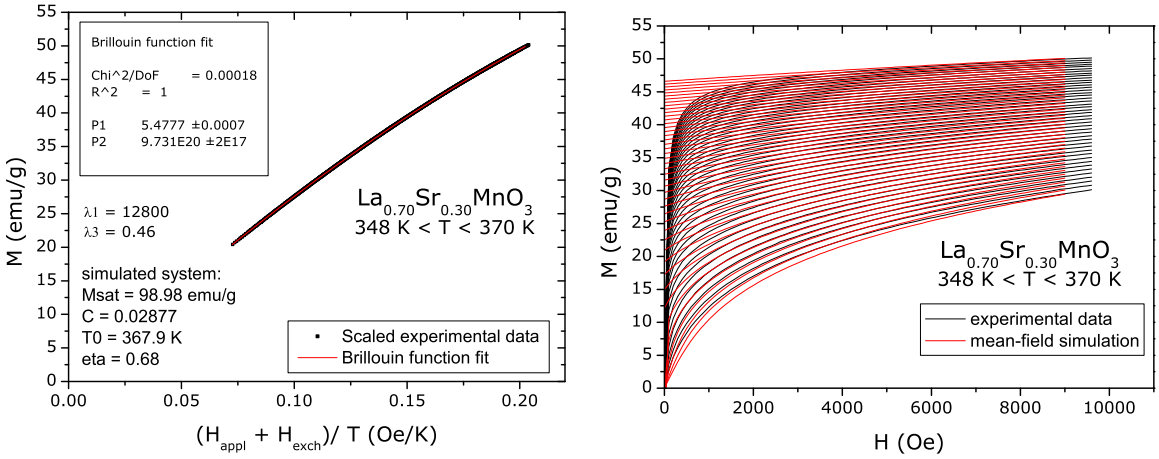

(a) (b)

Figure 7.18: a) scaling plot of $La_{0.70}Sr_{0.30}MnO_3$ magnetization data below 370 K, and corresponding Brillouin fit. b) Simulated M versus H behavior of corresponding mean-field system, compared to experimental data.

the Curie constant of the isolated ion does not match the Curie constant of the experimental magnetization data.

Considering then the 3-Mn ion clustered state, and magnetovolume coupling, we can compare the magnetic entropy change plots from the simulations and the experimental results. Since it is clear that there is some disorder present in this material, we plot also the result considering an additional 8 K FWHM T_C distribution, as shown in Figure 7.19.

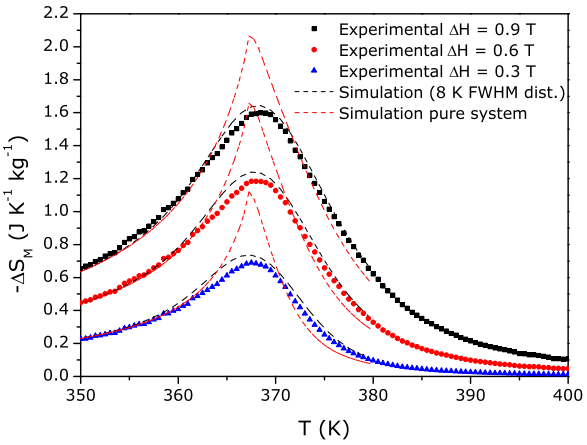

Figure 7.19: Magnetic entropy change of polycrystalline $La_{0.70}Sr_{0.30}MnO_3$, for a 0.3, 0.6 and 0.9 field change (solid points), from data of Figure 7.13(a). Dashed lines represent results from simulations considering a pure system (red lines) and a disordered system with a 8 K FWHM T_0 distribution (black lines).

It is possible to observe how important it is to consider disorder when trying to simulate

the magnetocaloric behavior of this material. Indeed, recent work [97] reports on the failure to describe the magnetic properties of Gadolinium and manganites using mean-field theory, but the magnetic measurements of the samples show that they are notably disordered, which was not taken into considerations in the simulations by the authors.

7.3.2 Disorder effects in the $La_{0.70-x}Eu_xSr_{0.30}MnO_3$ system

The chemical stability of the manganite structure makes these materials good candidates for magnetic refrigerant materials, since the magnetocaloric properties can be easily tuned by chemical substitution. Consider the parent compound $La_{0.70}Sr_{0.3}MnO_3$, as analyzed in section 7.3.1. With T_C around 370 K, lowering the value to around room-temperature would increase its applicability for magnetic refrigeration. One way to achieve this is to substitute Lanthanum by another rare-earth ion with a smaller ionic radius [98, 99], also keeping the mixed-valence ratio intact.

To this effect, we have studied the $La_{0.70-x}Eu_xSr_{0.30}MnO_3$ system, with $x = 0$, 0.035, 0.14 and 0.21. The main conclusions of this specific study have been published in Ref. [ARA+08]. Samples were prepared by the sol-gel combustion method described in reference [100], with intermediate grinding steps and sintering temperature of 1350°C for 68 hours. Structural properties of samples were analyzed by X-ray diffraction using a Phillips X'Pert MPD commercial X-ray diffractometer and microstrutural analysis by scanning electron microscopy with chemical analysis by electron energy dispersive spectroscopy using a Phillips FEI Quanta 400 and EDAX EDS detector. Magnetic properties of the samples were measured using the high-temperature VSM and SQUID systems at IFIMUP-IN. A detailed description of the structural and electron microscopy analysis of this materials is presented in Refs. [ARA+05a, ARA+05b].

Our choice of substitution with the Eu^{+3} ion is due to the fact that Europium in its +3 ionic state is non-magnetic. This fact simplifies the magnetic analysis of the system, since the extra magnetic moment/order that would eventually come from incorporating a magnetic ion into the lattice does not come into play. The ionic size of Eu^{+3} (1.12 Å) is smaller than La^{+3} (1.216 Å) [101]. We therefore expect T_C to decrease with an increase in Eu substitution [102, 103], and an added increase of chemical/structural distribution. From the analysis done in chapter 6.1, the consequence of this would be a lowering of the maximum value of magnetic entropy change, but also a substantial increase of the relative cooling power. Figure 7.20 shows the obtained dependence of T_C with Eu substitution.

The Curie temperature of this family of compounds can therefore be tuned by chemical substitution in a wide range of temperature values, above and below room temperature. We therefore assess the effects of this substitution on the magnetic and magnetocaloric properties of this system. Magnetic entropy change dependence on temperature for an applied field change of 1 T and corresponding relative cooling power is shown in Figures 7.21(a) and

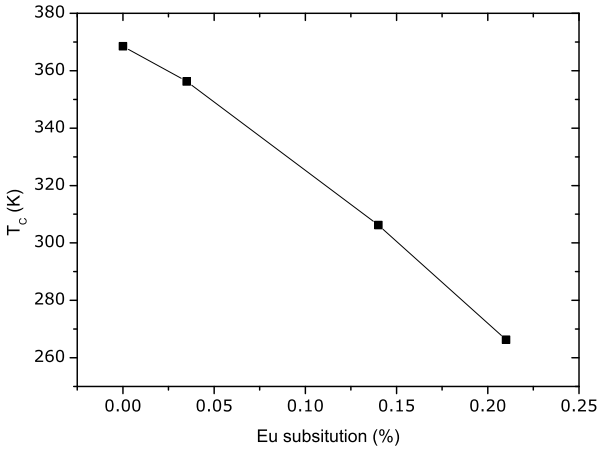

Figure 7.20: Curie temperature dependence of the $La_{0.70-x}Eu_xSr_{0.30}MnO_3$ system, as a function of x.

7.21(b), respectively.

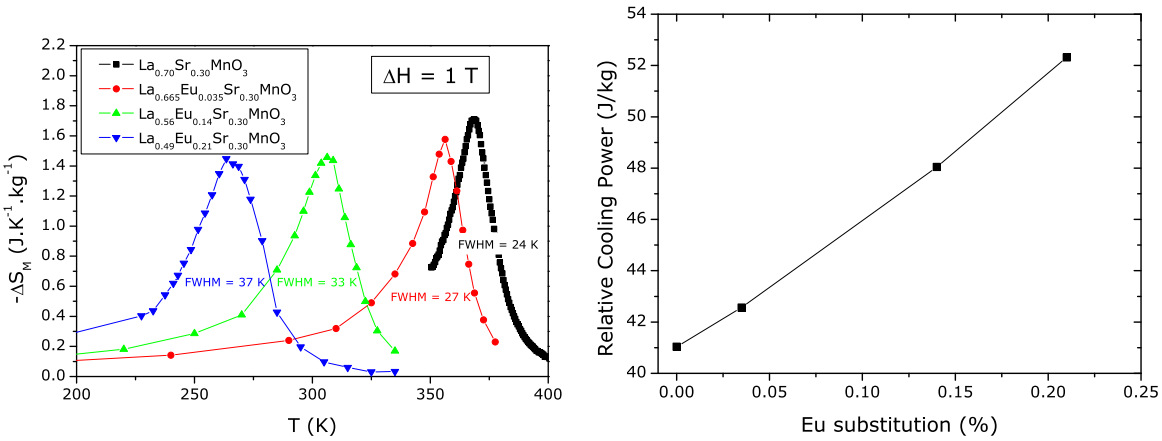

(a) (b)

Figure 7.21: a) Magnetic entropy change of $La_{0.70-x}Eu_xSr_{0.30}MnO_3$ as a function of temperature, for an applied magnetic field change of 1 T. b) Relative cooling power as a function of Eu substitution.

A good agreement between the results shown here and the simulation of chapter 6.1 leads us to the conclusion that disorder effects in the magnetic interaction, as a consequence from a chemical/structural from chemical substitution, plays an important role in the magnetic and magnetocaloric properties of this system. The manganite structure is able to withstand the ionic size mismatch of La and Eu up to 21% of substitution. It would appear that the chemical/structural distribution is approximately symmetrical in this case, since the Relative cooling power dependence on substitution (and so disorder) is similar to the results obtained

earlier considering Gaussian distributions (section 6.1).

7.3.3 Phase separation phenomena in the $La_{0.70-x}Er_xSr_{0.30}MnO_3$ system

The study of the rare-earth substituted manganite system, $La_{0.70-x}Er_xSr_{0.30}MnO_3$ allows to evaluate if and how the magnetic moment from the Er ion would interact with the Mn-Mn interaction, and so if there would be any observable changes in the magnetocaloric studies.

In this case, the ionic size mismatch is larger compared to the previous Eu substitution, since the ionic size of Er^{+3} (1.062 Å) is smaller than that of Eu^{+3} [101]. It is expected that a secondary phase will appear when the limit of Er substitution is reached, since the Goldschmidt perovskite tolerance factor [104] is considerably lower in this case. In a preliminary step of this study, samples of the $La_{0.70-x}Er_xSr_{0.30}MnO_3$ system were prepared, with x = 0.014, 0.035, 0.14 and 0.21.

It was verified that a secondary phase appears for higher substitution of Er. Structural and electron microscopy analysis of this secondary phase reveals it to have the $ErMnO_3$ structure (space group P 63 CM – 185), and composition with a 1:1 Mn-Er ratio, with only small amounts of La and Sr. The remaining sample shows the rhombohedral structure (space group $R\bar{3}C$ – 167), with en Er content no higher than 10%, even for the 21%-Er sample. The dependence of T_C with substitution also reaches a minimum value of 320 K. For a more detailed description of this study, see Refs. [Ama05, ARA$^+$05a].

To further investigate this phase separation phenomena, samples of the $La_{0.70-x}Er_xSr_{0.30}$-MnO_3 system with x = 0.06, 0.08 and 0.10, close to the estimated solubility limit of x $\sim$ 0.07 were prepared in the sample sample batch, using the same sol-gel method described earlier [100].

X-ray diffraction data confirms the presence of a hexagonal ErMnO3 phase, for Er substitution above 6%, as shown in Figure 7.22, where diffraction peaks around $2\Theta \sim 30^o$, corresponding to the secondary $ErMnO_3$ phase, appear in the $La_{0.62}Er_{0.08}Sr_{0.30}MnO_3$ sample, and are of increased intensity in $La_{0.60}Er_{0.10}Sr_{0.30}MnO_3$.

The dependence of T_C with Er substitution changes once the amount of Er is above 6%, as shown in Figure 7.23, together with data from the other samples [Ama05, ARA$^+$05a].

The clear lower limit to T_C establishes the limit of Er solubility in the $La_{0.70-x}Er_xSr_{0.30}$-MnO_3 structure. SEM imaging also shows the presence of the $ErMnO_3$-like phase for higher Er substitution values, as shown in Figure 7.24.

By estimating the magnetic entropy change of the samples near the solubility limit, we may be able to infer some more information on the type of chemical/structural distribution that rises from this phase separation phenomena. From the simulations of a disordered system of section 6.1, the effects of a symmetrical T_C distribution on the $\Delta S_M(T)$ plots are known. In this more complex case, where a phase separation phenomena occurs, interpreting the $\Delta S_M(T)$ plots may give us some insight on the properties of this 'self-composite' system.

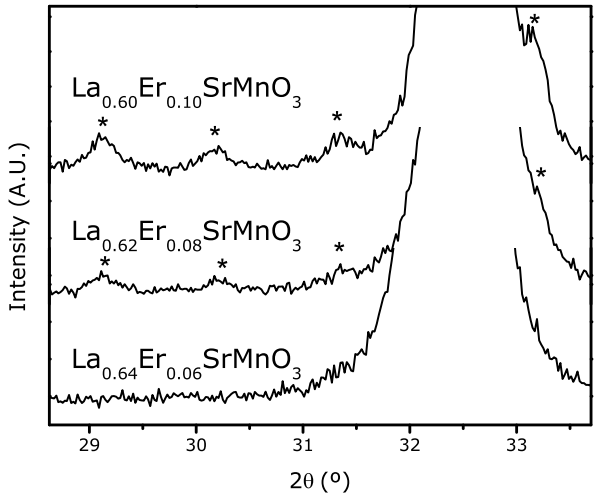

Figure 7.22: X-ray diffraction data of $La_{0.70-x}Er_xSr_{0.30}MnO_3$ with $x = 0.06$, 0.08 and 0.10. Symbol (*) indicates $ErMnO_3$ phase diffraction peaks.

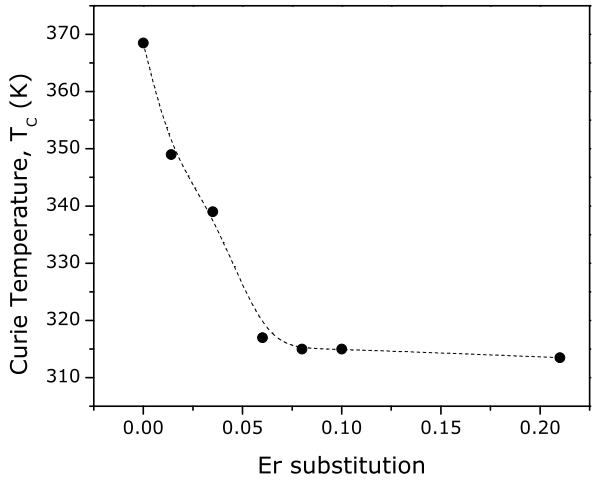

Figure 7.23: Dependence of T_C of $La_{0.70-x}Er_xSr_{0.30}MnO_3$ with Er substitution (x).

Figure 7.25 shows the magnetic entropy change dependence on temperature of the $x = 0.06$, 0.08 and 0.10 compounds, for an applied field change of 1 T.

The magnetic entropy dependence on temperature confirms the lower limit of T_C. Interestingly, the entropy curves of the three samples show similar behavior above T_C, but not below T_C. The entropy peaks broaden with increased substitution for $T < T_C$, also increasing the relative cooling power with substitution, but in an asymmetric/skewed way. This points us to a possible chemical/structural inhomogeneity of the material, when the Er content is above the solubility limit. This scenario can be justified if we analyze the microstructure of the material. From Figures 7.24(b) and 7.24(c), we see that the $ErMnO_3$ phase forms in inter-grain regions. This separation is also seen in the work of Ravindranath *et al.*, on the

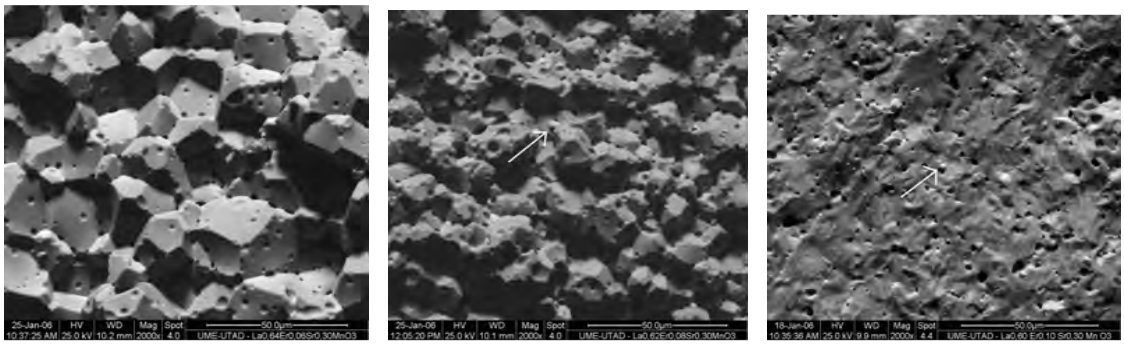

(a) $x = 0.06$ (b) $x = 0.08$ (c) $x = 0.10$

Figure 7.24: SEM imaging of $La_{0.70-x}Er_xSr_{0.30}MnO_3$ at 2000× magnifying factor, for a) $x = 0.06$, b) $x = 0.08$ and c) $x = 0.10$. White arrows indicate secondary $ErMnO_3$ phase.

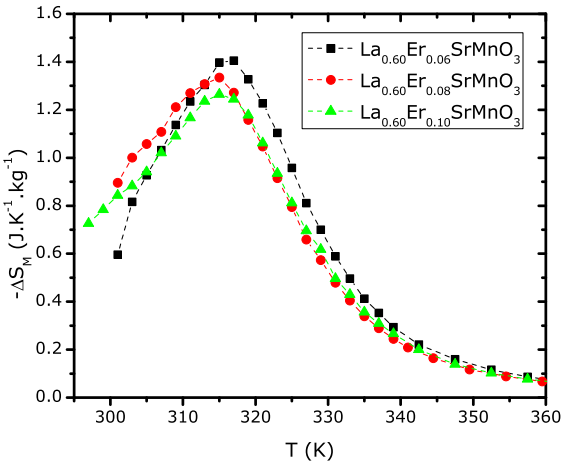

Figure 7.25: Dependence of the magnetic entropy change of $La_{0.70-x}Er_xSr_{0.30}MnO_3$ with temperature, for $x = 0.06$, 0.08 and 0.10, and maximum applied magnetic field change of 1 T.

phase separation phenomena of $La_{0.80-x}Er_xSr_{0.20}MnO_3$ [105]. Now, for this type of secondary phase formation to occur, the diffusion process of ions within the grain and then along the grain boundaries is a vital part of the process. Indeed, this is a dynamic process, occurring during the sintering step of the synthesis. It is possible (and to a certain extent very likely) that the sintering time used in this study is not enough to warrant the full diffusion process to occur, and so we do not obtain the material in its final thermodynamic equilibrium microstructure. So, the more Er that is over the solubility limit, the more atoms need to suffer diffusion processes in order to separate into the two phases. If the diffusion process is stopped midway, then more amount of the sample has Er content above the solubility limit, and consequently, lower T_C than the limit, explaining the asymmetry of the evolution of the entropy peak with Er content.

7.4 First-order magnetic phase transition manganites

7.4.1 $La_{0.665}Eu_{0.035}Ca_{0.33}MnO_3$

As an example of a first-order magnetic phase transition manganite system, we analyze the bulk magnetization properties of a polycrystalline sample of the $La_{0.665}Eu_{0.035}Ca_{0.33}MnO_3$ system. This particular system was chosen due to its convenient value of T_C ($\sim$ 220 K), permitting measurements in a wide range above and below the transition temperature. The low substitution amount of only 3.5% of Eu should correspond to a low amount of chemical/structural distribution.

Isothermal magnetization versus an applied magnetic field up to 10 T data was taken using the Cryogenics vibrating sample magnetometer at the University of Aveiro. To obtain a large density of $M(H,T)$ data, the temperature step was as low as 2 K, near T_C. Magnetization values at 5 K and 10 T give us a solid indication of the saturation value. Results are shown in Figure 7.26(a). The selected data has been corrected of demagnetizing field, as well as the remanent field of the superconducting coils.

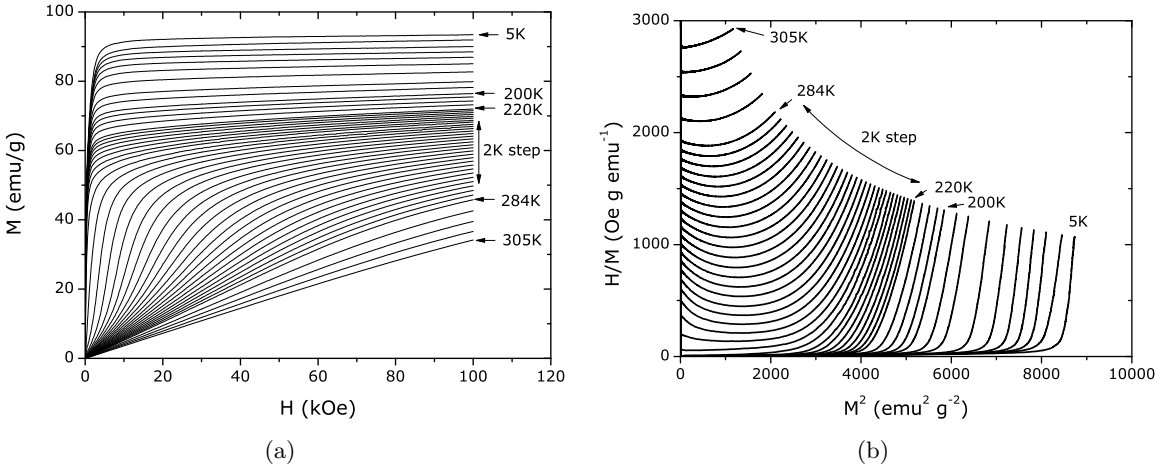

Figure 7.26: a) Experimental isothermal magnetization versus applied magnetic field data of a polycrystalline sample of $La_{0.665}Eu_{0.035}Ca_{0.33}MnO_3$ and b) corresponding Arrott plot.

The first-order nature of the transition is visible in the corresponding Arrott plots of Figure 7.26(b). The lack of true discontinuities in the magnetization data can be attributed to a small amount of chemical/structural distribution, as discussed in chapter 6.2. Since this is clearly a first-order transition (albeit of a disordered system), a critical phenomena analysis cannot be performed, and so the data is analyzed under a mean-field scenario.

The lack of discontinuities, together with the visible amount of chemical/structural distribution, gives us some security when applying the Maxwell relation to estimate magnetic entropy change. The magnetic entropy change as a function of temperature is shown in Figure

7.27(a).

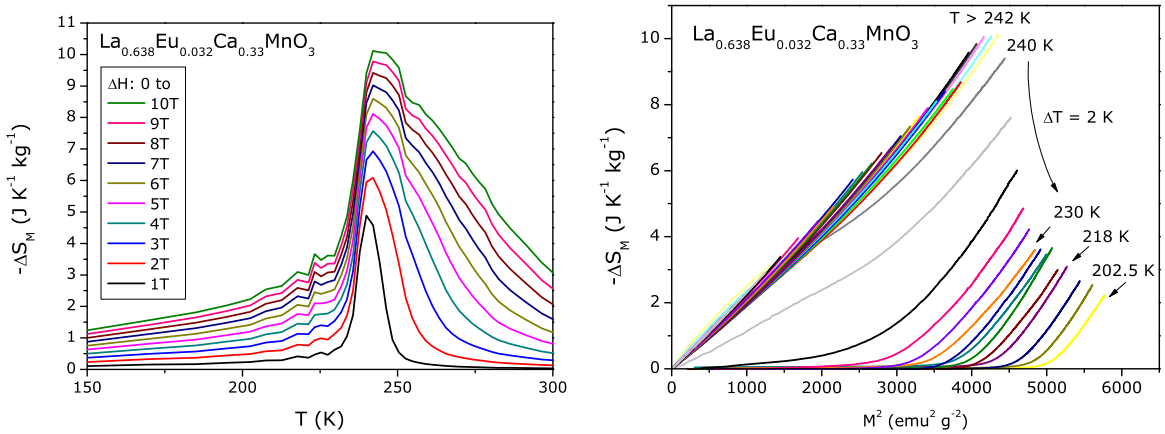

Figure 7.27: a) Magnetic entropy change versus temperature, calculated from the Maxwell relation and the magnetization data of $La_{0.665}Eu_{0.035}Ca_{0.33}MnO_3$ from Figure 7.26(a) and b) corresponding magnetic entropy change versus the square of magnetization.

We plot the dependence of the magnetic entropy change with the square of magnetization (Figure 7.27(b)). As discussed in section 2.2, a linear relation between these two quantities would indicate a behavior similar to a simplified Landau model. The curvature that appears for higher values of magnetization is be described by the mean-field model (section 2.3).

Aside from the expected deviations due to the existence of a small structural/chemical distribution, the $-\Delta S_M$ versus M^2 plot show an approximately linear behavior. In the paramagnetic phase, we can easily see if this relation is in accordance to the spin and number of ions of the system.

Figure 7.28(a) shows $-\Delta S_M$ versus M^2, for $T > T_C$. The colored lines show the result from simulations, considering various spin arrangements. Not taking into account the existence of spin clustering phenomena, one would expect that the magnetic properties of the system would be characterized by the mixed contribution of a ratio between 33% of spin 3/2 (Mn^{3+} ion) and 66% of spin 2 (Mn^{4+}) ion due to the mixed-valence composition. For these magnetization results, we see that such a scenario is not in agreement. A much more adequate description is achieved with $J \sim 5$ to 5.5, that is, if a magnetic cluster of 3 ions is considered, with combined spin value close to the total spin of the three ions, taking into consideration the mixed-valence ionic state.

Considering magnetic entropy values in the low magnetization region, the expected linear relation between magnetic entropy change and the square of magnetization is verified (Figure 7.28(b)). We can more carefully observe how the behavior is more closely matched by considering a three-ion clustering phenomena.

While this evidence is promising, it does not directly determine the cluster size, since the

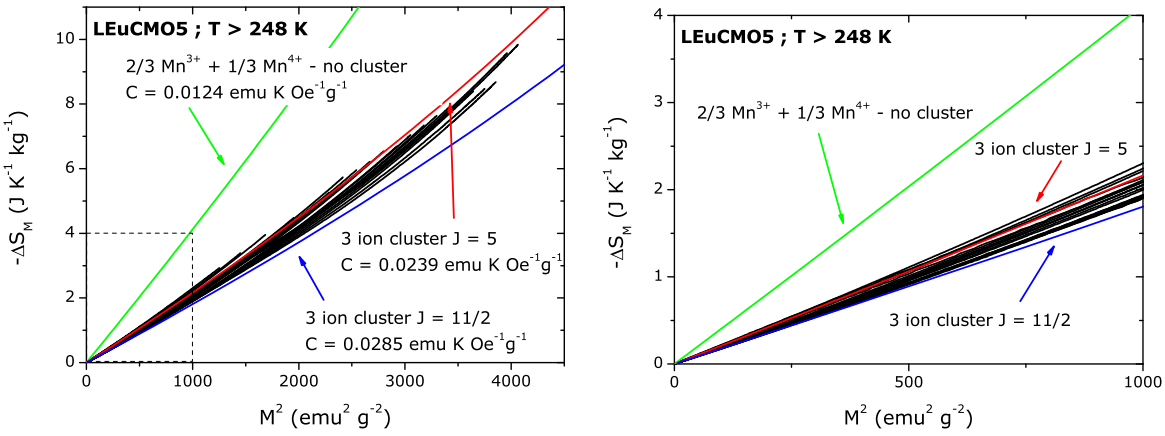

Figure 7.28: a) Magnetic entropy change versus the square of magnetization, calculated from the Maxwell relation and the magnetization data of $La_{0.665}Eu_{0.035}Ca_{0.33}MnO_3$ from Figure 7.26(a), for $T > T_C$. Colored lines correspond to mean-field simulations, and b) low magnetization detail.

important parameter in consideration is the Curie constant, which combines the spin value of the cluster and the number/density of clusters. Other clustering configurations that have Curie constants near the value of ~ 0.0250 emu K $Oe^{-1}g^{-1}$ would also adequately represent the experimental slope of the ΔS_M versus M^2 plots.

One way to have a more clear determination of cluster size would be from the mean-field scaling methods described in chapters 3 and 4. If the scaled magnetization data follows the Brillouin function, the spin value and also the number of spins would be directly determined. From the ΔS_M versus M^2 plots of Figure 7.28(a), the spontaneous magnetization is estimated (results are presented in Figure 2.7) and so all data for a given temperature value that is below the estimated spontaneous magnetization is removed from the data, in an effort to conservatively remove data from the magnetic domain region. From the total of $\sim$ 40.000 original data points, only $\sim$ 1.300 were removed by this approach. Figures 7.29(a) and 7.29(b) show the resulting goodness of scaling plots, from using the methodology described in chapter 4.

There is a clear region of λ_1, λ_3 parameters that correspond to the best mean-field scaling of experimental data. From the best λ_1, λ_3 values, we construct the scaling plot (Figure 7.30(a)). The scaled data is then fitted with a Brillouin function.

As is observed, both the scaling of magnetization data is very convincing, as well as the fit with the Brillouin function. The parameters obtained do indeed correspond to a three-ion cluster, with a total spin vale close to 5, and the number of clusters is very close to 1/3 of the total number of ions.

The low magnetization scaled data shown in Figure 7.30(b) show us the quality of the scaling at this scale. The Curie constant value obtained has the expected value of ~ 0.0243 emu

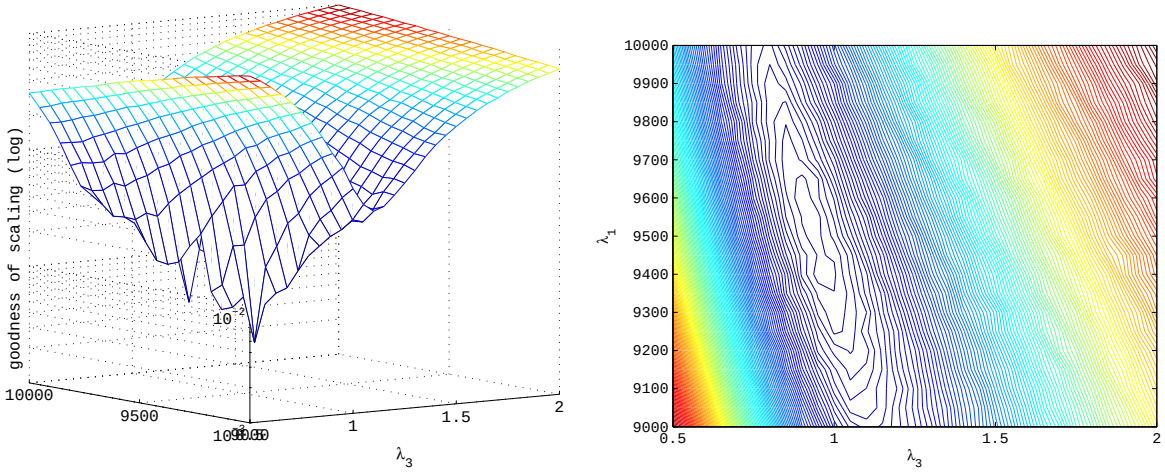

(a) (b)

Figure 7.29: a) mesh plot and b) contour plot results from the mean-field goodness of scaling analysis to magnetization data of $La_{0.665}Eu_{0.035}Ca_{0.33}MnO_3$.

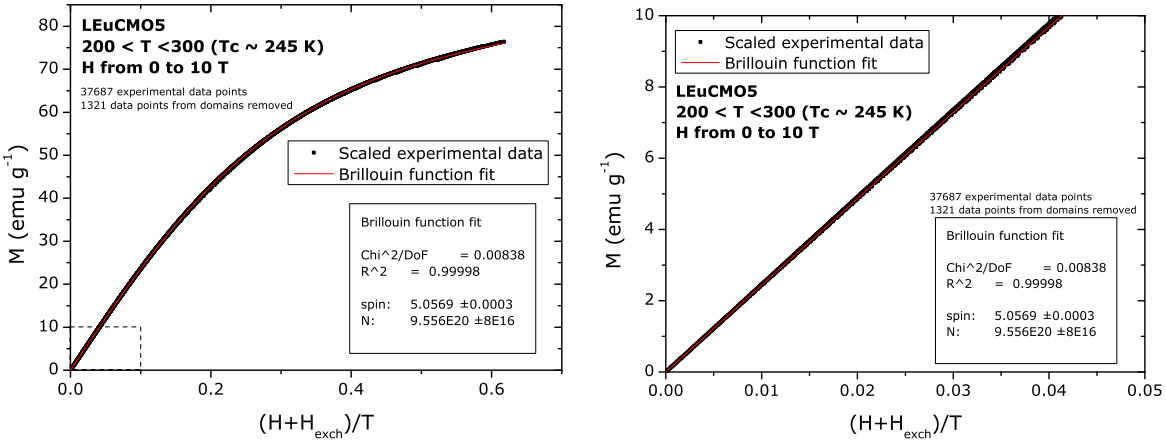

(a) (b)

Figure 7.30: a) Scaled magnetization data of $La_{0.665}Eu_{0.035}Ca_{0.33}MnO_3$, from the mean-field relation $M = (H + \lambda_1 M + \lambda_3 M^3)/T$. Solid line represents a fit with the Brillouin function. b) low magnetization detail.

K $Oe^{-1}g^{-1}$. With the mean-field exchange parameters obtained from the scaling approach, and the J and N parameters from the Brillouin fit, we can simulate a mean-field system, which has a saturation magnetization 89.7 emu g^{-1}, and the η parameters is > 1, indicating a first-order magnetovolume-induced first-order transition. The experimentally measured saturation magnetization of this system, estimated from data up to an applied field of 5 T at 5K (shown in Figure 7.26(a)) was of 92.5 emu g^{-1}, quite close to the modeled system.

Figure 7.31 shows the isothermal M versus H dependence at the experimentally measured

temperature values, compared to the experimental measurements.

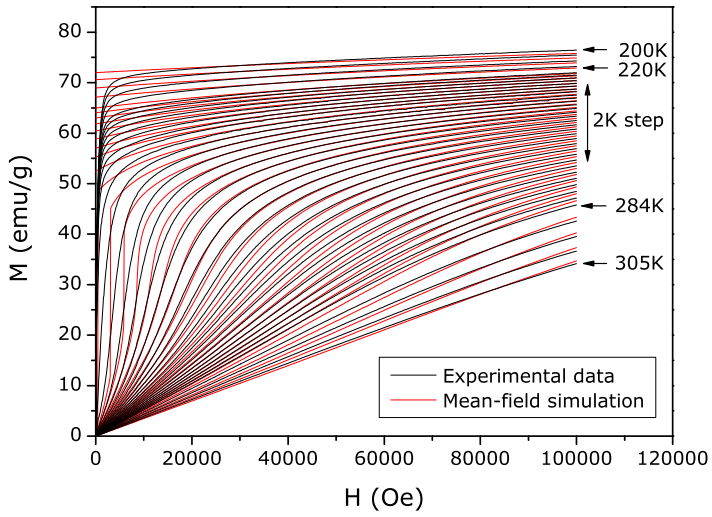

Figure 7.31: Isothermal M versus H dependence of $La_{0.665}Eu_{0.035}Ca_{0.33}MnO_3$, above and below T_C (black lines), and mean-field simulation with parameters taken from the goodness of scaling method and Brillouin function fit to the scaled data (red lines).

Apart from the above-mentioned existence of chemical/structural distribution, this mean-field analysis has led to a good description of the bulk magnetization properties of this first-order phase transition manganite.

The analysis of the magnetic entropy properties of both the second-order La-Sr-Mn-O and the first-order La-Ca-Mn-O ferromagnetic manganites, together with the scaling approaches, has given us ample evidence that the well-know short range interaction that has been reported for temperatures above T_C in manganites, is also present below T_C. In a way, it appears that the cluster size is frozen when the transition occurs, and is stable for a wide temperature range below T_C.

While the cluster state dynamics in ferromagnetic manganites have been widely studied and interpreted, further understanding the colossal magnetoresistance effect in this family of materials [106, 107, 108], these studies have been has mostly been limited to the paramagnetic phase. This has clearly shown to be a region of interest for these studies, revealing a Griffith's phase [109] presence in CMR manganites [110, 111]. Still, the usual methods for analyzing the cluster formation are only applicable in the paramagnetic phase (linear fittings of the Curie-Weis in the paramagnetic phase, and electron paramagnetic resonance). Only in a very recent work by Petit *et al.* [112], spin wave measurements were used to study the metallic (ferromagnetic) state of manganites, showing experimental evidence for clustered states. By combining mean-field simulations and analyzing the magnetocaloric properties of manganites, we have shown that it is possible to interpret the magnetization data in the ferromagnetic state and find evidence of the clustered states, and also quantify the number of ions per

cluster in a wide temperature range. The fact that our analyses are based on interpreting magnetic data obtained in standard isothermal magnetization versus applied magnetic field measurements will hopefully open the way to a more widespread study of the magnetic cluster states in the ferromagnetic state of manganites and also other materials.

7.4.2 Disorder effects in chemically substituted La-Ca manganites

As was shown in section 6.2 with mean-field simulations of disordered ferromagnetic systems, the effects of chemical/structural disorder are more dramatic in a first-order phase transition system, compared to a similar second-order phase transition system. In terms of magnetocaloric properties, the magnetic entropy change curves show that the discontinuity of a 'pure' system is lost with even a minimal distribution of T_C, and that for sufficiently wide distributions, the $\Delta S_M(T)$ mimics the distribution. In order to experimentally confirm these effects, a first-order phase transition system with considerable tolerance to chemical substitution would be the ideal case to study. Manganites were again the subject of studies of disordered ferromagnets (as previously shown for $La_{0.70-x}Eu_xSr_{0.30}MnO_3$ and $La_{0.70-x}$-$Er_xSr_{0.30}MnO_3$), but now the first-order $La_{0.70}Ca_{0.30}MnO_3$ system is chosen as the parent compound.

As reported by de Teresa *et al.* [113, 114], chemical substitution in the La-Ca-Mn-O system has been shown to induce a loss of long-range magnetic order in the $(Tb\text{-}La)_{2/3}Ca_{1/3}MnO_3$, $(Y\text{-}La)_{0.70}Ca_{0.30}MnO_3$ and $(Pr\text{-}La)_{0.70}Ca_{0.30}MnO_3$ systems, inducing a spin-glass state. Figure 7.32 shows the phase diagram of the Terbium-substituted system, from Ref. [114].

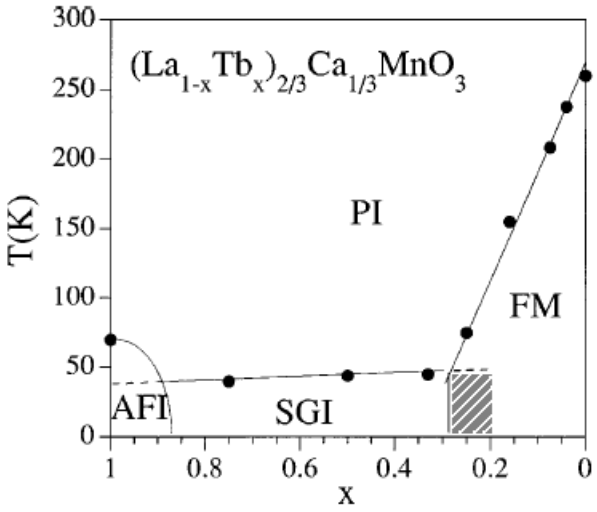

Figure 7.32: Magnetic and electrical phase diagram of the series $(La_{1-x}Tb_x)_{2/3}Ca_{1/3}MnO_3$. FM stands for 'ferromagnetic metallic' state, PI for 'paramagnetic insulator', SGI for 'spin-glass insulator', and AFI for 'antiferromagnetic insulator', from Ref. [114].

And so, while the parent compound $La_{0.70}Ca_{0.30}MnO_3$ is structurally more tolerable to

chemical substitution of La with a smaller ionic radius rare-earth, compared to the previously studied $La_{0.70}Sr_{0.30}MnO_3$, its magnetic properties will present a dramatic change for higher substitutions and consequently lower T_C values. Consequently, in order to study the effects of chemical substitution on the magnetocaloric properties of the La-Ca-Mn-O system, the amount of chemical substitution should not be enough to break the long-range magnetic ordering.

We have analyzed three first-order chemically-substituted $La_{0.70}Ca_{0.30}MnO_3$ samples: a single crystal of pure phase, prepared by the group of Prof. Y. Tokura, Tokyo, a La-Eu substituted sample, and a La-Y substituted sample. A 14% La-Er substituted sample was also synthesized, but the magnetic behavior was already that of a spin-glass material [Ama05], and so was not considered for this study.

We expect the La-Y-Ca system to be the most disordered, since it has the higher degree of substitution (7%) and also ionic size mismatch is larger than compared to Eu. Consequently the T_C value will be lower than the 3.5% Eu substituted sample. This reasoning is confirmed by examining the magnetocaloric properties, as shown in Figure 7.33.

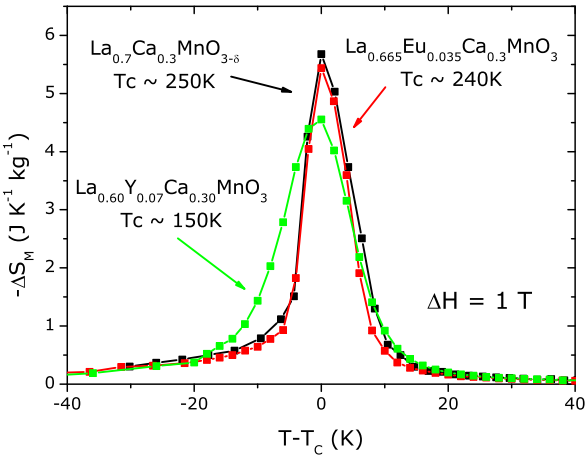

Figure 7.33: Dependence of the magnetic entropy change of various samples of the La-Ca-Mn-O system with temperature, at a maximum applied magnetic field change of 1 T.

By comparing the magnetic entropy plots, we can confirm that the Y-substituted sample is the most disordered one, compared to the single crystal and the Eu-substituted sample. While T_C values are considerably different, the magnetocaloric peak shape shows that the lower maximum entropy value, together with the smoother, more symmetrical curve are solid indications of disorder in a first-order phase transition material, as shown previously in Figure 6.16. The single crystal sample is shown to be the most chemically/structurally pure sample of the set, with the least symmetric magnetic entropy curve. For both the single crystal and Eu-substituted sample, the FWHM of the distribution should be comparable to the experimental temperature step size of magnetization measurements (2 K), while for

the Y substituted sample, the FWHM should be considerable larger ($>$ 10 K). In section 7.4.1, the magnetization dependence on field and temperature of $La_{0.665}Eu_{0.035}Ca_{0.33}MnO_3$ was analyzed using the mean-field 'goodness of scaling method'. The resulting mean-field parameters were then used for $M(H,T)$ simulations, as shown in Figure 7.31. Since the scaling method does not consider disorder effects, and the simulation also did not consider any distribution of the coupling parameters, the simulated data of Figure 7.31 is the 'pure' mean-field system that best reproduces the experimental data of $La_{0.665}Eu_{0.035}Ca_{0.33}MnO_3$.

To attempt to better describe the magnetic properties of the $La_{0.665}Eu_{0.035}Ca_{0.33}MnO_3$ manganite, particulary in the irreversibility region, we introduce a distribution to the mean-field coupling parameter λ_1. The width of the distribution should then be comparable to the experimental temperature step, as argued previously. Simulations where made with distributions with FWHM of 2, 3, 4 and 5 K. The most agreeable result was obtained for a FWHM of 4 K. Figure 7.34(a) shows the results of the simulations, compared to the experimental data, and Figure 7.34(b) the corresponding magnetic entropy change curves.

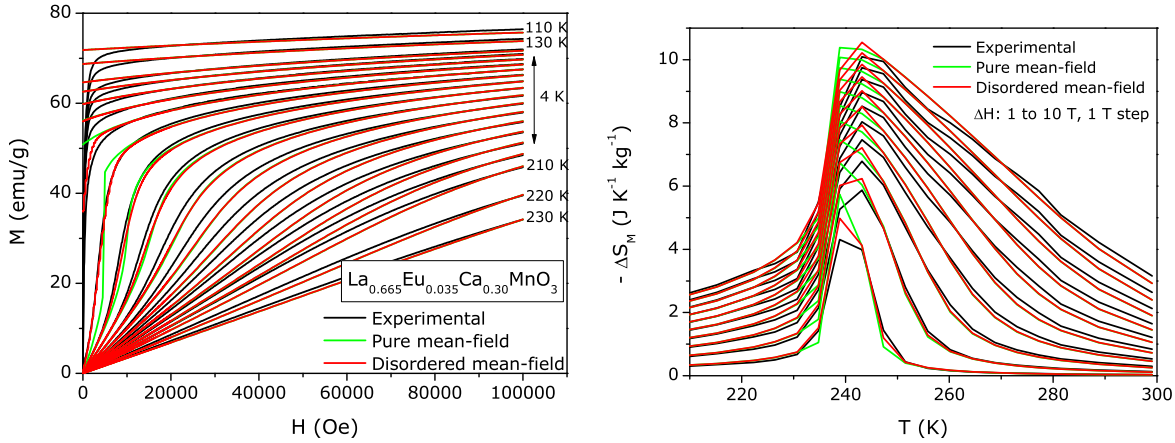

(a) (b)

Figure 7.34: a) Isothermal M versus H data of $La_{0.665}Eu_{0.035}Ca_{0.33}MnO_3$ (black lines) and mean-field simulations of a pure (green lines) and a 4 K FWHM T_C distributed (red lines) system. b) Corresponding magnetic entropy change curves.

Compared to the simulations of the pure system, as shown in Figure 7.31, we are now able to better describe the magnetic behavior of the material, by considering disorder. Consequently, the simulated magnetic entropy change plots more closely resemble the experimental results, in contrast to the a 'pure' system.

Analyzing the La-Y-Ca system becomes considerably more complicated, since the higher disorder of the system makes the mean-field 'goodness of scaling' approach less rigorous, as the scaling function does not consider disorder. Still, somewhat agreeable results were obtained, by considering a T_C distribution of 15 K FWHM, as shown in Figure 7.35. The magnetic

entropy change behavior (Figure 7.35(b)), particularly in the low-field region, is much better described by the disordered system than the pure system. Since this is a more disordered system than the La-Eu-Ca sample, the low field magnetocaloric effect is consequently more affected, and so to adequately simulate the magnetocaloric properties of this system using mean-field theory, disorder needs to be considered.

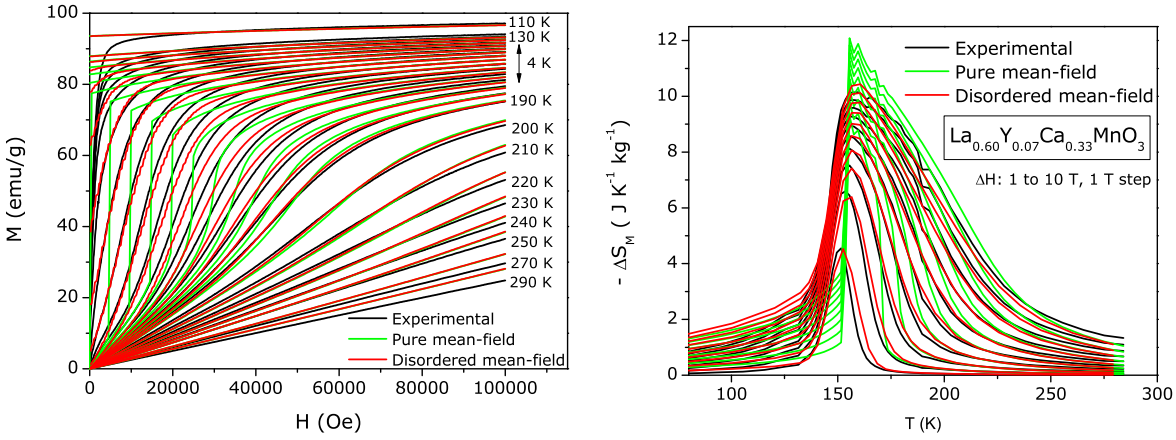

(a) (b)

Figure 7.35: a) Isothermal M versus H data of $La_{0.60}Y_{0.07}Ca_{0.33}MnO_3$ (black lines) and mean-field simulations of a pure (green lines) and a 15 K FWHM T_C distributed (red lines) system. b) Corresponding magnetic entropy change curves.

By combining the mean-field scaling method presented in chapter 4, and considering disorder effects as a Gaussian distribution of T_C, the magnetic and magnetocaloric properties of two first-order phase transition manganites were described. By estimating the low-field magnetic entropy change from experimental magnetization data, a good initial estimative of the width of T_C disorder for each material was made. This initial estimative proved to be in good agreement with the following simulations. It is important to point out that in the previous examples, the T_C distribution widths were 1.7 % of T_C for $La_{0.665}Eu_{0.035}Ca_{0.33}MnO_3$, and 10 % of T_C for $La_{0.60}Y_{0.07}Ca_{0.33}MnO_3$. Particularly for the La-Eu-Ca sample, evaluating such a comparatively small degree of disorder would certainly stress the limits of detection by normal structural studies. A possible way to quantify these disorder effects would be to make a statistically relevant number of measurements of local magnetization loops of the material. If the material is disordered, there is a distribution of critical fields for a given temperature values (a direct consequence of the T_C distribution). This could in principle be analyzed to quantitatively obtain the disorder width.

7.5 Polycrystalline MnAs and related systems

A polycrystalline sample of the MnAs system was kindly provided by Sérgio Gama, and magnetic measurements performed with the Cryogenics VSM system at the University of Aveiro by Soma Das. Isothermal bulk magnetization versus applied field curves were measured, at temperatures near T_C (Figure 7.36(a)).

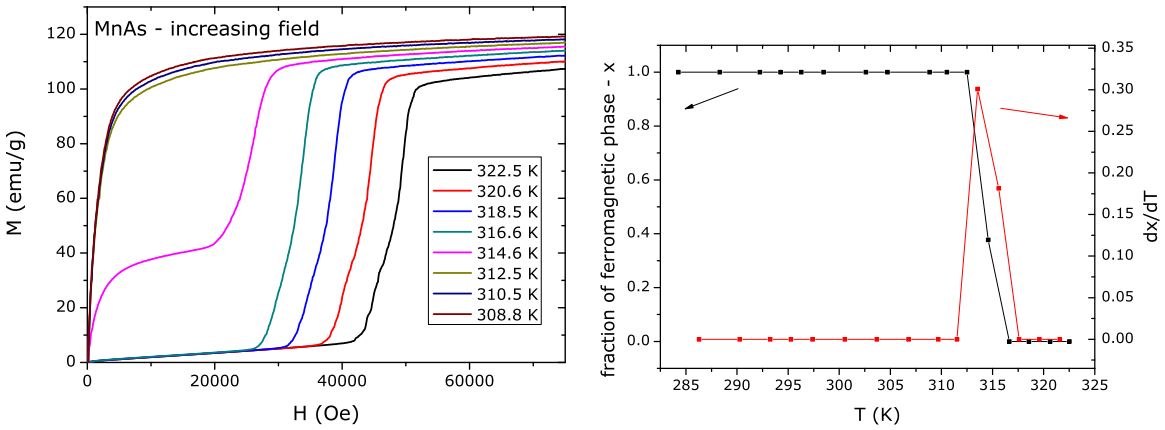

(a) (b)

Figure 7.36: a) M versus H plot of polycrystalline sample of MnAs, for increasing field. b) fraction of phases (x) as a function of temperature, and its temperature derivative.

Figure 7.36(a) shows us the mixed-phase behaviour of this system, as the magnetization isotherm at 314.8 K has the typical horizontal plateau shape. From the M versus H data, the phase fraction values can be estimated, and at $T = 314.8$ K, the value of x (fraction of ferromagnetic phase) is estimated to be $\sim 38\%$, while for $T < 314$, $x = 1$ and for $T > 314$, $x = 0$. Figure 7.36(b) shows the calculated temperature derivative of x, with two points where $\partial x/\partial T \neq 0$.

Estimating magnetic entropy change directly from the Maxwell relation integration (Eq. 1.10), we plot ΔS_M versus $\partial x/\partial T$, as shown in Figure 7.37(a).

The higher values of entropy change correspond to the temperature where $\partial x/\partial T \neq 0$, and so the main reason behind these high values is the mixed-phase conditions. As shown in Section 5.2, we remove the $\partial x/\partial T$ contribution to the entropy change calculations, by extrapolating the ΔS_M values to a null $\partial x/\partial T$. The result from this approach is presented in Figure 7.37(b). Indeed, the 'peak' effect is removed, and the resulting entropy change curve has the typical shape of a first-order transition.

7.5.1 Chemical substitution effects in $Mn_{1-x-y}Cu_xCr_yAs$

In order to have a more detailed study of the use of this method to estimate magnetic entropy change in mixed-state systems, the doped $Mn_{1-x-y}Cu_xCr_yAs$ system was analyzed. The

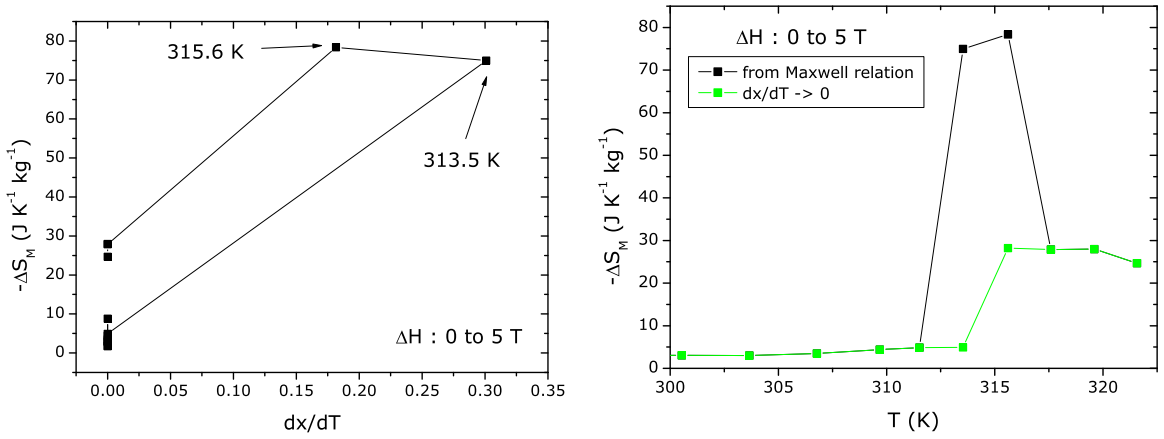

(a) (b)

Figure 7.37: a) Magnetic entropy change versus the temperature derivative of the phase fraction x. b) Magnetic entropy change versus temperature, for an applied field change from 0 to 5 T, calculated directly from the Maxwell relation (black line/dots) and without the $\partial x/\partial T$ contribution (green line/dots).

chosen compositions were $Mn_{0.99}Cu_{0.005}Cr_{0.005}As$, $Mn_{0.98}Cu_{0.01}Cr_{0.01}As$ and $Mn_{0.98}Cu_{0.015}$-$Cr_{0.005}As$. Samples were prepared by Daniel Rocco, following the procedure described in Ref. [31]. Isothermal magnetization measurements in the Aveiro Cryogenics VSM system were performed by Soma Das. In this work, the aim of chemical substitution is to control the mixed-phase dynamics of the system, hopefully making the mixed-phase temperature region larger than in the 'pure' MnAs sample. Results from this work have been recently submitted for publication [DAA09]. Figure 7.38(a) shows the isothermal magnetization data of the $Mn_{0.99}Cu_{0.005}Cr_{0.005}As$ sample, and Figure 7.38(b) the corresponding estimation of the fraction of ferromagnetic phase as a function of temperature, $x(T)$.

As can be seen from Figure 7.38(a), the introduction of Cu/Cr has made the mixed-phase behavior spread in a wider temperature region, compared to the data of the 'pure' MnAs sample (Figure 7.36(a)). The estimation of $x(T)$ for the remaining samples (Figure 7.38(b)) shows how the mixed-phase interval can be even wider.

Figure 7.39(a) shows the $\partial x/\partial T$ versus T plots corresponding to the $x(T)$ data of Figure 7.38(b) and Figure 7.39(b) the $-\Delta S_M$ versus $\partial x/\partial T$ plots.

The temperature derivative of the phase fraction shows how the distribution is approximately symmetric. The plots of entropy change versus $\partial x/\partial T$ have the characteristic shape, as shown in the simulations of chapter 5 (Figure 5.14). As can be seen, the maximum entropy change is reached for the sample with the sharpest (in temperature) mixed-phase distribution. Figure shows the correction to magnetic entropy change for lower field change values of 1, 2 and 3 T.

From the study of the $Mn_{1-x-y}Cu_xCr_yAs$ system, it was shown how the dynamics of a

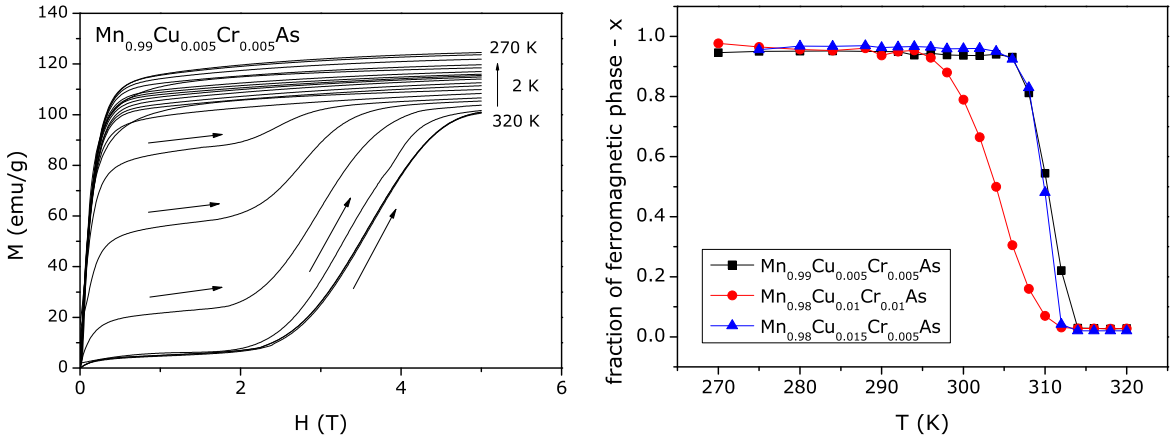

(a) (b)

Figure 7.38: a) Isothermal magnetization of $Mn_{0.99}Cu_{0.005}Cr_{0.005}As$, for increasing magnetic field and b) corresponding estimation of the fraction of ferromagnetic phase as a function of temperature, $x(T)$.

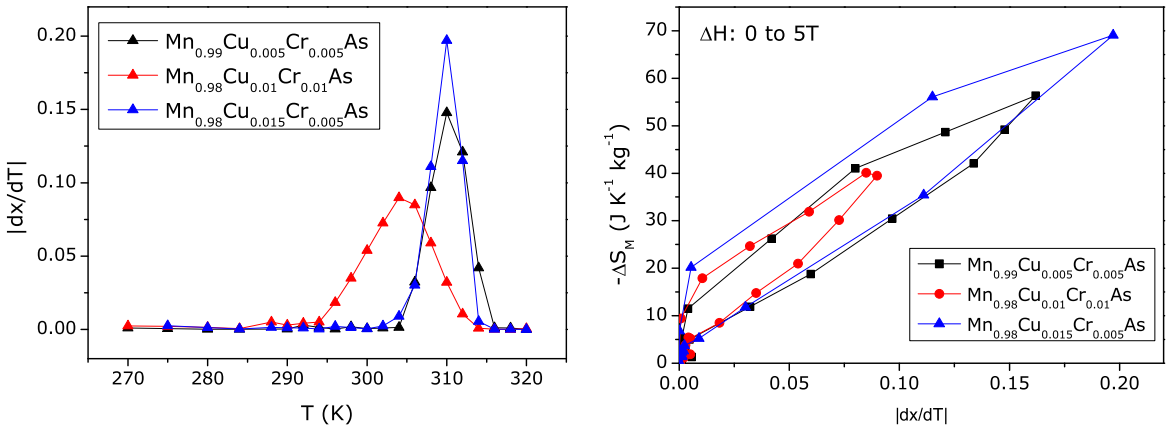

(a) (b)

Figure 7.39: a) Temperature derivative of the ferromagnetic fraction of the $Mn_{1-x-y}Cu_xCr_yAs$ system, and b) corresponding $-\Delta S_M$ versus $\partial x/\partial T$ plots, for a magnetic field change from 0 to 5 T.

mixed-phase transition can be controlled by chemical substitution, and how the corrections to the magnetic entropy change estimations from using the Maxwell relation can be used in a series of samples with different mixed-phase dynamics.

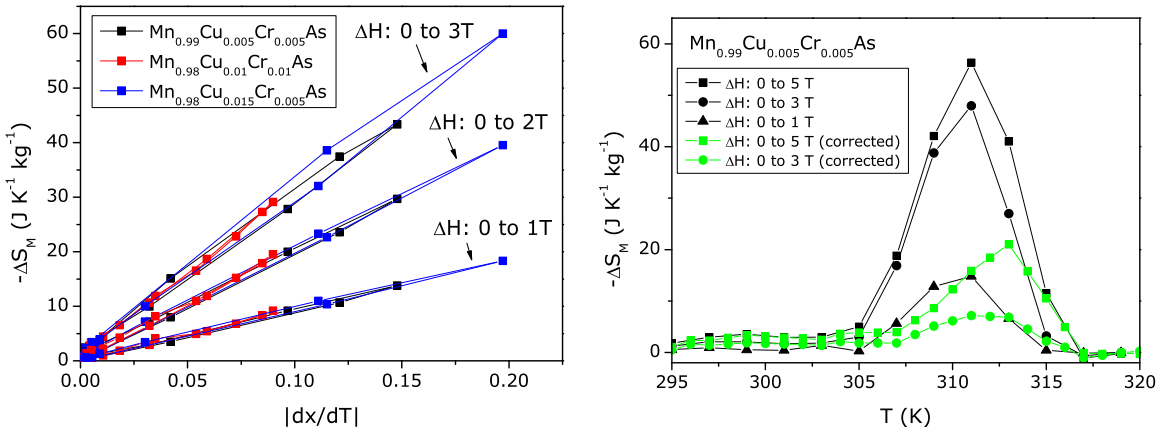

Figure 7.40: a) $-\Delta S_M$ versus $\partial x/\partial T$ plots of the $Mn_{1-x-y}Cu_xCr_yAs$ system, for a magnetic field change from 0 to 1, 2 and 3 T; b) Entropy change from the direct use of the Maxwell relation (black points and lines) and corrected results (green points and lines).

7.6 Pressure effects in giant magnetocaloric $LaFe_{11.5}Si_{1.5}$

The intermetallic $La(Fe,Si)_{13}$ is an interesting magnetic system, since it presents a first-order magnetostructural transition [18, 19], where there occurs a discontinuous lattice parameter change, but no associated change in symmetry. In terms of studying the magnetic properties of this family of materials, the Bean-Rodbell model is applied. We interpret the isothermal experimental bulk magnetization data of $LaFe_{11.5}Si_{1.5}$ of Jia and co-workers [115], where the authors have made measurements under several pressure values. Figure 7.41 shows M versus H plots of $LaFe_{11.5}Si_{1.5}$ at ambient pressure and at an applied pressure of 0.8 GPa.

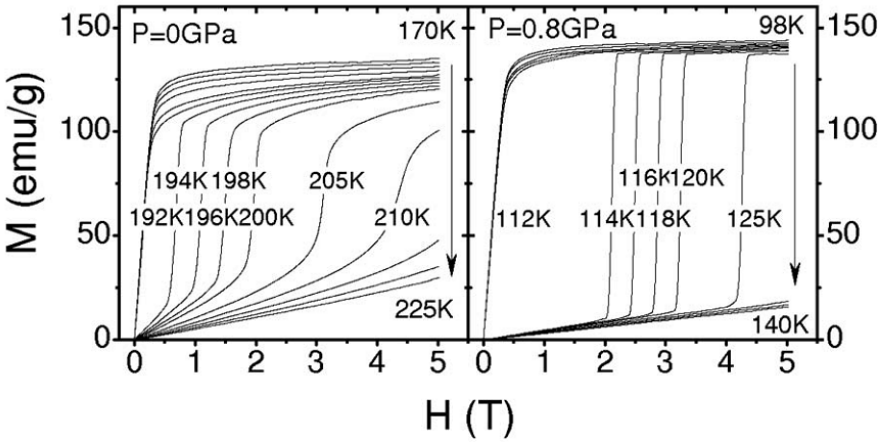

Figure 7.41: Isothermal magnetization values of $LaFe_{11.5}Si_{1.5}$, up to 5 T and at ambient pressure (left) and 0.8 GPa of external pressure (right), from Ref. [115].

The sharp field-induced jumps in magnetization indicate that the system is quite pure, with a negligible chemical/structural distribution, which will simplify the interpretation of data. The authors proceeded to estimate the magnetic entropy change by using the Maxwell relation, obtaining high values of magnetic entropy change, as shown in Figure 7.42.

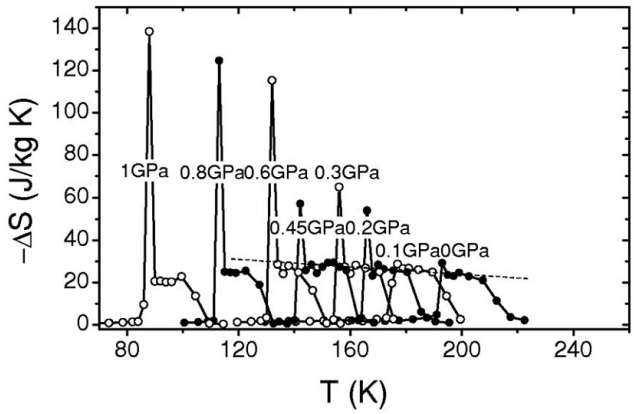

Figure 7.42: Estimative of magnetic entropy change from the use of the Maxwell relation and magnetization data, of $LaFe_{11.5}Si_{1.5}$, up to 5 T and at various values of applied pressure, adapted from Ref. [115].

The combination of results from Figures 7.41 and 7.42, as well as some previous knowledge of the system, give us a lot of experimental information in order to interpret of this data by a molecular mean-field model. The purpose is to assess if by considering hysteresis effects within the Bean-Rodbell an adequate description of the magnetization curves (data taken only from literature), and consequently the magnetic entropy change curves can be obtained, without performing any data fitting procedures.

The magnetization values at ambient pressure indicate a critical field at around 4 T, a critical temperature value between 205 K and 210 K. Saturation magnetization values [115] indicate a value of J $\sim$ 1.1, and the corresponding number of magnetic ions per gram is then 8.41×10^{21}. By establishing the J and N parameters, only two remain: λ_1 and λ_3. Magnetization data at 0 Gpa (Figure 7.41) give us these parameters, from the critical field value and the critical temperature, corresponding to a $\lambda_1 \sim 1.35 \times 10^4$ (Oe g emu^{-1}) and $\lambda_3 \sim 0.4$ (Oe g emu^{-1})^3. These give immediately give us an η value of 1.9, and a T_0 of $\sim$ 190 K. Calculating magnetization values from the mean-field model using these parameters then results in a first-order phase transition, and we calculate the M versus H dependence up to 5 T (0.01 T step), at the temperature values of Figure 7.41.

The resulting M versus T dependence is shown in Figure 7.43.

When simulating the same system, now for an applied pressure of 0.8 GPa, our approach is only to change the λ_1 parameter, changing T_0. The reasoning behind this approach is thus: by applying an external pressure, the magnetic interaction will change, inducing a change

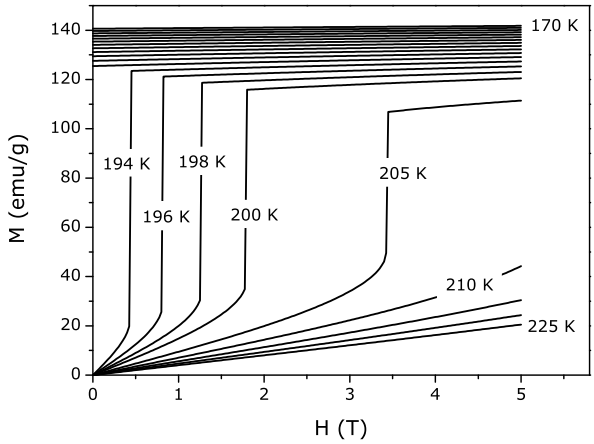

Figure 7.43: Simulated M versus H curves using the Bean-Rodbell model and parameters from experimental results of $LaFe_{11.5}Si_{1.5}$ (Figure 7.41).

on T_C (λ_1), but since there is no structural change, there should not a be a change on the dependence of T_C on volume (λ_3) due to a change in volume itself. This sets the λ_3 value as the same, independent on external pressure, and removes one free parameter change, and so only λ_1 is changed, from $\sim 1.35 \times 10^4$ (Oe g emu^{-1}) to $\sim 7.4 \times 10^3$ (Oe g emu^{-1}). This results in an η value of ~ 3.5 and a T_0 value of ~ 104 K. The corresponding M versus H simulations are shown in Figure 7.44.

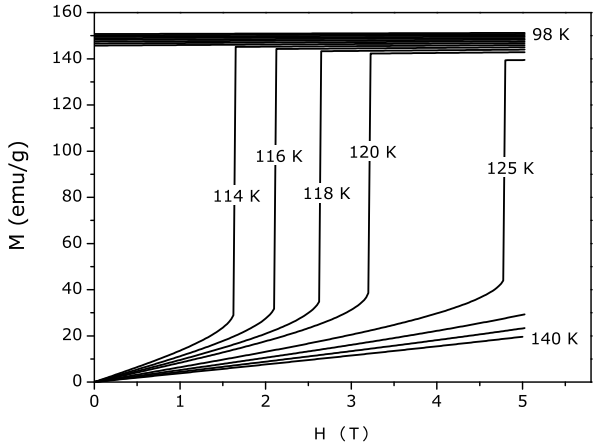

Figure 7.44: Simulated M versus H curves using the Bean-Rodbell model and parameters from experimental results of $LaFe_{11.5}Si_{1.5}$, for an applied external pressure of 0.8 GPa (Figure 7.41).

By only changing one parameter from the 0 GPa simulations to the 0.8 GPa simulations, we obtain very satisfying description of experimental results. We can assess how these simulated results also result on the magnetocaloric 'peak' effect, by using now the Maxwell relation integration to estimate magnetic entropy change, and compare it to the results of the authors

(Figure 7.42). This is shown in Figure 7.45.

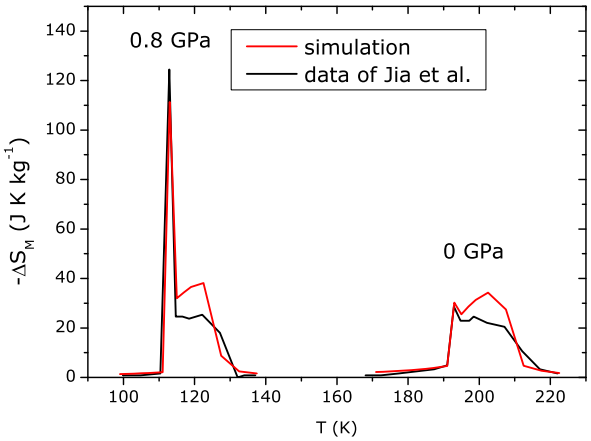

Figure 7.45: Result from applying the Maxwell relation to estimate ΔS_M on simulated and experimental magnetization data of $LaFe_{11.5}Si_{1.5}$.

Now this 'peak effect' was obtained by using non-equilibrium solutions. Since there is a good agreement between the experimental results and the theoretical simulations of the M versus H curves, consequently the results from the use of the Maxwell relation to estimate magnetic entropy change are also in agreement. We can now estimate the magnetic entropy change of this process, within the mean-field model, and compare it with the previous results, as shown in Figure 7.46.

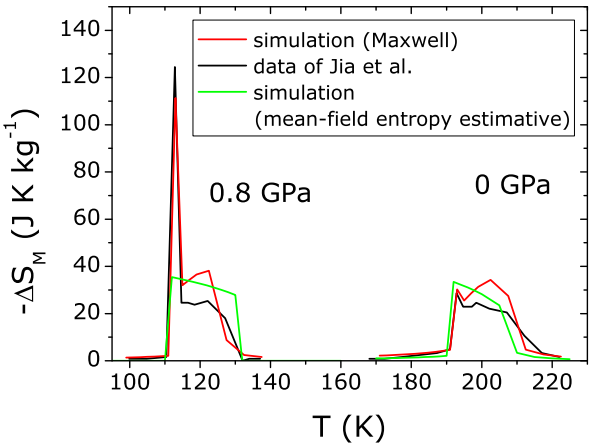

Figure 7.46: Result from applying the Maxwell relation to estimate ΔS_M on simulated (red lines) and experimental (black lines) magnetization data of $LaFe_{11.5}Si_{1.5}$, and from the mean-field model (green lines).

The simulated results of Figure 7.46 were obtained from estimating the magnetic entropy change of a process with the experimentally observed transition temperatures, but always respecting the sum rule, which limits the amount of free energy change (magnetic work) that

occurs in the process.

This analysis of pressure effects in the magnetic/magnetocaloric properties of the La-Fe-Si system has allowed us to verify that from easily obtained parameters such as: magnetic ion density and spin value (obtained from saturation magnetization and the compound chemical formula), and the mean-field exchange parameters (from the critical field and temperature of a magnetization curves), it was possible to describe the magnetic properties of the system. The first-order nature of the transition, together with the 'blind' use of the Maxwell relation produces the magnetocaloric 'peak' effect. From the mean-field analysis, it is possible to recreate this non-physical result, but also (and more importantly), correct it.

7.7 $Gd_5Si_2Ge_2$ single crystal

The $Gd_5Si_2Ge_2$ system is one of the most studied first-order giant magnetocaloric materials. While the 'boom' in the studies of the R-Si-Ge family of materials was due to the work of Pecharsky and Gschneidner in 1997, [8], the first report on this family of materials was presented by Holtzberg and co-workers in 1967 [116]. Figure 7.47 shows the phase diagram of the parent $Gd_5(Si_xGe_{1-x})_4$ compound.

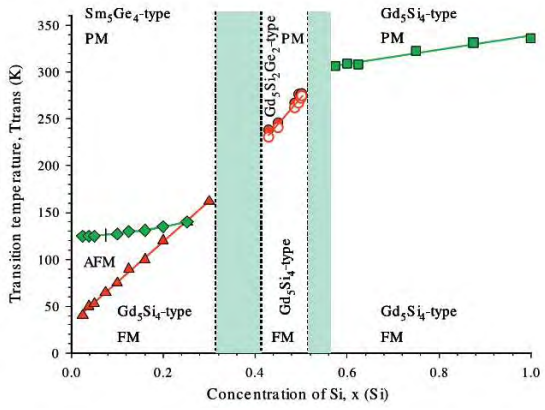

Figure 7.47: The structural and magnetic phase diagram of $Gd_5(Si_xGe_{1-x})_4$, from Ref. [25].

For compositions with Silicon content around 2, a fully-coupled magnetostructural transition occurs close to room temperature, from the ferromagnetic orthorhombic Gd_5Si_4 structure to the paramagnetic monoclinic $Gd_5Si_2Ge_2$ structure. Figure 7.48 shows both crystal structures. The transition from the ferromagnetic orthorhombic structure to the paramagnaetic monoclinic structure involves the opposing movement of 'slabs' and Ge-Si bond-breaking.

There have been numerous attempts to theoretically interpret the magnetocaloric properties of the $Gd_5Si_2Ge_2$ alloy. Using the Bean-Rodbell model [118] and Monte-Carlo simulations [119], an apparently successful description of the magnetocaloric properties of the material was presented. Still, no successful attempt to describe the *magnetic* properties of the mate-

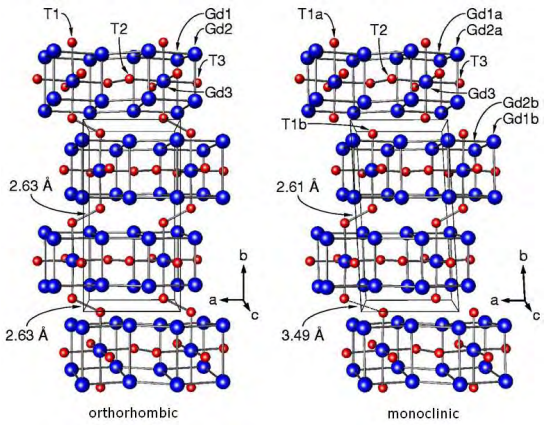

Figure 7.48: The crystal structures of the Gd_5Si_4-type orthorhombic (left) and $Gd_5Si_2Ge_2$-type monoclinic (right) phases of $Gd_5Si_2Ge_2$, adapted from Ref. [117].

rial has been presented. As it has been shown previously in this thesis, the magnetocaloric properties directly result from the magnetic properties, and so only by fully describing the magnetization dependence on field and temperature can it be said that the magnetocaloric properties are being adequately studied. In short, a magnetocaloric curve for a first-order system that seems to adequately describe experimental results for a given ΔH value can easily be generated, but such a result does not unequivocally imply that the magnetic behavior has been adequately interpreted.

We present here a description of the magnetic properties of this complex system, by using the magnetic data analysis tools presented in this thesis. As we will see, the fact that there occurs a structural change in this magnetostructural phase transition, in contrast to the simpler case of a change in lattice parameters in the La-Fe-Si system, will bring an added degree of complexity to the analysis. We begin by reviewing work published on the properties of this system.

While most of the recent works published on the study of the Gd-Si-Ge family of materials naturally focus on a study of the magnetocaloric properties it is interesting to note how the 1967 work of Holtzberg reported on the high saturation magnetization values of the Gd_5Si_4 material, which was higher than the $J = 7/2$ of the isolated Gd ion. The justification would be a spin contribution from the conduction electrons. This point was later discussed in detail thirty years later by Haskel *et al.* in 2007 [120], who by X-ray magnetic circular dichroism measurements observed and by density functional theory justified the spin-dependent hybridization between Ge 4p and Gd 5d conduction states, which is strong below but weakens above the Ge(Si) bond-breaking transition.

The sliding of the interslabs in opposite directions at the structural change is behind the unusually large magnetoresistance, magnetostriction and magnetocaloric effects of this material [121]. A more detailed analysis of the orbital hybridization of the Gd ions in this

material was presented by Paudyal *et al.* [117]. By using density functional theory and the LSDA+U approximation, the hybridization of the Gd s, p and d orbitals lead to a net average magnetic moment of 3.8 in the orthorhombic structure and a slightly lower value of 3.65 in the monoclinic structure. The calculated ordering temperature for both structures was determined as $\sim$ 300 K in the orthorhombic structure, and $\sim$ 220 K in the monoclinic structure.

Our magnetization measurements were performed on a $Gd_5Si_2Ge_2$ single crystal, synthesised at Ames labs by the group of Gschneidner and Pecharsky, kindly provided to us by the group of Morellon and Algarabel (Zaragoza University). Having a high-quality sample was important, since it would allow us to minimize the effects of disorder, in what is already a complex system in a pure form.

Magnetization measurements were made at the VSM system at the University of Aveiro, up to 10 T of applied magnetic field. Figure 7.49 shows the isothermal M versus H near the irreversibility region.

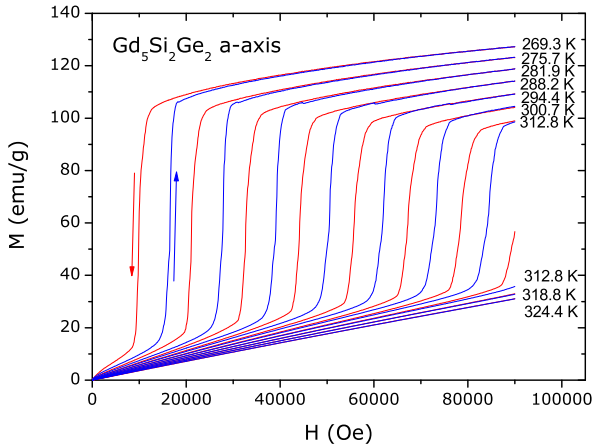

Figure 7.49: Isothermal M versus H dependence of $Gd_5Si_2Ge_2$, up to an applied field of 10T, corrected of the demagnetizing factor and remanent field.

The first attempt to interpret these magnetization results was to simulate a similar M versus H dependence within the Bean-Rodbell model, as presented in Figure 7.50. The experimentally observed critical fields are well defined, and so molecular mean-field simulations were made using the dependence of critical fields on temperature, $H_C(T)$, as control. And so the mean-field parameters such as spin, number of ions and the exchange parameters λ_1 and λ_3 were initially chosen so that the equilibrium simulated results would have a similar $H_C(T)$ dependence to the experimental measurements. While this is an empirical approach, it is important to assess if such a simplified approach presents adequate results.

A large number of M versus H curves, resulting from a wide range of parameters (spin values from 3.5 to 6.5, λ_1 from 1200 to 6500 Oe g emu^{-1}, and λ_3 from 0.03 to 0.4 Oe g^3

emu^{-3}) were calculated. The best $H_c(T)$ dependence was obtained with a spin value of 6.5, $\lambda_1 = 1475$ Oe g emu^{-1} and $\lambda_3 = 0.035$ Oe g^3 emu^{-3}, with the results shown in Figure 7.50.

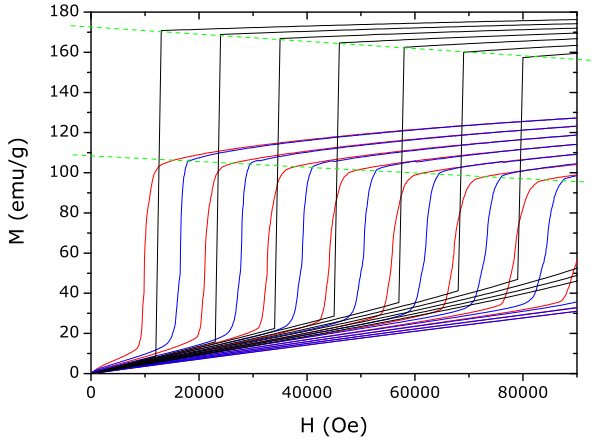

Figure 7.50: Experimental isothermal M versus H dependence of $Gd_5Si_2Ge_2$, up to an applied field of 10T for increasing field (blue lines) and decreasing field (red lines). Solid black lines represent molecular mean-field simulations, attempting to simulate a similar $H_C(T)$ behavior.

It appears to be possible to describe some properties of the first-order transition of this system, namely the critical field dependence on temperature, also the discontinuous magnetization change decrease on increasing temperature seems to be described as well (parallel green dashed lines of Figure 7.50). Still, the global magnetic behavior is not correctly described, and together with the high spin value (6.5), make these parameters unrealistic. Let us now consider the results of using the Maxwell relation on the magnetization data of Figure 7.49.

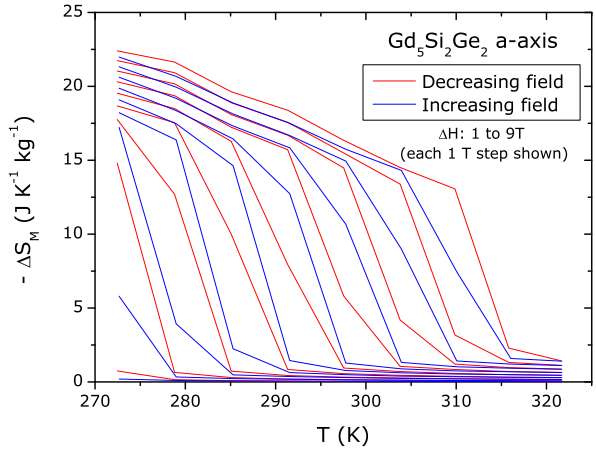

Figure 7.51: Magnetic entropy change of $Gd_5Si_2Ge_2$ as a function of temperature, calculated from the use of the Maxwell relation on field increasing (blue lines) and field decreasing (red lines) isothermal magnetization data.

Figure 7.51 shows how the use of the Maxwell relation on this set of magnetization data

shows slightly different results for the field-increasing and field-decreasing data. Still, the difference is small as to consider that the use of the Maxwell relation on this non-equilibrium data sets does not result in considerable errors since the observed irreversibility effects are actually low. Let us examine the dependence of the entropy change on the square of magnetization, where we take care to emphasize the entropy change on each one of the two possible phases (for each isotherm, above and below H_C). This is shown in Figure 7.52.

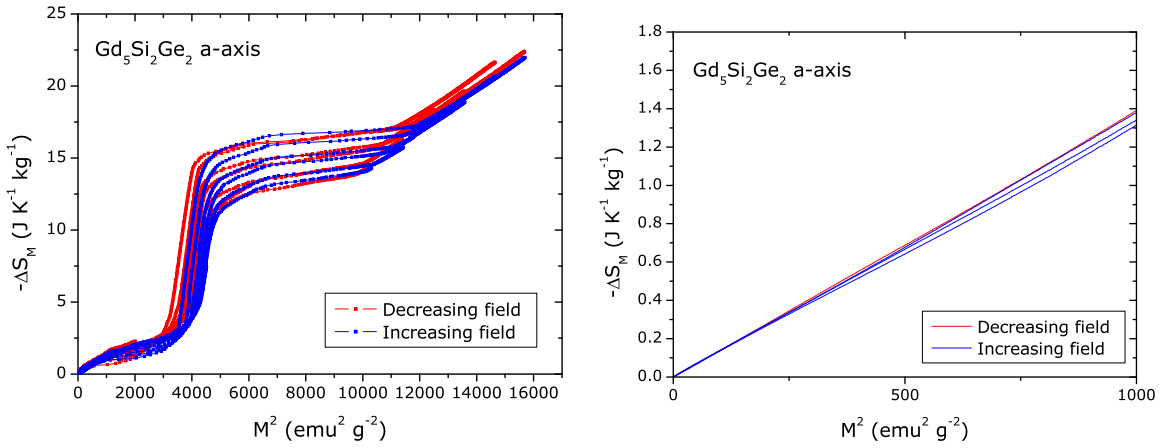

Figure 7.52: Magnetic entropy change of $Gd_5Si_2Ge_2$ as a function of the square of magnetization, for a) all M versus H data and b) only data of the monoclinic structure.

Figure 7.52(a) shows us a similar behaviour to mean-field first-order ΔS_M versus M^2 simulations. In the region where magnetization data below and above the structural transition is used to estimate the entropy change, there are deviations to the expected linear dependence of ΔS_M versus M^2. The ΔS_M versus M^2 is smooth for entropy data calculated with magnetization data of only one structure. Still, since attempting to simulate the magnetization data with the Bean-Rodbell model proved largely unsuccessful, let us look into magnetization data corresponding to each of the structural phases, and analyze each one independently by the mean-field goodness of scaling method. Figure 7.53(a) shows the M versus H dependence in the monoclinic phase (high temperature, fields below the critical value), and Figure 7.53(b) shows the contour plot resulting from the mean-field goodness of scaling method.

The best scaling parameters are around $\lambda_1 \sim 5750$ Oe g emu^{-1}, and low values of the λ_3 parameter (below 0.1 Oe g^{3}emu^{-3}). Let us consider that $\lambda_1 = 5750$ Oe g emu^{-1} and λ_3 is set as zero, and analyze the resulting scaling plot (Figure 7.54(a)).

The scaling plot of the high temperature/low magnetization data is an approximately linear function. So we are only analyzing the susceptibility behavior of the system, and can obtain a relation between the number of ions N, and the spin value J (Curie constant). By fixing the spin value to 3.5 (the theoretical value of an isolated Gd ion), we obtain an N value

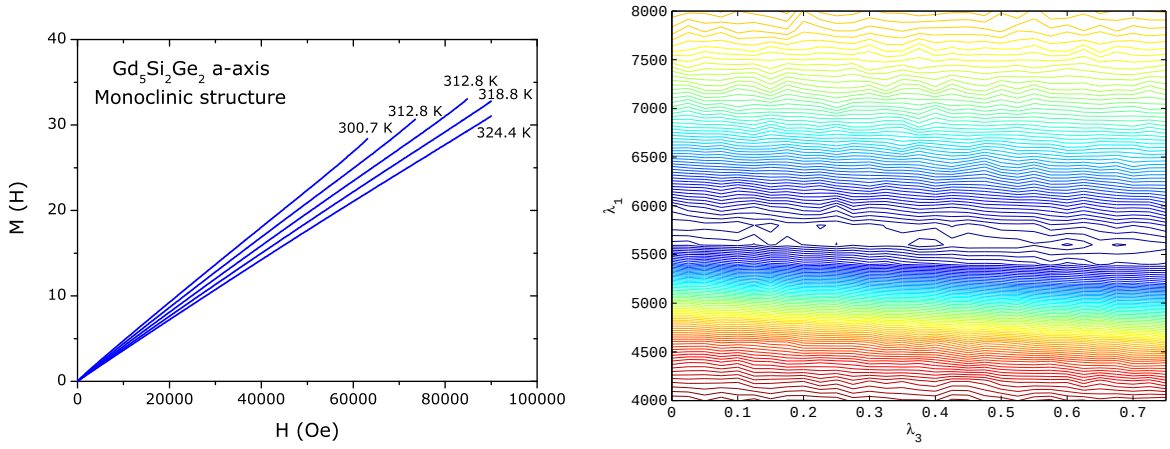

(a) (b)

Figure 7.53: a) M versus H data of $Gd_5Si_2Ge_2$ in the monoclinic structure and b) corresponding mean-field goodness of scaling contour plot.

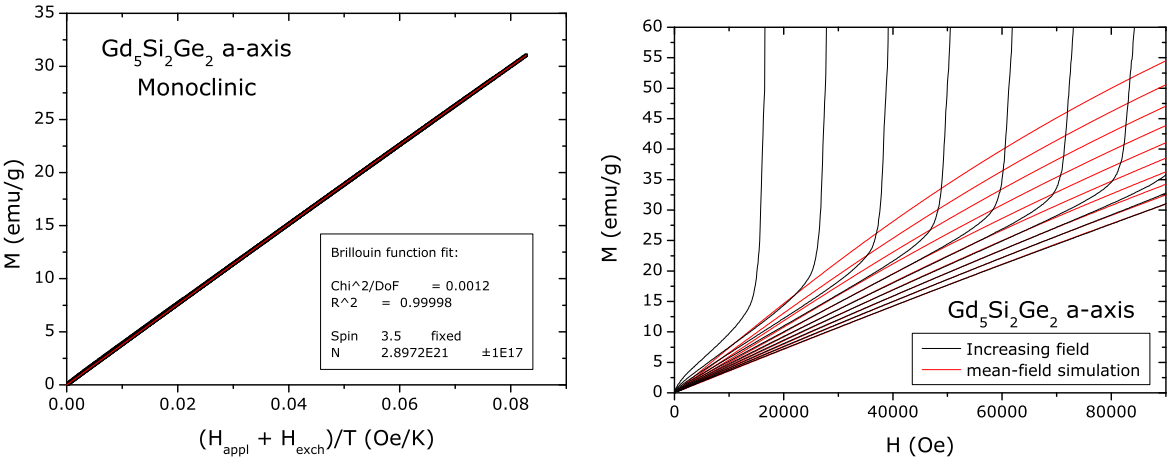

(a) (b)

Figure 7.54: Scaling plot of $Gd_5Si_2Ge_2$ magnetization data in the monoclinic structure and Brillouin function fit. b) Mean-field simulated M versus H data from parameters obtained from the Brillouin fit, compared to experimental data.

of $\sim 2.9\times10^{21}$ per gram. This results in a system with a Curie constant of 0.0380 emu K $Oe^{-1}g^{-1}$, saturation magnetization of 188.3 emu/g and a T_C value of 218.4 K. Figure 7.54(b) shows the mean-field simulated M versus H behavior of such a system, compared to the experimentally obtained magnetization data. Note that we have extrapolated somewhat the simulated M values, as to simulate the M versus H of the monoclinic phase, even when the field is high enough to induce the structural transition.

Let us now analyze the magnetic behavior of the high magnetization orthorhombic struc-

ture. Figure 7.55(a) show the M versus H behavior of the orthorhombic structure (high magnetization, low temperature).

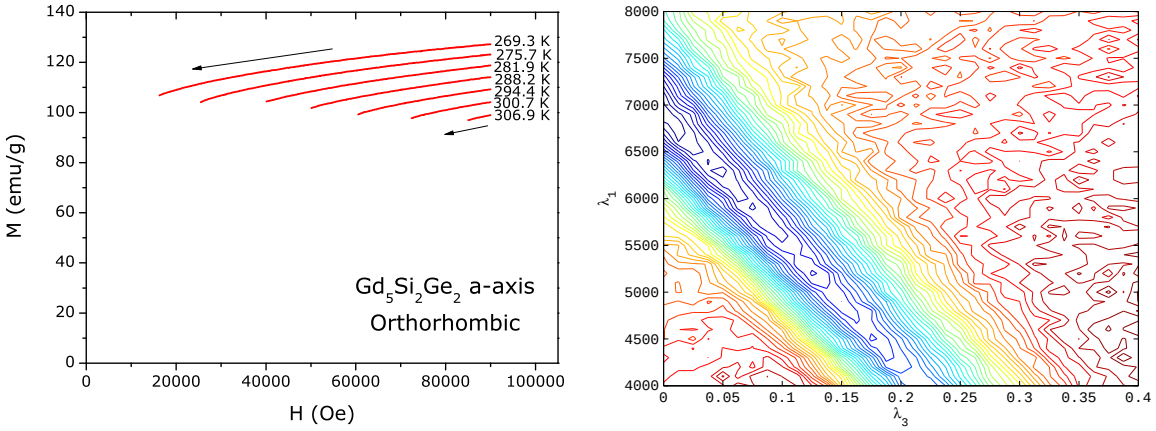

(a) (b)

Figure 7.55: a) M versus H data of $Gd_5Si_2Ge_2$ in the orthorhombic structure and b) corresponding mean-field goodness of scaling contour plot.

We use the magnetization data from the orthorhombic structure and search for mean-field scaling parameters λ_1 and λ_3 using the goodness of scaling method. The resulting contour plot is shown in Figure 7.55(b).

Like the monoclinic structure, the best mean-field scaling parameters correspond to a low λ_3, in this case below 0.025 Oe g^3emu^{-3}, with a λ_1 value around 6800 Oe g emu^{-1}. Let us again consider a null λ_3 value and analyze the resulting scaling plot (Figure 7.56(a)).

The scaling plot of Figure 7.56(a) shows some curvature, which now allows us to fit a Brillouin function with free spin and N parameters. We see that the obtained spin value is higher than 3.5, and the number of spins is basically equal to the one obtained for the monoclinic structure. This makes sense since it is the same sample, and the difference in spin value is not enough to consider local short-range interactions (clustering). So the N value should be the same. With the resulting spin value of $\sim$ 3.86 and $N = 2.9\times10^{21}$ ions per gram, we obtain a saturation magnetization value of $\sim$ 208 emu/g (note that experimental data reaches values of only 120 emu/g), a T_C value around 308.6 K and a Curie constant of 0.0454 emu K $Oe^{-1}g^{-1}$. We remark that the experimentally obtained value of saturation magnetization was $\sim$ 205 emu/g (10 T applied field at 5 K). Figure 7.56(b) compares the M versus H behavior of the mean-field system with the parameters obtained from the scaling method, compared to experimental results. Again, we have extrapolated the results of the orthorhombic structure beyond the H, T values where it is stable.

It is then possible to interpret each of the structural phases of $Gd_5Si_2Ge_2$ by a mean-field approach ($H \sim \lambda M$) using the scaling method. Let us see if we now can interpret the earlier

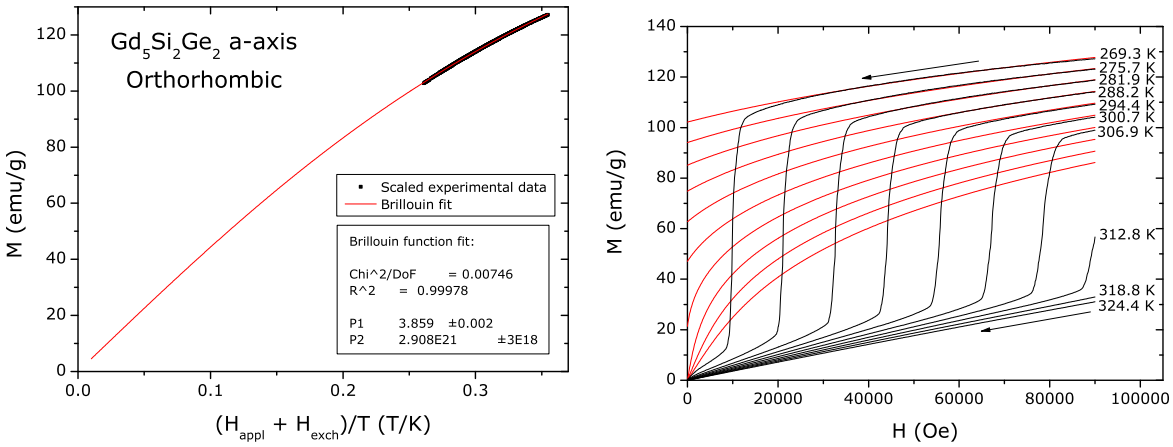

(a) (b)

Figure 7.56: Scaling plot of $Gd_5Si_2Ge_2$ magnetization data in the orthorhombic structure and Brillouin function fit. b) Mean-field simulated M versus H data from parameters obtained from the Brillouin fit, compared to experimental data.

ΔS_M versus M^2 plots (Figure 7.52). The mean-field scaling method has resulted in different Curie constants for each of the phases, due to the different spin values that were obtained (3.5 and 3.85, for the same N value). This tells us that the ΔS_M versus M^2 plots for each phase should be different. Let us plot simulated ΔS_M versus M^2 behavior and compare it to the experimental results, as shown in Figure 7.57.

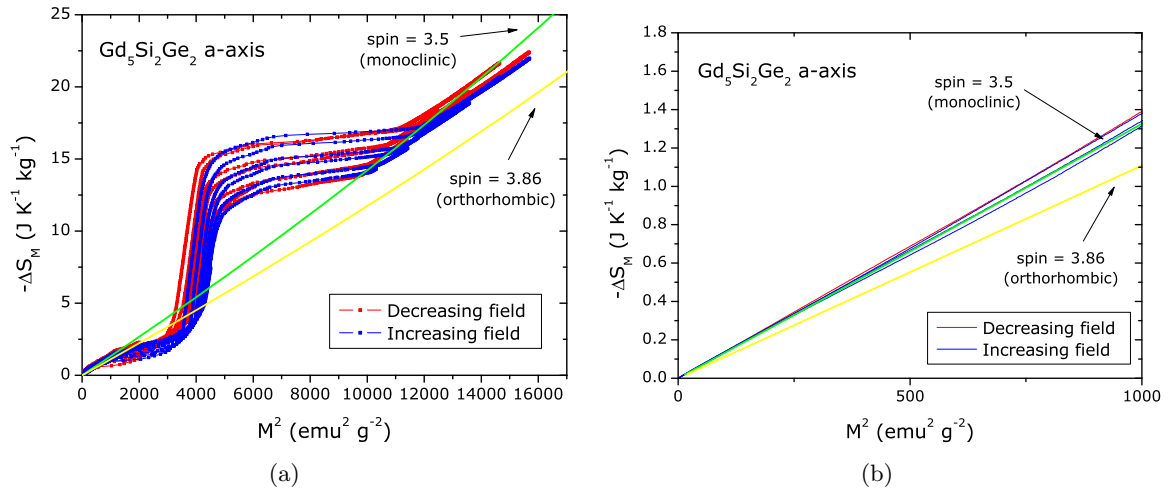

(a) (b)

Figure 7.57: Magnetic entropy change of $Gd_5Si_2Ge_2$ as a function of the square of magnetization, for a) all M versus H data and b) only data of the monoclinic structure.

First, let us analyze the low magnetization region, corresponding to the monoclinic structure (Figure 7.57(b)). We see how the simulated ΔS_M versus M^2 behavior is reproduced by

the mean-field simulation with a spin value of 3.5, as obtained previously. The spin value from the scaling of the orthorhombic structure does not adequately represent this region of data, showing how a small difference in spin value ($\sim 10\%$) produces a considerable change in the ΔS_M versus M^2 behavior. Since this region is basically the region of magnetic susceptibility, this tells us that the Curie constant for this structure was adequately determined. Comparing the simulated results to the global experimental ΔS_M versus M^2 data of Figure 7.57(a) is a bit more tricky. At a first glance it seems that the spin 3.5 curve is a better fit to the data. But looking more carefully, we note that the slope of the spin 3.86 curve is much closer to the experimental data in this region. It is important to remark that the slope is the relevant value, since the behavior of the system up to these H, T values also includes the monoclinic structure and the discontinuity effects. Since the spin value changes, we cannot expect a continuous ΔS_M versus M^2 dependence.

Until now, it appears that we are able to interpret the magnetic and magnetocaloric properties of each structure independently, but this does not explain at all why the system presents the transition between both structures. To study this, we need to compare the free energy of both structures, as a function of field and temperature, to see if the values are sufficiently close to each other, as to justify the change in structure. Ideally, the free energy plots for both structures should cross, justifying the structural transition, and also the irreversibility effects.

Since we have considered the mean-field λ_3 parameter to be null in the analysis of both the monoclinic and orthorhombic structure, we can write a simplified Gibbs free energy expression:

$$G_{min} = -Nk_B \left[\frac{3J}{2(J+1)} T_0 \sigma^2 - \frac{g\mu_B JH\sigma}{k_B} - TS_J(\sigma) \right] \tag{7.3}$$

and so plot the free energy of both structures as a function of H and T. The entropy values ($S_J(\sigma)$) were calculated using the mean-field integration of the corresponding inverse Brillouin function, calculated numerically.

Figure 7.58 shows the Gibbs free energy plots of the mean-field generated data, calculated using Eq. 7.3, for both the orthorhombic and monoclinic structures of $Gd_5Si_2Ge_2$.

It is interesting to note how the free energy minimum at a given temperature value changes from one structure to the other. This justifies the first-order transition in this material. Still, this simulation does not adequately describe the critical field dependence on temperature and field, as well as the observed irreversibility. Since we have ignored eventual magnetoelastic coupling effects, by considered the λ_3 mean-field exchange parameter as zero for both structures, largely due to the limitations of the scaling method, the higher order term to the free energy, proportional to η and σ^4 is zero. This term has a big influence in the free energy calculations, and so further analysis considering a non-zero η value can provide us with a better description of the first-order transition. Still, at this point it is very encouraging to see how the free energy of the two structures is very similar, and in a region of field and

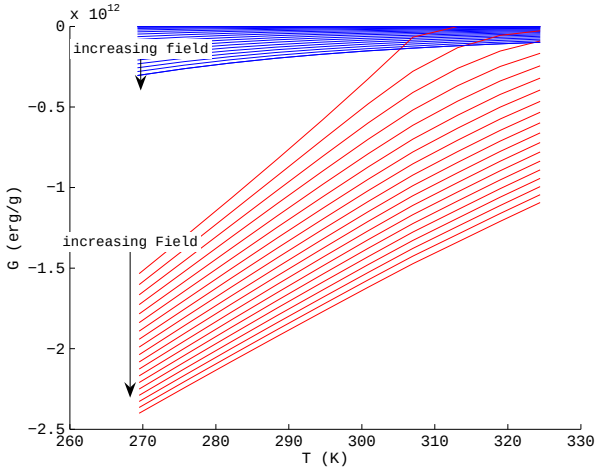

Figure 7.58: Gibbs free energy of the mean-field generated data of the orthorhombic and monoclinic structures of $Gd_5Si_2Ge_2$, as a function of temperature, for a field range from 0 to 9 T (0.5 T step).

temperature values the minimum of G shifts between structures, with a discontinuity in the free energy derivative, corresponding to a first-order phase transition.

Figure 7.59 shows a diagram to reflect the difference in describing the free energy as individual free energy functions for each structure, or as a single, continuous G function that has multiple minima (as resulting from magnetoelastic coupling).

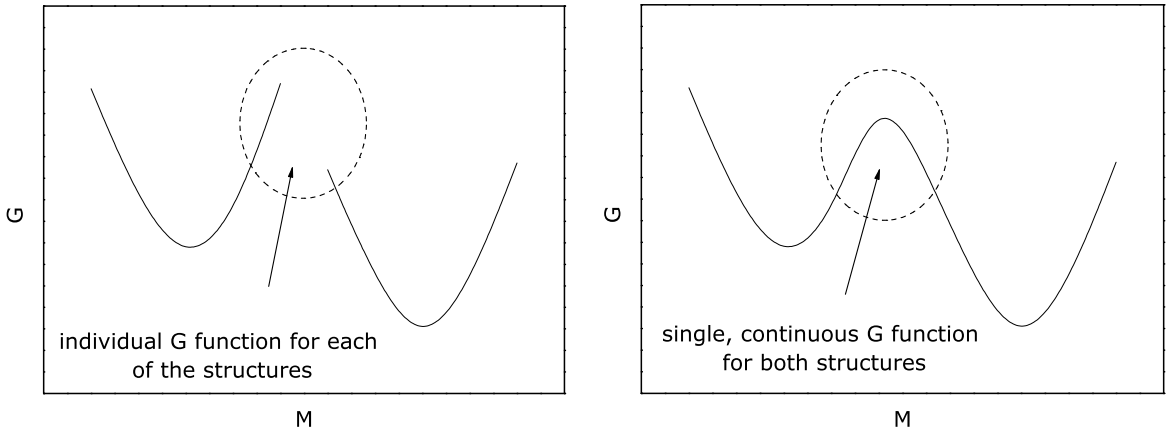

Figure 7.59: Description of the free energy of a system with a structural transition with a change in ionic magnetic moment a) and a system with a magnetostructural transition, but no spin change b).

The results presented here give two complementary paths to attempt to improve on the full free energy description of this material. First of all, each of the structures will have its own,

albeit small, magnetoelastic coupling. Considering this fact, the critical field dependence on applied magnetic field and temperature would be more realistic, compared to what is obtained from Figure 7.58. This would make it possible to have the simulated $M(H,T)$ curves include the structural transition. It is also possible to include an extra parameter in the free energy expansion, the spin contribution from orbital polarization. This can be formally considered an order parameter in the Landau theory perspective, since the value is null in the disordered phase, and is a non-zero value in the ordered phase. Including this extra order parameter would make it possible to have a single, continuous free energy function that might describe the full magnetization properties of this material.

Chapter 8

Conclusions

A review of the main results of this thesis is presented, together with plans for further studies in these topics. This section is divided into the review of the novel methodologies developed and presented in this thesis, the main conclusions from theoretical Landau theory and mean-field theory simulations and the main results from the analysis of the ferromagnetic systems under study.

8.1 Methodologies

A considerable part of this thesis is based on the development of new data analysis methodologies, based on theoretical models such as the Landau theory of phase transitions, mean-field model (with magnetoelastic coupling) and the theory of critical phenomena. These methodologies were developed in order to enable an in-depth analysis and interpretation of the magnetic and magnetocaloric properties of the ferromagnetic materials under study. We review here these methodologies.

8.1.1 Landau theory in magnetocaloric studies

Landau theory has proven to be a very useful tool in magnetocaloric studies of ferromagnetic materials. The purpose of its use in these studies is to provide a means of interpolating magnetization and magnetocaloric data with a physical background, and not purely numeric methods. The ease of calculations of the method, together with the physical insight that can be gained by its use, are major advantages.

As exemplified in the study of the ferromagnetic $La_{0.665}Er_{0.035}Sr_{0.3}MnO_3$ manganite in section 2.2.2, the Landau a, b and c coefficients, together with their temperature dependence, can be obtained from polynomial fits to the Arrott plots. This allows the estimation of the magnetic entropy change in the system directly from the temperature derivative of the Gibbs free energy. The b parameter and its dependence in temperature (which can be interpreted

as the result from magnetoelastic coupling and electron condensation/correlation effects) is evidenced in this analysis. In manganite systems, where magnetoelastic coupling and colossal magnetoresistance effects coexist, the b parameter and its dependence in temperature need to be taken into account in this interpretation.

This methodology was published [AA04], and later employed in the study of the magnetic/magnetocaloric properties of various manganite systems [ARA$^+$05a].

8.1.2 Estimating spontaneous magnetization from a mean-field analysis of magnetic entropy change

Due to the magnetic domain effect, bulk magnetization measurements do not directly reveal the spontaneous magnetization of the material. The use of adiabatic direct calorimetric measurements of the magnetocaloric effect, together with magnetization measurements can be used to estimate the spontaneous magnetization, since mean-field theory establishes a linear relation between ΔT_{ad} and M^2. The experimental complexity of directly measuring the magnetocaloric effect makes polynomial fits to Arrott plots a more practical approach. Still, these fits suffer from the fact that the curvature of the Arrott plots can either be interpreted as a consequence of a non-zero c parameter, or due to the domain formation. This affects the confidence in determining of the spontaneous magnetization value from the Arrott plots. An alternative methodology has been presented in this thesis. Landau theory establishes a linear relation between magnetic entropy and the square of magnetization, and so temperature-independent Landau parameters (of any order) will not induce any curvature in ΔS_M versus M^2 plots. In the ferromagnetic phase, the non-zero value of spontaneous magnetization will shift these plots horizontally, easily permitting its determination. Under mean-field theory, the methodology is the same, apart from a more complex relation between entropy and magnetization, which only deviates from linearity in high M values.

This methodology was successfully used to determine the spontaneous magnetization of the second-order phase transition $La_{0.665}Eu_{0.035}Sr_{0.30}MnO_3$ and first-order phase transition $La_{0.638}Eu_{0.032}Ca_{0.33}MnO_3$ manganites [ASA09].

8.1.3 Mean-Field scaling

Based on the general properties of the molecular mean-field formulation, a novel scaling method was proposed [ASA07]. This methodology allowed the interpretation of magnetization data within the mean-field model without any previous presumptions of the mean-field state function (usually presumed as the Brillouin or Langevin functions, or combinations), or the exchange field (usually presumed as having a linear dependence on M or a higher cubic term). The robustness of this approach was first explored using simulated mean-field results, showing in detail the methodology and its limitations.

The magnetic entropy change can be estimated within the mean-field model, using the exchange field dependence in M, T and the mean-field state function, resulting from the scaling method.

This method was employed in the study of the magnetic and magnetocaloric properties of the $La_{0.665}Er_{0.035}Sr_{0.30}MnO_3$ and $La_{0.638}Eu_{0.032}Ca_{0.33}MnO_3$ manganites, and mechanically-alloyed FCC FeCu. The use of this methodology resulted in a good rescription of the magnetic and magnetocaloric properties of the manganite systems, and in the case of the FeCu alloy, it revealed a complex exchange field behavior, indicating a bimodal Fe cluster distribution and superferromagnetic interaction [ASA07, SAA$^+$09].

8.1.4 Defining a 'goodness of scaling' parameter

To provide quantitative basis for data scaling analyses, a novel scaling methodology, and its application in mean-field and critical phenomena studies was presented, based on a criteria to quantitatively assess the best scaling variables for a given set of data, allowing for a fully automatized search algorithm. The usefulness of this approach has been presented in mean-field and critical phenomena studies. While the examples presented here have been for magnetic studies, it is worth to point out that this approach can be applied to the search of scaling phenomena and universal behavior in other topics.

8.1.5 Estimating entropy change in mixed-state systems

The colossal magnetocaloric effect, consisting of magnetic entropy change values that clearly exceed the theoretical limit, was found in estimating magnetic entropy change from magnetic measurements that show clear signs of mixed-phase behavior. Calorimetric measurements to determine entropy change did not confirm its existence, resulting in a controversial discussion theme. After a detailed analysis of common methods of magnetic entropy change calculation, in this thesis we have shown a method to correct the estimation of the magnetocaloric effect in mixed-phase systems, showing the colossal magnetocaloric effect to be a direct consequence of the temperature dependence of mixed phase fraction of the material, and the use of a Maxwell relation for calculation with data from an inhomogeneous system. This method was used in the study of the magnetocaloric properties of the 'colossal magnetocaloric' MnAs and $Mn_{1-x-y}Cu_xCr_yAs$ family of samples. The methodology and experimental studies have been submitted for publication [DAA09].

8.2 Results from theoretical simulations

The clarification of several points under discussion in the current magnetic and magnetocaloric state of the art required extensive use of theoretical simulations. To this extent, the

Landau theory of phase transitions and the molecular mean field model (with magnetoelastic coupling) were employed.

8.2.1 Irreversibility effects in estimating the MCE

A theoretical study of the magnetocaloric effect in first-order phase transition materials, particularly on estimating magnetic entropy change from magnetization measurements, was done based on the Landau theory of phase transitions and the Bean-Rodbell mean-field model. The so-called magnetocaloric 'peak effect', under discussion shortly after the discovery of the giant magnetocaloric effect, was found to be the result of the use of the Maxwell relation to estimate the magnetocaloric effect from non-equilibrium magnetization data. By considering the metastable solutions that can be considered in the magnetization simulations by both models, the 'peak effect' was successfully reproduced. The use of the Maxwell relation on non-equilibrium data to estimate magnetic entropy change was also shown to reproduce the colossal magnetocaloric effect, resulting in values exceeding the theoretical limit [AA09a, AA09b].

8.2.2 Simulating a mixed-phase system

The Bean-Rodbell mean-field model was used to simulate mixed-phase first-order phase transitions, to assess the consequences of estimating the magnetocaloric effect using the Maxwell relation on non-homogeneous magnetization data. It was found that a mixed-order system can show a colossal magnetocaloric effect, with a peak shape resembling the experimentally observed results of using the Maxwell relation on magnetization data of the Mn-As and La-Fe-Si systems. The temperature dependence of the mixed phase fraction was shown to be obtainable directly from isothermal magnetization data, and its temperature dependence defines the shape of the colossal MCE peak. Calculations and numerical simulations allowed us to formulate a method to correct the magnetocaloric values of these compounds. The main conclusions of this work have been published [AA09a, AA09b] or submitted for publication [DAA09].

8.2.3 Disorder effects in ferromagnetic systems

The use of the molecular mean-field model for the study of magnetic transitions has allowed an interpretation of the effects of chemical/structural disorder on the properties of a second-order phase transition material. In terms of the magnetocaloric effect, an approximately linear relation between the width of the T_C distribution and the relative cooling power has been shown. In a spin 2 system, a Gaussian T_C distribution with a full width at half maximum value of $\sim 7\%$ (20 K) of T_C (300 K) results in a decrease of the maximum entropy change by $\sim 15\%$, together with an increase of RCP $\sim 40\%$, for an applied field change from 0 to 1 T.

In order to interpret the effects of disorder on the magnetocaloric properties of a magnetic material it is important to distinguish them from the intrinsic properties of the non-disordered system. The main conclusions of this study have been published [ATR+08].

The effects of disorder in first-order phase transitions was also investigated, by the mean-field Bean-Rodbell model. Disorder effects were shown to induce curvatures in the M versus H and Arrott plots, smoothing the discontinuities present in the 'pure' system. The effects of disorder on the magnetocaloric properties of first-order transitions were also investigated, showing how disorder affects the magnetic entropy dependence on temperature, by broadening the entropy peaks, and reducing the intensity of the MCE. In a spin 2 system with a first-order magnetic phase transition, a Gaussian T_0 distribution with a full width at half maximum value of just $\sim 1.7\%$ (5 K) of T_C (300 K) results in a decrease of the maximum magnetic entropy change by $\sim 40\%$, for an applied field change from 0 to 1 T.

8.3 Analysis of ferromagnetic systems

In this thesis, a study of the magnetic and magnetocaloric properties of several ferromagnetic materials was presented. For each case, the appropriate methodologies for analysis, taking into account the particular physics of the system, were employed. Particular relevance was given to the insight that was obtained by the use of the novel methodologies, compared to standard methods of magnetization/magnetocaloric data analysis and also theoretical simulations.

8.3.1 Metallic Nickel

The magnetic properties of Nickel near T_C require an analysis that goes beyond the mean-field scheme. A critical phenomena study was undertaken, and the relevant critical exponents were sought for. The 'goodness of scaling' methodology, applied to the critical phenomena study of this material, allowed the simultaneous determination of the β and γ exponents and also the T_C value of this material. The robustness of this method was compared to the 'classical' methodology of power-law fitting to the critical isotherm and low-field inverse susceptibility fits. The obtained exponent values were $\beta = 0.372$ and $\gamma = 4.56$, in a good accordance with values obtained by Kouvel and Fisher ($\beta = 0.378$ and $\gamma = 4.58$). It was also shown how the correct determination of the T_C value is crucial to obtaining reliable exponent values. While this fact affects the classical power-law fitting methods (a 0.1% shift in T_C results in a $> 5\%$ shift in the obtained δ value), it is circumvented by the 'goodness of scaling' method. In a similar way, the problematic of fitting "exceedingly close close to T_C" and falsely obtaining exponents close to the mean-field values (as reported by Kuz'min and Tishin), is also avoided by this scaling method.

8.3.2 Mechanically alloyed fcc Fe-Cu

The use of the mean-field scaling method described in section 3 of this thesis has given us valuable insight on the magnetic properties of this system. From isothermal magnetization measurements, a bimodal Fe cluster configuration could be inferred, where the smaller clusters comprises about 14 atoms, close to a 13 atom icosahedral/cuboctahedral arrangement which is found in multiply twinned and isolated nanoparticles of fcc transition metals and of bcc Fe. The inter-cluster ferromagnetic interactions that lead to a Curie temperature $T_C \sim 220$ K can be described by a mean field determined by the smaller clusters only, which account for 90% of the magnetization.

8.3.3 Manganite systems

In this thesis, an extensive analysis of the magnetic and magnetocaloric properties of second- and first-order manganite systems was presented. These systems permitted the analysis of disorder effects and magnetic clustering phenomena, motivating the development of many of the methodologies presented in this work.

- The insight from mean-field simulations of disordered magnetic systems has given the background to interpret the magnetocaloric properties of the phase-separated system La-Er-Sr-MnO_3, justifying a complex microstructural and diffusion scenario. In the La-Eu-Sr-MnO_3 system, the increase of Relative Cooling Power with Eu substitution (up to 27% for an applied filed change of 1 T, corresponding to the sample with highest Eu substitution) could be understood as a direct consequence of increased chemical/structural disorder [ARA$^+$05b, ARA$^+$08].

- From the use of the 'goodness of scaling' method, a mean-field analysis of the magnetic properties of the second-order phase transition $La_{0.70}Sr_{0.30}MnO_3$ manganite and the first-order phase transition $La_{0.665}Eu_{0.035}Ca_{0.33}MnO_3$ manganite was performed. The analysis of the scaling magnetization function pointed to a three Mn ion cluster configuration in these compounds, that persists well within the ferromagnetic region. This cluster configuration was supported by Landau theory and mean-field theory analysis of the dependence of magnetic entropy change with magnetization. Although clustering effects in mixed valence manganites are well known for $T > T_C$, their persistence below T_C was only recently reported.

- By considering the above-mentioned clustering phenomena and a suitable T_C distribution in the $La_{0.70}Sr_{0.30}MnO_3$ manganite, the magnetization and magnetic entropy change dependence on field and temperature were successfully described by the mean-field model.

- the magnetic and magnetocaloric properties of the $La_{0.665}Eu_{0.035}Ca_{0.33}MnO_3$ and $La_{0.60}Y_{0.07}Ca_{0.33}MnO_3$, were analyzed using the mean-field model, considering magnetic disorder and clustering phenomena. The La-Y-Ca system is expected to have a higher A-cation disorder, since there is increased substitution (7% compared to 3.5%) and also due to the smaller radius of the Y^{+3} ion (1.075 Å versus 1.12 Å), increasing the variance. It was confirmed that the La-Eu-Ca manganite shows a smaller width of T_C distribution (4 K, 2% of T_C), compared to the 15 K (10% of T_C) value obtained for the La-Y-Ca manganite.

8.3.4 MnAs and the $Mn_{1-x-y}Cu_xCr_yAs$ system

The magnetic and magnetocaloric properties of MnAs and related doped alloys were investigated, taking into account the observed mixed-phase behavior of this compound. By determining the mixed-phase fraction and its dependence in temperature directly from magnetization data, and considering the previous mean-field simulations of mixed-phase systems, the results from the direct use of the Maxwell relation to estimate the magnetocaloric effect in this compound were corrected.

In $Mn_{1-x-y}Cu_xCr_yAs$, the amount of substituted Cu/Cr was shown to control the T_C and mixed-phase kinetics of the parent compound. This allowed us to apply the correction to the MCE calculations of experimental magnetization data with varying mixed-phase temperature ranges.

8.3.5 $LaFe_{11.5}Si_{1.5}$

In this system the first-order phase transition results in a discontinuous change in the lattice parameter, and no symmetry change, simplifying the scenario compared to MnAs or $Gd_5Si_2Ge_2$. The effect of pressure in the magnetic and magnetocaloric properties of $LaFe_{11.5}Si_{1.5}$ was investigated by the mean-field model and Bean-Rodbell model for magnetovolume interactions, on data from the literature. The magnetic properties presented no clear signs of chemical disorder. Analysing data with only a change in applied pressure, the effect can be separated from the induced complexity from chemical substitution effects. This system showed how the mean-field model, with its limited number of parameters in play (4), could describe the magnetic properties of this system, and also explaining the apparent existence of a pressure-induced colossal magnetocaloric effect.

8.3.6 $Gd_5Si_2Ge_2$ single crystal

$Gd_5Si_2Ge_2$ is an archetypical first-order magnetic phase transition and giant magnetocaloric material, that presents a structural symmetry change in its first-order phase transition. The magnetic measurements show no signs of disorder effects, but an attempt to describe

the magnetic properties of this system as two phases of the same magnetic system (in a similar way to the $LaFe_{11.5}Si_{1.5}$ study) proved unsuccessful. The two structural phases (monoclinic and orthorhombic) were therefore studied separately using the mean-field 'goodness of scaling method' and by analyzing the entropy/magnetization dependence.

This approach revealed how the magnetization data could be interpreted considering a change in the spin value per Gd ion due to the structural transformation. Indeed this effect was previously predicted by density functional theory calculations, and observed in X-ray magnetic dichroism measurements of this compounds. The obtained spin value in the orthorhombic phase was determined to be ~ 3.86 per Gd ion in formula, in a good accordance with the predicted value of 3.8 from Paudyal *et al.*, from LSDA+U DFT calculations.

By simulating the free energy dependence on field and temperature of both structures, it was possible to assess how the energy values are similar, and do indeed cross in the experimental range of (H,T) values. While these results do not completely describe the observed dependence of the critical field with temperature, they justify the occurrence of the first-order transition of this material, since the temperature derivative of the free energy is then discontinuous at the structural change.

8.4 Future plans

The methodologies developed in this thesis can circumvent some limitations of the more classic methods of magnetic data analysis. One example is the study of critical phenomena using the 'goodness of scaling' method, which can avoid potential problems in power-law fittings "exceedingly close to T_C", a point recently raised by Kuz'min and Tishin [77]. Indeed, one of the results that was questioned by these authors was the reported mean-field like critical exponents of Gd, by Srinath and Kaul [122]. The analysis of the critical behavior of Gd using the 'goodness of scaling' methodology could bring further insight to this ongoing discussion. To this extent, high quality single crystal and polycrystalline Gd samples are available, from an ongoing collaboration with Prof. Karl Gschneidner of Ames Laboratory, Iowa State University.

A more extensive analysis of the magnetic properties of MnAs, in a study similar to that of $Gd_5Si_2Ge_2$ here presented, could also bring additional insight to our understanding of the nature of the magneto-structural transition of this compound. It is worth pointing out that the very detailed Landau theory study of MnAs by Pylik and Zięba of 1985 [123] accounted for the possibility that "lattice distortion changes the magnetic moment value of the manganese atom" and obtained an excellent description of the phase diagram of MnAs. Still, a mean-field analysis should be able to better describe $M(H,T)$ behavior of the system, since values of magnetization near saturation (away from the validity region of the free energy Landau expansion) can be considered.

The presented study of the magnetic properties of the $Gd_5Si_2Ge_2$ compound can also be improved, by considering magnetoelastic coupling in the monoclinic and orthorhombic phases. Also, considering the magnetic moment change due to the structural transition as an order parameter can enable the formulation of a more complete free energy expression that describes both structures of the material, and also the first-order transition itself.

The studies on the effects of magnetic disorder on the magnetocaloric effect of materials has also given the background to consider controlling disorder as a parameter to optimize the magnetocaloric properties of materials. Indeed, the simulations here presented of disordered systems, together with the studies of Rodriguez-Martinez and Attfield [102, 124] can be used in a way to control both T_C and disorder of a ferromagnetic manganite system, to obtain a tailor-made material with controlled RCP around a desired temperature range. This approach is also valid for first-order phase transition materials, albeit with more complex effects in the magnetic/magnetocaloric properties due to disorder.

The results from estimating the amount of disorder in a magnetic material from its bulk magnetic and magnetocaloric properties, as shown in this thesis, should be compared to more direct techniques. One technique that is particularly appealing for such a study is the local Hall imaging technique, developed at the London Imperial College, that has permitted several analysis of magnetic materials, including the local magnetic properties of Gd_5Si_4 [125], $CoMnSi_{0.92}Ge_{0.08}$ [126] and $Gd_5Si_2Ge_2$ [127]. Such a technique, that allows the measurement of local $M(H,T)$ loops, is of particular interest in studying disordered materials, since a statistically relevant number of local $M(H,T)$ dependencies can be analyzed in order to estimate the global macroscopic disorder, comparing it to the results from the methods presented in this thesis.

The use of the 'goodness of scaling' method for the study of scaling laws and universal behavior in non-magnetic systems can also bring some added insight into existing, or novel scaling studies. One particular work, by Bak *et al.*, on the scaling laws of earthquakes [66] can present a good base for such a scaling study, since the data used by the authors (earthquake data from The Southern California Seismographic Network catalogs) is quite extensive, and should present sufficient data overlap for a rigorous use of the 'goodness of scaling' method.

The magnetic clustering behavior found in the ferromagnetic/metallic state of the manganite systems under study, recently corroborated by spin wave measurements [112], adds novel insight to the anomalous behavior of these materials near T_C. It is of clear interest to focus these studies in other systems of materials that show clustering behavior, in order to assess if the persistence of magnetic clustering for $T < T_C$ is a particular property of manganites and other complex strongly electron correlated systems.

Appendix A

Technical details of the used magnetometer devices

This appendix presents the relevant technical details of the magnetometer devices used for obtaining the magnetization data presented in this thesis.

A.1 High-temperature VSM system at IFIMUP-IN Porto

Figure A.1: The VSM system at IFIMUP-IN (top) and detail of the alumina sample holder (bottom).

Commercial Oxford high temperature Vibrating Sample Magnetometer:

- Operating temperature range: room temperature to 1000 K
- Sensitivity: 10^{-4} emu
- Field source: Water-cooled electromagnet (1 Tesla maximum applied field)
- High temperature measurements under primary vacuum
- Alumina sample holder (sample attached with teflon tape (< 500 K) or special cement for $T > 500$ K.)

A.2 VSM system at CICECO, Universidade de Aveiro

Figure A.2: VSM system at CICECO, Universidade de Aveiro.

Commercial Cryogenics Vibrating Sample Magnetometer.

- Operating temperature range: 5 to 320 K
- Sensitivity: 10^{-6} emu
- Field source: Superconducting magnet (10 T maximum applied field)

A.3 SQUID system at IFIMUP-IN Porto

Figure A.3: SQUID magnetometer at IFIMUP-IN, Porto.

Commercial Quantum Design MPMS5 SQUID magnetometer.

- Operating temperature range: 5 K to 400 K
- Sensitivity: 10^{-7} emu
- Field source: Superconducting magnet (5.5 Tesla maximum applied field)

Author's work

[AA04] V. S. Amaral and J. S. Amaral. Magnetoelastic coupling influence on the magnetocaloric effect in ferromagnetic materials. *J. Magn. Magn. Mater.*, 272-276:2104–2105, 2004.

[AA09a] J. S. Amaral and V. S. Amaral. The effect of magnetic irreversibility on estimating the magnetocaloric effect from magnetization measurements. *Appl. Phys. Lett.*, 94:042506, 2009.

[AA09b] J. S. Amaral and V. S. Amaral. On estimating the magnetocaloric effect from magnetization measurements. *J. Magn. Magn. Mater.*, In press, available at http://dx.doi.org/10.1016/j.jmmm.2009.06.013, 2009.

[Ama05] J. S. Amaral. Estudo de manganites modificadas com iões de terra rara. *MSc Thesis in Materials Science and Engineering, Universidade de Aveiro*, 2005.

[ARA+05a] J. S. Amaral, M. S. Reis, V. S. Amaral, T. M. Mendonça, J. P. Araújo, M. A. Sá, P. B. Tavares, and J. M. Vieira. Magnetocaloric effect in Er- and Eu-substituted ferromagnetic La-Sr manganites. *J. Magn. Magn. Mater.*, 290:686–689, 2005.

[ARA+05b] J. S. Amaral, M. S. Reis, V. S. Amaral, T. M. Mendonça, J. P. Araújo, P. B. Tavares, and J. M. Vieira. Tuning of magnetocaloric effect in ferromagnetic La-Sr manganites through Er and Eu doping. *Mat. Sci. Forum*, 514:299–305, 2005.

[ARA+08] J. S. Amaral, M. S. Reis, J. P. Araújo, T. M. Mendonça, P. B. Tavares, V. S. Amaral, and J. M. Vieira. Phase separation of $La_{0.70-x}Er_xSr_{0.30}MnO_3$ and its effect on magnetic and magnetocaloric properties. *Mat. Sci. Forum*, 587-588:338–342, 2008.

[ASA07] J. S. Amaral, N. J. O. Silva, and V. S. Amaral. A mean-field scaling method for first- and second-order phase transition ferromagnets and its application in magnetocaloric studies. *Appl. Phys. Lett.*, 91(17):172503–172506, 2007.

[ASA09] J. S. Amaral, N. J. O. Silva, and V. S. Amaral. Estimating spontaneous magnetization from a mean field analysis of the magnetic entropy change. *J. Magn. Magn. Mater.*, In press, available at http://dx.doi.org/10.1016/j.jmmm.2009.09.024, 2009.

[ATR+08] J. S. Amaral, P. B. Tavares, M. S. Reis, J. P. Araújo, T. M. Mendonça, V. S. Amaral, and J. M. Vieira. The effect of chemical distribution on the magnetocaloric effect: A case study in second-order phase transition manganites. *J. Non-Cryst. Solids*, 354:5301–5303, 2008.

[DAA09] S. Das, J. S. Amaral, and V. S. Amaral. Handling mixed state magnetization data for magnetocaloric studies – a solution to achieve realistic entropy behaviour. *Submitted to Journal of Physics D: Applied Physics*, 2009.

[SAA+09] N. J. O. Silva, J. S. Amaral, V. S. Amaral, B. F. O. Costa, and G. le Caër. Superferromagnetism in mechanically alloyed FCC $Fe_{23}Cu_{77}$ with bimodal cluster size distribution. *J Phys: Condens. Mat.*, 21:046003, 2009.

Bibliography

[1] E. Warburg, Magnetische untersuchungen, Ann. Phys. 249 (5) (1881) 141–164.

[2] P. Debye, Einige bemerkungen zur magnetisierung bei tiefer temperatur, Ann. Phys. 81 (1926) 1154.

[3] W. F. Giauque, A thermodynamic treatment of certain magnetic effects. A proposed method of producing temperatures considerably below 1° absolute, J. Am. Chem. Soc. 49 (1927) 1864.

[4] W. F. Giauque, D. P. MacDougall, Attainment of temperatures below 1° absolute by demagnetization of $Gd_2(SO_4)_3 \cdot 8H_2O$, Phys. Rev. 43 (1933) 768.

[5] W. Sucksmith, C. A. Clark, D. J. Oliver, J. E. Thompson, Spontaneous magnetization; techniques and measurements, Rev. Mod. Phys. 25 (1) (1953) 34.

[6] E. L. Resler, R. E. Rosenswieg, Regenerative thermomagnetic power, J. Eng. Power 89 (3) (1967) 399.

[7] G. V. Brown, Magnetic heat pumping near room-temperature, J. Appl. Phys. 47 (8) (1976) 3673–3680.

[8] V. K. Pecharsky, K. A. Gschneidner, Giant magnetocaloric effect in $Gd_5Si_2Ge_2$, Phys. Rev. Lett. 78 (23) (1997) 4494–4497.

[9] S. Gama, A. A. Coelho, A. de Campos, A. M. G. Carvalho, F. C. G. Gandra, P. J. von Ranke, N. A. de Oliveira, Pressure-induced colossal magnetocaloric effect in MnAs, Phys. Rev. Lett. 93 (23) (2004) 237202–1–237202–4.

[10] K. A. Gschneidner Jr., V. K. Pecharsky, Thirty years of near room temperature magnetic cooling: Where we are today and future prospects, Int. J. Refrig. 31 (6) (2008) 945–961.

[11] H. B. Callen, Thermodynamics and an introduction to thermostatistics, 2nd Edition, John Wiley and Sons, New York, USA, 1985.

[12] M. W. Zemansky, R. H. Dittman, Heat and Thermodynamics, McGraw Hill, New York, 1981.

[13] A. M. Tishin, Y. I. Spichin, The Magnetocaloric Effect and its Applications, IOP Publishing, London, 2003.

[14] V. K. Pecharsky, K. A. Gschneidner, Magnetocaloric effect from indirect measurements: Magnetization and heat capacity, J. Appl. Phys. 86 (1) (1999) 565–575.

[15] K. Gschneidner Jr., V. Pecharsky, A. Pecharsky, C. Zimm, Recent developments in magnetic refrigeration, Mater. Sci. Forum 315-317 (1999) 69–76.

[16] V. Provenzano, A. J. Shapiro, R. D. Shull, Reduction of hysteresis losses in the magnetic refrigerant $Gd_5Ge_2Si_2$ by the addition of iron, Nature 429 (6994) (2004) 853–857.

[17] F. X. Hu, B. G. Shen, J. R. Sun, Z. H. Cheng, G. H. Rao, X. X. Zhang, Influence of negative lattice expansion and metamagnetic transition on magnetic entropy change in the compound $LaFe_{11.4}Si_{1.6}$, Appl. Phys. Lett. 78 (23) (2001) 3675–3677.

[18] A. Fujita, S. Fujieda, Y. Hasegawa, K. Fukamichi, Itinerant-electron metamagnetic transition and large magnetocaloric effects in $La(Fe_xSi_{1-x})_{13}$ compounds and their hydrides, Phys. Rev. B 67 (10) (2003) 1044161.

[19] A. Fujita, K. Fukamichi, Large magnetocaloric effects and landau coefficients of itinerant electron metamagnetic $La(Fe_xSi_{1-x})_{13}$ compounds, IEEE T. Magn. 41 (10) (2005) 3490–3492.

[20] H. Wada, Y. Tanabe, Giant magnetocaloric effect of $MnAs_{1-x}Sb_x$, Appl. Phys. Lett. 79 (20) (2001) 3302–3304.

[21] O. Tegus, E. Brück, K. H. J. Buschow, F. R. de Boer, Transition-metal-based magnetic refrigerants for room-temperature applications, Nature 415 (6868) (2002) 150–152.

[22] A. M. Gomes, F. Garcia, A. P. Guimarães, M. S. Reis, V. S. Amaral, Field-tuned magnetocaloric effect in metamagnetic manganite system, Appl. Phys. Lett. 85 (21) (2004) 4974–4976.

[23] X. Z. Zhou, W. Li, H. P. Kunkel, G. Williams, A criterion for enhancing the giant magnetocaloric effect: (Ni-Mn-Ga) – a promising new system for magnetic refrigeration, J. Phys: Cond. Mat. 16 (6) (2004) L39–L44.

[24] N. H. Duc, D. T. K. Anh, P. E. Brommer, Metamagnetism, giant magnetoresistance and magnetocaloric effects in rco_2-based compounds in the vicinity of the curie temperature, Physica B 319 (1-4) (2002) 1–8.

[25] K. A. Gschneidner Jr., V. K. Pecharsky, A. O. Tsokol, Recent developments in magnetocaloric materials, Rep. Prog. Phys. 68 (6) (2005) 1479–1539.

[26] E. Brück, Developments in magnetocaloric refrigeration, J. Phys. D: Appl. Phys. 38 (23) (2005) R381–R391.

[27] V. K. Pecharsky, A. P. Holm, K. A. Gschneidner, R. Rink, Massive magnetic-field-induced structural transformation in Gd_5Ge_4 and the nature of the giant magnetocaloric effect, Phys. Rev. Lett. 91 (19) (2003) 197204.

[28] L. Morellon, Z. Arnold, C. Magen, C. Ritter, O. Prokhnenko, Y. Skorokhod, P. A. Algarabel, M. R. Ibarra, J. Kamarad, Pressure enhancement of the giant magnetocaloric effect in $Tb_5Si_2Ge_2$, Phys. Rev. Lett. 93 (13) (2004) 137201.

[29] L. Jia, G. J. Liu, J. R. Sun, H. W. Zhang, F. X. Hu, C. Dong, G. H. Rao, B. G. Shen, Entropy changes associated with the first-order magnetic transition in $LaFe_{13-x}Si_x$, J. Appl. Phys. 100 (12) (2006) 123904.

[30] A. de Campos, D. L. Rocco, A. M. G. Carvalho, L. Caron, A. A. Coelho, S. Gama, L. M. da Silva, F. C. G. Gandra, A. O. dos Santos, L. P. Cardoso, P. J. Von Ranke, N. A. de Oliveira, Ambient pressure colossal magnetocaloric effect tuned by composition in $Mn_{1-x}Fe_xAs$, Nat. Mater. 5 (10) (2006) 802–804.

[31] D. L. Rocco, A. de Campos, A. M. G. Carvalho, L. Caron, A. A. Coelho, S. Gama, F. C. G. Gandra, A. O. dos Santos, L. P. Cardoso, P. J. von Ranke, N. A. de Oliveira, Ambient pressure colossal magnetocaloric effect in $Mn_{1-x}Cu_xAs$ compounds, Appl. Phys. Lett. 90 (24) (2007) 242507–1–242507–3.

[32] N. K. Sun, W. B. Cui, D. Li, D. Y. Geng, F. Yang, Z. D. Zhang, Giant room-temperature magnetocaloric effect in $Mn_{1-x}Cr_xAs$, Appl. Phys. Lett. 92 (7) (2008) 3.

[33] P. J. von Ranke, N. A. de Oliveira, C. Mello, A. M. G. Carvalho, S. Gama, Analytical model to understand the colossal magnetocaloric effect, Phys. Rev. B 71 (5) (2005) 054410.

[34] G. J. Liu, J. R. Sun, J. Shen, B. Gao, H. W. Zhang, F. X. Hu, B. G. Shen, Determination of the entropy changes in the compounds with a first-order magnetic transition, Appl. Phys. Lett. 90 (3) (2007) 032507–1–032507–3.

[35] L. Tocado, E. Palacios, R. Burriel, Entropy determinations and magnetocaloric parameters in systems with first-order transitions: Study of MnAs, J. Appl. Phys. 105 (2009) 093918.

[36] J. L. Alonso, L. A. Fernández, F. Guinea, V. Laliena, V. Martín-Mayor, Variational mean-field approach to the double-exchange model, Phys. Rev. B 63 (5) (2001) 054411.

[37] H. Yamada, Metamagnetic transition and susceptibility maximum in an itinerant-electron system, Phys. Rev. B 47 (17) (1993) 11211.

[38] L. D. Landau, E. M. Lifshitz, Statistical Physics, 3rd Edition, Vol. 5 of Course of theoretical physics, Pergamon, Oxford, 1976.

[39] A. Arrott, Criterion for ferromagnetism from observations of magnetic isotherms, Phys. Rev. 108 (6) (1957) 1394.

[40] J.-C. Tolédano, P. Tolédano, The Landau Theory of Phase Transitions, World Scientific, New Jersey, USA, 1987.

[41] P. Weiss, L'hypothèse du champ moléculaire et la propriété ferromagnétique, J. Phys. Theor. Appl. 6 (1907) 661–690.

[42] J. S. Smart, Effective Field Theories of Magnetism, W. B. Saunders Co., Philadelphia, USA, 1966.

[43] G. J. Liu, J. R. Sun, J. Lin, Y. W. Xie, T. Y. Zhao, H. W. Zhang, B. G. Shen, Entropy changes due to the first-order phase transition in the $Gd_5Si_xGe_{4-x}$ system, Appl. Phys. Lett. 88 (21) (2006) 212505–1–212505–3.

[44] Y. Millev, M. Fahnle, General framework for the exact expressions for ferromagnetic magnetization in mean field-theory, Am. J. Phys. 60 (10) (1992) 947–948.

[45] Y. Millev, M. Fahnle, No longer transcendental equations in the homogeneous mean-field theory od ferromagnets, Phys. Stat. Sol. B 171 (2) (1992) 499–504.

[46] A. S. Arrott, Approximations to Brillouin functions for analytic descriptions of ferromagnetism, J. Appl. Phys. 103 (2008) 07C715.

[47] C. Kittel, Introduction to Solid State Physics, 7th Edition, John Wiley and Sons, New York, 1996.

[48] R. M. Bozorth, Ferromagnetism, D. Van Nostrand and Company, New York, USA, 1951.

[49] S. A. Ahern, M. J. C. Martin, W. Sucksmith, The spontaneous magnetization of Nickel+Copper alloys, Proc. R. Soc. London A 248 (1253) (1958) 145–152.

[50] C. P. Bean, D. S. Rodbell, Magnetic disorder as a first-order phase transformation, Phys. Rev. 126 (1) (1962) 104–115.

[51] T. Andrews, On the continuity of the gaseous and liquid states of matter, Proc. R. Soc. Lond. 18 (1869) 42–45.

[52] J. S. Rowlinson, Thomas Andrews and the critical point, Nature 224 (1969) 541–543.

[53] H. E. Stanley, Introduction to Phase Transitions and Critical Phenomena, Clarendon Press, Oxford, 1971.

[54] J. M. Yeomans, Statistical Mechanics Of Phase Transitions, Oxford, 1992.

[55] L.-P. Lévy, Magnétisme et supraconductivité, InterÉditions and CNRS éditions, Paris, 1997.

[56] N. Boccara, Symétries Brisées: Théorie des Transitions avec Paramêtre d'Ordre, Hermann, Paris, 1976.

[57] P. Schofield, J. D. Litster, J. T. Ho, Correlation between critical coefficients and critical exponents, Phys. Rev. Lett. 23 (19) (1969) 1098.

[58] J. T. Ho, J. D. Litster, Divergences of magnetic properties of $CrBr_3$ near critical point, J. Appl. Phys. 40 (3) (1969) 1270.

[59] J. T. Ho, J. D. Litster, Magnetc equation of state of $CrBr_3$ near critical point, Phys. Rev. Lett. 22 (12) (1969) 603.

[60] A. Arrott, J. E. Noakes, Approximate equation of state for Nickel near its critical temperature, Phys. Rev. Lett. 19 (14) (1967) 786–789.

[61] A. Szewczyk, H. Szymczak, A. Wisniewski, K. Piotrowski, R. Kartaszynski, B. Dabrowski, S. Kolesnik, Z. Bukowski, Magnetocaloric effect in $La_{1-x}Sr_xMnO_3$ for x = 0.13 and 0.16, Appl. Phys. Lett. 77 (7) (2000) 1026–1028.

[62] S. M. Bhattacharjee, F. Seno, A measure of data collapse for scaling, J. Phys. A: Math. Gen. 34 (33) (2001) 6375–6380.

[63] M. H. R. Stanley, L. A. N. Amaral, S. V. Buldyrev, S. Havlin, H. Leschhorn, P. Maass, M. A. Salinger, H. E. Stanley, Scaling behaviour in the growth of companies, Nature 379 (6568) (1996) 804–806.

[64] D. W. Sims, E. J. Southall, N. E. Humphries, G. C. Hays, C. J. A. Bradshaw, J. W. Pitchford, A. James, M. Z. Ahmed, A. S. Brierley, M. A. Hindell, D. Morritt, M. K. Musyl, D. Righton, E. L. C. Shepard, V. J. Wearmouth, R. P. Wilson, M. J. Witt, J. D. Metcalfe, Scaling laws of marine predator search behaviour, Nature 451 (7182) (2008) 1098–U5.

[65] J. G. Oliveira, A. L. Barabasi, Human dynamics: Darwin and Einstein correspondence patterns, Nature 437 (7063) (2005) 1251–1251.

[66] P. Bak, K. Christensen, L. Danon, T. Scanlon, Unified scaling law for earthquakes, Phys. Rev. Lett. 88 (17) (2002) 178501.

[67] J. Koda, Y. Sofue, K. Wada, A unified scaling law in spiral galaxies, Astrophys. J. 531 (1) (2000) L17–L20.

[68] V. K. Pecharsky, K. A. Gschneidner, Heat capacity near first order phase transitions and the magnetocaloric effect: An analysis of the errors, and a case study of $Gd_5(Si_2Ge_2)$ and Dy, J. Appl. Phys. 86 (11) (1999) 6315–6321.

[69] A. Giguère, M. Foldeaki, B. R. Gopal, R. Chahine, T. K. Bose, A. Frydman, J. A. Barclay, Direct measurement of the "giant" adiabatic temperature change in $Gd_5Si_2Ge_2$, Phys. Rev. Lett. 83 (11) (1999) 2262–2265.

[70] L. Jia, G. J. Liu, J. Z. Wang, J. R. Sun, H. W. Zhang, B. G. Shen, Field-induced entropy change in the manganite with significant short-range magnetic order, Appl. Phys. Lett. 89 (12) (2006) 122515–1–122515–3.

[71] A. Y. Romanov, V. P. Silin, On magnetocalorical effect of heterogeneous ferromagnets, Fiz. Met. Metalloved. 83 (2) (1997) 5–11.

[72] A. Aharoni, Amorphicity, heterogeneity, and the Arrott plots, J. Appl. Phys. 56 (12) (1984) 3479–3484.

[73] J. S. Kouvel, M. E. Fisher, Detailed magnetic behavior of Nickel near its curie point, Phys. Rev. A 136 (6A) (1964) 1626–1632.

[74] J. S. Kouvel, J. Comly, Critical magnetic behavior of Palladium-Iron alloys, in: R. E. Mills, E. Ascher, R. I. Jaffee (Eds.), Critical Phenomena in Alloys, Magnets and Superconductors, McGraw-Hill, New York, 1970, pp. 437–449.

[75] J. L. Oddou, J. Berthier, P. Peretto, Local critical behavior in Ni-Ta system, Phys. Rev. B 17 (1) (1978) 222–240.

[76] S. I. Hatta, S. Chikazumi, Critical exponents determined for Nickel from magnetization measurement in high magnetic-fields, J. Phys. Soc. Jpn. 40 (1) (1976) 52–55.

[77] M. D. Kuz'min, A. M. Tishin, Experimental critical exponents of "pure" ferromagnets: the cost of excessive proximity to Tc may be too high, Europhys. Lett. 73 (3) (2006) 396–400.

[78] S. N. Kaul, Comment on "Experimental critical exponents of "pure" ferromagnets: the cost of excessive proximity to Tc may be too high" by M. D. Kuz'min and A. M. Tishin, Europhys. Lett. 75 (5) (2006) 839–840.

[79] M. D. Kuz'min, A. M. Tishin, Reply to the comment by S. N. Kaul on "Experimental critical exponents of "pure" ferromagnets: The cost of excessive proximity to Tc may be too high", Europhys. Lett. 77 (5) (2007) 1.

[80] D. L. Connelly, J. S. Loomis, D. E. Mapother, Specific heat of Nickel near Curie temperature, Phys. Rev. B 3 (3) (1971) 924–934.

[81] M. Perez, F. Perrard, V. Massardier, X. Kleber, A. Deschamps, H. de Monestrol, P. Pareige, G. Covarel, Low-temperature solubility of copper in iron: experimental study using thermoelectric power, small angle x-ray scattering and tomographic atom probe, Philos. Mag. 85 (20) (2005) 2197 – 2210.

[82] P. J. Schilling, V. Palshin, R. C. Tittsworth, J. H. He, E. Ma, Overlapping solid solubility in mechanically alloyed fe-ni and fe-cu, Phys. Rev. B 68 (22) (2003) 224204–.

[83] E. Ma, Alloys created between immiscible elements, Prog. Mater. Sci. 50 (4) (2005) 413–509.

[84] L. M. Socolovsky, F. H. Sanchez, P. H. Shingu, Magnetic structure of Fe_xCu_{100-x} magnetoresistive alloys produced by mechanical alloying, Hyp. Interact. 133 (1-4) (2001) 47–52.

[85] D. Martinez-Blanco, P. Gorria, M. J. Perez, J. A. Blanco, M. A. Gonzalez, Low temperature neutron diffraction and magnetization of $Fe_{25}Cu_{75}$ solid solutions, J. Non-Cryst. Solids 353 (8-10) (2007) 859–861.

[86] J. Y. Huang, Y. D. Yu, Y. K. Wu, D. X. Li, H. Q. Ye, Microstructure and nanoscale composition analysis of the mechanical alloying of Fe_xCu_{100-x} (x=16, 60), Acta Mater. 45 (1) (1997) 113–124.

[87] N. Wanderka, U. Czubayko, V. Naundorf, V. A. Ivchenko, A. Y. Yermakov, M. A. Uimin, H. Wollenberger, Characterization of nanoscaled heterogeneities in mechanically alloyed and compacted CuFe, Ultramicroscopy 89 (1-3) (2001) 189–194.

[88] G. Rollmann, M. E. Gruner, A. Hucht, R. Meyer, P. Entel, M. L. Tiago, J. R. Chelikowsky, Shellwise Mackay transformation in iron nanoclusters, Phys. Rev. Lett. 99 (8) (2007) 083402.

[89] M. Eilon, J. Ding, R. Street, Magnetic and magnetoresistive properties of mechanically alloyed $Fe_{25}Cu_{75}$, J. Phys: Cond. Mat. 7 (25) (1995) 4921–4928.

[90] T. Mashimo, X. S. Huang, X. Fan, K. Koyama, M. Motokawa, Slater-pauling curve of Fe-Cu solid solution alloys, Phys. Rev. B 66 (13) (2002) 132407.

[91] G. Mazzone, M. V. Antisari, Structural and magnetic properties of metastable fcc Cu-Fe alloys, Phys. Rev. B 54 (1) (1996) 441–446.

[92] A. Yousif, K. Bouziane, M. E. Elzain, X. Ren, F. J. Berry, H. M. Widatallah, A. Al Rawas, A. Gismelseed, I. A. Al-Omari, Magnetic properties of nanocrystalline Fe_xCu_{1-x} alloys prepared by ball milling, Hyp. Interact. 156 (1) (2004) 213–221.

[93] L. E. Bove, C. Petrillo, F. Sacchetti, G. Mazzone, Experimental study of the spin density of metastable fcc ferromagnetic Fe-Cu alloys, Phys. Rev. B 61 (14) (2000) 9457–9466.

[94] S. L. Palacios, R. Iglesias, D. Martinez-Blanco, P. Gorria, M. J. Perez, J. A. Blanco, A. Hernando, K. Schwarz, High-temperature anti-Invar behavior of γ-Fe precipitates in Fe_xCu_{100-x} solid solutions: Ferromagnetic phases, Phys. Rev. B 72 (17) (2005) 172401.

[95] P. Gorria, D. Martinez-Blanco, J. A. Blanco, M. J. Perez, A. Hernando, L. F. Barquin, R. I. Smith, High-temperature induced ferromagnetism on γ-Fe precipitates in FeCu solid solutions, Phys. Rev. B 72 (1) (2005) 014401.

[96] P. Gorria, D. Martinez-Blanco, J. A. Blanco, M. J. Perez, M. A. Gonzalez, J. Campo, Magnetism and structure of Fe-Cu binary solid solutions obtained by high-energy ball milling, Physica B 384 (1-2) (2006) 336–340.

[97] C. R. H. Bahl, K. K. Nielsen, The effect of demagnetization on the magnetocaloric properties of Gadolinium, J. Appl. Phys. 105 (1) (2009) 5.

[98] H. Y. Hwang, S. W. Cheong, P. G. Radaelli, M. Marezio, B. Batlogg, Lattice effects on the magnetoresistance in doped $LaMnO_3$, Phys. Rev. Lett. 75 (5) (1995) 914–917.

[99] J. Fontcuberta, B. Martinez, A. Seffar, S. Pinol, J. L. Garcia-Munoz, X. Obradors, Colossal magnetoresistance of ferromagnetic manganites: Structural tuning and mechanisms, Phys. Rev. Lett. 76 (7) (1996) 1122–1125.

[100] C. Vazquez-Vazquez, M. C. Blanco, M. Lopez-Quintela, R. D. Sanchez, J. Rivas, S. B. Oseroff, Characterization of $La_{0.67}Ca_{0.33}MnO_{3\pm\delta}$ particles prepared by the sol-gel route, J. Mater. Chem. 8 (4) (1998) 991–1000.

[101] R. D. Shannon, Revised effective ionic-radii and systematic studies of interatomic distances in halides and chalcogenides, Acta Crystallogr. A 32 (Sep1) (1976) 751–767.

[102] L. M. Rodriguez-Martinez, J. P. Attfield, Cation disorder and size effects in magnetoresistive manganese oxide perovskites, Phys. Rev. B 54 (22) (1996) 15622–15625.

[103] P. V. Vanitha, P. N. Santhosh, R. S. Singh, C. N. R. Rao, J. P. Attfield, Effect of the cation size disorder on charge ordering in rare-earth manganates, Phys. Rev. B 59 (21) (1999) 13539–13541.

[104] V. M. Goldschmidt, The laws of crystal chemistry, Naturwissenschaften 14 (1926) 477–485.

[105] V. Ravindranath, M. S. R. Rao, R. Suryanarayanan, G. Rangarajan, Evidence of electronic phase separation in Er^{3+}-doped $La_{0.8}Sr_{0.2}MnO_3$, Appl. Phys. Lett. 82 (17) (2003) 2865–2867.

[106] R. Mathieu, D. Akahoshi, A. Asamitsu, Y. Tomioka, Y. Tokura, Colossal magnetoresistance without phase separation: Disorder-induced spin glass state and nanometer scale orbital-charge correlation in half doped manganites, Phys. Rev. Lett. 93 (22) (2004) 227202.

[107] J. Burgy, M. Mayr, V. Martin-Mayor, A. Moreo, E. Dagotto, Colossal effects in transition metal oxides caused by intrinsic inhomogeneities, Phys. Rev. Lett. 87 (27) (2001) 277202.

[108] C. Sen, G. Alvarez, E. Dagotto, Competing ferromagnetic and charge-ordered states in models for manganites: The origin of the colossal magnetoresistance effect, Phys. Rev. Lett. 98 (12) (2007) 127202–4.

[109] R. B. Griffiths, Nonanalytic behavior above the critical point in a random Ising ferromagnet, Phys. Rev. Lett. 23 (1) (1969) 17.

[110] M. B. Salamon, P. Lin, S. H. Chun, Colossal magnetoresistance is a Griffiths singularity, Phys. Rev. Lett. 88 (19) (2002) 197203.

[111] J. Deisenhofer, D. Braak, H. A. Krug von Nidda, J. Hemberger, R. M. Eremina, V. A. Ivanshin, A. M. Balbashov, G. Jug, A. Loidl, T. Kimura, Y. Tokura, Observation of a griffiths phase in paramagnetic $La_{1-x}Sr_xMno_3$, Phys. Rev. Lett. 95 (25) (2005) 257202.

[112] S. Petit, M. Hennion, F. Moussa, D. Lamago, A. Ivanov, Y. M. Mukovskii, D. Shulyatev, Quantized spin waves in the metallic state of magnetoresistive manganites, Phys. Rev. Lett. 102 (20) (2009) 207201.

[113] J. M. de Teresa, M. R. Ibarra, J. Garcia, J. Blasco, C. Ritter, P. A. Algarabel, C. Marquina, A. del Moral, Spin-glass insulator state in $(Tb\text{-}La)_{2/3}Ca_{1/3}MnO_3$ perovskite, Phys. Rev. Lett. 76 (18) (1996) 3392–3395.

[114] J. M. de Teresa, C. Ritter, M. R. Ibarra, P. A. Algarabel, J. L. Garcia-Munoz, J. Blasco, J. Garcia, C. Marquina, Charge localization, magnetic order, structural behavior, and spin dynamics of $(La\text{-}Tb)_{2/3}Ca_{1/3}MnO_3$ manganese perovskites probed by neutron diffraction and muon spin relaxation, Phys. Rev. B 56 (6) (1997) 3317–3324.

[115] L. Jia, J. R. Sun, B. G. Shen, D. X. Li, S. Nimori, Effect of high pressure on the magnetocaloric property of $LaFe_{11.5}Si_{1.5}$, J. Appl. Phys. 101 (10) (2007) 3.

[116] F. Holtzberg, R. J. Gambino, T. R. McGuire, New ferromagnetic 5 - 4 compounds in rare earth Silicon and Germanium systems, J. Phys. Chem. Solids 28 (11) (1967) 2283–2289.

[117] D. Paudyal, V. K. Pecharsky, K. A. Gschneidner, B. N. Harmon, Electron correlation effects on the magnetostructural transition and magnetocaloric effect in $Gd_5Si_2Ge_2$, Phys. Rev. B 73 (14) (2006) 144406.

[118] P. J. von Ranke, N. A. de Oliveira, S. Gama, Understanding the influence of the first-order magnetic phase transition on the magnetocaloric effect: application to $Gd_5(Si_xGe_{1-x})_4$, J. Magn. Magn. Mater. 277 (1-2) (2004) 78–83.

[119] E. P. Nobrega, N. A. de Oliveira, P. J. von Ranke, A. Troper, Monte Carlo calculations of the magnetocaloric effect in $Gd_5(Si_xGe_{1-x})_4$ compounds, Phys. Rev. B 72 (13) (2005) 7.

[120] D. Haskel, Y. B. Lee, B. N. Harmon, Z. Islam, J. C. Lang, G. Srajer, Y. Mudryk, K. A. Gschneidner, V. K. Pecharsky, Role of Ge in bridging ferromagnetism in the giant magnetocaloric $Gd_5(Si_xGe_{1-x})_4$ alloys, Phys. Rev. Lett. 98 (24) (2007) 4.

[121] V. K. Pecharsky, K. A. Gschneidner, $Gd_5(Si_xGe_{1-x})_4$: An extremum material, Adv. Mater. 13 (9) (2001) 683–686.

[122] S. Srinath, S. N. Kaul, Static universality class for Gadolinium, Phys. Rev. B 60 (17) (1999) 12166.

[123] L. Pytlik, A. Zieba, Magnetic phase diagram of MnAs, J. Magn. Magn. Mater. 51 (1-3) (1985) 199–210.

[124] L. M. Rodriguez-Martinez, J. P. Attfield, Cation disorder and the metal-insulator transition temperature in manganese oxide perovskites, Phys. Rev. B 58 (5) (1998) 2426–2429.

[125] J. D. Moore, G. K. Perkins, Y. Bugoslavsky, L. F. Cohen, M. K. Chattopadhyay, S. B. Roy, P. Chaddah, J. K. A. Gschneidner, V. K. Pecharsky, Correlating the local magnetic properties of the magnetic phase transition in Gd_5Ge_4 using scanning hall probe imaging, Phys. Rev. B 73 (14) (2006) 144426.

[126] K. Morrison, J. D. Moore, K. G. Sandeman, A. D. Caplin, L. F. Cohen, Capturing first- and second-order behavior in magnetocaloric $CoMnSi_{0.92}Ge_{0.08}$, Phys. Rev. B 79 (13) (2009) 134408.

[127] J. D. Moore, K. Morrison, G. K. Perkins, D. L. Schlagel, T. A. Lograsso, K. A. Gschneidner, V. K. Pecharsky, L. F. Cohen, Metamagnetism seeded by nanostructural features of single-crystalline $Gd_5Si_2Ge_2$, Adv. Mater. 21 (37) (2009) 3780–3783.